Energy Reconstruction in the Hadronic Tile Calorimeter and Early SUSY Fully Hadronic Searches in ATLAS

Joaquín Poveda Torres

Departament de Física Atòmica, Molecular i Nuclear and IFIC
(CSIC - Universitat de València)

Submitted on September 23, 2008
Defended on January 23, 2009

Declaration

This dissertation is the result of my own work, except where explicit reference is made to the work of others, and has not been submitted for another qualification to this or any other university.

Joaquín Poveda Torres

Preface

This thesis was finished on the days where the first beams were circulated in the Large Hadron Collider accelerator at the CERN laboratory near Geneva and the work summarized here is framed in the pre-operation phase of one of its experiments: ATLAS.

A general description of the experimental facilities in which this work has been developed is given in Chapter 1: CERN, LHC, the ATLAS experiment and its Hadronic Tile Calorimeter. Chapter 2 gives an overview of the situation of High Energy Physics at the verge of the LHC era together with a summary on the main New Physics beyond the Standard Model which could be discovered at the ATLAS experiment. Since most of the contents of this thesis are related to the calorimetry in ATLAS, Chapter 3 presents briefly the main physics concepts involved in the detection of particle showers in this type of detectors.

Chapters 4 and 5 present all the work done within the ATLAS TileCal collaboration in the field of energy reconstruction. In particular, the Optimal Filtering energy reconstruction algorithm implementation for offline uses and its validation studies with Monte Carlo and real data are presented. This algorithm combines a simple formulation with robustness in the reconstruction of signal amplitude and timing for data affected by electronics noise. Furthermore, the performance under a minimum bias pileup environment and the impact of this kind of physics noise are also shown. Finally, the calorimeter resolution and response for the different methods available and sources of noise (electronics and minimum bias) is discussed.

Chapters 6-8 are devoted to a contribution to the ATLAS Jet/Missing Transverse Energy ($\not{E}_{\mathrm{T}}$) and SUSY groups. Chapter 7 presents cleaning methods for events with large fake $\not{E}_{\mathrm{T}}$ which are based on one hand in the jet energy deposition in selected parts of the calorimeter system which are realted with jet leakage or dead material effects and, on the other hand, in the use of the $\not{E}_{\mathrm{T}}$ obtained just from the inner detector tracks. The application of these methods within SUSY analysis is also presented, discussing its QCD background reduction capabilities.

Chapter 8 shows the fully hadronic SUSY discovery analysis using Monte Carlo data with a signature characterized by at least 4 jets and no lepton in the final state. The cleaning methods described in Chapter 7 are also included in the event selection and the discovery significance which can be achieved with this analysis is discussed for several points in the minimal SuperGravity parameter space.

Finally, the closing Chapters are devoted to the conclusions and summary of the pieces of work included in the present thesis.

Geneva, September 2008.

Contents

“Everything happens for a reason. I’m used to it, I prepare for it. Like I say, at the end of the day, those in charge of their own destiny are going to do what’s right for them and their family.”

— S. O’Neal, b. 1972

Chapter 1

CERN, LHC and ATLAS

"[Atlas] stands immovably upholding the wide heaven upon his head and unwearying hands."
— Hesiod, *Theogony*, c. 700 BC.

1.1 CERN

In 1951, the so-called "Conseil Européen pour la Reserche Nucléaire" (European Council for the Nuclear Research, CERN) was created provisionally and two years later the council decided to build a central laboratory near Geneva. Later on, the name was changed for "European Organization for Nuclear Research", but the acronym lasts until nowadays.

CERN, a nuclear research facility created in the aftermath of World War II, has become more than 50 years after its creation in the world's largest particle physics center. It has 20 European Member States, but many non-European countries are also involved in different ways. It employs 3000 people and about 6500 visiting scientist (coming from over 500 universities and research institutes from more than 80 nations) come to CERN for their research. Apart from physicists, CERN's staff also includes highly specialized engineers, technicians, designers, etc.

The accelerator complex at CERN (shown schematically in Figure 1.1) consists in several machines where particle beams are injected from one to the next, bringing them to higher energies successively. The flagship of the complex is the Large Hadron Collider (LHC), whose first beams were circulated in September 10th 2008 and the first collisions are scheduled for spring 2009. In addition, the LHC injectors have their own experimental hall, where their beams are used for experiments at lower energies.

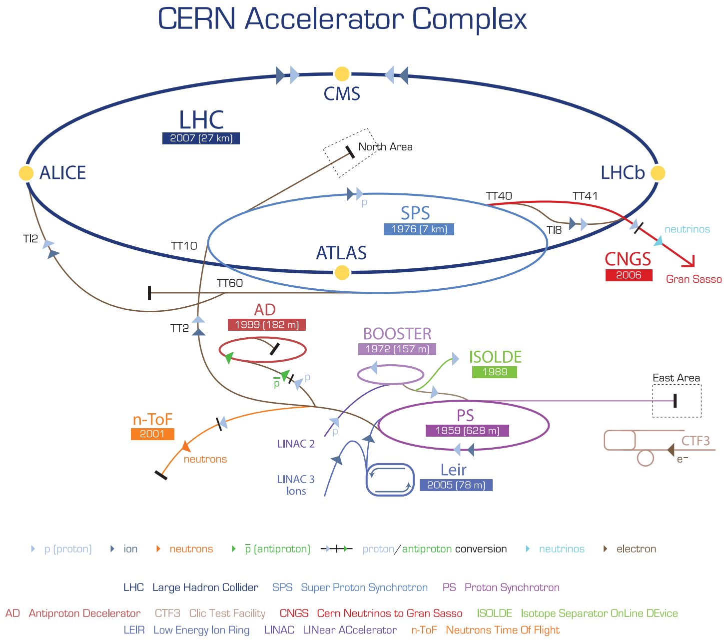

Figure 1.1: Scheme (not to scale) of the CERN accelerator facilities.

Some notable achievements done at CERN in the past were the Intersecting Storage Rings (ISR) proton-proton collider which was commissioned in 1971, and the proton-antiproton collider at the Super Proton Synchrotron (SPS), which came on the air in 1981 and produced the massive W and Z particles two years later, confirming the unified theory of electromagnetic and weak forces. Revolutionary technologic developments, as the invention of the multiwire proportional chamber in the 60s or the world wide web in the 80s, have also been done at CERN. In the 80s and 90s very precise measurements were made in the Large Electron-Positron Collider (LEP), including the measurement of the number of lepton and quark families. The results obtained at LEP confirmed experimentally the Standard Model.

The research program at CERN, apart from the challenge in Particle Physics that LHC is, also includes other fields as Nuclear Physics (with ISOLDE, Isotope Separation OnLine DEvice) or Neutrino Physics (with the project CERN Neutrinos to Gran Sasso, CNGS) and technology development in accelerators, detectors and computer science (such as the GRID project, meant for handling the huge amount of data which are taken at the LHC).

1.2 The Large Hadron Collider

The Large Hadron Collider Project [1] was approved by the CERN Council in December 1994. LHC is the first machine built at CERN with substantial material contribution from non-member states as machine hardware was constructed in laboratories from Canada, India, Japan, Russia and the USA.

The LHC is a two-ring superconducting accelerator and collider installed in the 27 km long LEP tunnel (see Figure 1.2) aiming at the discovery of the Higgs particle and the study of rare events with center of mass collision energies of up to 14 TeV. Table 1.1 summarizes some of the LHC characteristics.

Table 1.1: LHC main parameters.

	Injection	Collision
Ring circumference (m)	26658.883	
Proton Energy (GeV)	450	7000
Relativistic gamma	479.6	7461
Number of particles per bunch	1.1×10^{11}	
Number of bunches	2808	
Stored energy per beam (MJ)	23.3	362
Luminosity lifetime (h)	14.9	
Energy loss per turn (eV)	1.15×10^{-1}	6.71×10^{3}

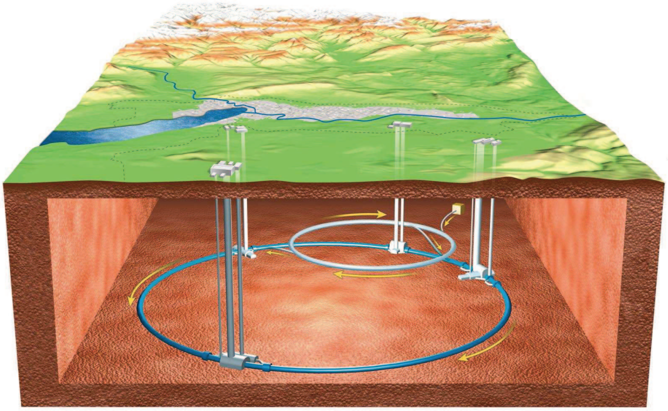

Figure 1.2: Simulation of the LHC placement and all its underground structures.

The LHC has two high-luminosity general-purpose experiments, ATLAS [2] and CMS [3], aiming at a peak luminosity of 10^{34} cm^{-2}s^{-1}. In addition to these high luminosity experiments, the LHC has three low luminosity experiments: LHCb [4] for B-physics intended for a peak luminosity of 10^{32} cm^{-2}s^{-1}, TOTEM [5] for the detection of protons from elastic scattering at small angles designed for a peak luminosity of 2×10^{29} cm^{-2}s^{-1} and LHCf [6] for the measurement of neutral pions produced in the forward direction by the collisions aiming at a peak luminosity of 2×10^{28} cm^{-2}s^{-1}. In addition to the proton beams the LHC is also operated with ion beams and there is a dedicated heavy ion experiment called ALICE [7], working at a peak luminosity of 10^{27} cm^{-2}s^{-1} for nominal Pb-Pb ion operation. Figure 1.3 shows some of the LHC experiments.

Figure 1.3: Simulation for some LHC experiments. From left to right: CMS, LHCb and Alice.

The high beam intensities implied by a luminosity of 10^{34} cm^{-2}s^{-1} exclude the use of anti-proton beams with one common vacuum and magnet system for both circulating beams (as it is done in the TeVatron) and consequently requires the use of two proton beams. Opposite magnet dipole fields are required in order to collide two beams of equally charged particles and since there is not enough room for two separate rings of magnets in the LEP tunnel, LHC uses twin bore magnets which consist of two sets of coils and beam channels within the same mechanical structure and cryostat. Figure 1.4 shows the structure of the LHC dipole magnet.

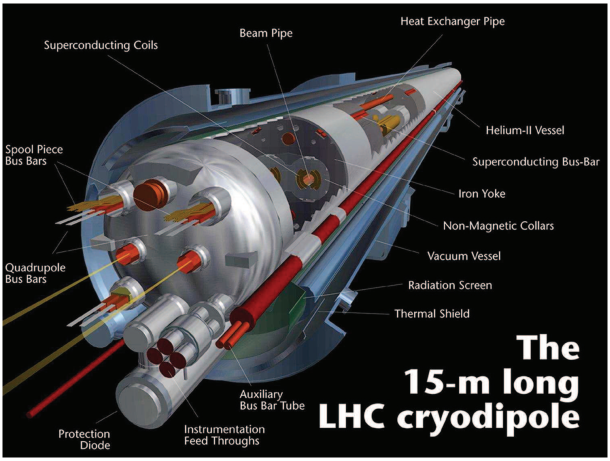

Figure 1.4: Cross section the LHC dipole magnet with its elements labelled.

The peak beam energy in a storage ring depends on the integrated dipole field along the storage ring circumference. Aiming at peak beam energies of up to 7 TeV inside the existing LEP tunnel implies a peak dipole field of 8.33 T and the use of superconducting magnet technology.

The luminosity in the LHC is not constant over a physics run but decays due to the degradation of intensities and emittances of the circulating beams. The main cause for the luminosity decay for nominal LHC performance are the collisions themselves, with a net luminosity lifetime of 14.9 hours.

1.3 The ATLAS Experiment

ATLAS (A Toroidal LHC ApparatuS) is a general-purpose p-p spectrometer designed to exploit the full discovery potential of the LHC. Figure 1.5 shows an illustration of ATLAS. The detector design is optimized for a long range of known, expected and hypothetical processes. This includes a very good electromagnetic calorimetry (for electron and photon identification and measurements), complemented by full-coverage hadronic calorimetry (for accurate jet and missing transverse energy measurements), a high-precision muon measurement system and a very efficient tracking system. In the following Sections, the different ATLAS subdetectors are presented and discussed.

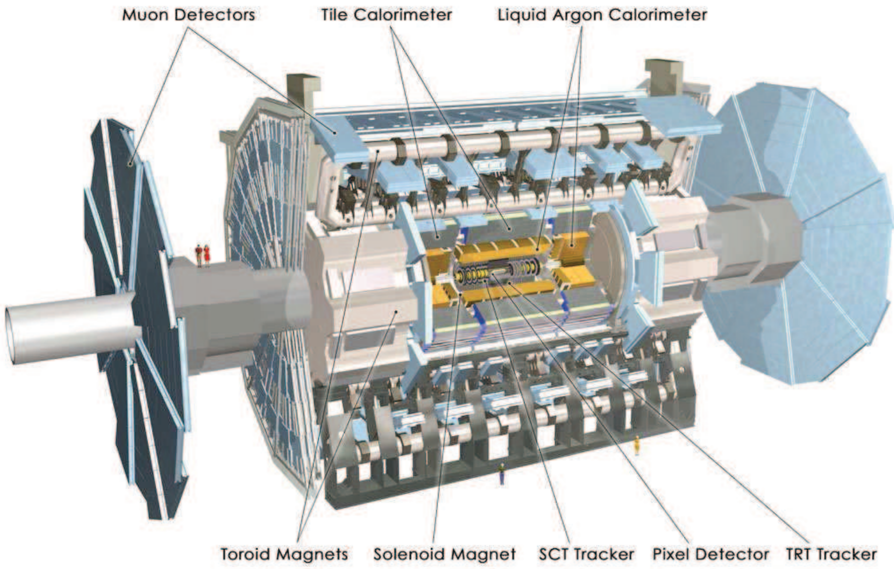

Figure 1.5: Simulation of the ATLAS experiment with all its subdetectors labelled.

1.3.1 Inner Detector

The task of the Inner Detector (ID) [8] is to reconstruct the tracks and vertices in the events with high efficiency, contributing together with the calorimeter and muon systems to the electron, photon and muon recognition, and supplying important extra signatures for short-lived particle decay vertices. In ATLAS, the ID covers the pseudo-rapidity range $|\eta|<2.5$. A three-dimensional view of the Inner detector is shown in Figure 1.6.

Close to the vertex region, silicon Pixel Detectors are used, providing a very high granularity. In an outer layer, the SemiConductor Tracker (SCT) which uses silicon microstrip detectors is placed. To increase the number of tracking points, the Transition Radiation Tracker (TRT) is used, which provides the possibility of continuous track and electron identification by the usage of straw detectors. The combination of the two techniques (silicon and straw detectors) gives very robust pattern recognition and high precision in both ϕ and z coordinates.

The Pixel Detector is designed to provide a very high granularity, high precision set of measurements as close as possible to the interaction point. The system consists of three barrels at average radii of ~4 cm, 11 cm, and 14 cm, and four disks on each side, between radii of 11 and 20 cm, which complete the angular coverage. It contains approximately

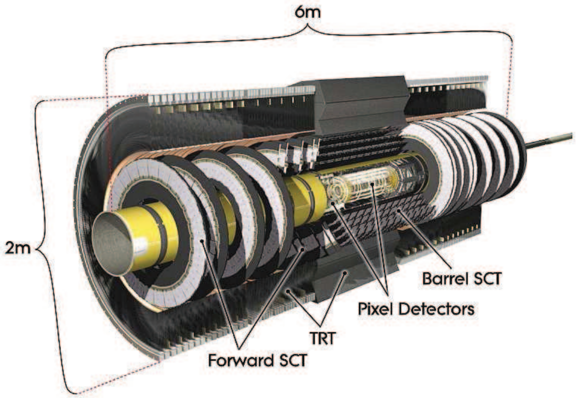

Figure 1.6: Simulation of the ATLAS Inner detector.

1500 identical barrel modules and 1000 identical disk modules with a total amount of 140×10^6 channels for read-out.

The SCT system is designed to provide four precision measurements per track in the intermediate radial range, contributing to the measurement of momentum, impact parameter and vertex position, as well as providing good pattern recognition by the use of high granularity. The barrel SCT uses four layers of silicon microstrip detectors to provide precision points in the r, ϕ and z coordinates. This subdetector contains 61 m^2 of silicon detectors, with 6.2×10^6 read-out channels.

As mentioned above, the TRT is based on the use of straw detectors. Each straw is a small cylindrical proportional chamber, with an anode wire in the center in 1.78 kV potential, and the straw wall acting as a cathode. Electron identification capability has been added by employing xenon gas to detect transition-radiation photons created in a radiator between the straws. The TRT barrel contains about 50000 straws and the endcaps contain 320×10^3 radial straws, with 420×10^3 total electronic channels.

1.3.2 Calorimetry

At the LHC about twenty soft collisions per bunch crossing will be produced when operating at design luminosity (see Section 2.2.2). In consequence fast detector response and fine granularity are required to minimize the impact of the pileup on the physics performance.

The calorimetry part of the ATLAS detector [9] consists of an electromagnetic (EM) calorimeter covering the pseudorapidity region $|\eta|<3.2$, a barrel hadronic calorimeter covering $|\eta|<1.7$, hadronic endcap calorimeters covering $1.4 <|\eta|<3.2$, and forward calorimeters covering $3.2<|\eta|<4.8$.

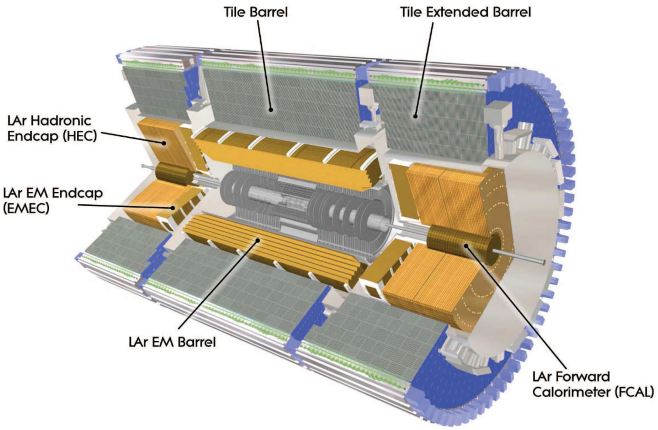

Figure 1.7: Simulation of the ATLAS calorimeter system.

The EM calorimeter is a lead/Liquid-Argon (LAr) [10] detector with accordion geometry. The hadronic barrel calorimeter (Tile Calorimeter [11]) is based on a sampling technique with plastic scintillator plates (tiles) embedded in an steel absorber. At larger rapidities, where higher radiation resistance is needed, the radiation-hard LAr technology is used for all the calorimeters: the Hadronic Endcap Calorimeter (HEC) and the Forward Calorimeter (FCal). A scheme with all the calorimeters for ATLAS can be seen in Figure 1.7.

Liquid Argon Calorimeter

The Liquid Argon sampling calorimeter technique with accordion-shaped electrodes is used for all electromagnetic calorimetry covering the pseudorapidity interval $|\eta|<3.2$. This technique is also used for hadronic calorimetry in the range $1.4<|\eta|<4.8$.

In the barrel, the electromagnetic calorimeter consists of two identical half-barrels covering the rapidity range $|\eta|<1.4$. For each half-barrel (divided into 16 modules) the calorimeter is made of 1024 accordion-shaped absorbers alternating with 1024 read-out electrodes, arranged with a complete ϕ symmetry around the beam axis. Between each pair of absorbers, there are two liquid argon gaps, separated by a read-out electrode.

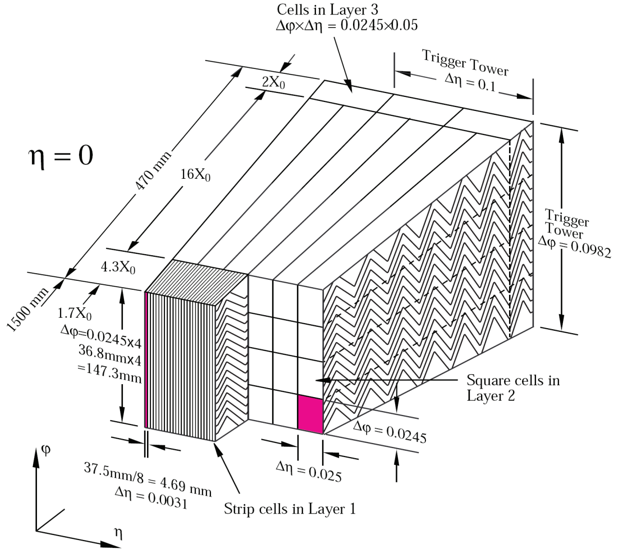

Figure 1.8: On the left, scheme of a LAr EM calorimeter barrel module, where the longitudinal segmentation and cell size is shown. On the right, picture of the calorimeter module, with its accordion structure.

The electromagnetic EndCap calorimeter (EMEC), the HEC and the FCal are placed inside the encap cryostat. The EMEC, which covers the range $1.375<|\eta|<3.2$, uses the same technique as in the barrel part

The HEC covers the range $1.5<|\eta|<3.2$ and uses copper plates as absorbers, with parallel geometry in this case. The FCAL placed in the $3.2<|\eta|<4.9$ region, providing coverage for electromagnetic and hadronic showers by using copper and tungsten as absorbers, respectively.

The EM calorimeter is segmented in three longitudinal samplings in the $|\eta|<2.5$ region and in two samples in the $|\eta|>2.5$ region, as Figure 1.8 shows. The total thickness of the EM calorimeter is above 24 radiation lengths for the barrel and above 26 for the endcaps.

Tile Calorimeter (TileCal)

The Tile Calorimeter is a sampling device made out of steel and scintillating tiles as absorber and active material respectively. It is divided in three sections: the Central Barrel (CB) and two Extended Barrels (EBs). The barrel covers the region $|\eta|<1.0$, and the extended barrels cover the region $0.8<|\eta|<1.7$. Azimuthally, the barrel and extended barrels are divided into 64 modules. Figure 1.9 shows one of these modules. The full depth of the TileCal is above 7 absorption lengths in the CB and about 10 in the EB.

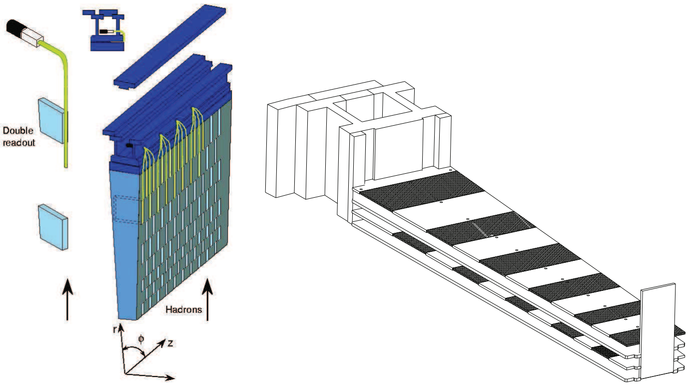

Figure 1.9: On the left, TileCal module design with the placement of all the optic elements (tiles, fibers and PMTs). On the right, view of an assembled tile calorimeter period with the steel parts in white and the scintillating tiles in dark.

The tiles are placed perpendicular to the colliding beams. This represents the main innovation of TileCal because in most hadronic calorimeters the active elements are placed longitudinally. This design optimizes the homogeneity in the signal sampling in the active elements. The TileCal Valencia group at Institut de Física Corpuscular (IFIC) contributed during 1999-2001 in the mechanical construction of 38 modules for one of the Extended Barrels.

The steel structure of each module consists of a stack of repeating elements (periods). As shown in Figure 1.9, each period is a stack of four layers. The first and third layer are formed by large trapezoidal steel plates (master plates), 5 mm thick and spanning the full radial dimension of the module. In the second and fourth layer, smaller trapezoidal steel plates (spacer plates) and scintillating tiles alternate along the radial direction. The spacer plates are 4 mm thick and of 11 different sizes. Scintillating tiles of 3 mm thickness are inserted into the modules after completion of the mechanical steel assembly. The iron to scintillator ratio is 4.67:1 by volume.

The light produced in the scintillating tiles has wavelength in the ultraviolet region and intensity proportional to the energy deposited by the particles. Both sides of the scintillating tiles are read-out along the outside faces of each module by WaveLength Shifting (WLS) fibers into two separate PhotoMultiplier Tubes (PMTs) to achieve a redundant read-out. The

WLS fibers shift the light to longer wavelengths, in order to match the sensitive region of the PMT. Figure 1.9 shows the disposition of the tiles, the fibers and the PMTs in a module.

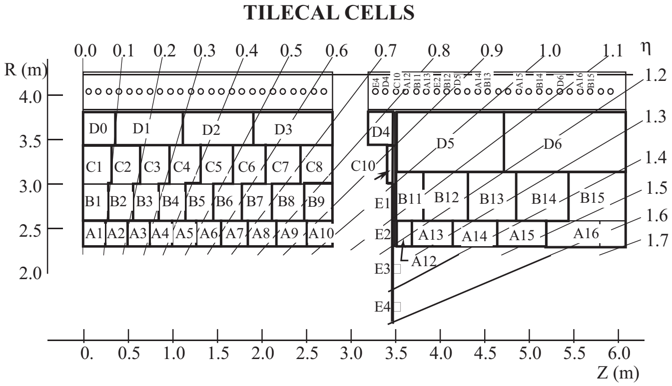

Figure 1.10: Cell granularity for TileCal shown in the rz plane. Note the 3 longitudinal layers (A, BC and D)

The use of fiber read-out allows defining a three-dimensional cell structure, creating a projective geometry for trigger and energy reconstruction, as Figure 1.10 shows. TileCal has a three-sampling longitudinal segmentation, with a $\Delta\phi\times\Delta\eta$ granularity equal to 0.1×0.1 in the first two samplings and 0.1×0.2 in the outermost sampling. A compact structure with all the front-end electronics (called drawer) is housed in the girder. All the TileCal read-out electronics is discussed in detail in Section 1.4.

1.3.3 Muon System

The ATLAS Collaboration has designed a high-resolution muon spectrometer [12] with standalone triggering and momentum measurement capability over a wide range of transverse momentum, pseudorapidity and azimuthal angle. Four chamber technologies are employed in the detector. The positions of these stations are optimized for good hermeticity and optimum momentum resolution. Two-dimensional views of the muon spectrometer in the xy and rz planes are shown in Figure 1.11.

For the precision measurement of muon tracks in the principal bending direction of the magnetic fields, Monitored Drift Tube (MDT) chambers are used except in the innermost ring of the inner station of the endcaps, where particle fluxes are highest. In this region, covering the pseudorapidity range $2<|\eta|<2.7$, Cathode Strip Chambers (CSCs) are employed. The trigger function in the barrel is provided by three stations of Resistive Plate

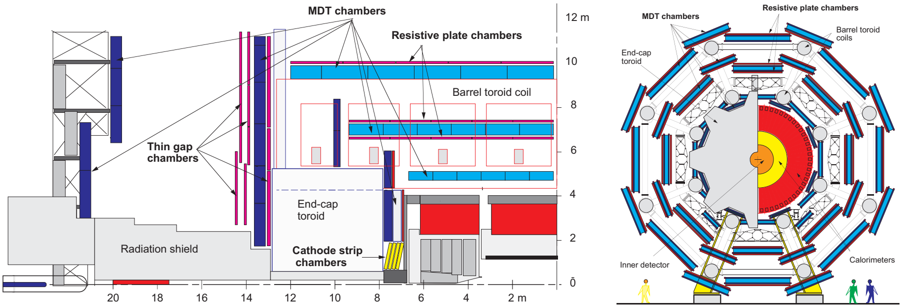

Figure 1.11: Scheme of the ATLAS muon spectrometer in the rz (left) and xy view (right).

Chambers (RPCs). They are located on both sides of the middle MDT station, and either directly above or directly below (depending on ϕ) the outer MDT station. In the endcaps, the trigger is provided by three stations of Thin Gap Chambers (TGCs) located near the middle MDT station.

1.3.4 Magnet System

The ATLAS magnetic field configuration has been optimized for particle bending around the various detectors in a light and open structure which minimizes scattering effects. The experiment magnet system [13] arrangement consists of a central solenoid servicing the inner detector trackers with an axial magnetic field, surrounded by a system of three large scale air-core toroids generating a tangential magnetic field for the muon spectrometer, as shown schematically in Figure 1.12. The niobium-titanium superconductor in a copper matrix technology is used in this case. The magnet system weights 1300 tons and is cooled by liquid helium at 4.5 K.

1.3.5 Trigger

The ATLAS trigger and data-acquisition system [14] is based on three levels of online event selection, as shown in Figure 1.13. Each trigger level verifies and refines the decisions made at the previous level and, where necessary, applies additional selection criteria. Starting from an initial bunch-crossing rate of 40 MHz at design luminosity the final rate of selected events must be reduced to 100 Hz for permanent storage. While this requires an overall rejection factor of 10^7, excellent efficiency must be retained for the rare new physics processes which will be searched for in ATLAS.

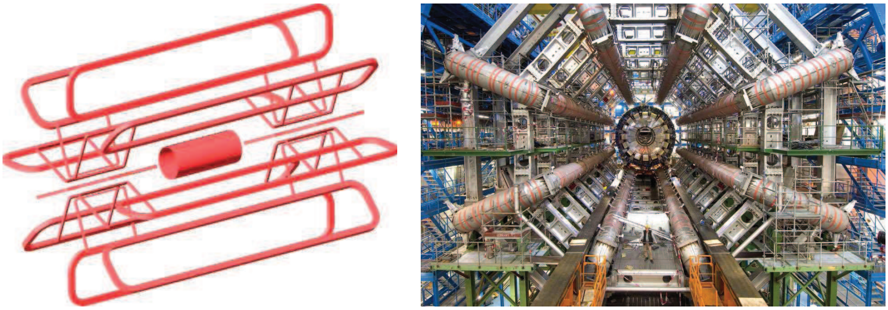

Figure 1.12: Scheme of the ATLAS magnet system (left) and picture of the central toroid (right).

The level-1 (LVL1) trigger is hardware-based and makes an initial selection based on reduced-granularity information from a subset of detectors in the calorimeters and muon system. This level looks for high-p_T muons, electrons, photons, hadronic jets, τ leptons decaying into hadrons, large total transverse energy (E_T) and large missing transverse energy ($\not\!\!E_\mathrm{T}$) in the events. When the LVL1 selection criteria are fulfilled information about the Region of Interest (RoI) is sent to the next level, including the position (η and ϕ) and p_T range of the candidate objects found.

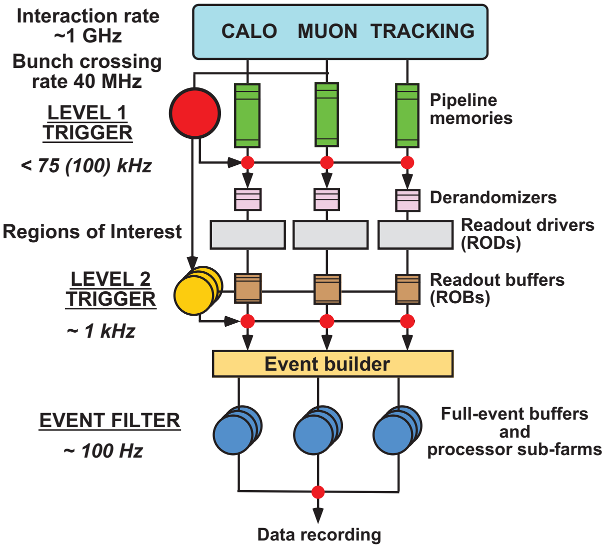

Figure 1.13: Diagram of the ATLAS trigger/DAQ system, showing the 3 trigger levels from the subdetector data taking to the permanent event storage.

The LVL2 trigger is software-based and makes use of RoI information provided by the LVL1 trigger having access to all of the event data, if necessary with the full precision and granularity. After LVL2, a last stage of selection is performed in the Event Filter (EF). Here the algorithms are based on offline code. The EF must reduce the rate to a level suitable for permanent storage, that is 100 Hz for full events of size 1 Mbyte. LVL2 and EF are commonly referred to as a whole by the term High Level Trigger (HLT).

1.4 TileCal Electronics

A general description of the Tile Calorimeter can be found in Section 1.3.2 and this Section is devoted to the description of the calorimeter front-end and back-end electronics.

Figure 1.15 shows schematically the full read-out chain in TileCal from the light signals produced in the optical elements (scintillating tiles and fibers) to the digital data which are transmitted for offline storage and analysis.

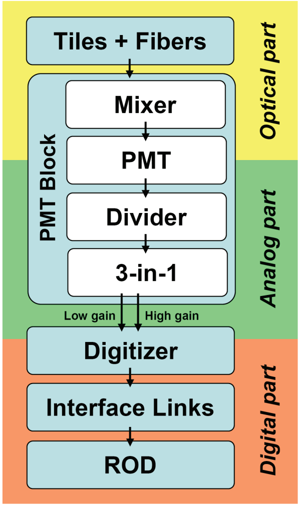

Figure 1.14: General scheme of the TileCal read-out.

1.4.1 Front-End Electronics

All front-end and digitizing electronics in the Tile Calorimeter is placed in the back-beam region of the calorimeter modules, into a girder appended to the end of each module, in a solid box called drawer, as shown in Figure 1.15. Drawers are physically paired into 3-meter-long structures called super-drawers.

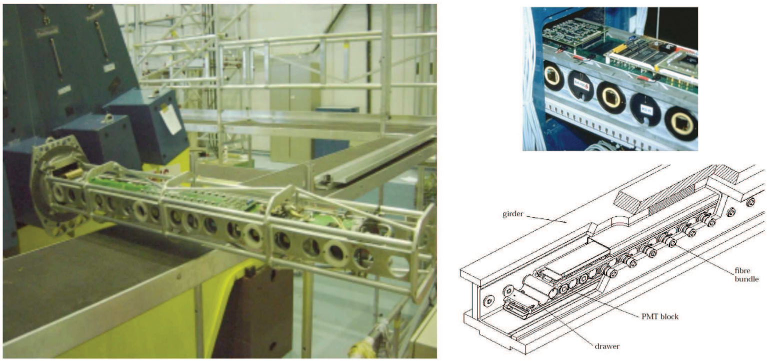

Figure 1.15: On the left, picture of a drawer being extracted from its module. On the right, detail of the PMT and the electronics in the drawer (top) and sketch of the drawer inside the girder with its parts labelled (bottom).

There are 256 super-drawers in TileCal, one for each half-barrel module (two per CB module) and for each EB module. The high voltages (HV) of the PMTs are regulated by special divider boards in the super-drawers.

Outside the super-drawers, in the ATLAS electronics room, the rest of the electronics is located: the HV power supply, the Level-1 trigger (LVL1), the Read-Out Drivers (RODs) and the control electronics for the calibration systems.

PMT block

As mentioned above, the function of the PMT block (shown schematically in Figure 1.16) is to convert light signals from the calorimeter cells into electric signals.

There is one PMT block assigned to each of the about 10000 fiber bundles in TileCal. Each PMT corresponds to one channel for read-out and its main elements are the following:

- **Photomultipliers**: This device is responsible for converting the light signal from the fiber bundles into electric charge. This photomultiplier should be able to work linearly in a wide range, from very low signals (coming from low-p_{T} muons) up to the signals coming from very energetic jets. After several studies, the TileCal Collaboration decided to use the Hamamatsu R5900 photomultiplier. From 2000 to 2003, the

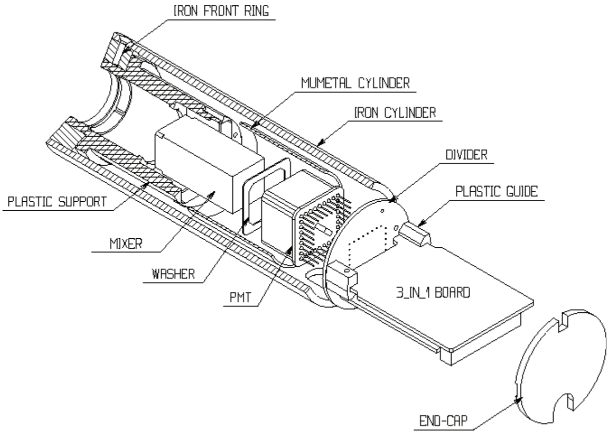

Figure 1.16: Sketch of the TileCal PhotoMultiplier Tubes.

Tilecal-Valencia group characterized at and tested at IFIC about 1750 photomultipliers which are being employed in TileCal.

- **Light Mixers**: As most of the photomultiplier response depends on the photocathode surface, a light mixer is responsible for mixing the light coming from all the fibers in the bundle, so that there is no correlation between the position of the fiber and the area of the photocathode receiving the light.
- **Magnetic Shielding**: The mu-metal and iron magnetic shielding in the PMT must prevent residual fields from the ATLAS solenoid and toroids from producing gain variations. It should provide a protection up to 500 Gauss magnetic fields in any direction.
- **HV Dividers**: The primary purpose of the divider is to partition the high voltage between the dynodes of the PMT. The Tile Calorimeter divider also serves as a socket to allow the connection of the PMT to the front-end electronics without any interconnecting wires. This design minimizes the capacitance between the PMT and the electronics and is important to reduce noise and unreliable connections.
- **3-in-1 Boards**: The main functions of this board are to provide a high and a low gain shaped pulse for the digitizer boards, the charge injection calibration system and slow integration of the PMT signals for monitoring and calibration.

Digitizer System

Fast pulse signals from the 3-in-1 cards are digitized in the digitizer boards and sent down a digital pipeline. On receipt of a LVL1 accept (L1A) signal, the digitizer boards capture an event frame consisting of a string of digitizations. The events (data frames) are stored locally and queued for transmission to the interface link.

Data are presented to the digitizer boards by the 3-in-1 system, which delivers two versions of each signal, a high and a low gain version (being 64 the gain ratio). These analog data are digitized at intervals of 25 ns and stored temporarily. The digitizers are formed mainly by commercial ADCs, TTCrx[1] for Trigger and Timing Control (TTC) information receipt and custom ASIC chip TileDMU (Data Management Unit). Sample saturation is the criteria used to decide which set of data (high or low gain) remains[2].

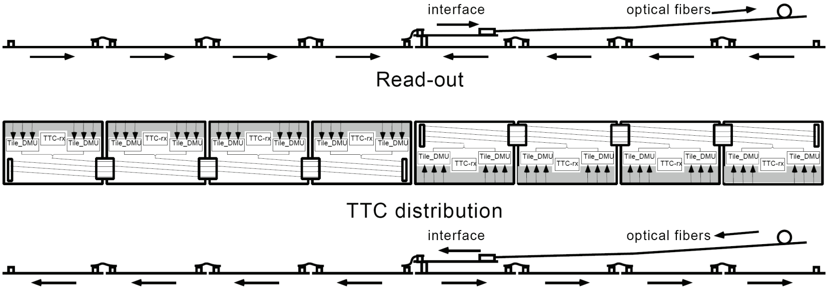

Figure 1.17: Sketch of the digitizer system inside a CB super-drawer. Note the 2 TileDMUs and the TTCrx chip in each digitizer board. The TTC and read-out signal distribution between the digitizers and the interface links is also shown.

On receipt of a L1A, the string of digital samples is sent for transmission to the interface link. The TileDMU is responsible for reformatting and reordering the digitized data and for sending them to the interface links. Each TileDMU manages 3 ADCs, and each digitizer board has 2 TileDMUs. Therefore there are 8 Digitizer boards for CB superdrawers (up to 48 channels, only 45 are needed), and 6 for EB superdrawers (36 possible channels, only 32 are needed). This configuration can be seen schematically in Figure 1.17.

Interface Links

The interface links have two main functionalities: receive the TTC information (two fibers) and distribute it to digitizers equipped with the TTCrx chip and receive the data from the up to 8 digitizer boards in a drawer, deserialize them and send them through an optical link to the input stage of the RODs (see Section 1.4.2). Dual channel read-out is implemented

---

[1] The TTCrx chip is a timing receiver application-specific integrated circuit which delivers the TTC signals to front-end electronics controllers.

[2] In the case that any of the samples is equal to 0, for instance due to errors in the front-end electronics, the channel is also set to have low gain to flag that problem.

to provide redundancy, with two optical fibers transmitting the same TTC and read-out information.

1.4.2 Back-End Electronics

The Read-Out Driver (ROD) board [15] (shown in Figure 1.18) is the central element of the TileCal back-end electronics. The ROD is a 9U VME module which receives as input the fibers from the interface links containing the digitized samples of the electronic pulses at a L1A rate of 100 kHz. One ROD can handle 8 input fibers from 8 different superdrawers. Thus, 32 RODs are needed to read out the whole calorimeter. The ROD processes the data in real time and transmit them to the LVL2 trigger. It is also responsible for error detection, busy generation, etc.

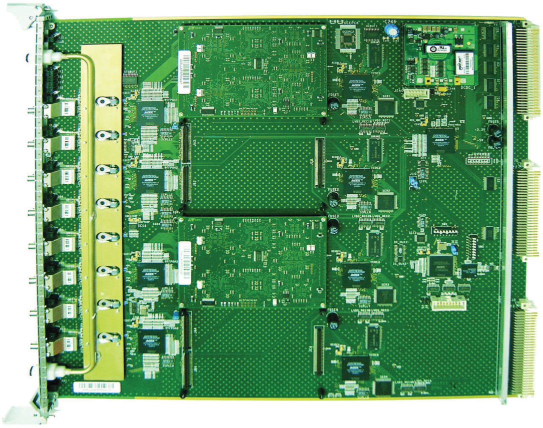

Figure 1.18: Picture of a ROD module. Note the 8 inputs to read-out data coming from 8 superdrawers.

The Tilecal-Valencia group at IFIC is responsible for the design, development, production, installation, deployment and operation of the ROD system in TileCal. During 2005 and 2006 the ROD production and installation was successfully completed. The boards are at present completely operational in the TileCal data taking tasks during detector commissioning and operation.

Since the ROD are equipped with Digital Signal Processors (DSPs), reconstruction algorithms can be applied online on the incoming data so that processed information and not only the raw data are sent to LVL2 trigger. First, a reconstruction algorithm has been implemented which gives as output the energy, timing and a quality factor (as a pileup estimation) for all the processed channels. The reconstruction method used in the ROD DSP is the Optimal Filtering algorithm, discussed extensively in Chapters 4 and 5. In addition, since the channel energy and time are already available in the DSPs, two further algorithms for HLT have been implemented: an online low-p_{T} muon tagging algorithm [16] (which is able to identify muons only from the deposited energy in TileCal and outputs the coordinates of those muons to LVL2 trigger in order to define secondary RoIs) and an algorithm to compute the transverse energy per super-drawer.

Chapter 2

Physics at the Dawn of LHC

"A theory is something nobody believes, except the person who made it. An experiment is something everybody believes, except the person who made it."
— A. Einstein, 1879-1955

2.1 High Energy Physics Overview

2.1.1 Standard Model

The Standard Model (SM) is a very successful description of the interactions of the components of matter at the smallest scales (up to 10^{-18} m) and highest energies (~200 GeV) available. It is a quantum field theory which describes the interaction of spin-1/2, point-like fermions, whose interactions are mediated by spin-1 gauge bosons. The bosons arise when local gauge invariance is applied to the fermion fields, and are a manifestation of the symmetry group of the theory, which for the Standard Model is $SU(3)\times SU(2)\times U(1)$. The fundamental fermions are leptons and quarks. There are three generations of fermions, each identical except for mass. The origin of this generational structure, and the breaking of generational symmetry (i.e. the different masses of each generation) is still unknown. Corresponding to the three generations, there are three leptons with electric charge -1, the electron (e), the muon (μ) and the tau (τ), and three electrically neutral (the neutrinos ν_{e}, ν_μ and ν_τ). Similarly there are three quarks with electric charge +2/3, up (u), charm (c) and top (t), and three with electric charge -1/3, down (d), strange (s) and bottom (b). The quark mass eigenstates are not the same as the eigenstates for the weak force, with mixing between the three generations of quarks, which in the SM is parametrized (but not explained) by the Cabibbo-Kobayashi-Maskawa (CKM) matrix.

The quarks are triplets of the SU(3) gauge group and so they carry an additional “charge”, referred to as color, which is responsible for their participating in the strong interaction (quantum chromodynamics or QCD). Eight vector gluons mediate this interaction; they carry color charges themselves, and are thus self-interacting. This implies that the QCD coupling α_s is small for large momentum transfers but large for soft processes, and leads to the confinement of quarks inside color-neutral hadrons (like protons and neutrons). Attempting to free a quark produces a jet of hadrons through quark-antiquark pair production and gluon *bremsstrahlung*.

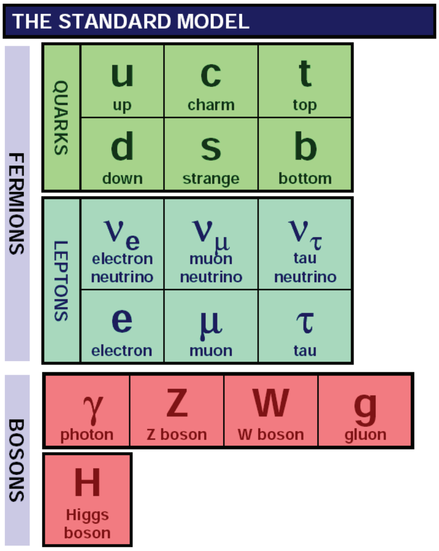

Figure 2.1: Particle content of the Standard Model.

In the SM, the SU(2)×U(1) symmetry group, which describes the so-called Electroweak Interaction, is spontaneously broken through the existence of a (postulated) Higgs field with non-zero expectation value. This leads to the emergence of massive vector bosons, the $W^{\pm}$ and the Z, which mediate the weak interaction, while the photon of electromagnetism remains massless. One physical degree of freedom remains in the Higgs sector, which could be manifest most simply as a neutral scalar boson H, which is presently unobserved. Figure 2.6 shows graphically all the particles in the SM.

The basics of the SM were proposed in the 1960’s and 1970’s [17–20]. Increasing experimental evidence of the correctness of the model accumulated through the 1970’s and

1980's. Deep inelastic scattering experiments at SLAC showed the existence of point-like scattering centers inside nucleons, later identified with quarks. The c and b quarks were observed and neutral weak currents (Z exchange) were identified. Three-jet final states (from gluon bremsstrahlung) were observed in e^+e^- and hadron-hadron collisions, and the W and Z were directly observed at the CERN SPS collider. Following these discoveries, the 1990's decade was largely an era of consolidation. Even more precise experiments were carried out at LEP and SLC which provided verification of the couplings of quarks and leptons at the level of 1-loop radiative corrections - $O(10^{-3})$. The top quark was discovered at FNAL in 1995, and it was found to have an unexpectedly large mass (∼175 GeV). After the discovery in 2000 of the ν_τ in the DONUT experiment also at FNAL, only one particle of the SM has yet to be observed: the Higgs boson. The last, but the most important as it holds the key to the generation of W, Z, quark and lepton masses.

2.1.2 Beyond the Standard Model

The successes of the Standard Model have drawn increased attention to its limitations. In its simplest version, the SM has 19 parameters - 3 coupling constants, 9 quark and lepton masses, the mass of the Z boson which sets the scale of the weak interaction, 4 CKM mixing parameters, and one (small) parameter describing the scale of *CP* violation in the strong interaction. The remaining parameter is associated with the mechanism responsible for the breakdown of the electroweak $SU(2)\times U(1)$ symmetry to $U(1)$ of electromagnetism ("electroweak symmetry breaking" or EWSB). This can be taken as the mass of the Higgs boson since the couplings of the Higgs are determined once its mass is given. Within the model we have no guidance on the expected mass of the Higgs boson. The current experimental lower bound from LEP2 is about 115 GeV, and the upper limit from global fits to electroweak parameters is about 470 GeV. As its mass increases, the self-couplings of the W and Z grow, and so the mass must be less than about 800 GeV, or the strong dynamics of WW and ZZ interactions will reveal new structure. It is this simple argument that sets the energy scale that must be reached to guarantee that an experiment will be able to provide information on the nature of electroweak symmetry breaking, which is the central goal of the LHC.

The presence of a single elementary scalar boson is distasteful to many theorists. If the theory is part of some more fundamental theory with a larger mass scale (such as the scale of grand unification, or the Planck scale) then radiative corrections will result in the Higgs mass being driven up to this large scale unless some delicate cancellations are engineered. There are two ways out of this problem which both result in New Physics on the scale of 1 TeV. New strong dynamics could enter that provide the scale of the W mass or new particles could appear which would cancel the divergences in the Higgs boson mass. In any of these eventualities - Standard Model, new dynamics or new particles - something must be discovered at the TeV scale, i.e. at the LHC.

Supersymmetry (see Section 2.2.7) is an appealing concept for which there is at present no experimental evidence. It offers the only presently known mechanism for incorporating gravity into the quantum theory of particle interactions and provides an elegant cancellation mechanism for the divergences affecting the Higgs mass, while retaining all the successful predictions of the Standard Model and allowing a unification of the three couplings of the gauge interactions at a high scale. Supersymmetric models postulate the existence of superpartners for all the presently observed particles. There are bosonic superpartners of fermions (squarks and sleptons), and fermionic superpartners of bosons (gluinos and gauginos χ_i^0, $\chi_i^\pm$). There are also multiple Higgs bosons: h, H, A and $\mathrm{H}^\pm$. There is thus a large spectrum of presently unobserved particles, whose exact masses, couplings and decay chains are calculable in the theory given certain parameters. Unfortunately these parameters are unknown; but if supersymmetry has anything to do with EWSB, the masses should be in the region 100 GeV - 1 TeV.

An example of the strong coupling scenario is "technicolor" models based on dynamical symmetry breaking. An elegant implementation of these ideas is lacking. Nonetheless, if the dynamics has anything to do with EWSB, we would expect new states in the region 100 GeV - 1 TeV. Most models predict a large spectrum and, at the very least, there must be structure in the WW scattering amplitude at around 1 TeV center-of-mass energy.

There are also other possibilities for New Physics that are not necessarily related to the scale of EWSB. There could be neutral or charged gauge bosons with masses larger than the Z or W. There could be new quarks, charged leptons or massive neutrinos or quarks and leptons might turn out not to be elementary objects. While we have no definite expectations for the masses of such particles, the LHC must be able to search for them over its entire available energy range.

2.2 Physics at ATLAS

This section is a non-exhaustive summary of part of the ATLAS SM physics program and some of the most promising New Physics discovery searches, with a general discussion on the properties of the p-p collisions in first place. All the results shown in this section were obtained with Monte Carlo simulations.

2.2.1 Phenomenology of Proton-Proton Collisions

Inelastic processes dominate high-energy hadron collisions which are characterized by multiple production of secondary mesons and baryon-antibaryon pairs.

The features of hadron-hadron interactions at high energy are overpowered by small momentum transfers (soft collisions) with suppression of particle scattering at large angles. The particles in the final state have large longitudinal momentum but small transverse momentum. Therefore most of the energy escapes in a very narrow cone along the beam pipe. The final states arising from soft collisions, called *minimum bias* (MB) events, represent by far the majority of the p-p interactions, but they are not of big interest due the long-distance interactions of the elementary quark/gluon constituents of the hadrons.

However, it is possible to select very rare events characterized by the short-distance interaction of the elementary constituents. Since a monochromatic proton beam can be seen as a beam of partons (quarks and gluons) with a wide band of energy, these events correspond to the occasional "head-on" or hard collisions between two partons of the incoming hadrons.

These interactions, occurring at small distance, are featured by large momentum transfers, thus particles in the final state can be produced at large angles and massive particles can be created. These interesting physics events are extremely rare compared to soft interactions: for instance, the production of W bosons at LHC has a cross-section of $\sim$150 nb, i.e. 10^5 times smaller than the total inelastic p-p cross-section. Figure 2.2 shows the cross-sections for hard scattering processes as a function of the center-of-mass energy.

In the hard collisions of constituents at hadron colliders the effective center-of-mass energy ($\sqrt{\widehat{s}}$) is smaller than the center-of-mass energy of the machine (14 TeV in the case of LHC) and is given by $\sqrt{\widehat{s}} = \sqrt{x_a x_b s}$ where x_a and x_b are the fractions of the proton momentum carried by the colliding partons. If $x_a \sim x_b$ then the above relation becomes $\sqrt{\widehat{s}} = x\sqrt{s}$ and therefore a particle of mass 5 TeV can only be produced if the two interacting partons carry at least a fraction x $\sim$0.35 of the proton momentum.

The momentum distributions of partons inside a proton are called parton distribution functions (PDF). Figure 2.3 shows the proton PDFs for two different values of the 4-momentum exchanged in the interaction (Q^2). Valence quarks contribute to the quantum numbers of protons and therefore carry a large fraction of the momentum. But protons contain also gluons and other quarks, mainly produced by the gluon radiation from valence quarks, which give rise to the so-called "sea" and which exhibit much smaller momenta.

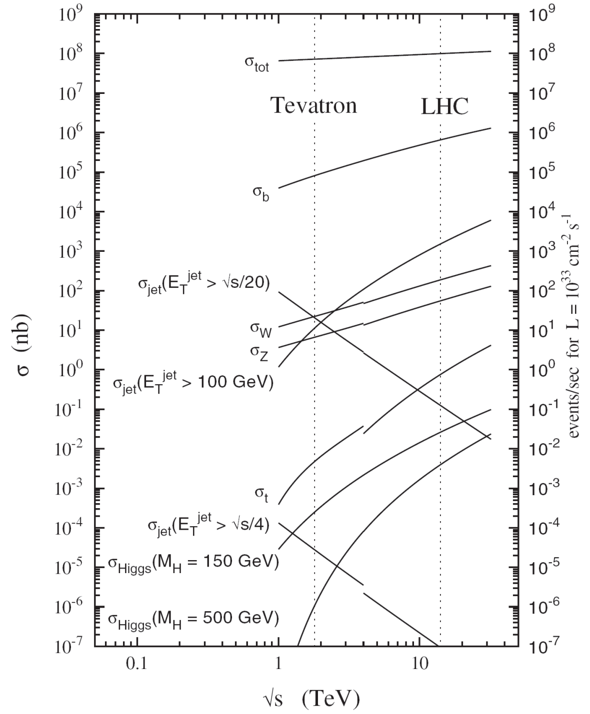

Figure 2.2: Cross sections (left axis) and expected event rates at a luminosity of 10^{33} $\mathrm{cm}^{-2}\mathrm{s}^{-1}$ (right axis) for hard scattering processes in proton-(anti)proton collision at the LHC and TeVatron energy range.

2.2.2 Minimum Bias Events

At the LHC, minimum bias will be a major background for luminosities above 10^{33} $\mathrm{cm}^{-2}\mathrm{s}^{-1}$, where the average number of such events per bunch crossing is greater than 1 (see Section 4.2). In order to understand precisely their contribution to the measured quantities for the hard scattering events of interest, a detailed knowledge of the structure of the minimum bias events is required.

The inelastic component in the p-p interactions can be divided in: non-diffractive, single-diffractive and double-diffractive components. Minimum bias interactions have previously been studied at the CERN ISR, SPS and FNAL TeVatron colliders. Based on these results, Monte Carlo models have been tuned to generate prediction for the LHC conditions. Figure 2.4 shows the η and p_{T} distributions of the charged particles generated with PYTHIA [21] for non-diffractive, single- and double-diffractive inelastic p-p interactions at

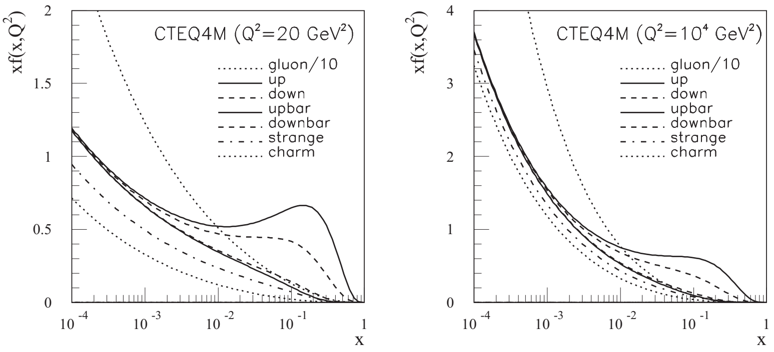

Figure 2.3: Proton parton distribution functions at Q^2=20 GeV^2 (left) and 10^4 GeV^2 (right). The gluon distribution has been reduced by a factor of 10.

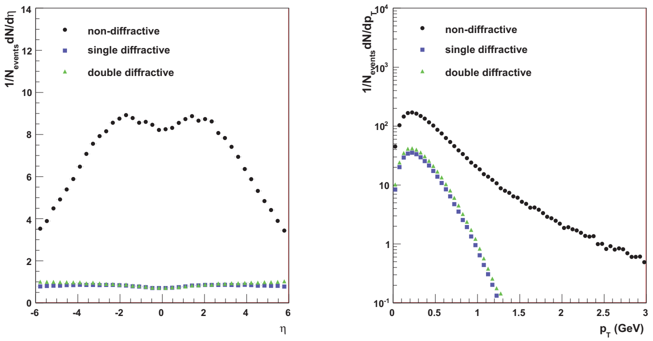

Figure 2.4: Pseudo-rapidity (left) and transverse momentum (right) distributions for stable charged particles from simulated 14 TeV p-p inelastic collisions using the PYTHIA event generator.

$\sqrt{s}$=14 TeV. They clearly show that the minimum bias events are dominated by low-p_{T} particles with highest densities in $|\eta|$<3.0.

2.2.3 Physics of Electroweak Gauge Bosons

Gauge bosons and gauge-boson pairs will be abundantly produced at the LHC. The large statistics and the high center-of-mass energy will allow several precision measurements to be performed, which should improve significantly the precision achieved at present machines, such as:

- **Measurement of the W mass:** The W mass, which is one of the fundamental parameters of the Standard Model, is related to other parameters of the theory and precise measurements of both the W mass and the top mass allow constraining the mass of the SM Higgs boson or of the h boson of the Minimal Supersymmetric Standard Model (MSSM) (see below).

- **Gauge-boson pair production:** The principle of gauge invariance is used as the basis for the SM. The non-Abelian gauge-group structure of the theory of Electroweak Interactions predicts very specific couplings between the Electroweak gauge bosons. Any theory predicting physics beyond the Standard Model, while maintaining the SM as a low-energy limit, may introduce deviations in the couplings. Measurements of these Triple Gauge-boson Couplings and Quadruple Gauge-boson Couplings of the W, Z and γ gauge bosons will not only be a stringent test of the SM and the electroweak symmetry breaking, but also probe for New Physics in the bosonic sector.

2.2.4 B-physics

The rate of B-hadron production at the LHC is enormous thanks to the large hadronic cross-section for b-quark production and the high luminosity of the machine: about one collision in every hundred will produce a b-quark pair. The B-event rate will be higher than in any accelerator in operation before the start-up of the LHC.

An important range of B-physics studies is planned. In fact, an important aim of the B-physics work is to test the SM through precision measurements of B-hadron decays that together will over-constrain the CKM matrix, possibly giving indirect evidence for New Physics.

- ***CP*-violation in B-meson decays:** Within the Standard Model, *CP* violation in weak decays is introduced by the phase of the CKM quark-mixing matrix. The unitarity of this matrix is used to derive triangle relation between the matrix elements, defining the so-called unitary triangle which has 3 angles denoted as α, β and γ.

  The most important channels for studying the *CP* violation in ATLAS are the following:

  - $\mathrm{B_d}^0 \rightarrow \mathrm{J}/\psi\, \mathrm{K_s}^0$, with $\mathrm{J}/\psi \rightarrow \mu\mu$ or $\mathrm{J}/\psi \rightarrow \mathrm{ee}$ and $\mathrm{K}_s^0 \rightarrow \pi^+\pi^-$: This channel can provide a clean measurement of the angle β of the unitary matrix. It is experimentally a very clean channel with relatively low backgrounds.

  - $\mathrm{B}_s^0 \rightarrow \mathrm{J}/\psi\,\phi$, with $\mathrm{J}/\psi \rightarrow \mu\mu$ and $\phi \rightarrow \mathrm{KK}$: Only a very small asymmetry is predicted for this channel in the SM, but an observation of a sizeable effect would be a clear sign of New Physics.
  - $\mathrm{B}_d^0 \rightarrow \mathrm{D}^0\mathrm{K}^{*0}$: The study of the decay amplitude in this channel would be used to determine the angle γ of the unitary matrix.
- **Measurements of $\mathbf{B}_s^0$ oscillations:** The observed B_s^0 and $\overline{\mathrm{B}_s^0}$ states are linear combinations of two mass eigenstates, denoted here as H and L. Due to the non-conservation of flavour in charged weak-current interactions, transitions between B_s^0 and $\overline{\mathrm{B}_s^0}$ states occur with a frequency proportional to $\Delta m_\mathrm{s} = m_\mathrm{H} - m_\mathrm{L}$. Experimentally, these oscillations have not yet been observed directly and simulations show that it will be possible to measure Δm_s at LHC with a good sensitivity.
- **Rare B-decays:** Certain decays, such as $\mathrm{B}_{s,d} \rightarrow \mu\mu(\mathrm{X})$, involve Flavour-Changing Neutral Currents (FCNC) and are strongly suppressed in the Standard Model, with predicted branching ratios typically in the range 10^{-5} to 10^{-10}. These decay modes are forbidden at the tree level in the SM, so the decays involve loop diagrams. In non-standard models of electroweak interactions, FCNC processes can be allowed at the tree level and thus, the branching ratios of these rare decays would not be so suppressed. In addition, in the presence of New Physics, additional particles may be present in the loops again enhancing the decay probability.

2.2.5 Top Physics

The top quark is the only known fundamental fermion with a mass on the electroweak scale. The LHC will be a “top quark factory”, and a very large variety of top physics studies will be possible with the high statistics samples which will be accumulated. As a result, study of the top quark may provide an excellent probe of the sector of the EWSB, and New Physics may well be discovered in either its production or decay.

On top of that, within the Standard Model, an accurate measurement of the top quark mass (m_t) helps constrain the mass of the SM Higgs boson (m_H). In addition, top quark events will be the dominant background in many searches for New Physics at the TeV scale; extraction of New Physics will therefore require detailed measurement and understanding of the production rate and properties of top quark events.

The mass of the top quark is a fundamental parameter of the SM and should be measured as accurately as possible. The most recent combined value of the top quark mass from CDF and DØ is m_t = 170.9 ± 1.1 (stat) ± 1.5 (syst) GeV [22]. With the large number of top quark events which will be available at the LHC, the uncertainty in the measurement of m_t will be dominated by systematic errors.

For instance, within the context of the Standard Model, the decay t→Wb is dominant, with a branching ratio of approximately 99.9%. Expectations for the CKM-suppressed decays are approximately 0.1% and 0.01% for t→Ws and t→Wd, respectively. However, the large top mass implies that the top quark would tend to couple strongly to other massive particles. Therefore, determining whether the top quark has the couplings and decays predicted by the SM provides a sensitive probe of physics beyond the SM.

2.2.6 Higgs Hunting

The Standard Model Higgs boson is searched for at the LHC in a wide variety of decay channels, the choice of which is given by the signal rates and the signal-to-background ratios in the various mass regions. However, most of them suffer from their very small production rate and from very large QCD backgrounds. Excellent detector performance in terms of energy/momentum resolution and unprecedented particle-identification capabilities are required. The most promising channels for Higgs discovery at ATLAS are the following:

- H$\rightarrow \gamma\gamma$ either in direct production or from the associated production WH, ZH and ttH.
- H$\rightarrow \mathrm{b}\overline{\mathrm{b}}$ from the associated production WH, ZH and ttH.
- H$\rightarrow 4l$ (mediated by 2 virtual Z bosons)
- H$\rightarrow 2l2\nu$ (mediated by 2 virtual W bosons)
- H$\rightarrow$ ZZ $\rightarrow 2l2\nu$
- H$\rightarrow$ WW $\rightarrow l\nu 2j$

Figure 2.5 shows the estimated discovery potential for these channels in the ATLAS experiment for a Higgs mass range from 100 GeV to 1 TeV for an integrated luminosity of 100 fb^{-1}.

2.2.7 Supersymmetry

Supersymmetry (SUSY) is a generalization of the space-time symmetries of quantum field theory that transforms fermions into bosons and vice versa. Supersymmetry also provides a framework for the unification of particle physics and gravity, which is governed by the

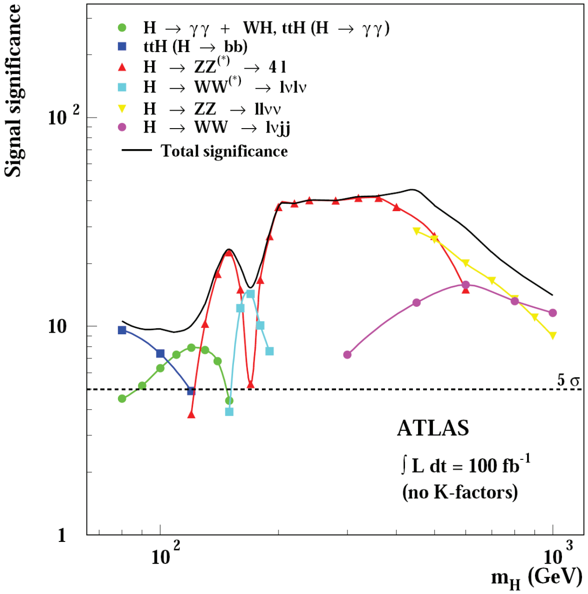

Figure 2.5: ATLAS sensitivity to the discovery of the SM Higgs boson for a 100 fb^{-1} integrated luminosity as a function of the Higgs mass for several decay channels.

Planck energy scale, $M_{\mathrm{Pl}} \sim 10^{19}$ GeV (where the gravitational interactions become comparable in magnitude to the gauge interactions). In particular, it is possible that supersymmetry will ultimately explain the origin of the large hierarchy of energy scales from the W and Z masses to the Planck scale, the so-called gauge hierarchy. The stability of the gauge hierarchy in the presence of radiative quantum corrections is not possible to maintain in the SM, but can be maintained in supersymmetric theories.

If supersymmetry were an exact symmetry of nature, then particles and their superpartners (which differ in spin by half a unit) would be degenerate in mass. Since superpartners have not (yet) been observed, supersymmetry must be a broken symmetry. Nevertheless, the stability of the gauge hierarchy can still be maintained if the supersymmetry breaking is *soft*, and the corresponding SUSY-breaking mass parameters are no larger than a few TeV.

Another argument which supports the existence of SUSY is the fact that there are experimental evidences that about 90% of the matter of the universe is dark. Furthermore, the large scale structure of the universe may be accommodated supposing two kinds of dark matter. One kind is composed of particles which were relativistic at the time of the structure formation. This is called Hot Dark Matter (HDM). The other kind is composed of particles which were non-relativistic at the time of structure formation. These constitute the Cold

Dark Matter (CDM) component of the universe. In any case the CDM component of the universe is at least 60%.

The existence of dark matter cannot be explained within the Standard Model of particle physics. It is tempting to attribute the dark matter to the existence of a neutral stable thermal relic (i.e., a particle that was in thermal equilibrium with all other fundamental particles in the early universe at temperatures above the particle mass). Remarkably, the existence of such a particle could yield the observed density of dark matter if its mass and interaction rate were governed by New Physics associated with the TeV-scale. The lightest supersymmetric particle is a promising (although not the unique) candidate for the dark matter.

Minimal Supersymmetric Standard Model

The Minimal Supersymmetric Standard Model (MSSM) is the SUSY model with the minimal particle content. Each-left handed and right-handed fermion of the SM is postuled to have its own bosonic superpartner with equal mass and coupling strengths. Similarly, each SM boson would have its own fermionic superpartner with equal mass and couplings.

Figure 2.6 shows the particle content of the MSSM. The Higgs sector consist of two complex doublets of Higgs fields, leading to five physical states: one CP-odd neutral pseudoscalar (A), two neutral CP-even scalars (h and H) and two charged bosons ($H^{\pm}$). The superpartners of the SM fermions are denoted with the prefix s- (so there would be a slepton, squark, etc) and the superpartner of the SM bosons have the suffix -ino (photino, zino, wino, etc.). In shorthand notation, these superpartners are denoted with a tilde ($\tilde{e}$, $\tilde{g}$, $\tilde{q}$, $\tilde{Z}$, etc.). The partners of the gauge and Higgs bosons are called gauginos and higgsinos, respectively. Note that the charged (neutral) gauginos and higgsinos are mixed to give physical mass eigenstates called charginos (neutralinos).

As a consequence of barion-lepton number invariance, the MSSM has a multiplicative R-parity invariance, $R = (-1)^{3(B-L)+2S}$ where B, L, and S are the baryon number, lepton number and spin. Note that this implies that all the ordinary Standard Model particles have even R parity, whereas the corresponding supersymmetric partners have odd R parity. The conservation of R parity in scattering and decay processes has a crucial impact on supersymmetric phenomenology. For example, starting from an initial state involving ordinary (R-even) particles, it follows that supersymmetric particles must be produced in pairs. In general, these particles are highly unstable and decay into lighter states. However, R-parity invariance also implies that the Lightest Supersymmetric Particle (LSP) is absolutely stable,

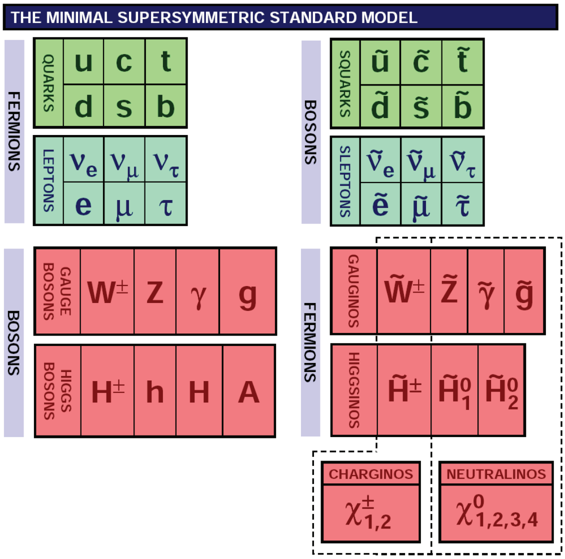

Figure 2.6: Minimal Supersymmetric Standard Model particle content.

and must eventually be produced at the end of a decay chain initiated by the decay of a heavy unstable supersymmetric particle.

In order to be consistent with cosmological constraints, a stable LSP is almost certainly electrically and color neutral. Consequently, the LSP in an R-parity-conserving theory is weakly interacting with ordinary matter, i.e., it behaves like a stable heavy neutrino and will escape collider detectors without being directly observed. Thus, the canonical signature for conventional R-parity-conserving supersymmetric theories is missing transverse energy due to the escape of the LSP.

In the MSSM there are a total of 105 new parameters in addition to the Standard Model ones. Clearly it is not possible to explore the complete parameter space of the MSSM and in the absence of experimental help some theoretical prejudice must be imposed. Hence, with additional assumptions on top of the MSSM, several models have been developed such as supergravity (SUGRA), minimal supergravity (mSUGRA), Gauge Mediated Supersymmetry Breaking (GMSB), R-parity violating scenarios, etc. Even if the general MSSM is correct, none of these scenarios is likely to be the whole truth, but they do provide self-consistent frameworks in which to test the ability of the ATLAS detector to study supersymmetry at the LHC.

Chapter 6 is devoted to the inclusive mSUGRA analysis at ATLAS in the 0-lepton channel.

2.2.8 Extra-dimensions

Theories involving extra spatial dimensions have been developed to find mechanisms to unify gravity with quantum mechanics and/or the M_{W}-M_{Pl} hierarchy problem and can have direct implications for collider experiments.

Let us consider a D-dimensional spacetime (called “bulk”) with $D = 4 + \delta$, where δ is the number of extra spatial dimensions. Standard Model fields are assumed to be localized on a (3+1)-dimensional subspace (called “brane”). This assumption can be realized in field theory, but it is most natural in the setting of string theory, so that gauge and matter fields can be confined to live on branes. On the other hand, gravity, which according to general relativity is described by the spacetime geometry, extends to all D dimensions and gravitons are allowed to propagate in the bulk. These particles lead to the appearance in the brane of a tower of massive particles: Kaluza-Klein (KK) excitations with the same properties as the original particle but with a mass proportional to the size of the extra-dimensions (R).

Since the produced gravitons interact with matter only with rates suppressed by inverse powers of M_{Pl}, they will remain undetected leaving a $\not{E}_{\mathrm{T}}$ signature. The D-dimensional graviton can then be recast as a tower of KK states with increasing mass. Since R^{-1} is smaller than the typical energy resolution in collider experiments, the mass distribution of KK gravitons is practically continuous.

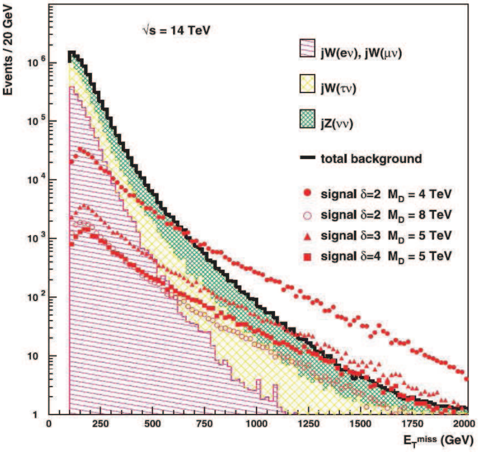

Figure 2.7: Distribution of the missing transverse energy for background and signal events for 100 fb^{-1} for several values of (δ,M_{D}).

Although each KK graviton has a purely gravitational coupling suppressed by M_{Pl}^{-1}, inclusive processes in which we sum over the large number of available gravitons have cross sections suppressed only by powers of the effective gravitational scale (M_{D}), which is then connected to the Planck scale through:

$$M_{\mathrm{Pl}}^{2} \sim M_{\mathrm{D}}^{2+\delta} R^{\delta}. \tag{2.1}$$

Processes involving gravitons are therefore detectable in collider experiments if M_{D} is in the TeV region. The current combined LEP 95% CL limits are $M_{\mathrm{D}} > 1.60$, 1.20, 0.94, 0.77, 0.66 TeV for $\delta = 2,\ldots, 6$ respectively. The most promising channels for extra-dimensions discovery are pp→jet+$\not\!\!E_{\mathrm{T}}$ and pp→ γ+$\not\!\!E_{\mathrm{T}}$ [23]. Figure 2.7 show the $\not\!\!E_{\mathrm{T}}$ distribution for extra-dimension signal at several δ and M_{D} for the single jet channel. The single photon channel has more limited sensitivity but could be a cross check in case of a discovery in the jet channel.

2.2.9 Other Physics Beyond the Standard Model

- **Fourth generation of quarks and leptons:** Data from LEP imply the existence of only three SM families with light neutrinos. However, extra generations with heavy neutrinos are not excluded, and models which include them have been proposed. The current experimental limits on fourth family quarks and leptons are $m_{\mathrm{l}} > 80$ GeV and $m_{\mathrm{q}} > 128$ GeV.

  The replication of three generations of quarks and leptons suggests the possibility that they are composite structures made up of more fundamental constituents.

- **Compositeness:** If quarks and leptons are made of constituents, at the scale of constituent binding energies, new interactions among quarks and leptons should appear. At energies much below the compositeness scale (Λ), these interactions are suppressed by inverse powers of Λ. Another typical consequence of compositeness is the appearance of excited leptons and quarks (l^* and q^*). Phenomenologically, an excited lepton is defined to be a heavy lepton which shares leptonic quantum number with one of the existing leptons (an excited quark is defined similarly).

- **New vector bosons:** The W′ (Z′) boson is a hypothetical massive particle of electric charge ±1 and spin 1 (electrically-neutral and color-singlet particle of spin 1), which are predicted in various extensions of the standard model. The discovery of the W′ could be performed in ATLAS via its decays leptonic decays (such as W′→eν, as Figure 2.8 shows), W′→$\bar{\mathrm{t}}$b or W′→WZ→(ln)(ll).

  Promising channels for the Z′ discovery are ee, $\mu\mu$, eμ, $\tau\tau$ and t$\bar{\mathrm{t}}$ or Z′→WW→(jj)(eν_{e}).

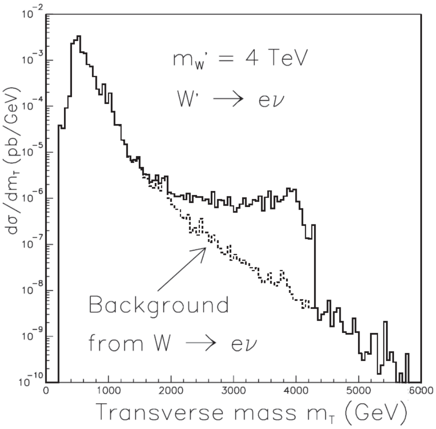

Figure 2.8: Expected transverse mass distribution for W′→eν decays above the dominant W→eν background, with $m_{\mathrm{W}'}$=4 TeV and for an integrated luminosity of 100 fb^{-1}.

- **Leptoquarks:** Leptoquarks (LQs) are hypothetical particles carrying both baryon number and lepton number. Leptoquark states are a generic prediction of Grand Unified Theories (GUTs), of composite models, of technicolor schemes, of supersymmetry with R-parity violation, etc. At LHC scalar leptoquarks can be produced via gg fusion and q$\bar{\mathrm{q}}$ annihilation. If the two LQs are assumed to decay to a charged lepton and a quark a topology with two high-p_{T} leptons and two high-E_{T} jets is provided. In the case that both LQs are assumed to decay to a neutrino and a quark, events will present a topology with two high-E_{T} jets and large $\not{E}_{\mathrm{T}}$.
- **Technicolor:** Technicolor theory provides a dynamical means of breaking electroweak symmetry. It assumes the existence of technifermions possessing a technicolor charge and interacting strongly at a high scale. The ATLAS detector will be sensitive to these new resonances predicted in technicolor theory, up to the TeV range. Although the parameter space is very large, the number of potential channels allows for combinations of signatures to help in understanding the nature of the resonances, and determine the possible existence of techniparticles.

Chapter 3

Physics of Calorimetry

“Experience does not ever err; it is only your judgment that errs in promising itself results which are not caused by your experiments.”
— L. da Vinci, 1452-1519

3.1 Electromagnetic Showers

The particles that constitute an electromagnetic shower are electrons, positrons and photons. They interact with matter via processes that can be described by Quantum Electrodynamics (QED). The most important process are ionization, *bremsstrahlung* (“deceleration radiation”) and pair production. Properties of electromagnetic showers can be described with several empirical functions in a simpler way than with the full proper QED formulation.

3.1.1 Charged Particles

Charged particles, like electrons or positrons, which go through matter lose their energy according to some well known energy-loss mechanism which can be summarized as follows [24]:

- Charged particles can ionize the medium if their energy is enough to unbind an electron from the atomic nucleus Coulomb field. An higher energies, more energetic knock-on electrons (δ rays) can be produced.
- Atoms or molecules can be excited and left in a metastable state.

- The charged particle can emit Čerenkov light if it travels faster than the speed of light in the medium.
- At high energies, photons from *bremsstrahlung* are emitted if the charged particle interacts with an electromagnetic field.
- Nuclear reactions can be induced at very high energies but the probability is very small.

Most of the time the total energy loss by a charged particle is a mixture of the processes above, their relative importance depending on the particle energy, mass (A) or the atomic number (Z) of the traversed medium.

For energies lower than 10 MeV, electrons lose their energy mainly ionizing with atoms or molecules. Above 10 MeV, *bremsstrahlung* is the main source of energy loss. The spectrum of the radiated photons goes as $1/E$, that is, most of the created photons have small energies, but it is possible to have photons carrying up to the whole energy of the radiating particle. Figure 3.2 shows the energy loss by these mechanisms as a function of the electron energy.

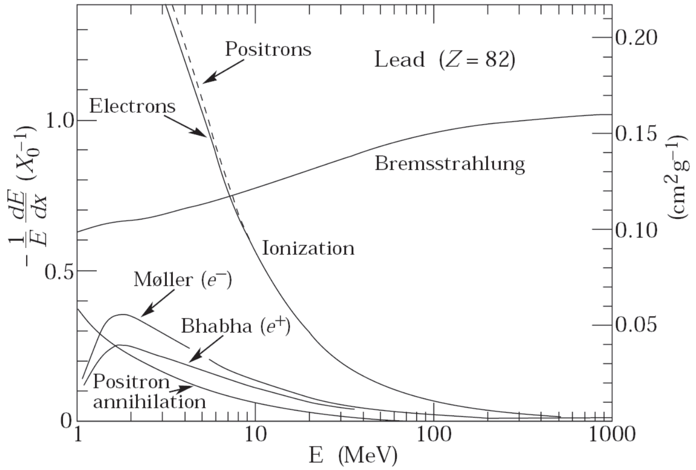

Figure 3.1: Electron or positron fractional energy loss per radiation length in lead as a function of their energy.

3.1.2 Photons

Photons interact differently than charged particles. Although without charge, they are the force carrier particles for the electromagnetic interaction and therefore play an important role in EM showers. The main process in which photons interact with matter are:

- **Photoelectric effect**: in this process an atom absorbs a photon and emits an electron. The atom, which is left in an excited state, returns to the ground state by the emission of X-rays or Auger electrons. At low energies, this is the most probable process and its cross section is strongly dependent on the number of available electrons and scales with Z^n, where n is 4 to 5 and has a energy dependence with E^{-3}.
- **Rayleigh (coherent) scattering**: in this process the photon is deflected by an atomic nucleus but does not lose any energy. Thus it does not contribute directly to the energy loss and it is important at low energies only.
- **Compton scattering**: it occurs when a photon is scattered by an atomic electron and enough energy is transfered so that the electron enters an unbound state. It is by far the most probable process for the energy range between few hundred keV and 5 MeV (except for high Z absorber materials). The cross section for Compton scattering is almost proportional to Z. With increasing energy the cross section decreases with $\sim 1/E$, therefore above a certain threshold Compton scattering becomes more probable than photoelectric effect.
- **Pair production**: if the photon has more energy than twice the electron rest mass, it can create an electron-positron pair in the field of a charged particle. Typically 99% of these processes are caused by nuclear electromagnetic fields. Only for low-Z materials and high energies the e^+e^- creation in fields of atomic electrons contribute significantly. Once created, the e^+ and e^- produce *bremsstrahlung* and ionization along their paths. The electron is eventually absorbed by an ion and the positron annihilates with an electron in the medium. If the positron was at rest, two 511-keV photons are produced. The cross section for pair production rises with energy and reaches a plateau at very high energies (above 1 GeV).
- **Photonuclear reactions**: these processes play only a modest role in the energy range between 5 and 20 MeV.

The relative importance of these processes depends on the photon energy and the electron density ($\sim Z$). Figure 3.2 shows the cross section for these processes for photons going through two different materials.

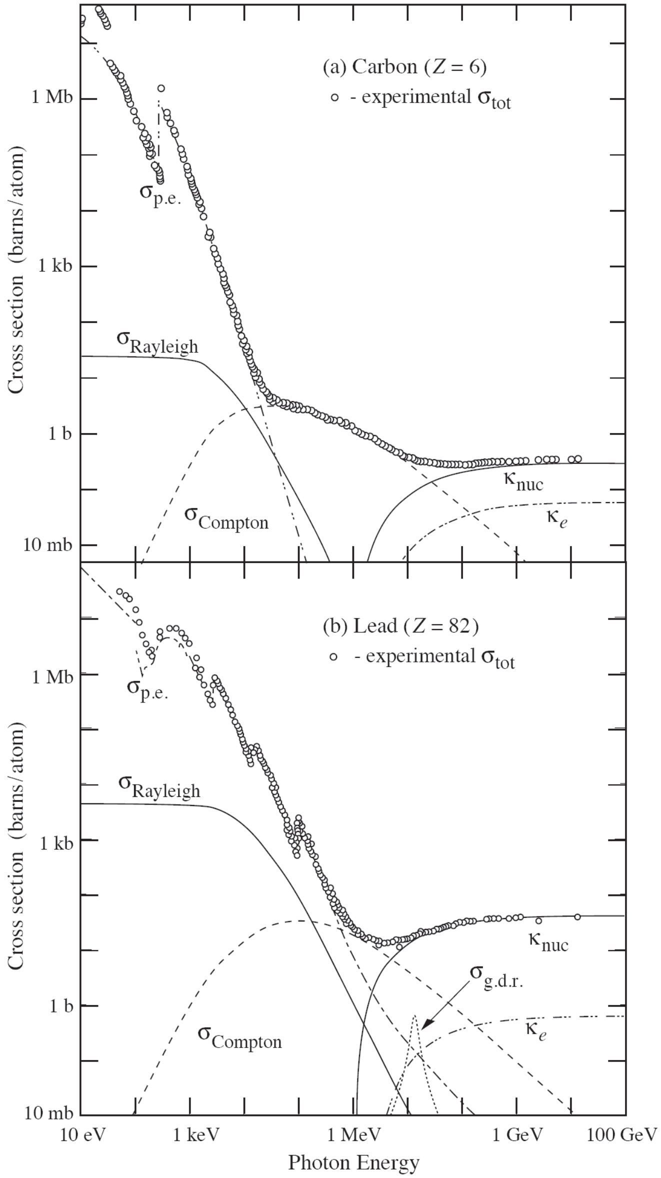

Figure 3.2: Photon total cross sections as a function of energy in carbon (top) and lead (bottom), showing the contributions of different processes: photoelectric effect ($\sigma_{\text{p.e.}}$), Rayleigh scattering (σ_{Rayleigh}), Compton scattering (σ_{Compton}), pair production in nuclear and electron field (κ_{nuc} and κ_{e}) and photonuclear interactions ($\sigma_{\text{g.d.r.}}$).

3.1.3 Shower Development

Having discussed the possible interactions of the EM shower particles with matter, we can now take a closer look at how an EM shower is created and discuss some of its properties.

A multi-GeV electron or photon impinging on a block of matter will start to produce secondary photons through *bremsstrahlung* or secondary electrons and positrons through pair production. If these secondary particles are energetic enough, they will again produce new particles according to the processes above successively. This avalanche effect creates a cascade (or shower) of particles with decreasing energy. The number of particles in the shower increases until the energy of the electrons falls bellow the critical energy E_c, where the energy is mainly dissipated by ionization and excitation and not by generation of other particles.

Two different definitions can be used for the critical energy: the energy at which the average energy losses from *bremsstrahlung* equals those from ionization or the energy a which the ionization loss per radiation length equals the electron energy. This latter definition is preferred by the Particle Data Group (PDG) [25, 26] and takes the following expression for electrons in solids and liquids:

$$E_c = \frac{610\ \text{MeV}}{Z + 1.24}. \tag{3.1}$$

For heavier particles of mass m, e.g. muons, the critical energy scales with $(m/m_e)^2$.

3.1.4 Radiation Length

A convenient way to measure the thickness of a material is to express it in radiation lengths (X_0) since this quantity is material independent in first approximation. It is defined as the distance over which a high energy electron (≫1 GeV) loses all but $1/e$ (36.8%) of its energy by *bremsstrahlung*:

$$E(x) = E_0 \mathrm{e}^{-\frac{\mathrm{x}}{\mathrm{X}_0}}. \tag{3.2}$$

For photons a similar definition can be made. Photons are absorbed mainly through pair production. The intensity of a photon beam is reduced to $1/e$ of the initial intensity after traveling $x = 9/7X_0$, that is:

$$I(x) = I_0 \mathrm{e}^{-\frac{7}{9}\frac{\mathrm{x}}{\mathrm{X}_0}}. \tag{3.3}$$

The independence of X_0 on materials makes the use of this unit very convenient to compare EM showers in different materials. For example, high-energy electrons lose the same fraction of energy in 180 mm of water ($0.5X_0$) as in 2.8 mm of lead ($0.5X_0$).

3.1.5 Longitudinal Shower Profile

The longitudinal length of the shower profile depends logarithmically on the incident particle energy. A typical shower profile of electrons is shown in Figure 3.3. As shown, relatively little material is needed to contain high energetic particles. Considering the Rossi-Heitler model [24] for EM shower development, where it is assumed that the incoming particles divide their energy between two daughter particles every radiation length, only one additional X_0 is needed to absorb showers with twice more energy.

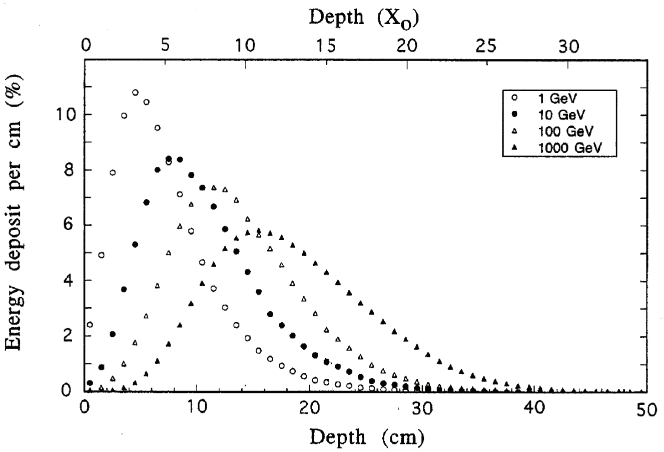

Figure 3.3: Normalized energy deposition as a function of the depth for showers created by electrons at different energies in cooper.

Therefore, to contain 99% of the energy of 300 GeV electrons inside a calorimeter, only 25 X_0 are needed. This makes the EM calorimeters relatively compact devices, even for LHC energies.

3.1.6 Lateral Shower Profile

Due to multiple scattering of electrons, positrons and *bremsstrahlung* photons, the EM shower grows in the transverse direction. The Molière radius (R_M) gives an approximate description of the transverse development of electromagnetic showers in different materials. It can be computed with the following expression:

$$R_{\mathrm{M}} = X_0 \frac{21 \text{ MeV}}{E_c}. \tag{3.4}$$

On average, about 90% of the shower energy is deposited inside a cylinder with radius $R \approx R_{\mathrm{M}}$. For most calorimeters R_{M} is on the order of a few centimeters, making EM showers very narrow. In addition, their transverse size is almost energy independent.

3.2 Interaction of Muons in Matter

High energy muons going through a material lose their energy due to the following electromagnetic processes: ionization, *bremsstrahlung*, direct pair production and photonuclear reactions. The mean rate of energy loss or stopping power ($\mathrm{d}E/\mathrm{d}x$) strongly depends on the energy of the particle as shown in Figure 3.4. After a peak for very low muon energies, the stopping power reaches a minimum and then undergoes the so-called "relativistic rise" until radiative losses begin to play a major role. Muons or other particles with unitary charge, with an energy corresponding to that at which the stopping power curve reaches its minimum are called "Minimum Ionizing Particles" or MIPs.

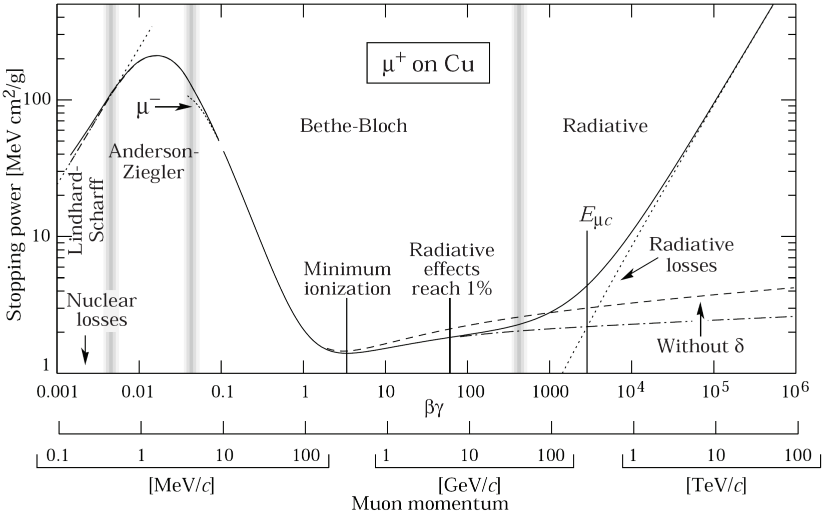

Figure 3.4: Stopping power for positive muons in copper as a function of $\beta\gamma = p/Mc$ over nine orders of magnitude in momentum (12 orders of magnitude in kinetic energy).

Muons only lose a small fraction of their energy in the calorimeters due to the small number of collisions with atomic electrons. In addition, the energy transfer in these collisions is subject to large fluctuations. Thus, the energy loss distributions reach their maximum value in general below the value calculated on the basis of $\mathrm{d}E/\mathrm{d}x$ and have a long tail towards large energy losses, showing a Landau distribution. Only for very thick calorimeters, e.g. 100 m of water equivalent, the energy loss distributions become Gaussian.

3.3 Hadronic Showers

The principle of a hadronic shower is similar to that of an electromagnetic shower. The hadron creates a cascade of particles with degraded energy that deposit their energy in the detector material. But this time it is the strong interaction which plays the major role in the shower development making hadronic showers much more complicated than electromagnetic ones.

In the EM showers all the energy carried by the electrons or photons is used eventually in medium ionization and can therefore be measured. In the hadronic shower, a important part of the incoming energy is used in the nuclear binding energy and in processes leading to the so-called “invisible energy”, fundamentally undetectable.

The development of a a hadronic shower can be divided in three parts:

- Fast component: the incident hadron interacts with the nuclear matter originating energetic secondary particles, mostly fast pions, which escape from the nucleus. On average, 1/3 of the pions are neutral and decay into two photons which give rise to a purely EM shower.
- Nuclear shower: mainly formed by nucleons from the target nuclei, extracted from the nucleus by the incident particle with intermediate energy.
- Nuclear evaporation and spallation: this is a slow phase of the shower in which the residual nucleus (in an excited state and with recoil momentum) decays emitting photons, neutrons, protons and heavier fragments with energies on the MeV scale. Although less energetic, they carry a substantial part of the total energy of the shower.

3.3.1 Nuclear Interaction Length

Since hadronic shower development is based on nuclear interactions, the shower dimensions are governed by the nuclear interaction length (λ_{int}). It is defined as the average distance a high-energy hadron has to travel inside a medium before a nuclear interaction occurs. Therefore the probability that the particle traverses a distance z in the medium without causing a nuclear interaction is:

$$P = \mathrm{e}^{-\frac{z}{\lambda_{\mathrm{int}}}}. \tag{3.5}$$

The interaction length is inversivelly proportional to the total cross section for nuclear interactions:

$$\sigma_{\mathrm{tot}} = \frac{A}{N_{\mathrm{A}}\lambda_{\mathrm{int}}} \tag{3.6}$$

where A is the atomic weight of the medium nuclei and N_{A} is the Avogrado's number.

3.4 Calorimeters

Calorimeters in particle physics can be defined as the blocks of instrumented material that measure the energy of incident particles. The incident particle deposits all its energy in the calorimeter and is absorbed. It interacts with the material of the calorimeter and produces a cascade of secondary particles with progressively degraded energy. The charged particles of this showers induce a signal in the calorimeter which serves as a measure of the energy of the incident particle.

In general calorimeters can be divided into electromagnetic and hadronic calorimeters. Electromagnetic calorimeters are designed to measure mainly electrons and photons while hadronic calorimeters measure mainly single hadrons or jets (a bunch of hadrons produced via strong interaction by a single quark or gluon). In a experiment the electromagnetic calorimeter is placed in front of the hadronic one. Therefore hadrons go through interact first in the EM calorimeter and are later absorbed in the hadronic calorimeter.

Calorimeters can be further divided into homogeneous and sampling calorimeters. Homogeneous calorimeters are made of only one type of material in which the particles are absorbed and a signal is produced. In sampling calorimeters those tasks are accomplished by two different materials: an absorber and an active material, which are installed in alternative layers. The absorber is very dense (iron, lead, uranium, etc.) and a lot of energy is deposited in a relative small amount of material. The active material produces a signal when charged particles go through it. The sampling technology allows very compact devices which can still absorb all the energy of EM and hadronic showers in a limited space.

The importance of calorimeters in particle physics can be understood for the following reasons:

- The energy resolution improves with $1/\sqrt{E}$, where E is the energy of the incident particle (see below).
- They are sensitive to all types of particles, even neutral ones. Furthermore, they can even provide an indirect measurement of the energy from non-interacting particles with the missing energy measurement.
- They can provide very fast signals which can be used for triggering interesting events or to measure the arrival of the particles.
- They are space and cost effective because the shower length increases only logarithmically with energy.
- They can give information about the shower position, size or direction and help in particle identification.

3.4.1 Energy Resolution of Calorimeters

The energy measurement is based on the principle that the energy of the incident particle is proportional to the number of particles (N) in the shower: $E \propto N$. Fluctuations in the deposited energy (ΔE) can therefore be expressed like:

$$\frac{\Delta E}{E} \propto \frac{\Delta N}{N} \propto \frac{\sqrt{N}}{N} = \frac{1}{\sqrt{N}} \propto \frac{1}{\sqrt{E}}. \tag{3.7}$$

Therefore the resolution of calorimeters improves with increasing energy as $1/\sqrt{E}$. This estimation is based purely on statistical arguments. The actual energy resolution of a realistic calorimeter can be written as:

$$\frac{\sigma}{E} = \frac{a}{\sqrt{E}} \oplus \frac{b}{E} \oplus c, \tag{3.8}$$

where the $a/\sqrt{E}$ term is called “stochastic term”, the b/E term “noise term” and c “constant term”.

Stochastic Term

As described above, it represents the fluctuations related to the physical development of the shower. Homogeneous calorimeters have a very small stochastic term because the whole shower is absorbed in the active material. Typically they achieve values for a at the level of the few percent. Sampling calorimeters have a much bigger stochastic term because the energy deposited in the active material can fluctuate in an event-by-event basis. Those so-called "sampling fluctuations" constitute the major contribution to the energy resolution. In principle the sampling fluctuations can be reduced by reducing the thickness of the absorber layers, but in practice this is not feasible because that would increase the calorimeter size to ensure a proper containment.

Noise Term

This term depends on the noise of the electronic read-out chain. Calorimeters based on the collection of scintillating light can have very low noise terms if they use phtosensistive devices, like photomultipliers, to read out and amplify the signal. On the contrary, detectors based on the collection of charge have higher noise terms because the first component of the read-out chain is usually a preamplifier.

Methods like signal shaping of optimal filtering can help to reduce the noise term. For decreasing energies the noise term becomes more and more dominant.

Constant Term

This term summarizes all the contributions which do not depend on the particle energy. It includes material non-uniformities, imperfections of the mechanical structures, temperature gradients, radiation damage, etc. Modern detectors impose very rigorous specifications on their components to keep this term low since it is dominant at high energies. Usual values for this term are $\sim 1\%$ or smaller.

Additional Contributions

Other factors can contribute to the calorimeter resolution such as longitudinal or lateral leakage, upstream material, dead material and cracks, etc.

3.4.2 Sampling Fraction

An important parameter describing sampling calorimeters is the so-called "sampling fraction". It is defined as the energy deposited in the active material divided by the total energy deposited in the calorimeter:

$$S_\mathrm{f} = \frac{E_\mathrm{active}}{E_\mathrm{active} + E_\mathrm{passive}}. \tag{3.9}$$

For a MIP this variable can be relatively easily computed by taking into account the geometry of the detector and the path through the active and passive material. For other particles the sampling fraction is usually determined by Monte Carlo simulations.

Chapter 4

Offline Implementation of the Optimal Filtering Reconstruction Algorithm

“Beginning is easy - Continuing is hard.”
— Japanese proverb

4.1 TileCal Reconstruction Methods

As mentioned in Chapter 1, the only information available at the ROD level from the particles impinging TileCal is the output from the front-end electronics, that is, the string of digital samples extracted from the PMT analog pulses.

In order to obtain the energy deposited by the particles from the digital samples, together with their time of arrival, pileup estimation, etc., several reconstruction methods have been developed within the TileCal collaboration. This section is devoted to their description, with special interest in the Optimal Filtering (OF) method, proposed and developed in the past by the IFIC-Valencia group. The Optimal Filtering implementation inside the offline software framework is also presented in this Chapter.

4.1.1 Pulse Shapes

As mentioned above, the input to the reconstruction methods in TileCal is the digital samples obtained in time slices of 25 ns. Let us denote by S_i the value of the digital sample at the bunch crossing i, with $i = 1, \ldots, n$. Most of the reconstruction methods take advantage of the knowledge of the pulse shape from the TileCal electronics. This way, the contribution of the noise is reduced and the timing of the deposition can be determined.

The pulse shape was considered in the past not to be sensitive to the type of incident particle or the amount of energy deposited. However, recent developments show that the pulse shape is actually dependent on the amplitude [27]. This refinement is not implemented in current offline software and an average pulse shape is used for simulation and reconstruction for all the channels.

The pulse shapes normalized to unit amplitude, $g(t)$, were obtained separately for channels with high and low gain and for physics and calibration data, having a FWHM of 50 ns for physics events and 45 ns for calibration events. Consequently, the value of the samples can be expressed as:

$$S_i = Ag(t_i - t) + ped \tag{4.1}$$

where A is the amplitude of the signal, t_i is the time where the sample i was acquired, ped is the pedestal and t the time of the peak of the pulse. Figure 4.2 shows the normalized pulse shape for physics events for high- and low-gain channels.

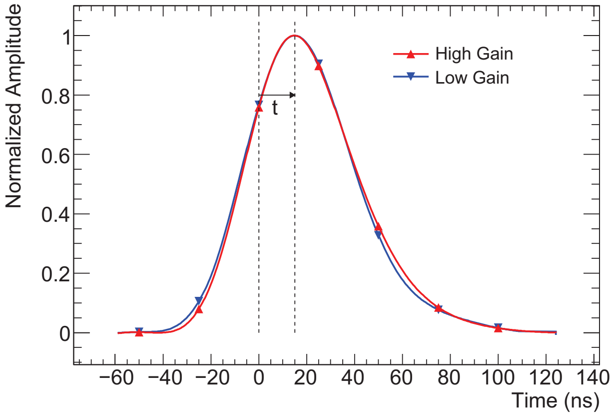

Figure 4.1: Normalized pulse shapes for physics data in high and low gain.

The method used to extract the normalized pulse shapes uses real data with different amplitudes and reaching the detector with different phases. The signal of each individual event is normalized to unit integral and shifted to peak at a fixed time. Overlaying the signals of many events makes it possible to visualize and extract the complete underlying pulse shape [27].

Independently, the pulse shape was also derived from an electronic simulation of the shaper circuit when introducing the standard PMT pulse shape on the input, with compatible results with respect to the shapes obtained directly from data.

4.1.2 Flat Filtering

The Flat Filtering (FF) method is the simplest reconstruction algorithm and was the first developed inside the collaboration. It evaluates the integral of the pulse (Ω) as the maximum sum of 5 consecutive samples:

$$\Omega = max_{j=1,n-5} \left\{ \sum_{i=j}^{j+5} (S_i - ped) \right\}. \tag{4.2}$$

The FF introduces a positive bias for signals that are almost compatible with noise due to the fact that searches for the maximum possible sum of the available samples. For this reason, in practice this method is not used at present.

4.1.3 Fit Method

This method [28] uses the pulse shapes obtained as explained above to reduce the contribution of the electronic noise to the energy measurement. This also allows the determination of the timing of the energy deposition. It is based on a fit to the function in Eq. (4.1) with 3 free parameters: amplitude, phase and pedestal. The expression to be minimized is:

$$\chi^2 = \sum_{i=1}^{n} \left(\frac{S_i - [Ag(t_i) - Atg'(t_i) + ped]}{\sigma_i} \right)^2 \tag{4.3}$$

where σ_i is the error of the sample i, obtained as the sigma of the individual sample distributions (with typical values of 1.5 ADC counts for high gain channels and 0.6 ADC counts for low gain). Equation (4.3) makes use of a first order approximation of Equation (4.1) for S_i:

$$S_i = Ag(t_i - t) + ped \approx Ag(t_i) - Atg'(t_i) + ped. \tag{4.4}$$

In case of pedestal-like events (small signals) and in order to avoid the positive bias as in the FF method a 2 parameter fit (amplitude and pedestal) is performed assuming the timing to be 0 ns. The decision about whether a 2- or 3-parameter fit is more appropriate is taken depending on the option which shows the smallest χ^2 value.

The Fit method has been used by default for test beam and commissioning cosmics reconstruction, both from real and simulated data.

4.1.4 ManyAmps Method

This method is based on a multiple amplitude fit and is meant to handle events affected by minimum bias pileup. It performs a fit to one central amplitude at the central time slice (for the amplitude from the interaction giving the trigger) and several auxiliary amplitudes at t=±25, ±50, ±75,. . . ns (to handle amplitudes coming from minimum bias interactions in the adjacent bunch crossings). Fits are performed to several amplitudes and a common pedestal, with all the times fixed, as shown in Figure 4.2 with an example.

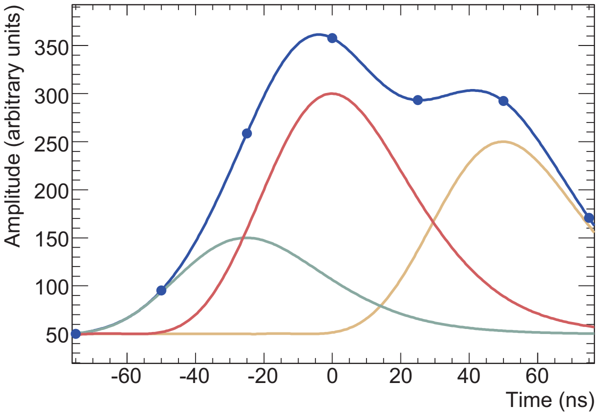

Figure 4.2: Example of fit to multiple amplitude with the ManyAmps method. The samples and total shape form are shown together with the individual amplitudes used for the reconstruction.

The procedure starts by the fit to the central amplitude and if the resulting χ^2 is not satisfactory additional amplitudes are successively added at the bunch crossings with highest residuals until a good χ^2 is achieved. The final result of the reconstruction only includes the central amplitude and hence t=0 ns always, ignoring all the additional amplitudes used in the fit procedure.

The ManyAmps method has been used by default for full ATLAS reconstruction with simulated data, either with or without minimum bias pileup. Despite the good handling of events with minimum bias, its main limitation is the lack of timing information.

4.1.5 Optimal Filtering

The Optimal Filtering (OF) method is based on the use of linear combinations of the signal samples to obtain the amplitude of the pulse. The coefficients of these combinations are chosen in such a way that the impact of the noise to the calorimeter resolution is minimized. OF has been used to reconstruct TileCal in past test beam periods [29] and due to its simplicity in the mathematical formulation, OF has been implemented in the core of the ROD DSPs for online energy reconstruction [30] for commissioning and normal LHC operation.

Two versions of the Optimal Filtering algorithm have been used, which for historical reasons are named OF1 (based on a 2-parameter approach and gives as output A and t) and OF2 (based on a 3-parameter approach and gives as output A, t and ped). The mathematical expressions used in OF1 are:

$$A = \sum_{i=1}^{n} a_i \left(S_i - ped\right) \tag{4.5a}$$

$$At = \sum_{i=1}^{n} b_i \left(S_i - ped\right). \tag{4.5b}$$

Likewise, the expressions used in OF2 are the following:

$$A = \sum_{i=1}^{n} a_i S_i \tag{4.6a}$$

$$At = \sum_{i=1}^{n} b_i S_i \tag{4.6b}$$

$$ped = \sum_{i=1}^{n} c_i S_i. \tag{4.6c}$$

Note that since OF1 itself does not provide as output the pedestal, it is usually estimated as the average of S_1 and S_n, or just as the value of the first sample S_1. The pedestal value obtained this way should then be subtracted from each sample S_i. Due to the lack of statistics, as only one or two samples are considered for the pedestal computation, the results obtained showed limited accuracy. OF2 presents better pedestal treatment and therefore only this version will be discussed in this work.

Additionally, in both versions, the quality of the reconstruction is estimated by the expression:

$$Q_F = 50 \sum_{i=1}^{n} \left| \frac{S_i - (Ag_i + ped)}{S_i} \right| \tag{4.7}$$

Lots of studies have been performed on the definition of this factor in terms of its implementation in the ROD DSP (using reduced number of divisions and no powers) and the goodness in the quality description of the reconstruction even in non-zero luminosity data. See Section 5.3.5 for full details on this matter.

As shown below, the OF method is based on the assumption that $t{\approx}0$, hence with increasing t the quality of the reconstruction decreases. In order to properly handle events with large t an iterative procedure has been set up. This way, the value of t obtained using Eq. (4.5, 4.6) is used to recompute new OF weights and apply them on the samples in a next iteration. This procedure finishes when convergence is obtained in terms of t (see Section 4.5.2).

In the following all the basis and development of the algorithm as well as the procedure for to calculate the OF coefficients is shown in detail.

Theoretical Justification for OF2

The digital samples can be affected by two main sources of noise:

- Series thermal noise, which has a white spectrum and whose amplitude depends only upon the characteristics of the detector and the signal processing circuitry.
- Pileup or physics noise, which depends on the machine luminosity and the cell depth in the calorimeter.

Therefore, the signal samples can be mathematically expressed as in Eq. (4.8) with a new noise term in each sample (n_i):

$$S_i \approx Ag(t_i) - Atg'(t_i) + ped + n_i \equiv Ag_i - Atg'_i + ped + n_i. \tag{4.8}$$

One can define the following quantities u, v, w:

$$u = \sum_{i=1}^{n} a_i S_i \quad v = \sum_{i=1}^{n} b_i S_i \quad w = \sum_{i=1}^{n} c_i S_i \tag{4.9}$$

where a_i, b_i and c_i are free parameters of the algorithms known as OF weights. Since the OF weights are constant, the expectation values for u,v and w will be:

$$\begin{aligned}
\langle u \rangle &= \left\langle \sum_{i=1}^{n} a_i S_i \right\rangle = \sum_{i=1}^{n} a_i \langle S_i \rangle \\
\langle v \rangle &= \left\langle \sum_{i=1}^{n} b_i S_i \right\rangle = \sum_{i=1}^{n} b_i \langle S_i \rangle \\
\langle w \rangle &= \left\langle \sum_{i=1}^{n} c_i S_i \right\rangle = \sum_{i=1}^{n} c_i \langle S_i \rangle
\end{aligned} \tag{4.10}$$

Making use of Eq. (4.8) and taking into account that all parameters are constant except the noise term n_i, and under the assumption that $\langle n_i \rangle$=0 (which is true for a Gaussian distribution, associated to a model for thermal noise used also for minimum bias noise), the following expressions can be written:

$$\begin{aligned}
\langle u \rangle &= \sum_{i=1}^{n} \big(a_i ped + a_i A g_i - At g'_i + a_i \langle n_i \rangle \big) = ped \sum_{i=1}^{n} a_i + A \sum_{i=1}^{n} a_i g_i - At \sum_{i=1}^{n} a_i g'_i \\
\langle v \rangle &= \sum_{i=1}^{n} \big(b_i ped + b_i A g_i - At g'_i + b_i \langle n_i \rangle \big) = ped \sum_{i=1}^{n} b_i + A \sum_{i=1}^{n} b_i g_i - At \sum_{i=1}^{n} b_i g'_i \\
\langle v \rangle &= \sum_{i=1}^{n} \big(c_i ped + c_i A g_i - At g'_i + c_i \langle n_i \rangle \big) = ped \sum_{i=1}^{n} c_i + A \sum_{i=1}^{n} c_i g_i - At \sum_{i=1}^{n} c_i g'_i
\end{aligned} \tag{4.11}$$

However, if $\langle n_i \rangle \neq$0 but still constant, it can be absorbed in the pedestal term. The point is that the noise has to be stationary, i.e., the statistics average must be time independent. By requiring that the expectation values of u, v and w after a series of events is equal to A, At and ped, i.e., Eqs. (4.5, 4.6), the following constraints are extracted for the OF weights:

$$\begin{aligned}
&\sum_{i=1}^{n} a_i = 0 \quad \sum_{i=1}^{n} a_i g_i = 1 \quad \sum_{i=1}^{n} a_i g'_i = 0 \\
&\sum_{i=1}^{n} b_i = 0 \quad \sum_{i=1}^{n} b_i g_i = 0 \quad \sum_{i=1}^{n} b_i g'_i = -1 \\
&\sum_{i=1}^{n} c_i = 1 \quad \sum_{i=1}^{n} c_i g_i = 0 \quad \sum_{i=1}^{n} c_i g'_i = 0
\end{aligned} \tag{4.12}$$

These are 3×3 sets of n equations with $3n$ unknowns, so for $n>3$ further constraints should be imposed on the values of a_i, b_i and c_i.

Weight Computation

The OF weights are also required to minimize the variances of u, v and w:

$$\begin{aligned}
\mathrm{Var}\,(u) &= \mathrm{Var}\left(\sum_{i=1}^{n} a_i S_i\right) = \mathrm{Var}\left(ped\sum_{i=1}^{n} a_i + A\sum_{i=1}^{n} a_i g_i - At\sum_{i=1}^{n} a_i g_i + \sum_{i=1}^{n} a_i n_i\right)\\
\mathrm{Var}\,(v) &= \mathrm{Var}\left(\sum_{i=1}^{n} b_i S_i\right) = \mathrm{Var}\left(ped\sum_{i=1}^{n} b_i + A\sum_{i=1}^{n} b_i g_i - At\sum_{i=1}^{n} b_i g_i + \sum_{i=1}^{n} b_i n_i\right)\\
\mathrm{Var}\,(w) &= \mathrm{Var}\left(\sum_{i=1}^{n} c_i S_i\right) = \mathrm{Var}\left(ped\sum_{i=1}^{n} c_i + A\sum_{i=1}^{n} c_i g_i - At\sum_{i=1}^{n} c_i g_i + \sum_{i=1}^{n} c_i n_i\right)
\end{aligned} \tag{4.13}$$

As all the parameters are constant except n_i:

$$\begin{aligned}
\mathrm{Var}\,(u) &= \mathrm{Var}\left(\sum_{i=1}^{n} a_i n_i\right) = \sum_{i,j=1}^{n} a_i a_j \langle n_i n_j\rangle\\
\mathrm{Var}\,(v) &= \mathrm{Var}\left(\sum_{i=1}^{n} b_i n_i\right) = \sum_{i,j=1}^{n} b_i b_j \langle n_i n_j\rangle\\
\mathrm{Var}\,(w) &= \mathrm{Var}\left(\sum_{i=1}^{n} c_i n_i\right) = \sum_{i,j=1}^{n} c_i c_j \langle n_i n_j\rangle
\end{aligned} \tag{4.14}$$

Using Lagrange multipliers to minimize the variances in Eq. (4.12), the following functions can be constructed:

$$\begin{aligned}
I_u &= \sum_{i,j=1}^{n} a_i a_j \langle n_i n_j\rangle - \alpha\left(\sum_{i=1}^{n} a_i g_i - 1\right) - \beta\sum_{i=1}^{n} a_i g_i' - \gamma\sum_{i=1}^{n} a_i\\
I_v &= \sum_{i,j=1}^{n} b_i b_j \langle n_i n_j\rangle - \delta\sum_{i=1}^{n} b_i g_i - \left(\varepsilon\sum_{i=1}^{n} a_i g_i' + 1\right) - \zeta\sum_{i=1}^{n} a_i\\
I_w &= \sum_{i,j=1}^{n} c_i c_j \langle n_i n_j\rangle - \eta\sum_{i=1}^{n} c_i g_i - \theta\varepsilon\sum_{i=1}^{n} c_i g_i' - \kappa\left(\sum_{i=1}^{n} c_i - 1\right)
\end{aligned} \tag{4.15}$$

As usual, to minimize the expressions in Eq. (4.15) the partial derivatives with respect to the OF weights are set to 0, that is:

$$\begin{aligned}
\frac{\partial I_u}{\partial a_i} &= 2\sum_{j=1}^{n} a_j \langle n_i n_j \rangle - \alpha g_i - \beta g_i' - \gamma = 0 \\
\frac{\partial I_v}{\partial b_i} &= 2\sum_{j=1}^{n} b_j \langle n_i n_j \rangle - \delta g_i - \varepsilon g_i' - \zeta = 0
\end{aligned} \tag{4.16}$$

$$\frac{\partial I_w}{\partial c_i} = 2\sum_{j=1}^{n} c_j \langle n_i n_j \rangle - \eta g_i - \theta g_i' - \kappa = 0$$

The term $\langle n_i n_j \rangle$ in the expressions above can be substituted by R_{ij} which represents an element of the noise autocorrelation function evaluated at time $t_i - t_j$ (see Section 4.1.5). Now we have 3 sets of n+3 equations with n+3 unknowns. Then, the following equations can be written for a_i, b_i and c_i:

$$\begin{array}{llll}
\sum_{i=1}^{n} a_i g_i = 1 & \sum_{i=1}^{n} a_i g_i' = 0 & \sum_{i=1}^{n} a_i = 0 & \sum_{j=1}^{n} a_j R_{ij} - \alpha g_i - \beta g_i' - \gamma = 0 \ \ \forall i \\
\sum_{i=1}^{n} b_i g_i = 0 & \sum_{i=1}^{n} b_i g_i' = -1 & \sum_{i=1}^{n} b_i = 0 & \sum_{j=1}^{n} b_j R_{ij} - \delta g_i - \varepsilon g_i' - \zeta = 0 \ \ \forall i \\
\sum_{i=1}^{n} c_i g_i = 0 & \sum_{i=1}^{n} c_i g_i' = 0 & \sum_{i=1}^{n} c_i = 1 & \sum_{j=1}^{n} c_j R_{ij} - \eta g_i - \theta g_i' - \kappa = 0 \ \ \forall i
\end{array} \tag{4.17}$$

Equivalently, in matrix format Eq. (4.17) can be expressed as:

$$\begin{pmatrix}
R_{11} & R_{12} & \cdots & R_{1n} & g_1 & g_1' & 1 \\
R_{21} & R_{22} & \cdots & R_{2n} & g_2 & g_2' & 1 \\
\cdots & \cdots & \cdots & \cdots & \cdots & \cdots & \cdots \\
R_{n1} & R_{n2} & \cdots & R_{nn} & g_n & g_n' & 1 \\
g_1 & g_2 & \cdots & g_n & 0 & 0 & 0 \\
g_1' & g_2' & \cdots & g_n' & 0 & 0 & 0 \\
1 & 1 & \cdots & 1 & 0 & 0 & 0
\end{pmatrix}
\begin{pmatrix} a_1 \\ a_2 \\ \cdots \\ a_n \\ \alpha \\ \beta \\ \gamma \end{pmatrix}
=
\begin{pmatrix} 0 \\ 0 \\ \cdots \\ 0 \\ 1 \\ 0 \\ 0 \end{pmatrix} \tag{4.18}$$

$$\begin{pmatrix} R_{11} & R_{12} & \cdots & R_{1n} & g_1 & g'_1 & 1 \\ R_{21} & R_{22} & \cdots & R_{2n} & g_2 & g'_2 & 1 \\ \cdots & \cdots & \cdots & \cdots & \cdots & \cdots & \cdots \\ R_{n1} & R_{n2} & \cdots & R_{nn} & g_n & g'_n & 1 \\ g_1 & g_2 & \cdots & g_n & 0 & 0 & 0 \\ g'_1 & g'_2 & \cdots & g'_n & 0 & 0 & 0 \\ 1 & 1 & \cdots & 1 & 0 & 0 & 0 \end{pmatrix} \begin{pmatrix} b_1 \\ b_2 \\ \cdots \\ b_n \\ \delta \\ \varepsilon \\ \zeta \end{pmatrix} = \begin{pmatrix} 0 \\ 0 \\ \cdots \\ 0 \\ 0 \\ -1 \\ 0 \end{pmatrix} \tag{4.19}$$

$$\begin{pmatrix} R_{11} & R_{12} & \cdots & R_{1n} & g_1 & g'_1 & 1 \\ R_{21} & R_{22} & \cdots & R_{2n} & g_2 & g'_2 & 1 \\ \cdots & \cdots & \cdots & \cdots & \cdots & \cdots & \cdots \\ R_{n1} & R_{n2} & \cdots & R_{nn} & g_n & g'_n & 1 \\ g_1 & g_2 & \cdots & g_n & 0 & 0 & 0 \\ g'_1 & g'_2 & \cdots & g'_n & 0 & 0 & 0 \\ 1 & 1 & \cdots & 1 & 0 & 0 & 0 \end{pmatrix} \begin{pmatrix} c_1 \\ c_2 \\ \cdots \\ c_n \\ \eta \\ \phi \\ \kappa \end{pmatrix} = \begin{pmatrix} 0 \\ 0 \\ \cdots \\ 0 \\ 0 \\ 0 \\ 1 \end{pmatrix} \tag{4.20}$$

Solving the systems of equations above, the a_i, b_i and c_i are obtained. The different values of the pulse phase are considered in this framework by means of the corresponding pulse shape and its derivative. Then, by introducing the proper g_i, g'_i the appropriate weights are obtained. The phase (τ) is defined as the time used for the OF weight computation.

Noise Autocorrelation Function

The noise autocorrelation function contains the correlation of the signal pulses with themselves. This way R_{ij} contains the correlation between the sample i and the sample j in the same string of digitizations after a series of N events. This function is computed from empty events or pedestal runs and two different definitions can be used:

- **"Rigorous" correlation ($\boldsymbol{R_{ij}}$):** the correlation between samples i and j is obtained with the following expression:

$$R_{ij} = \frac{N\sum_{l=1}^{N} S_i S_j - \sum_{l=1}^{N} S_i \sum_{l=1}^{N} S_j}{\sqrt{\left(N\sum_{l=1}^{N} S_i^2 - \left(\sum_{l=1}^{N} S_i\right)^2\right)\left(N\sum_{l=1}^{N} S_j^2 - \left(\sum_{l=1}^{N} S_j\right)^2\right)}} \tag{4.21}$$

  where the index l loops over the N events in the pedestal run used.

- **Average correlation:** under the assumption that R_{ij} is the same for all the (i,j) pairs with the same lag $k = |i-j|$, one can alternatively obtain the average correlation for each lag (r_k) which, under this assumption, verifies that $r_k = R_{ij} = R_{ji}$. The expression to obtain the values of r_k is the following:

$$r_k = \frac{(N-k)\sum_{l,i=1}^{N,n} S_i S_{i+k} - \sum_{l,i=1}^{N,n} S_i \sum_{l,i=1}^{N,n} S_{i+k}}{\sqrt{\left((N-k)\sum_{l,i=1}^{N,n} S_i^2 - \left(\sum_{l,i=1}^{N,n} S_i\right)^2\right)\left((N-k)\sum_{l,i=1}^{N,n} S_{i+k}^2 - \left(\sum_{l,i=1}^{N,n} S_{i+k}\right)^2\right)}} \tag{4.22}$$

  Note that under the assumption that correlations are small ($r_k \simeq 0 \ \forall k$), one common scenario is to replace the R_{ij} matrix by the unitary matrix ($R_{ii} = 1$; $R_{ij} = 0$ for $i \neq j$). Section 5.1 discusses in detail the results obtained for the autocorrelation in several noise environments.

4.2 LHC Commissioning and Early Running

For any beam with rotating bunches of particles, the beam luminosity $\mathcal{L}$ can be expressed by:

$$\mathcal{L} = \frac{f N^2 k_b \gamma}{4\pi\beta^* \epsilon_N}\mathcal{F}(\theta), \tag{4.23}$$

where f is the revolution frequency, N is the number of particles per bunch, k_b is the number of bunches per beam, γ is the relativistic factor, ϵ_N is the normalized transverse emittance, β^* is the betatronic function at the interaction point and $\mathcal{F}$ is the geometric luminosity reduction factor due to the crossing beam angle (θ), which is $\sim$0.85 at LHC.

A detailed run plan was prepared in order to progressively achieve the nominal LHC luminosity by varying the accelerator parameters (k_b, N, β^*, etc.). It was split in several main stages:

- **Stage A (Pilot physics run):** this stage covers from beam commissioning to the first physics runs, aiming at a peak luminosity of 10^{32} cm^{-2}s^{-1}. During this stage, the number of bunches will rump from 43 to 156 and from 300 GeV to 7 TeV in energy, with up to 3.9 collisions per crossing in average.
- **Stage B (Intermediate physics run):** this stage consists in operation for physics runs using a bunch spacing of 75 ns, leading to peak luminosities 10^{33} cm^{-2}s^{-1}. The initial aim is to use 96×96 bunches (bunch intensity of 10^{10}), with a maximum aim 936×936 bunches (9×10^{10}). The average number of collisions per crossing is 7 at the maximum aim of this stage.

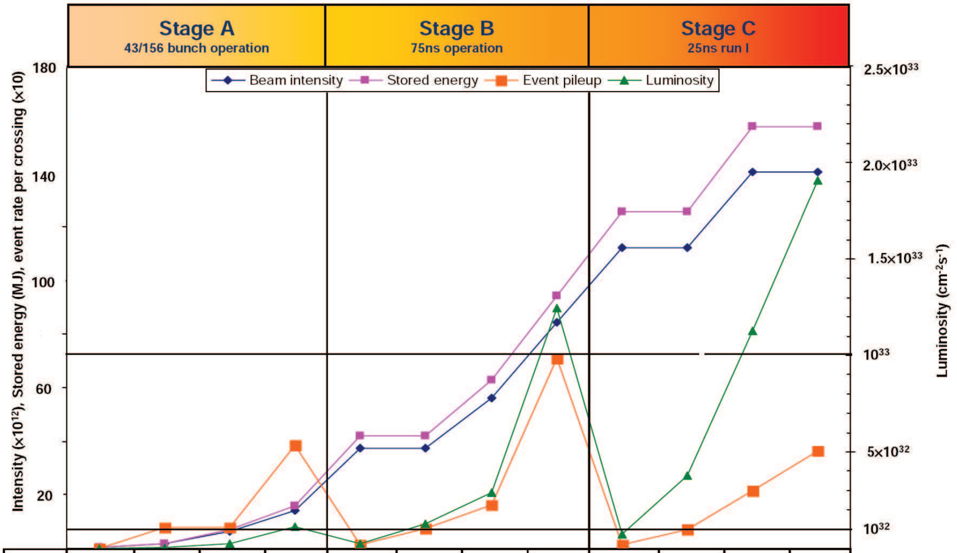

k_b	43	43	156	156	936	936	936	936	2808	2808	2808	2808
β^* (m)	11	2	2	2	11	2	2	1	11	2	1	0.55
N($\times10^{10}$)	4	4	4	9	4	4	6	9	4	4	5	5

Figure 4.3: Evolution of beam parameters and luminosities in LHC operation stages A to C.

- **Stage C (25 ns run I):** the aim of this stage is to have 2808×2808 bunches with the nominal bunch separation of 25 ns and an intensity of 5×10^{10} protons per bunch. The peak luminosities in this stage is 2×10^{33} cm^{-2}s^{-1} with an average number of collisions per crossing of 3.6.
- **Stage D (25 ns run II):** this stage starts after the installation of phase II collimators and full beam dump diluters, and the objective is to chieve the nominal performance, operating with nominal bunch separation of 25 ns and at design luminosity (10^{34} cm^{-2}s^{-1}).

Figure 4.3 show the variation of the luminosity and other accelerator performance variables as a function of the accelerator parameters during the LHC early operation (from stage A to C).

4.3 ATLAS Offline Software: Athena

Offline computing in ATLAS covers all processing from storing raw data up to the final analysis, as well as Monte Carlo generation, detector simulation and event display. Athena [31] is the general framework for the ATLAS offline software, based upon the Gaudi [32] architecture. The Athena code is based on the C++ language and uses all of its object oriented features.

Athena can be seen as an skeleton which provides most of the common functionalities and into which the developers can insert their own code. This way, the software developed in Athena can use many useful background classes (physical units manipulation, geometry entities, etc.) or prepared services for things such as loop over events. Figure 4.4 shows the main Athena components and their relationships.

ATLAS software is organized into a hierarchical structure of projects and packages. All packages are stored in an official Concurrent Version System (CVS) repository, which enables efficient sharing of source code among the members of a distributed development team. Each package has a tag number which distinguishes between different versions. A project consists of a complete collection of tagged packages and it is identified with a release number.

A Configuration Management Tool (CMT) [33] is used to manage, build (i.e., compile and link) and run ATLAS software. The information needed to build or run a package is grouped in a single *requirements* file, from which CMT sets automatically the configuration parameters required to operate the packages.

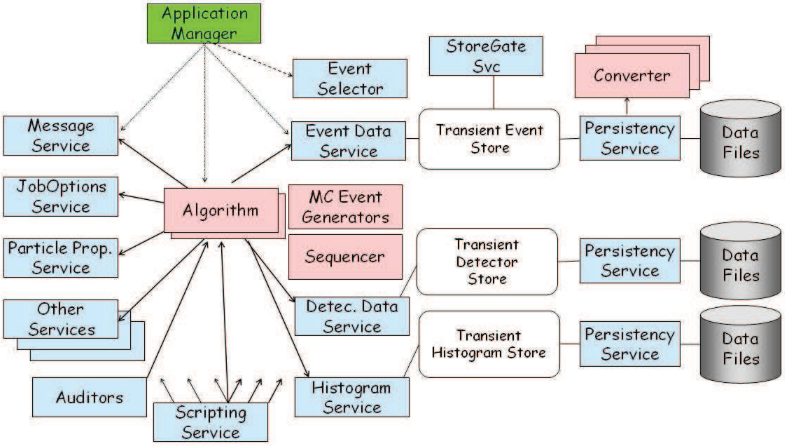

Figure 4.4: Athena architecture object diagram.

The Athena framework distinguishes between data objects and algorithm objects very strictly. A quantity-like entities (hits, points, tracks, digits, raw channels, etc.) should be implemented by deriving their class from the *DataObject* base class. On the other hand, anything like a procedure should be designed as a child class of the *Algorithm* base class.

4.3.1 Algorithms

The principal functionality of an algorithm is to take input data, manipulate them and produce new output data. All data objects are kept in the common StoreGate (see Section 4.3.3). All algorithms are able to save or retrieve any data object from there via the StoreGate Service.

The interface of the Algorithms (inherited from Algorithm class) provides connection to Athena common services. Three methods (initialize, execute and finalize) have to be implemented in each algorithm, in addition to the constructor and destructor.

Algorithms are required to be configurable, so that certain parameters can be initialized when the algorithm is called. These parameters, known as properties, are specified with JobOptions files, which are conventional python scripts used to control the configuration of algorithms and other applications at run time.

Tools and AlgTools

Often some of the processing is delegated by the Algorithms to AlgTools. In the Athena framework, a Tool is an encapsulated piece of code which needs to be executed only when special events occur. AlgTools inherit from the AlgTool base class to guarantee compatibility with Algorithms and grant a set of basic services and functions.

4.3.2 Services

The main services that algorithm objects use in Athena are the following:

- **Event Data Service:** provides storing and retrieving all event related data, whose lifetime is one simple event only.
- **Detector Data Service:** stores information about detector, such as its geometrical and environment parameters.
- **Histogram Service and Ntuple Service:** histograms and ntuple made by these services have lifetime longer than a simple event, and typically collect some parameters through all events. Ntuples cannot be kept only in memory, data are accumulated and written to disk continuously during the execution of a job.
- **Message Service:** provides reporting about progress and other communication with the outside world.

4.3.3 Data Store

The Transient Data Store (TDS) is the main channel of communication among different Athena modules. The ATLAS implementation of the TDS is called StoreGate. Each algorithm can create Data Objects and save them into the StoreGate. Any algorithm is able to retrieve data from the StoreGate[1], no matter if they were generated by another algorithm (a transient source) or a file or database (persistent sources). Several different transient stores build up the entire TDS (e.g. the Transient Event Store, the Transient Detector Store, the Transient Histogram Store, the Transient Ntuple Store, etc.).

---

[1] Data objects are stored in StoreGate using ”Containers”, i.e. C++ Standard Template Library Containers, which are holder objects that store a collection other objects (their elements). They are implemented as class templates, which allows a great flexibility in the types supported as elements.

The TDS also manages conversion of Data Objects from/to their persistent form (e.g. reading from/saving to a file) via the persistence services. The structure of the entire TDS and its integration into the Athena framework are shown in Figure 4.4.

4.3.4 Running Athena

An Athena job starts by creating an instance of the Application Manager component. The Application Manager initializes a minimal set of basic and essential services and then gives the control to specialized service called the Event Loop Manager. The Event Loop Manager firstly initializes all top algorithms (specified via the JobOption Service), executes them in the physical-event loop, and finalizes them at the end. This is done by invoking the special methods mentioned above. The top algorithms are executed unconditionally in the order they have been declared and invoke execution of another components (such as AlgTools) according to the hierarchical structure of the software.

4.3.5 TileCal Related Objects in Athena

During the full simulation-digitization-reconstruction chain, the information available at each stage for each subdetector is stored in dedicated objects inside the Athena StoreGate. In the case of TileCal, the following objects are used:

- **TileHit:** they store visible energy deposited in active parts of TileCal within the Geant4 simulation. Due to the fact that the active material is scintillator, Birks' law (the phenomenological description of the response attenuation of organic scintillators [34]) is applied on every Geant4 hit when building the TileHit.
- **TileDigits:** they contain the output from the front-end electronics to be sent to the RODs, that is, the string of digital samples measured in 25 ns time slices.
- **TileRawChannels:** they contain the output from the reconstructions algorithms: the amplitude, time, quality and pedestal for each channel.
- **TileCells:** total energy deposited in a cell, calibrated with the electromagnetic scale. In TileCal almost all cells are read out by two PMTs and, to preserve information about both PMTs in a cell, the energy difference between two PMTs is also stored.

4.4 TileCal Digitization in Athena

4.4.1 Standard Digitization

Inside Athena, TileDigits are obtained from the TileHits using the normalized pulse shape by means of an algorithm called TileDigitsMaker. In first place, all the TileHits for an event are retrieved from the Athena TileHitContainer in the StoreGate and they are convoluted with the pulse shapes for high and low gain. Once the digital samples are extracted at time slices of 25 ns, a common pedestal term and electronic noise following a Gaussian distribution is added to each sample.

If any of the samples is larger than 10^{10} (the maximum range of the Tile ADCs) in the default high gain, i.e. is saturated, the whole channel is then switched to low gain. The resulting TileRawChannels are stored in a dedicated TileRawChannelContainer in the Athena StoreGate, where they are available as input for all the possible reconstruction algorithms.

4.4.2 Digitization with Minimum Bias Pileup

Two source of background events are considered for pileup in the ATLAS simulation framework:

- **Minimum bias:** multiple inelastic collisions, following a Poisson distribution with mean determined by luminosity. Section 2.2.2 describes in detail the properties of minimum bias events.
- **Cavern background:** this background is composed of additional hits created by long living secondary particles. The high luminosity design of the LHC beams generate important levels of secondary radiation in the ATLAS experimental hall, such as particles interacting with the beam line system and structures near it or creating showers in the calorimeters. Those secondary time-uncorrelated particles diffuse in the apparatus like a gas for a few seconds, potentially degrading its physics performance.

  In fact, the beam pipe creates a line of source of secondary particles and though its low mass it is not self shielding. Due to the thickness of the calorimeters, this source feeds secondary particles mostly into the thinnest region of the forward shield and the core of the forward toroid magnet. This radiation background is created not only in the forward region but also on the muon barrel with the contribution from the service gap being relative small. The particle content in the cavern background has been estimated to be mostly neutrons (52%) and photons (44%), with small contributions from electrons(3%), protons(1%), muons, pions and kaons.

The muon chambers are the system most affected by this cavern background (higher fake-track rate, decreased resolution, lower efficiency, etc.). Regarding TileCal, its performance is not degraded as the iron is impervious to radiation damage and possible effects on the scintillating tiles and WLS fibers, estimated to be 1-2% after 10 years of LHC operation, will be corrected with the calibration systems.

Monte Carlo samples of minimum bias events and cavern background have been generated for ATLAS. During offline digitization, a certain amount of events from these background streams are selected and merged with the event from the main interaction. Background events are reused during pileup jobs in order to save memory resources. Three main scenarios are usually considered in the context of standard ATLAS data production with pileup:

- **Very Low Luminosity:** it represents a luminosity of 10^{33} cm^{-2}s^{-1}, with an average of 2.3 p-p and 2 cavern background events.
- **Low Luminosity:** it represents a luminosity of 2×10^{33} cm^{-2}s^{-1}, with 4.6 p-p and 5 cavern background events in average.
- **High Luminosity:** it represents a luminosity of 10^{34} cm^{-2}s^{-1}, with an average of 23 p-p interactions and 23 cavern background events.

So far, only 25-ns bunch crossing time is considered within Athena release 12. As mentioned above, the cavern background is not important for TileCal and, taking into account the front-end electronics pulse shape, we can distinguish two kinds of pileup events:

- In-time pileup: for those minimum bias events produced in the 5 central bunch crossings (that is, with t=-50, . . .,+50 ns), once convoluted with the pulse shape, part of the pulse will be in the region close to t=0. In consequence these pileup events cannot be separated from in-time signals.
- Out-of-time pileup: amplitudes from minimum bias produced elsewhere would clearly be separated from in-time signals since the electronics pulse FWHM is only ∼50 ns. Therefore, the presence of out-of-time pileup should have small effects in the signal measurement.

When performing the digitization with pileup activated, TileHits are retrieved from two different sources from the main physics interaction and additionally from the background (minimum bias and cavern), and they are overlapped and stored in a TileDigitsContainer. This way, the presence of pileup is transparent for TileDigitsMaker algorithms, which is executed in the same way and does not distinguish whether the TileHits came from background streams or from the main interaction.

4.5 Optimal Filtering Implementation in Athena

4.5.1 Weight Computation Tool

The OF weights are stored in ASCII files in the TileConditions package, from where they are retrieved by the reconstruction algorithm during Athena execution. Each file stores the weights for 201 values of τ, from τ=-100 ns to τ=100 ns in steps of 1 ns. There are files for each kind of weight (a_i, b_i or c_i), gain (high or low), method used (OF1 or OF2), pulse shape employed (Physics or charge injection calibration -CIS-) and number of samples (7 or 9). This way, for instance, the file containing the a_i weights for OF2 in low gain channels for Physics runs acquired with 7 samples is named “ai_lo_of2_Delta_Phys_7Samples.dat”. The structure of this file is shown in Table 4.1. The first column is the phase for which the weights are computed and the next numbers correspond to (a_1,a_2,. . .,a_n).

Table 4.1: Structure of the ASCII files holding the OF weights.

				. . .			
-75	-0.2000785459	-0.2000785459	-0.2000785459	-0.2006025124	-0.2319507548	0.05018190518	0.9826069998
-74	-0.2082923741	-0.2082923741	-0.2082923741	-0.2099994113	-0.2314256983	0.1177480602	0.9485541718
-73	-0.2159726861	-0.2159726861	-0.2159726861	-0.2183521973	-0.2290475277	0.18042321	0.9148945733
				. . .			
-1	-0.36775134	-0.3499343414	0.1651187023	0.8022780561	0.2936643443	-0.1967084204	-0.346667001
0	-0.3677149743	-0.3446927571	0.2005654317	0.8025674869	0.2646508437	-0.2059753768	-0.3494006541
1	-0.3678190008	-0.3383856797	0.2367050519	0.8002958774	0.235818016	-0.2147772937	-0.3518369711
				. . .			
74	0.9644024507	0.1174736223	-0.1630388472	-0.2424379742	-0.2387314039	-0.2122540133	-0.2254138343
75	1.006060892	0.04384156322	-0.1738303189	-0.235747558	-0.2225681604	-0.2088782092	-0.2088782092
				. . ....			

The weight computation is currently performed via a tool called TileOptFiltTool which is used by the TileCondComputingAlg algorithm (which also takes care of the pedestals, noise and calibration constants computation). TileOptFiltTool makes use of an auxiliary class called TileOFCorrelation, responsible to compute the correlation and all the calculations needed to obtain the values of the OF weights. This tool can be executed on any pedestal run.

The TileOptFiltTool Tool

The properties of the TileOptFiltTool class which can be configured via jobOptions are:

- `nSample`: number of samples used in the data (n).
- `SevenToNineSamples`: in case n=9, by enabling this property, the OF weights to obtain will only consider the 7 first values of the correlation matrix and therefore would be appropriate to reconstruct data with n=7.
- `OptFilterDeltaCorrelation`: this bool property indicates whether the correlation obtained from the data should be used for the weight computation or simply the identity matrix.
- `AveragedCorrelation`: with this property the user decides to use average correlation over same time lags (r_k) or the rigorous correlation (R_{ij}) during execution.
- `CIS`: it indicates which pulse shape should be used for weight computation, either CIS (when true) or Physics (when false).
- `ChannelThresholdCorrAverage`: it contains the number of events after which correlations are computed. This way the first events where fluctuations are larger are not considered.

During TileOptFiltTool initialization, an instance of TileOFCorrelation is created and during execution, if OptFilterDeltaCorrelation is disabled, the methods used to compute the sums needed for correlation are called. Finally, after the last event in the run is processed, correlations and weights are calculated and stored in ASCII files for all the channels present in the run if requested.

The TileOFCorrelation Class

The main methods of this class are the following:

- `Sum`: Computes on an event-by-event basis over the N events in the run the following variables:

$$\mathsf{S}_i = \sum_{l=0}^{N} S_i, \quad \mathsf{SS}_{ij} = \sum_{l=0}^{N} S_i S_j. \tag{4.24}$$

- `CalcCorrelation`: Computes rigorous correlation between sample i and j (R_{ij}) for all the channels:

$$R_{ij} = \frac{N\mathsf{SS}_{ij} - \mathsf{S}_i\mathsf{S}_j}{\sqrt{\left(N\mathsf{SS}_{ii} - (\mathsf{S}_i)^2\right)\left(N\mathsf{SS}_{jj} - (\mathsf{S}_i)^2\right)}}. \tag{4.25}$$

- `RunningCorrelation`: it computes on an event-by-event basis over the first N' events in the run the following variables:

$$\begin{aligned}
\mathsf{S1}_k &= \sum_{l=0}^{N'} S_i, & \mathsf{S2}_k &= \sum_{l=0}^{N'} S_{i+k}, \\
\mathsf{S12}_k &= \sum_{l=0}^{N'} S_i S_{i+k}, & \mathsf{S21}_k &= \sum_{l=0}^{N'} S_{i+k} S_i, \\
\mathsf{S22}_k &= \sum_{l=0}^{N'} S_{i+k} S_{i+k}, & N_k^{pairs} &= \sum_{l=0}^{N'} 1.
\end{aligned} \tag{4.26}$$

  For all events above ChannelThresholdCorrAverage, it also computes the average correlation:

$$r_k = \frac{N_k^{pairs}\mathsf{S12}_k - \mathsf{S1}_k\mathsf{S2}_k}{\sqrt{\left(N_k^{pairs}\mathsf{S11}_k - (\mathsf{S1}_k)^2\right)\left(N_k^{pairs}\mathsf{S2}_k - (\mathsf{S2}_k)^2\right).}} \tag{4.27}$$

- `CalcRunningCorrelation`: This method is executed at the end of the run (when $N' = N$) and assigns the final value of the correlation computed in the class as the average correlation: $R_{i(i+k)} = R_{(i+k)i} = r_k$.
- `CalcWeights`: Solves the system for weight calculation expressed in Eqs. (4.18-4.20). obtaining the values for the a_i, b_i and c_i weights.

4.5.2 Reconstruction Algorithm

All the TileCal reconstruction methods available are implemented in the Athena framework using an algorithm called TileRawChannelMaker, inside the TileRecUtils package. It retrieves the TileDigits from the TileDigitsContainer and by the use of one or several AlgTools performs the reconstruction and stores the resulting TileRawChannels in dedicated containers. The AlgTools available for TileRawChannelMaker are the following:

- `TileRawChannelBuilderFlatFilter`.
- `TileRawChannelBuilderFitFilter`.
- `TileRawChannelBuilderManyAmps`.

- `TileRawChannelBuilderOptFilter`.

The TileRawChannelMaker Algorithm

This common algorithm provides interface to all the reconstruction methods employed as AlgTools with some common infrastructure to all of them. The following properties are defined for the algorithm:

- `TileDigitsContainer`: name of the container to grab TileDigits from.
- `TileRawChannelBuilder`: this is a vector of strings with the names of the AlgTools to be used. This way the same digits can be reconstructed by more than one method in the same Athena job.

The two main methods of the algorithm are:

- `initialize`: in this method all the requested AlgTools are retrieved, that is, instances are created and their initialize methods are called.
- `execute`: this method takes care of retrieving the TileDigitsContainer from the Athena StoreGate and calls the createContainer method for all the AlgTools. It loops over all the TileDigits available in the event and builds the TileRawChannels by calling to the rawChannel method of the daughter AlgTools. Finally the TileRawChannels are committed to the TileRawChannelContainer by calling the commitContainer method.

The TileRawChannelBuilderOptFilter AlgTool

This class inherits from the TileRawChannelBuilder base class and is implemented in Athena as an AlgTool. The following properties can be configured through jobOptions for its execution:

- `MaxIterations` (i_{max}): maximum number of iterations to be performed in the OF algorithm, which takes 5 as default value.
- `TimeForConvergence` (Δt): when iterations are applied, minimum difference between the time obtained (t) and the phase (τ) to quit the iteration procedure once convergence is reached.
- `PedestalMode`: this property takes integer values and determines how the pedestal is determined inside the AlgTool, either for OF1 execution and/or for treatment of

pedestal-like events when iterations are applied (see below). The following values can be used:

  - 19: $ped = (S_1 - S_9)/2$
  - 12: $ped = (S_1 - S_2)/2$
  - 17: $ped = (S_1 - S_7)/2$
  - 1(default): $ped = S_1$
  - 9: $ped = S_9$
  - 7: $ped = S_7$

- `OF2`: this bool property determines whether OF2 is executed (when true) or OF1 instead (when false).
- `Minus1Iteration`: by enabling this bool property the user decides whether the first guess of the phase known as "-1 iteration" should be used during execution.
- `AmplitudeCorrection`: when this bool property is activated, the resulting values of the amplitude after algorithm execution are corrected taking into account the time obtained (see Section 5.3.4). It should only be used when no iterations are applied.
- `ConfTB`: old option used for reconstruction of test beam data using specific weights computed for that occasion.

Apart from the common algorithm methods (initialize, finalize, execute), the following methods are implemented in TileRawChannelBuilderOptFilter:

- `initialize`: in this method the TileRawChannelBuilder base class is initialized and all the OF weights and pulse shapes needed for execution are retrieved using dedicated methods from the TileConditions package. High and low gain pulse shapes and their derivatives for Physics and CIS runs are loaded in this method. So far, they are extracted from ASCII files stored in the TileConditions package and used for Monte Carlo and real data reconstruction. However, it is foreseen to use different pulse shapes and weights for each channel during ATLAS execution.
- `rawChannel`: This method takes as input the TileDigits and call the Filter method responsible for the actual application of the OF reconstruction. The resulting amplitude is calibrated to the right units (ADC counts, pC, Cs-equalized-pC or MeV) and the time is corrected taking into account the results from Laser calibration runs. Finally, the TileRawChannel objects are built with the amplitude, time, pedestal and quality obtained.
- `Compute`: this method performs the linear combinations involved in OF and it is called either by the Filter or Iterator methods in the AlgTool. It takes as input the string

of TileDigits and outputs the values of (A, ped, t, $Q_{\rm F}$). This piece of code selects according to τ the appropriate weights (a_i, b_i, c_i) to use, performs the sums described in Eqs. (4.5-4.6) and computes the quality factor using Eq. (4.1.5). Figure 4.5 shows the flow chart of this method.

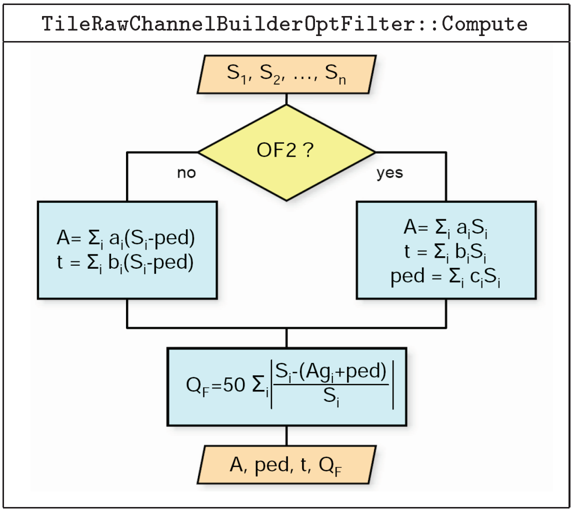

Figure 4.5: Flow chart for the Compute method in the TileRawChannelBuilderOptFilter class.

- `Iterator`: this method is meant to perform the iterative procedure involved in OF when applied to events of unknown phase (test beam and commissioning data). It is called by the Filter method (see below) and takes as input the string of digital samples. In first place, if the Minus1Iteration property was selected, it performs a first guess of the phase as the time of the largest sample:

  $$\tau_0 = time(S_{max}). \tag{4.28}$$

  This is done to start the iterative procedure as close as possible to the actual value of the time for signal events.

  Afterwards, a while loop is executed by calling the Compute method and for each iteration i the Iterator method outputs the values of (A_i, t_i, p_i, Q_{F_i}). The new value of the phase is obtained as:

  $$\tau_i = \tau_{i-1} - int\,(t_i)\,. \tag{4.29}$$

  Convergence is reached when $t_i < \Delta t$ or when the maximum number of iterations ($i = i_{max}$) is performed. The final values of the time of the signal is set to $t = t_i - \tau_i$.

Additionally, in case $|t| > (n - 1/2) \times 25$ ns ($|t| > 75$ ns for 7 samples and $|t| > 100$ ns for 9 samples) it is forced to be $t = \pm(n - 1/2) \times 25$ ns. Figure 4.6 shows the flow chart of this method.

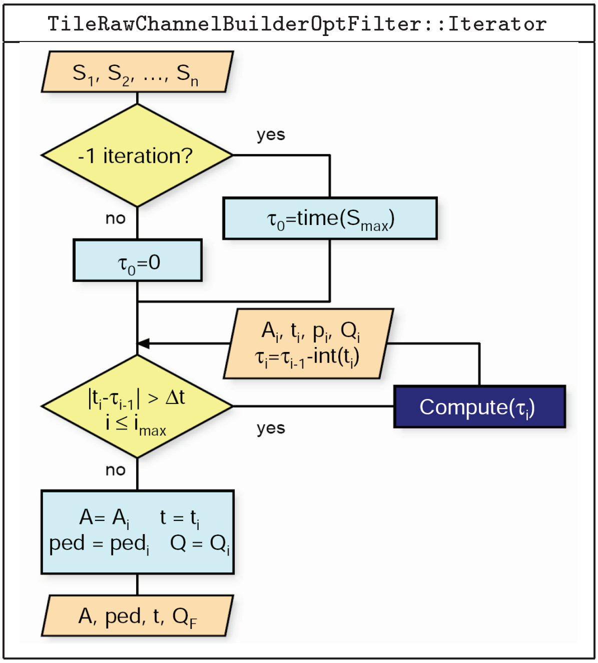

Figure 4.6: Flow chart for the Iterator method in the TileRawChannelBuilderOptFilter class.

- `Filter`: Figure 4.7 shows the flow chart of this method. During its execution, in first place, the maximum and minimum samples (S_{max} and S_{min}, respectively) are found in the string of digits, as they can be used afterwards. A check is performed to see if all the samples are exactly 1023, which is the value put by default by the ROD in the raw data in case no data from the front-end are received. In this particular case, the amplitude, time, pedestal and quality is set to zero.

  If no iteration is requested the Compute method is called using weights for τ=0. If the AmplitudeCorrection is enabled, afterwards the CorrectAmp method is called.

  In the case that iterations are requested in order to avoid biases in the amplitude reconstruction, 3 cases are distinguished and reconstructed differently:

  - If $(S_{max} - S_1) > \sigma$ or $(S_1 - S_n) > 4\sigma$: those events will likely present significant signal and are reconstructed normally with up to i_{max} iterations until $|\tau - t| < \Delta t$ by calling the Iterator method. The values currently used for σ are 5 ADC counts

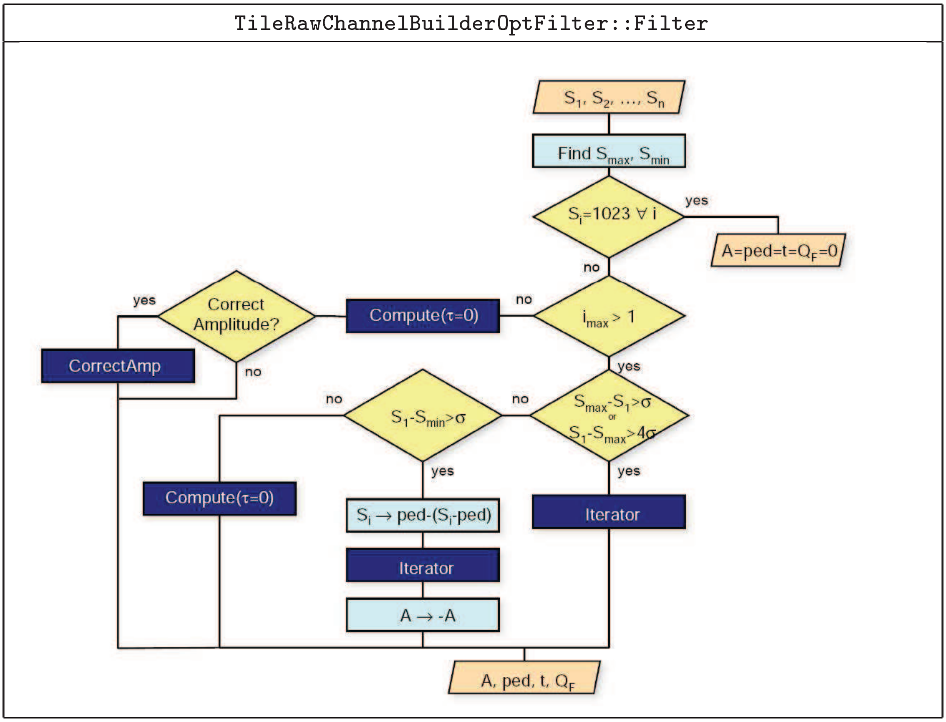

Figure 4.7: Flow chart for the Filter method in the TileRawChannelBuilderOptFilter class.

for high gain and 3 ADC counts for low gain, that is, 3 and 5 times the typical electronic noise sigma, respectively.

- If the above condition is not fulfilled and $(S_0 - S_{min}) > \sigma$: this kind of events probably contain just noise fluctuations and will be treated especially. All the samples will be mirrored around the pedestal (as defined by the PedestalMode property) and reconstructed with iterations by calling the Iterator method. The sign of the amplitude obtained will be inverted so that the negative side of the Gaussian bell is reproduced.
- If the two conditions above are not fulfilled: the event is reconstructed without iterations by calling the Compute method with τ=0, obtaining this way the central part of the noise distribution.

See Section 5.3.1 for the performance of this noise treatment when iterations are used.

- `CorrectAmp`: this method implements in the algorithm the correction to be applied for the approximation of weight granularity when no iterations are performed, see Section 5.3.4 for results on this.

- `Are3FF`: small method used by the Filter method to check whether all the samples are 1023 (0x3FF), as sent by the ROD DSP when no data arrive.
- `FindMaxDigit`: small method to find the position of the highest sample.
- `MaxDigit`: small method to find the value of the highest sample.
- `MaxDigDiff`: small method to find the maximal difference between two samples.
- `createContainer`: it creates an instance of TileRawChannelContainer and records it into the StoreGate.
- `commitContainer`: Once the execution of the algorithm has finished and all the raw channels are stored, the container is locked.

Chapter 5

Optimal Filtering Performance and Validation

“Debes empezar por el principio, con paciencia, no te descontroles, abandona toda especulación que creas cierta y aférrate a los hechos. Esto no es un trabajo para filósofos, chico, sino para artesanos.”
— N. Masot, *La sombra del templario*, 2004

The aim of this Chapter is to show the validation studies performed for the Optimal Filtering algorithm together with its first performance results. In first place, the results on the noise autocorrelation obtained with real and simulated data are presented (Section 5.1) as well as the resulting OF weights (Section 5.2). Studies on the validation of OF have been performed in comparison with the other methods available (Fit and ManyAmps) not only with electronics noise (Section 5.3) but also with minimum bias pileup (Section 5.4). Finally, Section 5.5 presents the effects of the TileCal reconstruction method in the global calorimeter resolution and response.

5.1 Noise Autocorrelation Results

The noise autocorrelation is one of the elements involved in the computation of the OF weights, together with the pulse shape and its derivative. Thus, the elements of the autocorrelation matrices have to be evaluated on real and simulated data, and with MB pileup and electronics noise. Furthermore, its impact on the OF weights obtained from those matrices has to be estimated as well.

On one hand, real data from pedestal runs with $\sim$10000 events have been taken during detector commissioning for noise studies, such as pedestal determination, sample noise, amplitude variance, etc. To reduce the impact of the statistical fluctuations in the autocorrelation results, ~40000 events are taken in pedestal runs meant for autocorrelation studies.

On the other hand, to emulate a pedestal run using Monte Carlo data, custom samples containing TileHits from single non-interacting particles (such as neutrinos or "geantinos") generated at the interaction point were produced. Once these TileHits are digitized, the resulting TileDigits only contain noise. This way, noise studies with simulation can be performed in the whole calorimeter. Furthermore, during digitization, MB pileup can also be added so that noise autocorrelations may be computed in that environment too.

Summing up, the main objectives of this study are to test the goodness of the unitary matrix approximation in the noise autocorrelation as well as to compare the differences in the values of the OF weights in all the cases considered.

5.1.1 Electronic Noise Environment - Real Data

Run number 70183 with 39583 events taken with 71 TileCal modules on 7-2-2007 is used in the analysis in this Section. It was taken with 7 samples in bi-gain mode (saving the output from both high and low gain). The two methods implemented for the autocorrelation calculation (average and rigorous correlation) are tested using the data from this run.

First, histograms with the values obtained for the autocorrelation per channel and time lag $k = |i - j|$ are prepared. From those distributions, the graph of the autocorrelation as a function of the time lag (usually known as correlogram) is built taking the mean and RMS from the above distributions.

The distribution for the average autocorrelation r_k for all channels enabled is shown in Figure 5.4. The corresponding correlograms can be found in Figure 5.1 with the mean and RMS from the distributions in Figure 5.4, showing an overall picture of the average noise autocorrelation in the calorimeter.

Clearly, most of the channels show autocorrelation values not compatible with the unitary matrix approximation for both gains, which are still small although sizeable ($r_k \lesssim 10\%$ for high gain and $r_k \lesssim \pm 6\%$ for low gain).

Figure 5.5 shows the distributions for the average of the rigorous autocorrelation values R_{ij} in each channel with $k = |i - j| = 1, \ldots, 6$ ($\langle R_{i\ \ i \pm k} \rangle$). For instance, $\langle R_{i\ \ i \pm 4} \rangle$ is the average from R_{15}, R_{26} and R_{37}. The distributions obtained are qualitative and quantitatively very similar to the ones from the average correlation approach and, therefore, very similar correlograms are also obtained in this case (Figure 5.2).

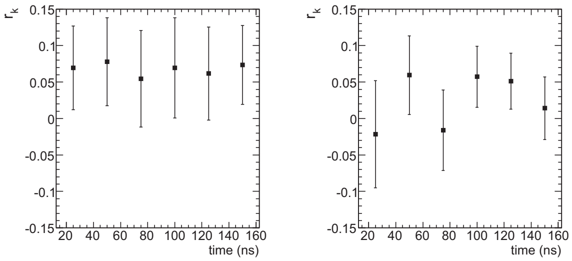

Figure 5.1: Average autocorrelation (r_k) correlogram obtained with real data for high gain (left) and low gain (right).

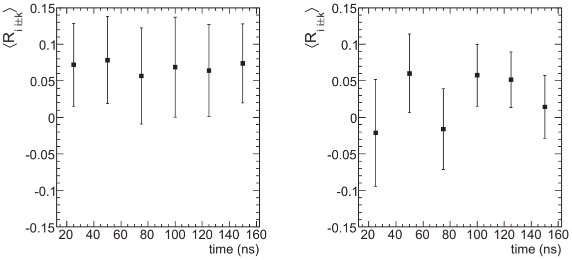

Figure 5.2: Rigorous autocorrelation correlogram obtained with real data for high gain (left) and low gain (right).

Table 5.1 summarizes the mean and RMS from the distributions in Figures 5.4 and 5.5, used for the correlograms in Figures 5.1 and 5.2.

For completeness, Figure 5.6 shows the difference between each $R_{i\ i\pm k}$ with respect to $\langle R_{i\ i\pm k}\rangle$. These variables show how much each individual $R_{i\ i\pm k}$ differs from the average. Following the previous example, the variables are added to the histogram for $k = 4$ are: $R_{15}-\langle R_{i\ i\pm 4}\rangle$, $R_{26}-\langle R_{i\ i\pm 4}\rangle$ and $R_{37}-\langle R_{i\ i\pm 4}\rangle$. The distributions obtained are symmetric and centered at zero, showing that deviations from the average are at the level of ~1-2% for individual R_{ij} within an average of $\langle R_{i\ i\pm 4}\rangle \lesssim \pm 10\%$.

All these results validate the usage of the average autocorrelation instead of the rigorous one, since very small differences are found between the R_{ij} elements with the same time lag and the values obtained with both approaches are very similar. Since average correlations are obtained with a larger statistical sample, only this approach will be considered from now on.

Table 5.1: Autocorrelations for average and rigorous approach.

	High Gain		Low Gain	
time (ns)	Mean	RMS	Mean	RMS
Average Correlation (r_k)				
25	0.0695	0.0573	-0.0215	0.0734
50	0.0778	0.0602	0.0594	0.0540
75	0.0546	0.0662	-0.0161	0.0551
100	0.0694	0.0687	0.0573	0.0419
125	0.0617	0.0639	0.0512	0.0383
150	0.0736	0.0540	0.0141	0.0430
Rigorous Correlation ($\langle R_{i\ \ i\pm k}\rangle$)				
25	0.0721	0.0567	-0.0211	0.0732
50	0.0783	0.0598	0.0600	0.0539
75	0.0567	0.0658	-0.0160	0.0551
100	0.0688	0.0683	0.0577	0.0422
125	0.0639	0.0632	0.0515	0.0382
150	0.0739	0.0540	0.0143	0.0430

5.1.2 Electronic Noise Environment - Simulated Data

The same procedure used for real data treatment has been repeated with a 40000-event Monte Carlo sample of single non-interacting particles digitized only with electronics noise. Figure 5.3 shows the correlograms obtained in this case for high and low gain, respectively.

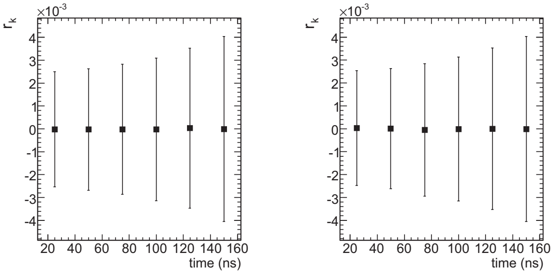

Figure 5.3: Average autocorrelation correlogram obtained with simulated data (electronics noise only) for high gain (left) and low gain (right).

The average values are very close to zero in all time lags, as expected from the uncorrelated Gaussian noise used in the simulation. Furthermore, the RMS from the correlation distributions, which is due only to statistical fluctuations, is very small (less than 0.5% in all cases).

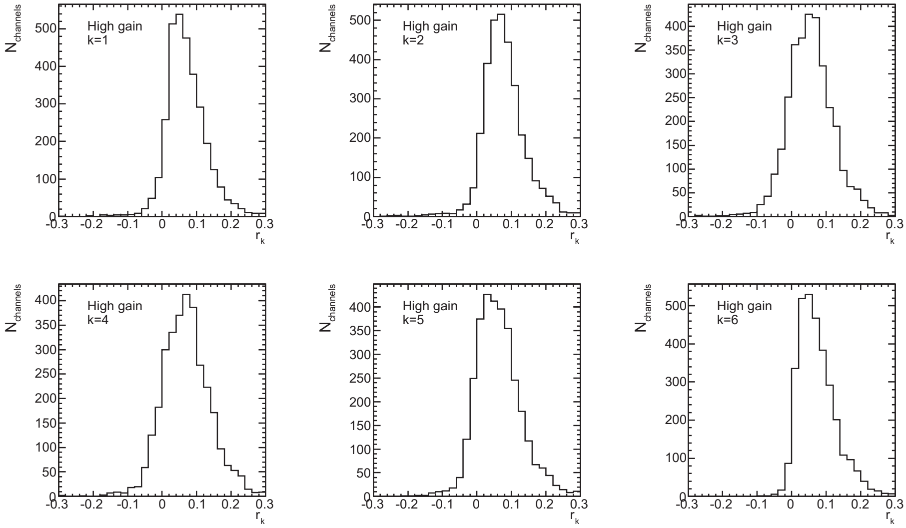

(a) High gain

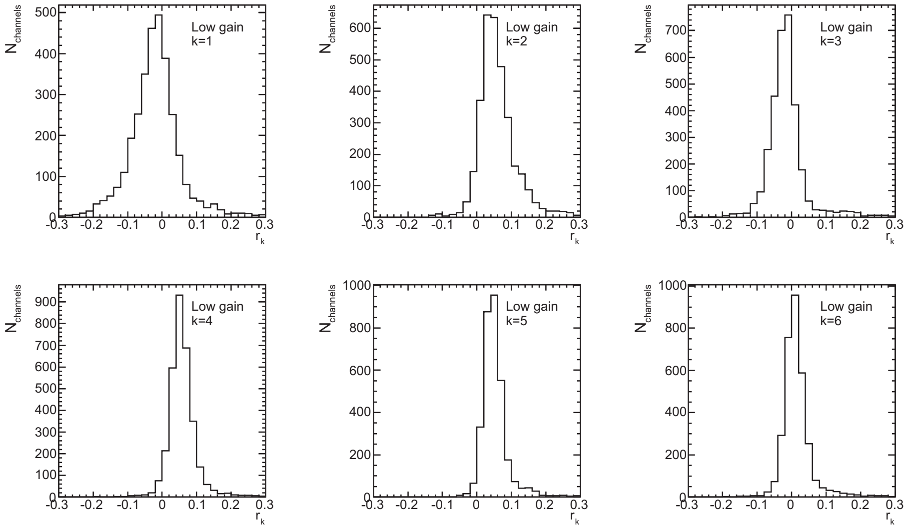

(b) Low gain

Figure 5.4: Distributions of the average autocorrelation (r_k) from real data and for all channels: (a) for high gain and (b) for low gain.

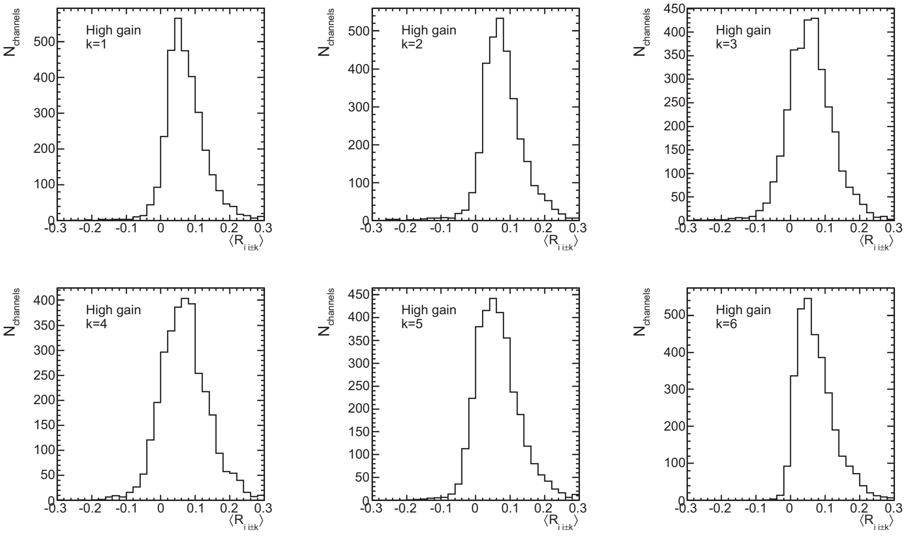

(a) High gain

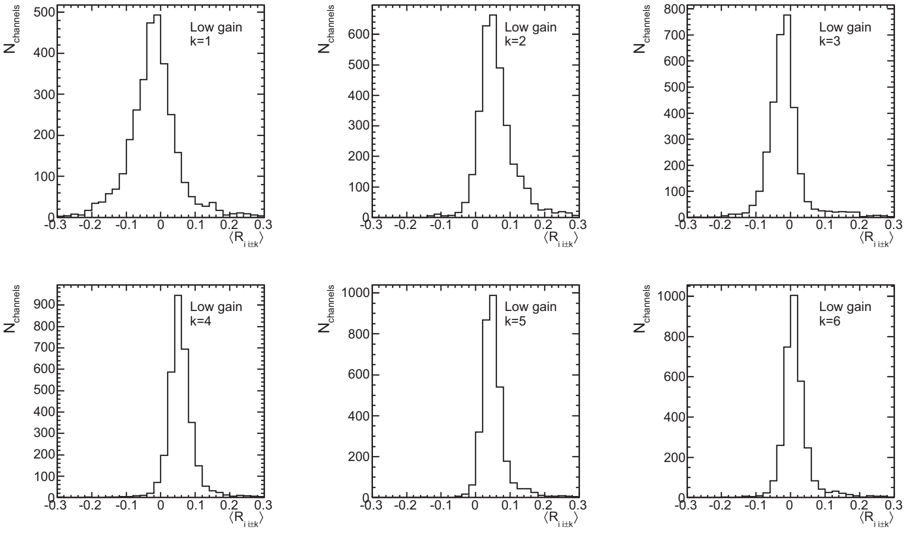

(b) Low gain

Figure 5.5: Distributions of the difference between the rigorous autocorrelation in each channel for $k = |i - j|$ ($R_{i\ i\pm k} - \langle R_{i\ i\pm k}\rangle$) from real data and for all channels: (a) for high gain and (b) for low gain.

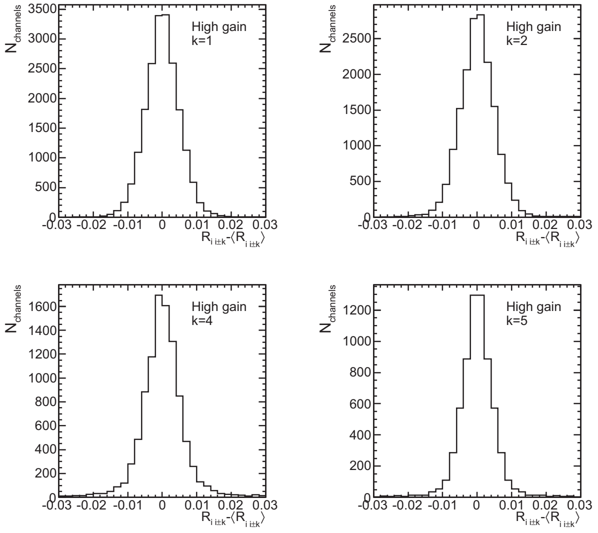

(a) High gain

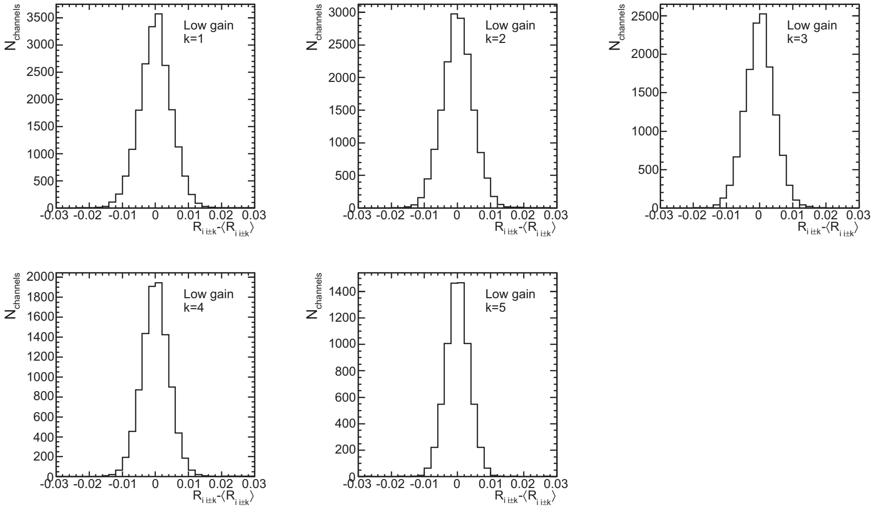

(b) Low gain

Figure 5.6: Distributions of the difference between the rigorous autocorrelation in each channel for $k = |i-j|$ ($R_{ii\pm k} - \langle R_{ii\pm k}\rangle$) from real data and for all channels: (a) for high gain and (b) for low gain.

5.1.3 Minimum Bias Pileup Noise Environment - Simulated Data

The autocorrelation obtained using the same single non-interacting particle Monte Carlo but performing the digitization with electronic noise and low luminosity minimum bias pileup is presented in this Section. Several approximations can be assumed considering the characteristics of the MB events as a noise source. Hence, we can beforehand assume that it is symmetric in ϕ, so the channels with the same (η, r) should present the same behaviour. Although the dependence of the p_{T} spectrum for MB events in η is small we will study separately the channels corresponding to each η-tower in the calorimeter. Furthermore, channels at different depths (i.e., with different r values) are also treated separately as the particle multiplicity from minimum bias events is larger at small values of this coordinate.

Therefore, distributions for the average noise autocorrelation obtained for channels in all ϕ for different (η, r) are built for each time lag. Figure 5.7 shows as an example those distributions for the innermost TileCal layer ($r\sim$2.5 m) and the fifth tower ($\eta\sim$0.45). For high gain channels, the largest correlations are seen for k=1, 2, as expected due to the fact that the electronics pulse has a FWHM of 50 ns. Much smaller correlations are seen for low gain channels, due to the smaller impact of physics noise in this gain.

Figures 5.8-5.13 show the correlograms obtained for all TileCal layers and towers. Negligible correlations are found for low gain channels in all cases. Regarding high gain channels, the autocorrelation clearly decreases for higher values of r as expected, but no strong dependence is found as a function of the η coordinate. For this reason and in order to have a simplified approach to handle MB pileup noise, we can define a common autocorrelation value in each calorimeter layer for a given lag by taking the weighted mean of the values obtained in all the towers. Table 5.2 shows the results obtained for all time lags and calorimeter layers with this approach.

Table 5.2: Average autocorrelation in each TileCal layer for simulated data with electronic noise and low luminosity minimum bias pileup.

	Layer A		Layer BC		Layer D	
time (ns)	High Gain	Low Gain	High Gain	Low Gain	High Gain	Low Gain
25	0.3359	0.0016	0.1384	0.0003	0.0324	0.0001
50	0.1315	0.0006	0.0541	0.0002	0.0133	-0.0001
75	0.0316	0.00001	0.0130	0.0002	0.0036	0.0000
100	0.0037	0.0001	0.0014	0.0000	0.0004	-0.0001
125	-0.0017	0.0000	-0.0010	0.0000	-0.0003	-0.0002
150	-0.0023	0.0001	-0.0013	0.0000	-0.0004	-0.0002

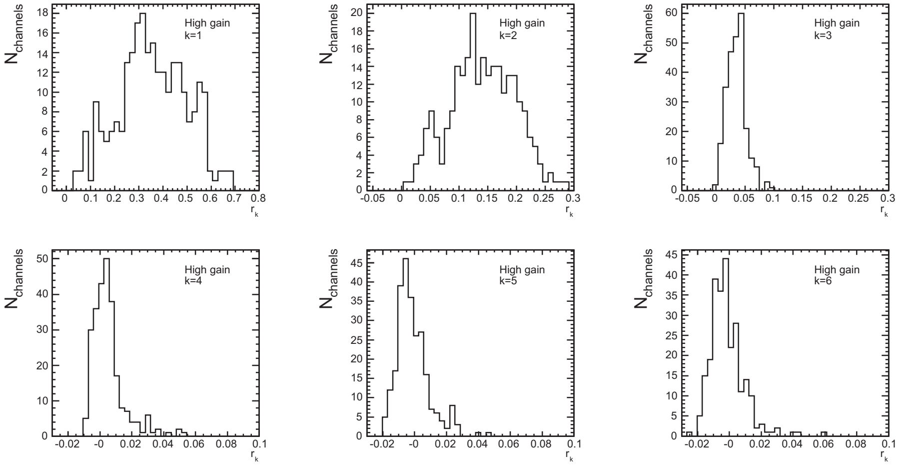

(a) High gain channels

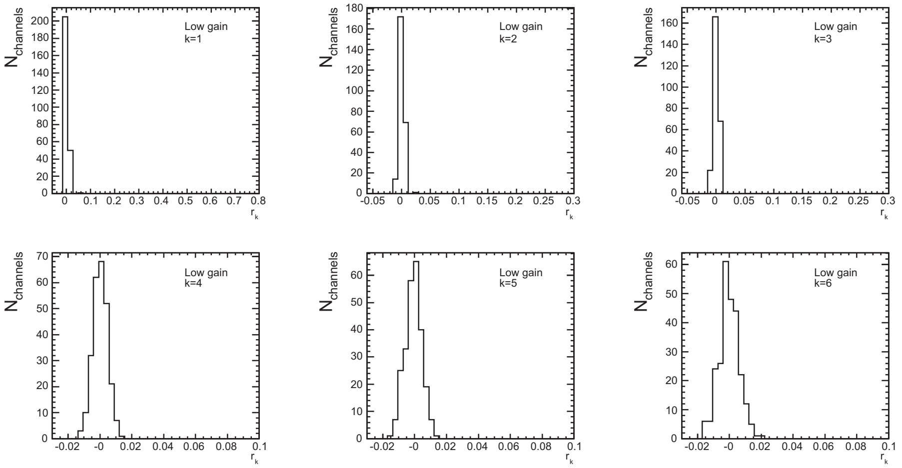

(b) Low gain channels

Figure 5.7: Average correlation distributions for the channels in the fifth tower ($\eta\sim0.45$) in the first layer of TileCal ($r\sim2.5$ m). Note the different scale for k=1, 2.

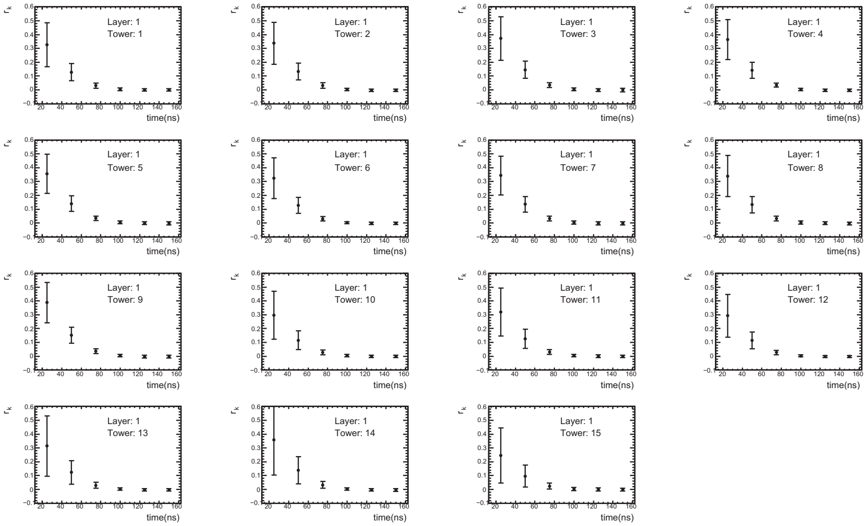

Figure 5.8: Correlograms for high gain channels in the layer A from MC data with electronic noise and MB pileup.

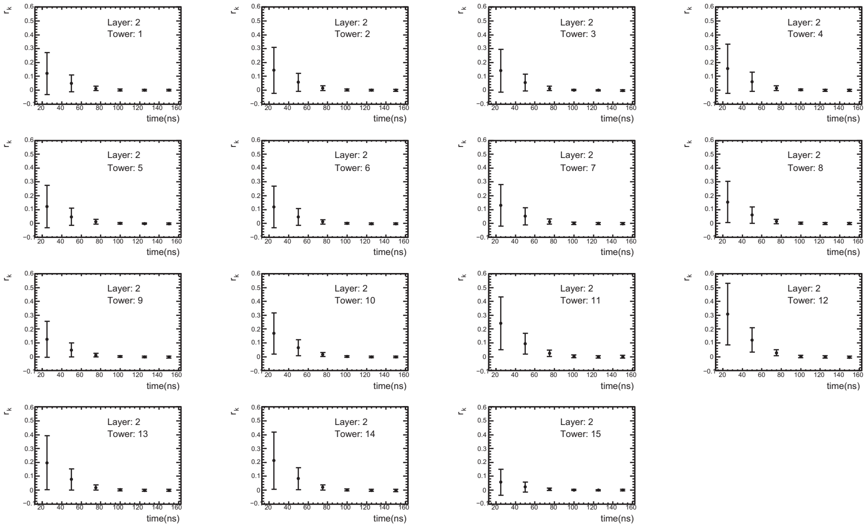

Figure 5.9: Correlograms for high gain channels in the layer BC from MC data with electronic noise and MB pileup.

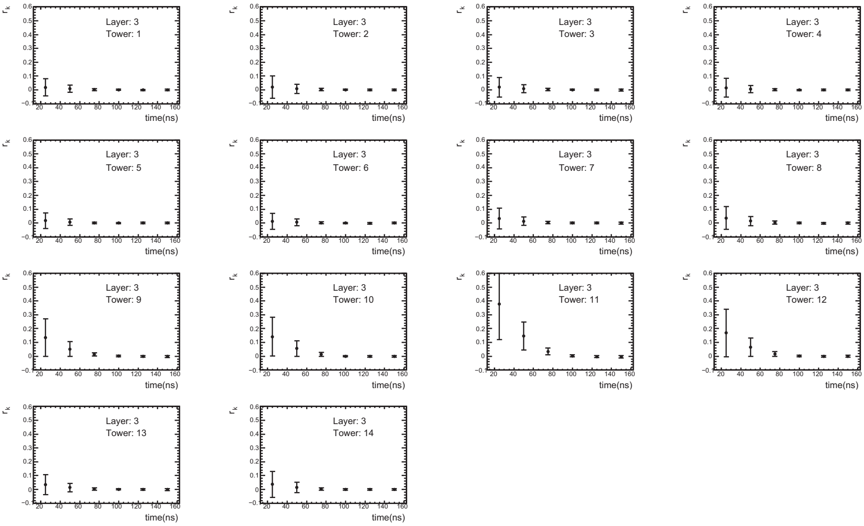

Figure 5.10: Correlograms for high gain channels in the layer D from MC data with electronic noise and MB pileup.

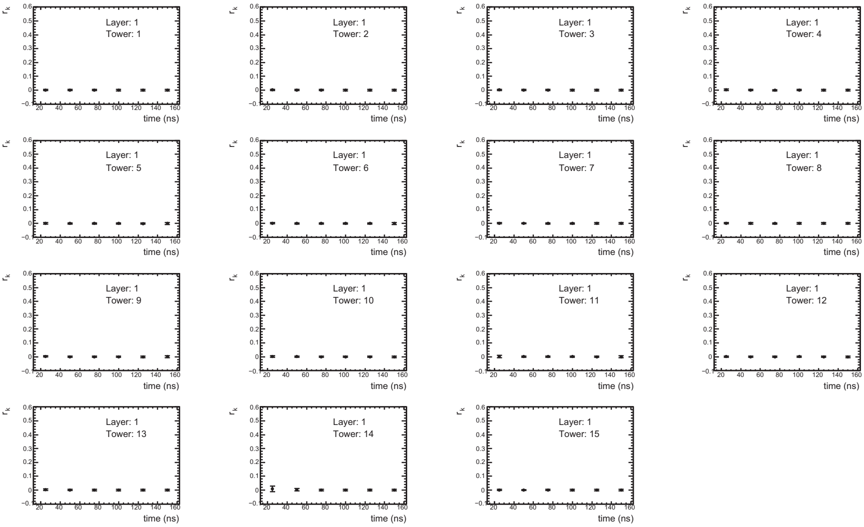

Figure 5.11: Correlograms for low gain channels in the layer A from MC data with electronic noise and MB pileup.

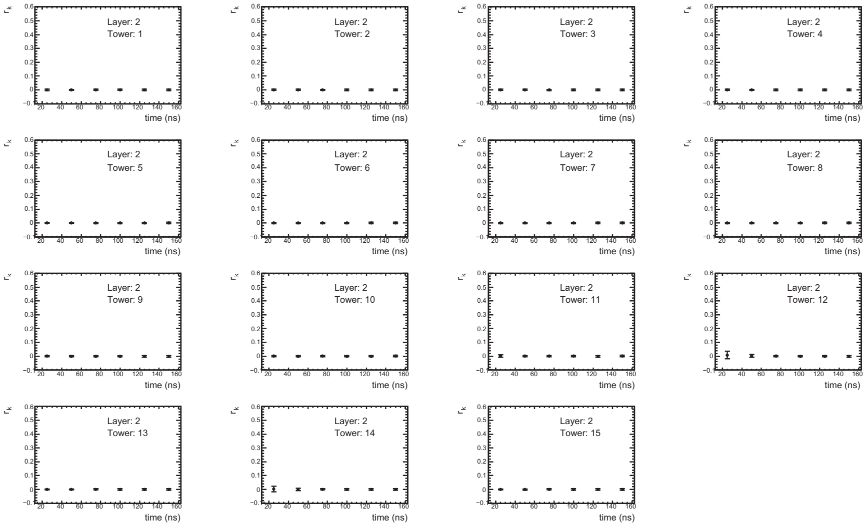

Figure 5.12: Correlograms for low gain channels in the layer BC from MC data with electronic noise and MB pileup.

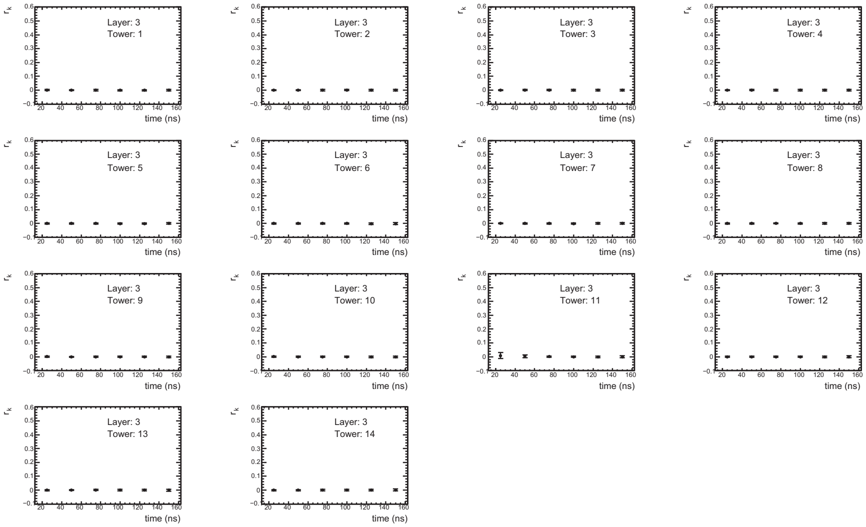

Figure 5.13: Correlograms for low gain channels in the layer D from MC data with electronic noise and MB pileup.

5.2 Optimal Filtering Weights

Figure 5.15 shows the values for the a_i, b_i and c_i OF weights as a function of the phase τ when using the delta correlation approximation (i.e., assuming r_k=0 for k⩾1). However, as non-zero values for r_k have been found in real data as well as in simulated data with MB pileup, the impact of such correlations on the weights has to be evaluated. We will focus on the high gain only, since in low gain smallest correlations are found in real data and they are negligible with MB simulated data.

The five main scenarios to be considered for weight calculation are delta correlation (r_k=0 for k⩾1), real electronic noise (with the values summarized in Table 5.1), MB noise in layer A, in layer BC and in layer D (with the values summarized in Table 5.2).

Figure 5.14 shows the difference between the central OF weights (a_4, b_4 and c_4) as computed in the 4 latter scenarios compared with the ones obtained with the delta correlation assumption (a_4^δ, b_4^δ and c_4^δ). As expected, no difference is found for layer BC and D with MB pileup, but sizeable differences are obtained in layer A. The deviation from the delta weights is however much bigger when electronic noise from real data is considered, showing that autocorrelations coming from MB at the level of $r_{1(2)}$~35(15)% have smaller effects on the weights obtained than autocorrelations of the order of ~5-7% in all time lags.

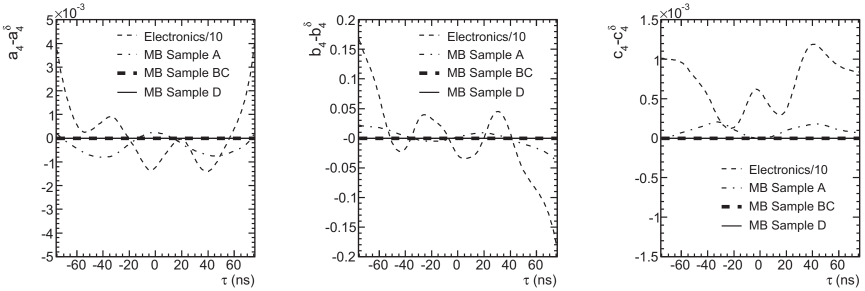

Figure 5.14: Comparison of the a_4 (left), b_4 (center) and c_4 (right) OF weights for high gain channels for the autocorrelation scenarios described in the text taking as reference the delta correlation weights (a_4^δ, b_4^δ and c_4^δ). Note that the values are reduced by a factor 10 in the case of the electronic noise.

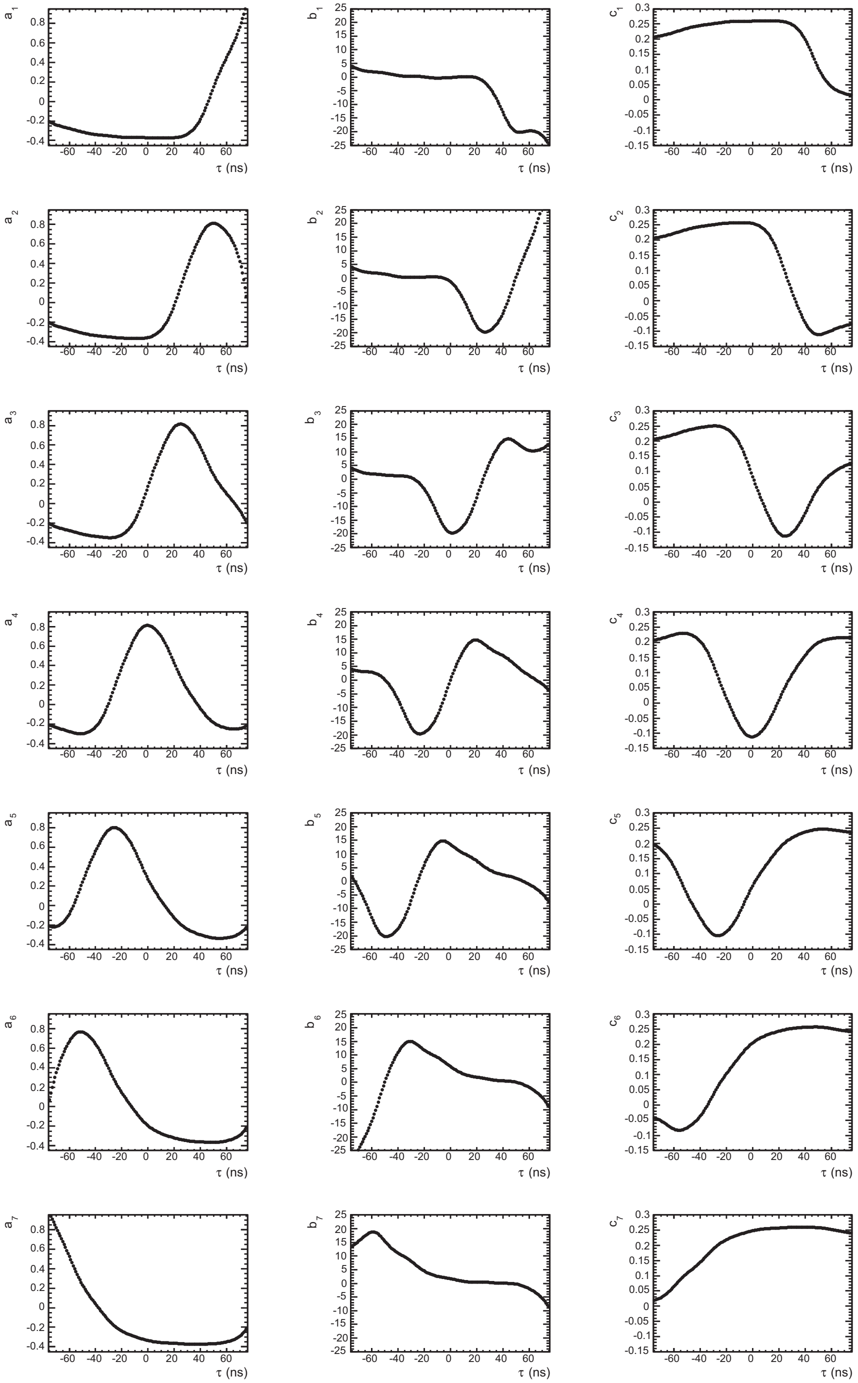

Figure 5.15: Optimal Filtering weights for high gain channels obtained with the delta correlation approximation.

5.3 Validation Under Electronic Noise Environment

5.3.1 Amplitude Variance for Empty Events

This Section is devoted to the study of the reconstructed amplitude variance in pedestal-like events. Note that this variable is not the same as the so-called "high-frequency noise" (the RMS of the 7 samples taken in pedestal events) or "low-frequency noise" (pedestal variation in a event-by-event basis), but the distribution of the resulting amplitude from the reconstruction methods applied to non-signal events.

OF with Iterations

As shown in Section 4.5.2 when iterations are enabled in the Optimal Filtering algorithm, a special treatment for pedestal-like events is used to avoid any bias towards positive amplitudes. Real data from Commissioning run 61621 (7 samples, automatic gain), taken on 7-11-2006, is used here for the comparison of OF and the Fit method.

Figure 5.16 shows the distributions for the amplitude variance for both methods selecting events with $A<20$ ADC counts. The distributions are symmetric and centered at zero, as expected for pedestal-like events, with a long tail in the positive region due to events where signals are present. However, it is clear that the distribution for OF is slightly narrower.

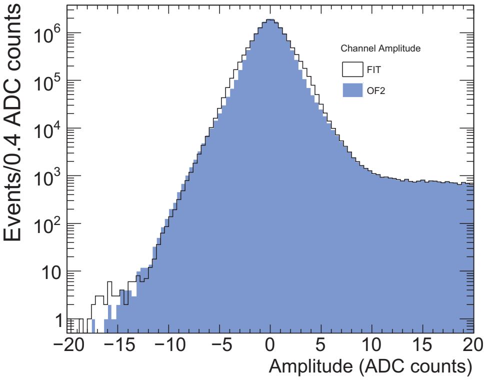

Figure 5.16: Distribution of the amplitude for Fit and OF2 (with iterations) for commissioning data run 61621.

Figure 5.17 shows the amplitude obtained with OF (A_{OF2}) as a function of the amplitude obtained with Fit (A_{Fit}) for all events and, in addition, separately for the 3 cases used for the noise treatment in OF (negative iterations, no iterations and positive iterations). Although a small fraction of events has completely uncorrelated behaviour between OF and Fit, the positive and negative tails are strongly correlated as well as most of the events in the central region. Nevertheless, this result validates the procedure implemented in OF for pedestal-like events treatment when using iterations as it describes correctly the positive and negative regions of the distributions and presents a very similar behaviour as from the Fit method.

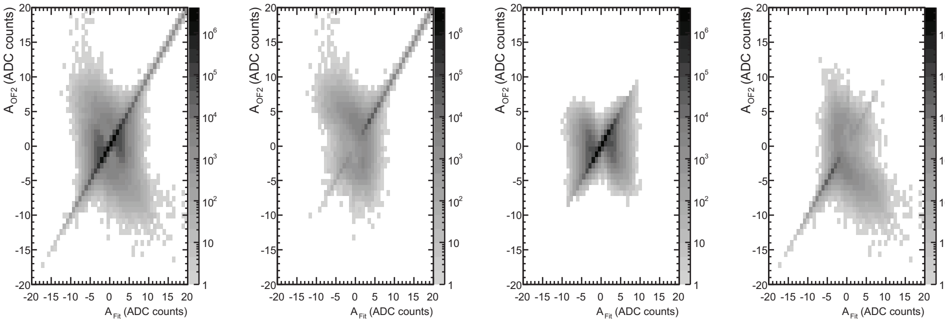

Figure 5.17: Correlation between the amplitudes obtained with Fit and OF2 with iterations enabled for events with A<20 ADC counts for commissioning run 61621. From left to right: all channels, case 1 (positive iterations), case 2 (no iterations) and case 3 (negative iterations)

OF without Iterations

Figure 5.18 shows the results for the amplitude variance for commissioning cosmic run 46968 (7 samples, automatic gain) taken on 14-3-2008 for Fit, OF without iterations and OF with iterations.

The same performance is found for Fit and OF with iterations as in the previous case. However, the distribution obtained for OF without iterations is much narrower.

One can conclude that the iteration procedure used with unknown phase data and the mechanism introduced to handle pedestal-like events results in a larger amplitude variance, but it is needed to properly reconstruct this kind of data.

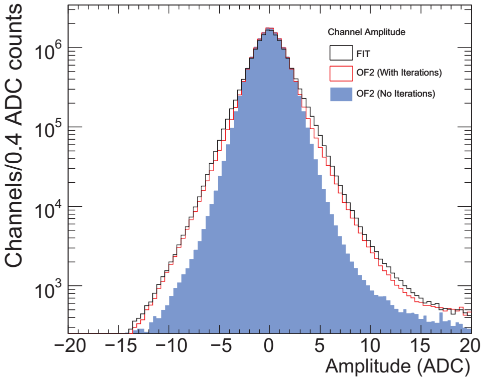

Figure 5.18: Distribution of the amplitude obtained with the Fit method (black line), OF with iterations (red line) and OF without iterations (solid blue) for commissioning run 46968.

To conclude, Figure 5.19 shows the amplitude variance for Monte Carlo data in order to check the OF performance not only as compared with Fit, but also with the ManyAmps method. A sample of single pions with E=50 GeV generated and simulated in full ATLAS is used. Very similar results are obtained for OF without iterations and ManyAmps, with Fit providing wider distributions.

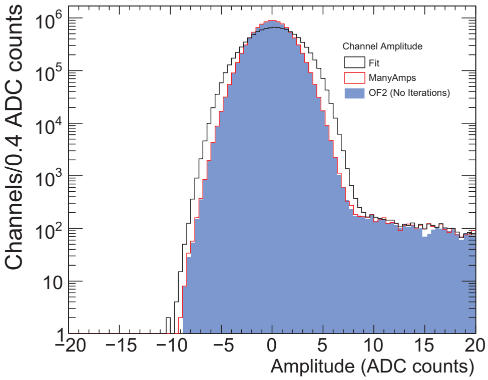

Figure 5.19: Distribution of the amplitude obtained with the Fit method (black line) with ManyAmps method (red line) and with OF without iterations (solid blue) for simulated single pions with E=50 GeV.

Table 5.3 summarizes the mean and RMS from the amplitude variance distributions considering only channels with $|A|<7$ ADC counts to avoid any bias which could be introduced in the computation by the positive tail.

Table 5.3: Amplitude variance mean and RMS for Fit and OF2 for all the data considered.

	Mean (ADC counts)	RMS (ADC counts)
Real data run 46968 (November 2006)		
Fit	0.013938	1.579458
OF2 with iterations	0.003843	1.443401
Real data run 46968 (March 2008)		
Fit	0.023293	1.733377
OF2 with iterations	0.009521	1.597536
OF2 without iterations	0.000034	1.446327
Simulated pions (E=50 GeV)		
Fit	0.153798	1.579458
ManyAmps	0.000877	1.757498
OF2 without iterations	0.000851	1.75845

5.3.2 Amplitude and Phase with Simulated Data

This Section is devoted to the study of the results for amplitude and time from the Optimal Filtering algorithm when used to reconstruct Monte Carlo data. In order to better check the influence of the noise in the reconstruction, the data sample used was selected to contain only low energy particles, so that the signal-to-noise ratio were relatively small. Hence, a sample of single pions with E=50 GeV simulated in the full ATLAS environment is used in all this Section. Indeed, small amplitudes will be reconstructed in each channel due to the fact that, on one hand, part of the total energy will be deposited in the electromagnetic calorimeter before reaching TileCal and, on the other hand, the fraction of the pion energy deposited in TileCal is actually shared between several channels.

The performance of the OF algorithm is checked by comparing its results with the results from the Fit method and also from ManyAmps whenever iterations are not used.

OF with Iterations

Since these data are simulated in the full ATLAS environment, the timing of the signal is expected to be $t{\approx}0$ because the trigger is synchronized with the LHC bunch crossing. However, we still use here OF with iterations is tested on these simulated data.

Figure 5.20 shows the distributions of the amplitude obtained from OF and Fit, $A_{\rm OF2}$ and $A_{\rm Fit}$, and the correlation between them for channels with $A{>}15$ ADC counts. Only small differences are observed with a very strong correlation in the values obtained with both methods.

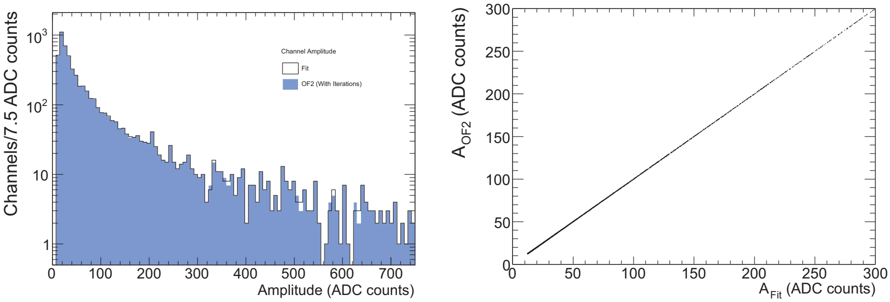

Figure 5.20: On the left, distribution of the amplitudes obtained with the Fit method (black line) and with OF with iterations (solid blue) for those channels with $A{>}15$ ADC counts. On the right, $A_{\rm OF2}$ as a function of $A_{\rm Fit}$ for channels with $A{>}15$ ADC counts.

Figure 5.21 shows the values obtained for the time by both algorithms. The first conclusion one can draw from this Figure is that even though most of the channels have times close to 0, some of show bigger times, even with $t{\sim}5$ ns. This effect is due to the size of the read-out tiles (drifting time of the photons inside the scintillating plastic) and also to late particles produced during the hadronic shower development.

It is also important to note that certain channels with exactly $t_{\rm Fit}{=}0$ ns show $t_{\rm OF2}{\neq}0$ ns. These channels with $t_{\rm Fit}{=}0$ ns correspond to those cases where the Fit method selects to use the 2-parameter fit is performed because the resulting χ^2 is better than in the 3-parameter fit (see Section 4.1.3). Note also that the channels shown have $A{>}15$ ADC counts, so these channels do not correspond to pedestal-like events. This is due to the trigger synchronization, which produces cases where the actual energy deposited is not unlikely to be better reconstructed with the 2-parameter fit approach than with the 3-parameter approach.

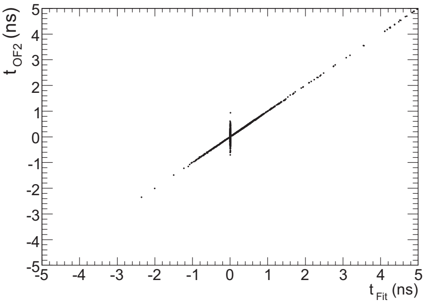

Figure 5.21: Values obtained for $\tau_{\rm OF2}$ as a function of $\tau_{\rm Fit}$ for the channels with A>15 ADC counts using simulated single pions with E=50 GeV.

Figure 5.22 shows the relative difference in amplitude between the methods studied for all channels with A>70 ADC counts. Looking at the distribution for this variable, values are concentrated in the region where relative differences are less than 1‰. The asymmetry in this distribution can be explained the relative difference of the amplitudes as a function of the time is plotted (Figure 5.22, right). A clear structure is seen in slices of 1 ns (from -0.5 to 0.5 ns, from 0.5 to 1.5 ns, etc.). Each slice is also divided in two parts with positive differences ($A_{\rm OF2} > A_{\rm Fit}$) in the lower part and negative differences ($A_{\rm OF2}$<$A_{\rm Fit}$) in the higher part.

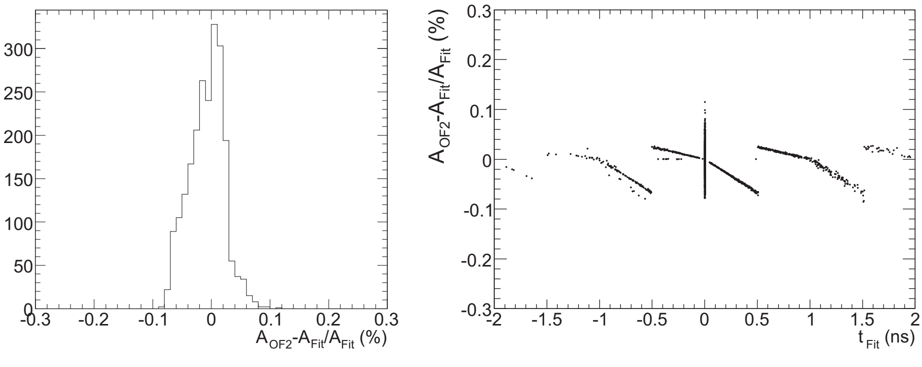

Figure 5.22: On the left, distribution for the relative difference of the amplitudes (in %) for events with A>70 ADC counts. On the right, relative difference of the amplitudes as a function of the time obtained in the Fit method.

This behaviour can be understood by noting that the OF weights are computed and stored in steps of 1 ns. When the time corresponds exactly to the phase where the OF weights were computed (τ=0 ns, ±1 ns, ± 2 ns,...), the amplitudes obtained in both methods agree completely. As the time differs from the phase used for weight calculation, the results are worse as implied in Eq. (4.8). This also explains why there are either positive or negative differences at each side. The different slope in the difference (up to -0.9‰ at $t-\tau$=0.5 but only 0.2‰ at $t-\tau$=-0.5) is due to the different pulse shape derivative at each edge of the maximum.

OF without Iterations

As mentioned above, the time in Monte Carlo data is expected to be $t{\approx}0$ since the trigger is synchronized with the LHC bunch crossing.Thus, the performance of OF without iterations (using only the weights computed for τ=0 ns) has been tested by comparing its results with the Fit method. In addition, the ManyAmps method, default for full ATLAS data up to Athena release 13, is also used for comparison.

Figure 5.20 shows the distributions of the amplitudes obtained with the 3 methods for all channels in which either A_{OF2}, A_{Fit} or A_{ManyAmps} are larger than 20 ADC counts. At high amplitudes, the agreement between the 3 methods is very good, but at low amplitudes discrepancies are high, with a non-negligible amount of events with A_{OF2} or $A_{\mathrm{ManyAmps}} < 20$ ADC counts and A_{Fit}>20 ADC counts.

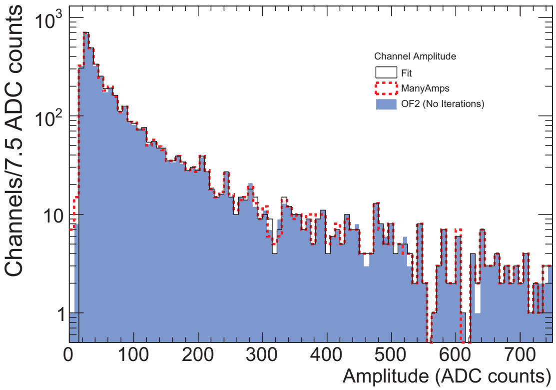

Figure 5.23: Distribution of the amplitude obtained with the Fit method (black line), ManyAmps method (dashed red line) and with OF without iterations (solid blue).

The explanation for this can be found when looking at the values of A_{Fit} and A_{ManyAmps} as a function of A_{OF2} (Figure 5.24). In most of the cases a good correlation is obtained, but for some events $A_{\mathrm{OF2}}<A_{\mathrm{Fit}}$ and also $A_{\mathrm{OF2}}>A_{\mathrm{ManyAmps}}$.

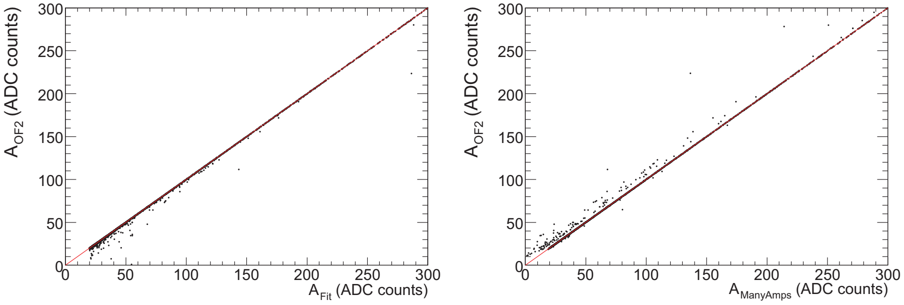

Figure 5.24: On the left (right), correlation between A_{OF2} and A_{Fit} (A_{ManyAmps}) for channels with A>15 ADC counts for simulated data.

In order to check whether these trends are related with the time of the signal, one must first confirm that this variable as output from the reconstruction is correct. Figure 5.25 shows the correlation for t_{OF2} as a function of t_{Fit}, with very similar results as in the case of OF with iterations (Figure 5.21) although only weights for τ=0 ns are used. At large values of t, the correlation is slightly worse, but the results are nevertheless in good agreement for $t\sim\pm5$ ns, and hence consistent for the range expected for full ATLAS data.

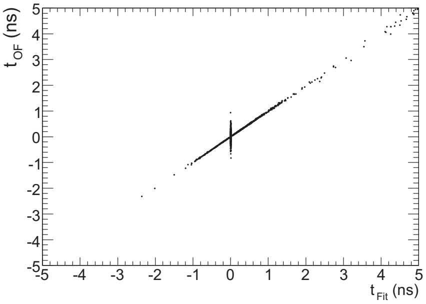

Figure 5.25: Values obtained for t_{OF2} as a function of t_{Fit} for the channels with A >15 ADC counts for simulated data.

At this point we can plot the Relative difference of the amplitudes as a function of the time (Figure 5.26). In this case, the differences between all the methods are evaluated taking as reference A_{Fit} and plotted as a function of τ_{OF2}.

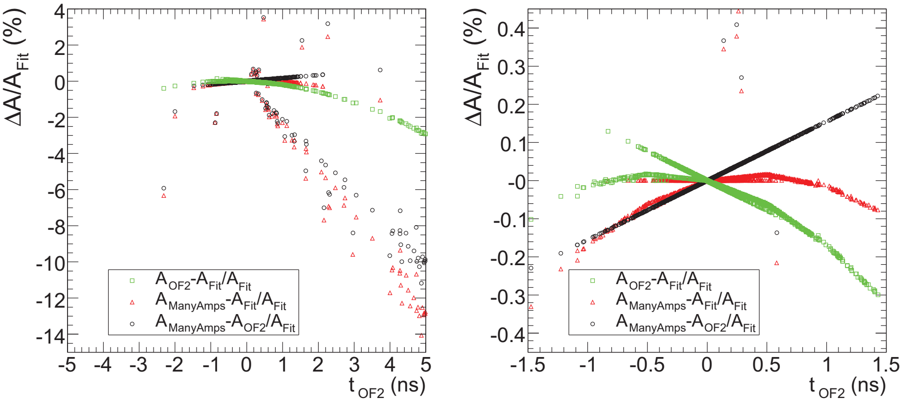

Figure 5.26: Relative difference of the amplitudes as a function of τ_{OF2} for the 3 methods considered. On the left, for $|\tau|<5$ ns (left) and $|\tau|<1.5$ ns (rigth).

The most surprising feature seen when making this comparison is that in the ManyAmps method some cases show smaller amplitudes than the other methods, with up to ∼10-12% difference for $t=5$ ns. Those events are produced for cases where during the fitting procedure lower χ^2 values are found when using 2 amplitudes instead of 1. In other words, the defect in the resulting amplitude at $t=0$ ns is caused by the another small amplitude at $t=\pm25$ ns used for the reconstruction.

Table 5.4 shows an example of one of those events. Fit and OF provide amplitudes of $A\approx166$ ADC counts with $\tau\sim2.6$ ns, but ManyAmps assigns an additional amplitude with 25 ADC counts at $t=25$ ns. Thus, the central amplitude reconstructed at $t=0$ ns has only $A\approx153$ ADC counts.

Table 5.4: Example of the reconstruction for a given channel in a simulated event.

Raw samples						
49	51	117	214	161	89	58

Reconstruction			
	A (ADC counts)	t (ns)	ped (ADC counts)
Fit	166.6	2.73	53.5
OF2	165.1	2.55	54.0
ManyAmps	153.2 25.4	0 25	49.8

Furthermore, in the region where $|t| \lesssim 1.5$ ns, apart from the differences stated above in the ManyAmps method, there is a linear deviation between ManyAmps and Fit with up to 2‰ at $t=1.5$ ns. But for higher times, this trend is broken and all the events are misreconstructed.

Regarding the differences between OF2 without iterations and Fit, the same behaviour as observed in the OF with iterations case is seen here also for $|t| < 0.5$ ns (maximum difference on the order of ∼1‰), but this discrepancy increases for higher times up to 3% at $t=5$ ns. The conclusion is that the amplitude is strongly affected by the usage of non suitable weights. In fact, the deviations in the amplitude are much more important than in the time, as correct values for t are obtained at high times but considerable differences are found for the amplitude.

In the real ATLAS environment, no iterations are performed in order to handle properly the minimum bias pileup (see Section 5.4) and such differences in amplitude due to the usage of weights computed for $t=0$ should be corrected as shown in Section 5.3.4.

5.3.3 Amplitude and Phase with Real Data

Commissioning

During this Section, cosmic run 28940 taken on 2007-10-27 during the M5 commissioning milestone week is used to validate the OF results for amplitude and time. The detectors which were used in a combined way in this run were: LAr electromagnetic calorimeter, HEC, FCal, TileCal, MDT and RPC. Data from TileCal were taken with 9 samples and automatic gain with a total of 1.5×10^6 events recorded during more than 17 hours. From those events only events triggered by the TileCal cosmics trigger[1] were used for this analysis as for those events the cosmic muons will most likely go through TileCal and, thus, energy will be deposit in the calorimeter.

It is worth to mention that the data acquired from cosmics show different features as in the final ATLAS data. In first place, the acquisition was performed during this milestone week with 9 samples instead of the 7 which are used in normal ATLAS running. Since the cosmics are not synchronized with the LHC clock, events are acquired with unknown time so one would expect a wide range of times, and iterations are needed to properly reconstruct the data with OF.

---

[1] The TileCal cosmic Level-1 trigger is generated by a custom set of 9U VME coincidence boards, connected to the analogue trigger sums from the calorimeter.

Figure 5.27 shows the distribution of the amplitudes obtained in OF with iterations and the Fit method and the correlation between them. As regards the amplitude distribution, the energy spectrum is dominated by low energy channels, far more than in 50-GeV pions simulated data from Section 4.2 (cosmic muons typically deposit 2-3 GeV in a TileCal module). Good agreement for the times obtained in both methods is also found.

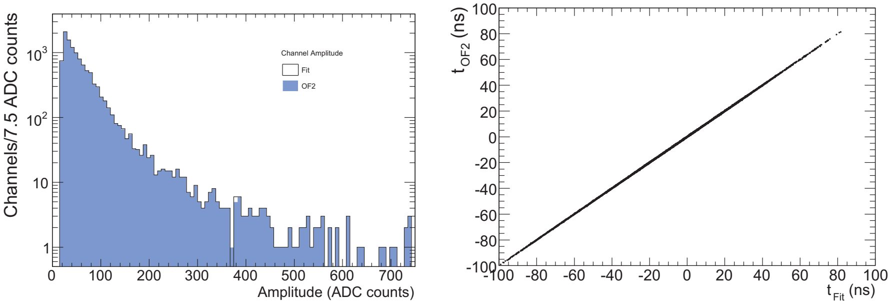

Figure 5.27: On the left, distribution of the amplitude obtained with the Fit method (black line) and with OF with iterations (solid blue) for those channels with A>15 ADC counts. On the right, t_{OF2} as a function of t_{Fit} for channels with A>15 ADC counts.

Indeed, Figure 5.28 shows the distribution for the absolute difference in amplitude and time for both methods, with most of the channels lying in a band between ΔA<0.1-0.2 ADC counts and Δt<0.1 ns.

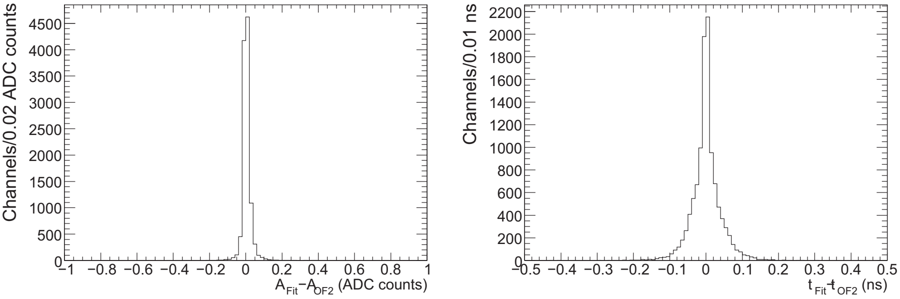

Figure 5.28: On the left, distribution of the amplitude difference for the channels with A>20 ADC counts. On the right, distribution for the time difference for channels with A>20 ADC counts.

Figure 5.29 shows the relative difference between the amplitudes obtained in OF and Fit. Although most of the cases fall well within a ± 1‰ band, there is a clear structure in steps of 25 ns, with larger differences as t increases. This is due to the fact that each 25 ns one sample from the falling edge of the pulse is lost and the fluctuations between the results from the different methods increase. Sparks towards bigger differences are found in the proximity of the transition regions ($t \approx 0$, ±25 ns, etc.).

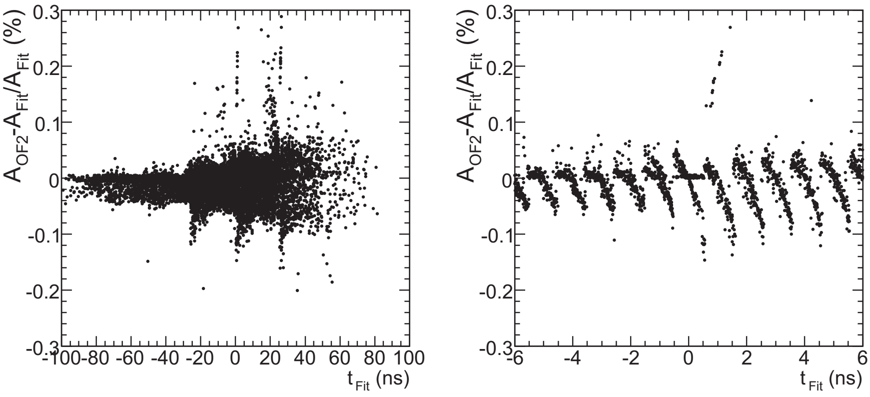

Figure 5.29: Relative difference of the amplitudes obtained from Fit and OF as a function of t_{Fit} for cosmics data.

When looking in detail in the small time region (Figure 5.29 right), the same structure found on MC data (Figure 5.22 right) is seen, with not so defined trends due to the non-ideal noise environment and pulse shape variations present in real data.

5.3.4 Amplitude Correction

As shown previously, the usage of iterations ensures a proper reconstruction of amplitudes and times in data with unknown time (as in the cases of cosmic commissioning data). On the contrary, during LHC operation no iterations are applied in OF and the amplitude of channels out of time (i.e., with non-zero time) is known to be underestimated. To compensate this effect, a correction function was proposed to prevent its impact in the overall calorimeter performance [30].

Data from the 2004 Combined Test Beam (CTB) period was used to extract the correction function since, as will be discussed in the next section, high energy pion beams provide a wider amplitude range, much more than with cosmic commissioning data. In particular, run 2102202 taken on 20-10-2004 with a single pion beam of 180 GeV impinging the TileCal modules at η=0.55 is used for the following studies.

Figure 5.30 shows the profiles for the relative difference of the amplitudes between Fit and OF as a function of the OF reconstructed time. By fitting these plots, the functional form for the deviation can be assumed to be a second order polynomial:

$$\frac{A_{\rm Fit} - A_{\rm OF2}}{A_{\rm Fit}} \times 100 = \alpha + \beta t_{\rm OF2} + \gamma t^2_{\rm OF2} \tag{5.1}$$

Thus, the correction to apply on $A_{\rm OF2}$ obtained from weights for t=0 is:

$$A^{\rm corr}_{\rm OF2} = A_{\rm OF2}\left(1 + \frac{\alpha + \beta t_{\rm OF2} + \gamma t^2_{\rm OF2}}{100}\right) \tag{5.2}$$

The results obtained from the parameters in the fit to Eq. (5.1) in the profiles of Figure 5.30 are shown in Table 5.5.

Table 5.5: Results of the parabolic fit to the profiles in Figure 5.30.

	α	β	γ
$\|t\|$ <5 ns	0.00368	0.0845	0.0894
5 ns< $\|t\|$ <15 ns	0.565	0.116	0.0751

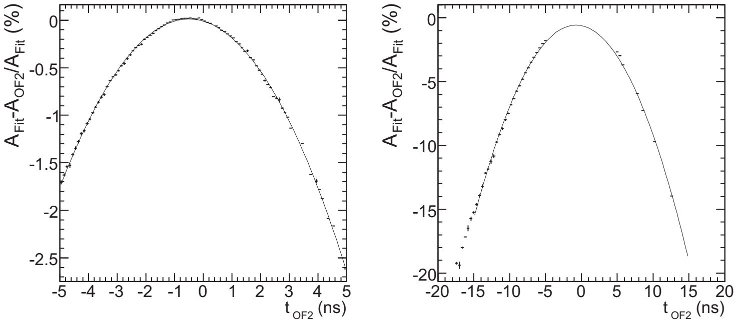

Figure 5.30: Profile for the amplitude relative difference as a function of the time for $|t_{\rm OF2}|$ <5 ns (left) and 5 ns< $|t_{\rm OF2}|$ <20 ns (right) as obtained from the combined test beam run 2102202.

Figure 5.31 shows the performance of such an amplitude correction. The relative difference of the amplitudes for all channels as a function of the time in the $|t|$ <10 ns as well as the corrected amplitude in this range are shown. This way, up to 7% discrepancies are reduced significantly to only 0.5-1%. Moreover, in the $|t|$<4 ns region the correction is even more accurate reducing the discrepancy between Fit and OF2 to a level of less than ∼1‰.

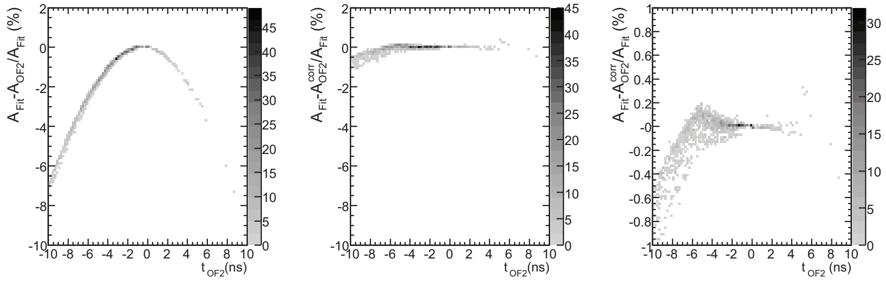

Figure 5.31: Relative difference of the amplitudes between A_{OF2} and A_{Fit} as a function of t_{OF2} for uncorrected amplitudes (left) and once the correction is applied (center), with a zoom in the 1% difference (right) as obtained from the combined test beam run 2102202.

Since the time during ATLAS during operation will be well synchronized with the LHC clock, very few channels will have big values of t (as shown in Figure 5.21 with Monte Carlo data). Precisely in the low-t region, where most of the events lay, is where this amplitude correction reduces the relative difference to only $\sim$0.5‰.

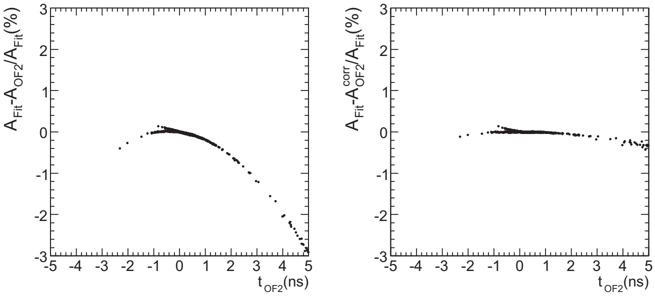

Figure 5.32: Relative difference of the amplitudes between A_{OF2} and A_{Fit} as a function of t_{OF2} for uncorrected amplitudes (left) and once the correction is applied (right) for simulated data.

The same correction can also be applied on simulated data for the few cases where $t{\neq}0$. Figure 5.32 shows the difference between A_{OF2} and A_{Fit} for single pions with E=50 GeV (as in Figure 5.26), with a great improvement in the values provided by OF once the correction is applied.

5.3.5 Quality Factor

Quality Factor Definition

Once the Optimal Filtering performance has been studied in terms of the reconstructed amplitude and time, only one paremeter of the algorithm is left to be studied: the quality factor (Q_{F}). Considering the aspects of the data to be reconstructed over the ATLAS operating life, the main properties of the definition of the OF quality factor should be:

- To distinguish the goodness or badness of the energy reconstruction over a wide range of amplitudes.
- To be equally valid for environments where the dominating source of noise is either electronic noise or minimum bias pileup.
- Provided that the minimum bias is present in any hadronic collider, it should be able to discriminate events strongly affected by minimum bias.
- To provide a feasible online implementation in the ROD DSP (using only sums and multiplications in an ideal case).

First of all, let us remember the definition of the χ^2 used for the Fit method:

$$\chi^2 = \sum_{i=1}^{n} \left(\frac{S_i - [Ag(t_i) - Atg'(t_i) + ped]}{\sigma_i} \right)^2 \tag{5.3}$$

The error in the estimation of the value of the samples (σ_i) is obtained from the sigma of the individual sample distribution in pedestal runs. Hence, it is implicitly assumed that the only uncertainty in the sample determination is the fluctuations in the electronics chain and not in other sources, like uncertainties in the pulse shape, etc. In addition, the values of σ_i are approximately the same for all the samples in one channel, no matter the value of S_i.

Figure 5.18 shows the values obtained for the Fit method χ^2 as a function of the amplitude for the CTB run 2102202, already used in Section 5.3.4. Note that the sign of the Fit χ^2 is changed when the channel is reconstructed using the 2-parameter fit, so that they are distinguished for the cases when the 3-parameter fit is used. The most impressing feature in Figure 5.33 is that the values for the χ^2 increase with the amplitude. This is due to a non-constant pulse shape at different values of the amplitude [27]. Such an increase is not observed in Monte Carlo data (see below) because a constant pulse shape is used in the simulation environment. Note that, a constant quality over the whole amplitude range is nevertheless desirable for the definition of the OF quality factor.

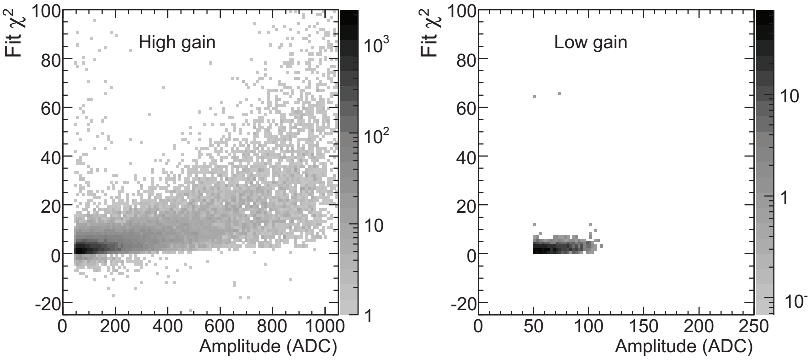

Figure 5.33: Values obtained for the χ^2 from the Fit method reconstruction as a function of the amplitude for high (left) and low gain channels (right).

In particular, to meet the requirement of the DSP, instead of considering the square of the residuals ($[S_i - (Ag_i + ped)]^2$), the absolute value of this difference will be used: $|S_i - (Ag_i + ped)|$. Furthermore, one can intuitively consider that a deviation between S_i and $Ag_i + ped$ or 1 ADC count is not equally meaningful when S_i=50 or S_i=900 ADC counts. Thus, weighting each term in the sum with something decreasing for high values of S_i would be convenient for the quality factor definition.

As a result of these considerations, several definitions have been proposed:

- $q_1 = \sum_{i=1}^{n} |S_i - (Ag_i + ped)|$: this is the simplest definition possible, just evaluating the difference between the expected value of each sample according to the reconstructed amplitude without further considerations in the value of S_i. Note that this definition is equivalent except for a constant to weight each term by a constant error for each sample. Figure 5.34-top shows the behaviour of q_1 as a function of the amplitude. Like in the Fit case, the quality factor also increases with the amplitude, even faster than in the Fit method.
- $q_2 = \frac{1}{A}\sum_{i=1}^{n} |S_i - (Ag_i + ped)|$: this definition was used for the OF reconstruction outside Athena in the 2003 CTB [29]. Figure 5.34-middle shows the behaviour of this definition. The increasing trend with the amplitude disappears completely, but at low amplitudes it is dominated by the $1/A$ term removing the significance in terms of reconstruction quality description from the q_2 numerator term. Furthermore all samples are equally weighted, not depending on their value.

- $q_3 = \sum_{i=1}^{n} \frac{(S_i - (Ag_i + ped))^2}{S_i}$: this definition uses the squares of the residuals (like in a proper χ^2), and estimates the error of each sample as $\sqrt{S_i}$. The behaviour is shown in Figure 5.34-bottom. Note that the increasing trend is strongly reduced in this case.

The main conclusion to be extracted is that by using a $\sim 1/S_i$ weight for each sample a meaningful quality factor definition with a small dependence on the amplitude can be obtained. Provided the DSP limited computing time, the usage of powers is rejected and the most appropriate definition for the quality factor is:

$$Q_{\mathrm{F}} = 50 \sum_{i=1}^{n} \frac{|S_i - (Ag_i + ped)|}{S_i}.$$

The behaviour of such a definition in terms of the amplitude is shown in Figure 5.35-top. The growing trend is strongly reduced although Q_{F} is not completely constant in the full amplitude range. Nevertheless, with this behaviour a discriminating threshold can be established so that bad reconstructed events can be considered to have $Q_{\mathrm{F}} \gtrsim$60-80. Note that the factor 50 is used to scale the values from Q_{F} to something comparable to $Q_{\mathrm{F}}^{\mathrm{approx}}$ which is defined below.

Furthermore, since the usage of divisions inside the DSP requires look-up tables, an approximate value to Q_{F} can be set as:

$$Q_{\mathrm{F}}^{\mathrm{approx}} = \sum_{i=1}^{n} w(S_i)|S_i - (Ag_i + ped)|, \quad \text{with} \quad \mathrm{w(S_i)} = \left\{ \begin{array}{ll} 1 & \text{for } S_i < 60 \\ 0.5 & \text{for } 60 < S_i < 150 \\ 0.25 & \text{for } S_i > 150 \end{array} \right\}.$$

This way, the main effect of the $1/S_i$ factor is reproduced in such a way that it could be easily implemented in the DSP core: smaller weights for high values of S_i. Figure 5.35 (bottom) shows the values of this $Q_{\mathrm{F}}^{\mathrm{approx}}$ as a function of the amplitude. The shape is similar to the case before, although with a bigger increase than Q_{F} but much smaller than in the q_1 case.

Summing up, from all these considerations the definition which will be used in the rest of the present thesis is Q_{F}, which we have seen that presents a good performance on real data, although the studies in the rest of the chapter are used used Monte Carlo data.

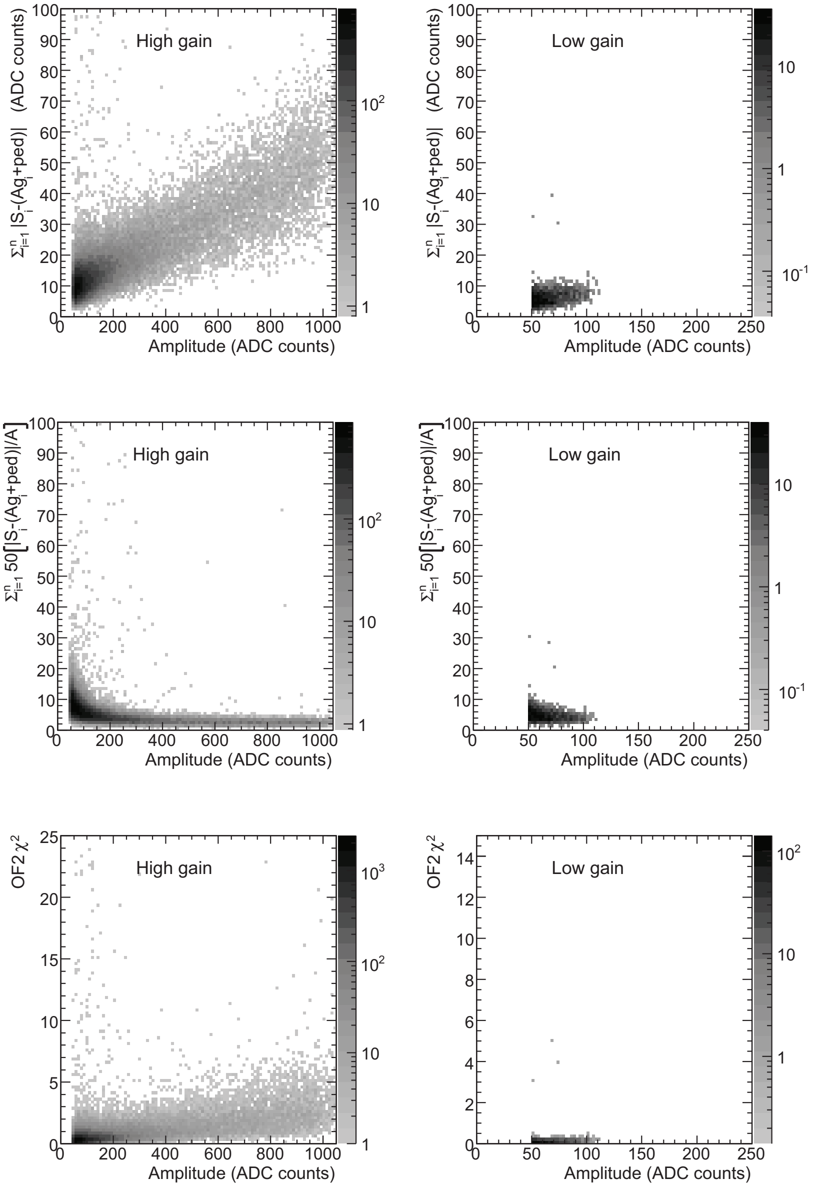

Figure 5.34: Results for the quality factor following the definitions q_1 (top), q_2 (center) and q_3 (bottom) as a function of the reconstructed amplitude for high (left) and low gain channels (right).

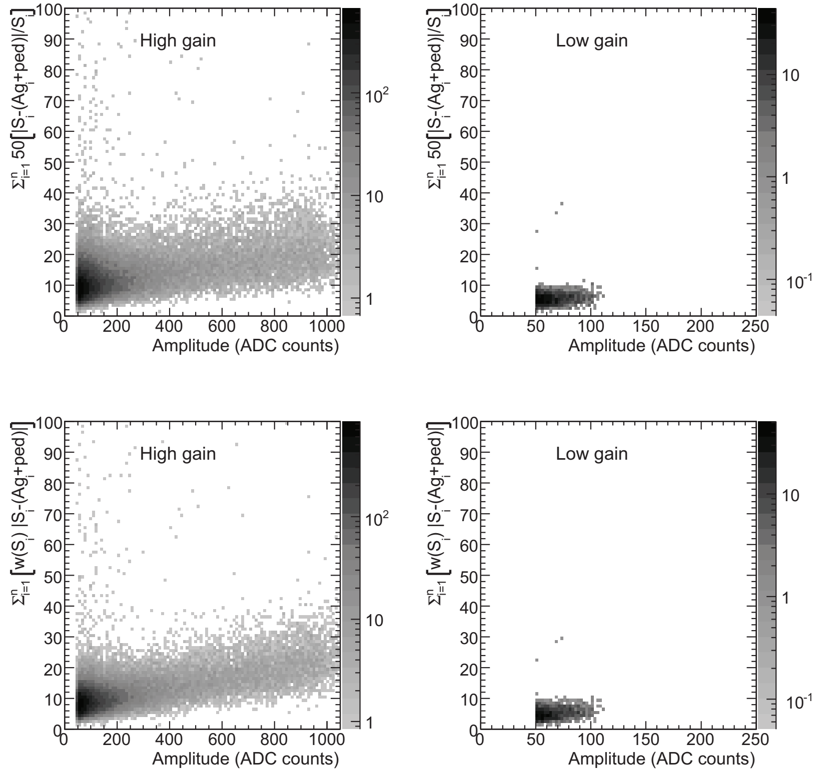

Figure 5.35: Results for the quality factor following the definitions Q_{F} (top) and $Q_{\mathrm{F}}^{\mathrm{approx}}$ (bottom) as a function of the reconstructed amplitude for high (left) and low gain channels (right).

Performance on Simulated Data with Electronic Noise

Once a final definition for Q_{F} is found, this Section is devoted to its performance with simulated data (since MB pileup will only be studied in this environment) in comparison with the χ^2 from the Fit and ManyAmps methods. In this Section, a sample of single pions with E=500 GeV is used, so that high amplitudes are also found in part of the channels.

Figure 5.36 shows the values obtained for the Q_{F} or χ^2 in all the 3 methods as a function of the reconstructed amplitude for the cases in which A<30 ADC counts. For the OF and ManyAmps methods and for pedestal-like cases their quality factors Q_{F} and χ^2 respectively, show similar values as in the case of signal events. On the contrary, the Fit method presents channels with small amplitudes which have $|\chi^2|{\sim}80$, more than 8 times the typical values for signal events. As a conclusion, it is clear that selection criteria based on the reconstruction quality must clearly distinguish between signal and pedestal-like events due to their different behaviour, especially for the Fit method.

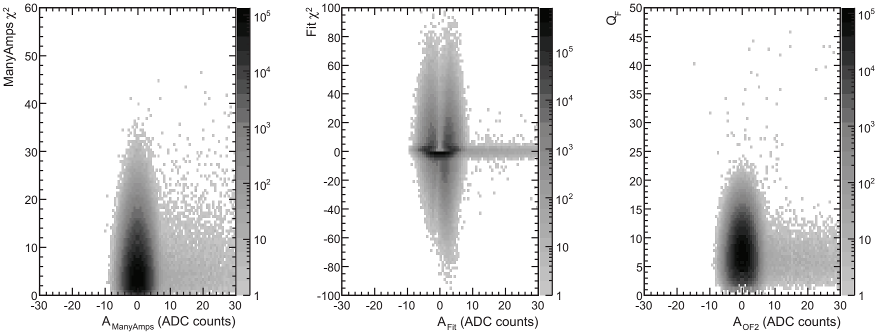

Figure 5.36: Quality of the reconstruction (expressed with Q_{F} or χ^2) as a function of the amplitude for ManyAmps (left), Fit (center) and OF (right) for channels with A<30 ADC counts.

For events which present considerable amplitudes (A>30 ADC counts) (Figure 5.37), the increasing values of the quality factor as a function of the amplitude are not observed with these simulated data, neither on Fit nor OF. In fact, most of the events clearly fall on the low $|\chi^2|$ or Q_{F} region, with very few cases with abnormal high values. Hence, if one wants to apply a cut on the quality of the reconstruction it can be set as 15 for Fit, 25 for OF and 40 for ManyAmps.

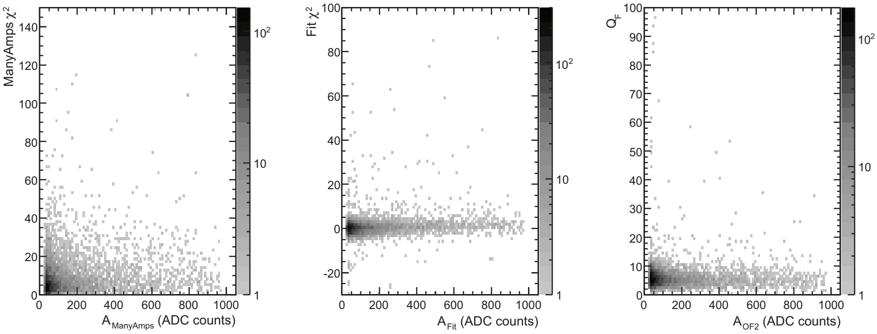

Figure 5.37: Quality of the reconstruction (expressed with Q_{F} or χ^2) as a function of the amplitude for ManyAmps (left), Fit (center) and OF (right) for channels with A>30 ADC counts.

Table 5.6 shows as an example a couple of events which present a bad reconstruction flagged with a high Q_{F} in OF or χ^2 in Fit. However, in both cases ManyAmps achieve a good χ^2 by using 2 or 3 amplitudes although no MB pileup is used in the sample. In the first case shown in the table, very similar (A, t and ped) values are obtained for Fit and OF, although the residuals are big in some of the samples. In the second case, the Fit method makes use of the 2-parameter fit, event though $t_{\mathrm{OF2}}{\approx}2$ ns.

Table 5.6: Two examples of channels showing a bad reconstruction as flagged by the quality factors.

<table>
<tr><td colspan="8">Raw samples</td></tr>
<tr><td colspan="8">51 56 317 682 454 189 81</td></tr>
<tr><td colspan="8">Reconstruction</td></tr>
<tr><td></td><td colspan="2">A (ADC counts)</td><td colspan="2">t (ns)</td><td colspan="2">ped (ADC counts)</td><td>Q_{F},χ^2</td></tr>
<tr><td>Fit</td><td colspan="2">633.70</td><td colspan="2">1.76</td><td colspan="2">63.19</td><td>128.43</td></tr>
<tr><td>OF2</td><td colspan="2">634.22</td><td colspan="2">1.68</td><td colspan="2">64.21</td><td>32.26</td></tr>
<tr><td>ManyAmps</td><td colspan="2">600.4
65.2</td><td colspan="2">0
25</td><td colspan="2">53.4</td><td>15.57</td></tr>
<tr><td colspan="8">Residuals</td></tr>
<tr><td>Fit</td><td>-10.72</td><td>-9.36</td><td>13.46</td><td>-13.00</td><td>8.83</td><td>15.67</td><td>-4.86</td></tr>
<tr><td>OF2</td><td>-11.76</td><td>-10.12</td><td>18.21</td><td>-10.67</td><td>5.97</td><td>13.58</td><td>-6.16</td></tr>
<tr><td>ManyAmps</td><td>-0.92</td><td>-1.63</td><td>2.02</td><td>-0.23</td><td>-2.39</td><td>4.87</td><td>-1.71</td></tr>
<tr><td colspan="8">Raw samples</td></tr>
<tr><td colspan="8">50 51 161 307 202 136 97</td></tr>
<tr><td colspan="8">Reconstruction</td></tr>
<tr><td></td><td colspan="2">A (ADC counts)</td><td colspan="2">t (ns)</td><td colspan="2">ped (ADC counts)</td><td>Q_{F},χ^2</td></tr>
<tr><td>Fit</td><td colspan="2">237.80</td><td colspan="2">0</td><td colspan="2">69.02</td><td>-235.41</td></tr>
<tr><td>OF2</td><td colspan="2">238.48</td><td colspan="2">1.90</td><td colspan="2">69.34</td><td>60.34</td></tr>
<tr><td>ManyAmps</td><td colspan="2">254.7
33.8
21.6</td><td colspan="2">0
50
75</td><td colspan="2">53.4</td><td>20.92</td></tr>
<tr><td colspan="8">Residuals</td></tr>
<tr><td>Fit</td><td>-18.35</td><td>-18.65</td><td>2.89</td><td>0.69</td><td>-11.37</td><td>25.31</td><td>19.48</td></tr>
<tr><td>OF2</td><td>-18.80</td><td>-19.06</td><td>3.52</td><td>1.55</td><td>-11.54</td><td>24.87</td><td>19.03</td></tr>
<tr><td>ManyAmps</td><td>1.05</td><td>-0.37</td><td>0.73</td><td>2.46</td><td>-5.76</td><td>3.26</td><td>-1.37</td></tr>
</table>

5.4 Performance Under Minimum Bias Pileup Environment

So far the study of the performance of the ATLAS detector under minimum bias pileup environment can only be done with Monte Carlo data. This Section is focused to the study of the impact of low luminosity MB pileup obtained inside the Athena framework with an average of 4.6 MB collisions per bunch crossing. Note that currently only 25-ns bunch spacing is available inside the simulation framework.

Figure 5.38 shows the multiplicity of channels affected by MB pileup for all TileCal layers. A sample of neutrinos digitized without electronic noise but only with minimum bias pileup is used. We consider the three scenarios discussed in Section 4.4.2: high luminosity ($\langle n_{coll} \rangle$=23.0), low luminosity ($\langle n_{coll} \rangle$=4.6) and very low luminosity ($\langle n_{coll} \rangle$=2.3). The amplitude has been estimated without any proper reconstruction method and simply as $\tilde{A}$=S_{max}-S_{min}, because no electronic noise is used in this simulation. Although the amount of channels which are affected at some extend by the presence of pileup is significant (1000 in high luminosity for Layer A), once seen in correlation with the resulting amplitude in the channel, very few channels have significant amplitudes (less than 20 with $\tilde{A}$>50 ADC counts and 4 with $\tilde{A}$>150 ADC for high luminosity in Layer A).

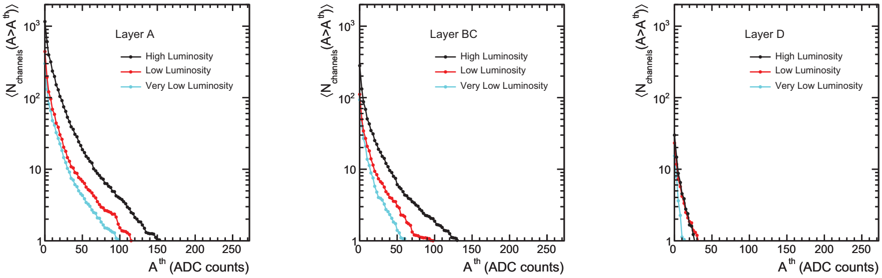

Figure 5.38: Multiplicity of channels affected by minimum bias pileup for each TileCal layer. The average number of channels with amplitudes above a threshold ($\tilde{A}$>A^{th}, with $\tilde{A}$=S_{max}-S_{min}) as a function of A^{th} is shown for the 3 main minimum bias pileup scenarios considered in Athena.

For the performance studies, a sample of single pions with an energy of 50 GeV is used, so that the potential effects in the performance will be more evident due to the relative low amplitudes from the main interaction. For this comparison, we will use these single pion sample digitized in a low luminosity environment including the electronic noise (which will be refereed to from now on as LowLumi data) and the same events digitized not only without minimum bias, but also without the electronic noise (refereed to as ZeroLumi data). According to the behaviour in ZeroLumi, we will have, on one side, channels in which A>0 already without pileup. The amplitudes from these channels, which come from the main interaction, can be distorted due to MB pileup, but will likely still be significant. On the other hand, in the "empty events", where A=0 exactly (due to the absence of electronic noise), any non-zero amplitude obtained at LowLumi will be caused only by the effects of the minimum bias pileup.

5.4.1 Results with Simulated Data - Empty Events

Figure 5.39 shows the distributions obtained for the amplitude in presence of minimum bias pileup (A_{LowLumi}) for the channels with A_{ZeroLumi}=0 for the 3 methods under consideration. Clear differences from the distributions without MB pileup (Figure 5.19): deviations from the Gaussian noise bell is found not only in the A>0 region (as expected from minimum bias events being reconstructed), but also in the A<0 region.

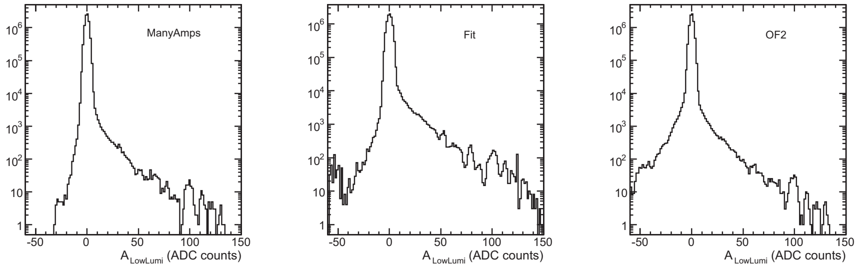

Figure 5.39: Distributions for the amplitude obtained with low luminosity minimum bias pileup using ManyAmps (left), Fit (center) and OF (right). Only empty events in the absence of pileup are considered.

Broader distributions are found for OF2 and Fit (which is the worst case) and ManyAmps has by far the better behaviour, as expected from the characteristics of the methods. Anyhow, sizeable deviations from the central Gaussian are found only at least 2 orders of magnitude below the peak. One can cross check that the effect of the low luminosity pileup is in average very small in TileCal (as expected due to a separation from the interaction point of more than 2 meters in radius).

Although the case of negative amplitudes in low luminosity is less intuitive than the case of positive amplitudes, it corresponds to cases where fits to a higher pedestal and a negative amplitude are more likely performed than fits to the same ZeroLumi pedestal with a positive amplitude. Consequently, the values of the amplitudes obtained can be better understood in comparison with the values of the pedestal.

Figure 5.40 shows in the left column the difference between the pedestal in ZeroLumi and LowLumi ($ped_{\mathrm{LowLumi}} - ped_{\mathrm{LowLumi}}$). As shown, most of the cases with A>0 correspond to cases where $ped_{\mathrm{LowLumi}} = ped_{\mathrm{ZeroLumi}}$, as expected from the presence of an actual amplitude in the event. This behaviour is practically exact in the ManyAmps method, but not for the rest.

For OF2 and Fit method the cases where A_{LowLumi}<0 are correlated with an increasing pedestal in LowLumi. For the Fit this dependence is clearly linear, with a value of A_{LowLumi}≈-50 ADC counts which corresponds to $(ped_{\mathrm{LowLumi}} - ped_{\mathrm{ZeroLumi}})$≈+35 ADC counts. On the contrary, the channels in OF2 follow $\sim$4 different trends, but still large negative amplitudes correspond to higher values of the pedestal.

The right column in Figure 5.40 shows the reconstruction χ^2 (or Q_{F}) as a function of A_{LowLumi}. Most of the channels with non-zero amplitudes have the χ^2 corresponding to signal events (see Figure 5.37). This behaviour is what would be expected from in-time pileup for all the methods.

For instance, in the case of the ManyAmps method, the cases with large χ^2 values are not especially correlated with high amplitudes, neither negatives or positives. For the Fit method, the χ^2 from the events with A<0 can hardly be distinguished due to the large χ^2 which are obtained for the pedestal-like events (up to χ^2~100).

However, for the OF2 method, the Q_{F} for the A>0 corresponds mostly to the case of signals as shown in Figure 5.37. However, the cases with high Q_{F} correspond precisely to the cases where the $|A|$<50 ADC counts. This way, most of the effect of the minimum bias pileup in these empty events can be removed by setting a cut on, for instance, Q_{F}<25.

Figure 5.41 shows the difference in pedestal as function of the amplitude once such a cut is applied. Most of the deviation in the amplitude are rejected and only the well reconstructed amplitudes, correlated with negligible variations in the pedestal remains.

Figure 5.41 also shows the comparison for the amplitude distributions obtained with ManyAmps, OF2 without restrictions and OF2 with the cut on Q_{F}<25. In this latter case, mostly only the tail towards positive values is kept, even improving the performance of the ManyAmps method.

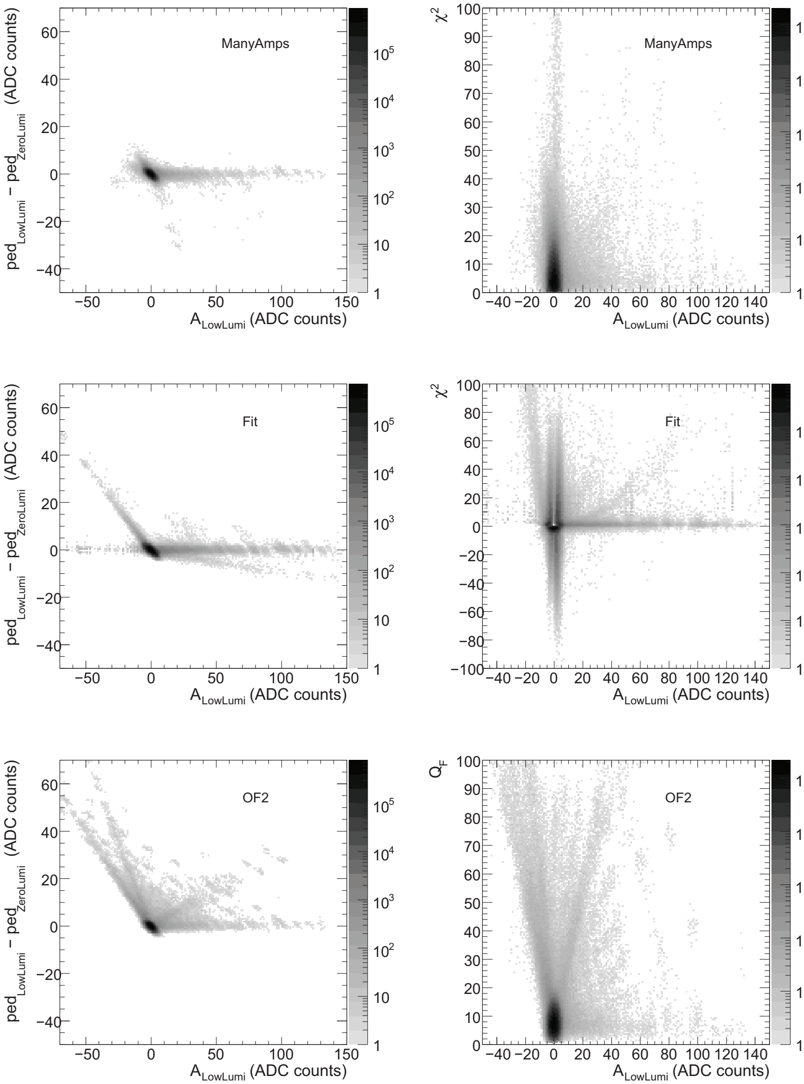

Figure 5.40: On the left, pedestal differences from ZeroLumi and LowLumi as a function of the LowLumi amplitude for several reconstruction methods. On the right, quality factor as a function of the amplitude for LowLumi data.

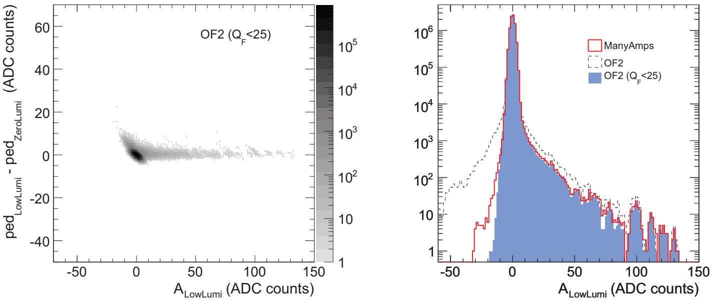

Figure 5.41: On the left, pedestal differences from ZeroLumi and LowLumi as a function of the LowLumi amplitude for OF once a cut on quality factor is applied. On the right, amplitude distribution for ManyAmps, OF and OF with quality factor cut.

5.5 Resolution and Response Studies

All the studies shown so far in this chapter for OF validation in comparison to the other methods available have been limited to the channel level, where disagreements and performance issues can be better identified and understood. On the other hand, the present section is meant to evaluate the impact of the reconstruction methods at a higher level but still considering only TileCal. Therefore, only the calorimeter cells are considered without higher reconstruction structures because the effects introduced by the usage of a certain method in TileCal may be masked by other effects related to the topological clustering or jet finding algorithm.

The main objective of this Section is to determine the impact of the TileCal reconstruction methods in the resolution and response of the calorimeter, not only with electronics noise but also under a minimum bias pileup environment. Dedicated studies on this matter were performed using real data during past test beam periods in TileCal either standalone (during 2002-2003) [29] or combined with other subdetectors (2004) [35], always with electronics noise only. The interest of this section is not to obtain the value for the resolution of the detector, but mostly to evaluate the effects in the final detector resolution of minimum bias pileup and the way it is handled by the reconstruction algorithm.

In the TileCal standalone approach with test beam, the original energy of the particles is known and they don't interact with any other system before reaching TileCal. However, in the CTB case, the beam goes through several subdetectors before TileCal: the Inner Detector and, of most importance, the LAr electromagnetic calorimeter. Since in this combined approach the particles in the beam can interact heavily in LAr, losing a significant part of their energy, a selection procedure is arranged so that only particles with known energy are kept.

5.5.1 Simulation Strategy

In order to achieve a relevant statistical significance, more events than provided by the official ATLAS Monte Carlo samples are needed. In consequence, custom Monte Carlo samples including hits from single pions at different energies (50, 100 and 200 GeV) were used in this study. In order to increase the fraction of pions in the simulation which actually go through TileCal, a filter was applied at the generator level which only accepts particles with $|\eta|<1.4$.

The hits from this production were digitized inside athena following two different chains:

1. With the default digitization in TileCal and LAr calorimeter with electronics noise and without minimum bias pileup.
2. With low luminosity ($\mathcal{L}=10^{33}$ cm^{-2}s^{-1}) minimum bias pileup in TileCal but with no pileup in LAr. Although this is a non-standard digitization procedure, it is needed to keep the same event selection in LAr.

The digits obtained this way where then reconstructed with the Fit, OF2 and ManyAmps methods for the case of TileCal and with the default reconstruction for LAr.

For each energy point 2×10^5 events were generated and digitized following these two chains. Separated reconstruction with each of the 3 TileCal reconstruction methods considered were executed on each set of digitized data obtaining as output the energy in each calorimeter cell.

5.5.2 Event Selection

In the CTB the total energy of the particles was computed using the calorimeter cells inside a cone around the known beam direction. Due to the fact that in the present simulation there is no beam parameters to use as a reference about where the single pion goes through in TileCal, the Monte Carlo truth from the simulation is used to define an acceptance cone where to compute the total energy deposited by the particle.

Using that the single pions are generated at the interaction point with fixed energy (E_π), the original particle can be identified in the event using that:

$$E_\pi = \frac{p_T^{truth}}{\sin\left[2\mathrm{arctan}\left(\mathrm{e}^{-|\eta_{\mathrm{truth}}|}\right)\right]} \tag{5.4}$$

Applying Eq. (5.5.2), the pion (η, ϕ) coordinates are known from the truth information in the simulation like in the CTB they were obtained from the beam detectors.

Since this study will only consider the resolution and response in the barrel part, only pions with $|\eta_{truth}|$<0.65 were used. According to the (η,ϕ) coordinates of the muon, a cone around the particle is considered, which in the following will be taken as $\Delta\eta\times\Delta\phi$=0.4×0.4[2].

Hence, the total energy released by the pions in the Tile and LAr calorimeters is computed as the sum of the energy in all the cells inside the cone which pass a noise removal cut set to $1\sigma_{noise}^{cell}$ for TileCal and $2\sigma_{noise}^{cell}$ for LAr:

$$E_{tot} = \sum_{cells} E_{cell} \qquad \text{if } |E_{cell}|>2(1)\sigma_{noise}^{cell} \text{ in LAr(Tile)}$$

The values to be used for σ_{noise}^{cell} in all the calorimeter cells were obtained with a sample of simulated neutrinos digitized with electronics noise in the standard ATLAS offline environment.

The typical energy deposition pattern in the two calorimeter systems is shown in Figure 5.42. Most of the particles start developing the hadronic shower within the LAr calorimeter, where it is not fully contained and therefore deposit part of their energy in both systems. However, in a fraction of the events very few energy is released inside LAr and all the deposition is fully comprised in TileCal. These events correspond to the pions which behave like a MIP during its path until they reach TileCal. In those cases, the energy of the incoming particle is known ($E_\pi - \langle E_{MIP}\rangle$) and the whole hadronic shower is developed in TileCal. These are precisely the kind of events which should be used to study the calorimeter resolution. Similar selection procedure were used during CTB period, when LAr modules where placed in the bean line before Tile.

In order to know the energy deposition from MIP particles in LAr, samples of muons going through LAr at the energies used in this study were simulated. The condition required for a pion to be considered as a MIP in LAr is that: $E_{layer} < \langle E_{layer}\rangle^{MIP} + 2\sigma_{layer}^{MIP}$, which is applied in each layer individually. Figure 5.43 shows the distribution from the energy

---

[2] Due to the fact that only 3 TileCal modules were used in the CTB, an asymmetric cone of $\Delta\eta\times\Delta\phi$=0.4×0.3 was used there.

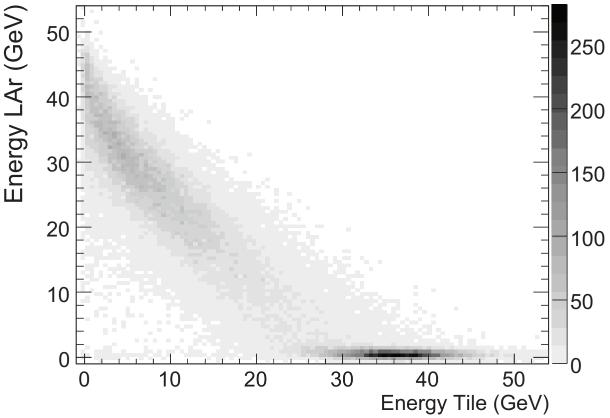

Figure 5.42: Energy deposition in the LAr calorimeter as a function of the energy deposited in the Tile calorimeter for simulated single pions (E_π=50 GeV). The total energy is obtained as the sum of all the cells in LAr (Tile) with $|E|>2(1)\sigma^{cell}_{noise}$ in a $\Delta\eta\times\Delta\phi$=0.4×0.4 cone around the Monte Carlo truth pion.

released by the muon in each of the LAr calorimeter layers. As expected, the distributions are not centered at zero but slightly shifted towards positive values, although the typical Landau-like behaviour can only be seen in the two outermost layers (which are the biggest in depth).

Mean and sigma are determined by a Gaussian fit to the distributions in the figure and their values are summarized in Table 5.7 for each layer and muon energy (E_μ). Small dependence is found as a function of the muon energy, with an average deposition of 506 MeV at E_μ=50 GeV and 590 MeV at E_μ=200 GeV.

Table 5.7: Mean and RMS from the total energy deposited in each layer by simulated single muons. The total energy is obtained as the sum of all the cells with $|E|>2\sigma^{cell}_{noise}$ in a $\Delta\eta\times\Delta\phi$=0.4×0.4 cone around the Monte Carlo truth muon.

	E_μ=50 GeV		E_μ=100 GeV		E_μ=200 GeV	
	$\langle E\rangle$ (GeV)	σ (GeV)	$\langle E\rangle$ (GeV)	σ (GeV)	$\langle E\rangle$ (GeV)	σ (GeV)
Presampler	0.0360	0.2410	0.0363	0.2407	0.0371	0.2478
Layer1	0.0804	0.1682	0.0822	0.1698	0.0897	0.1751
Layer2	0.3474	0.2976	0.3631	0.3161	0.4103	0.3194
Layer3	0.0426	0.1839	0.0441	0.1893	0.0527	0.1886

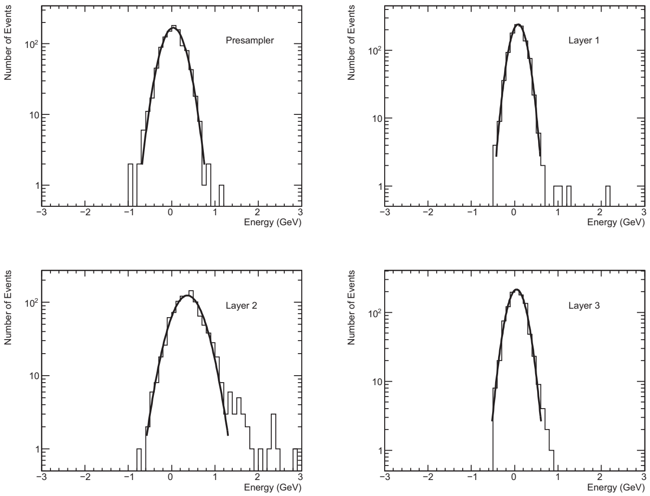

Figure 5.43: Energy deposited by simulated single muons (E_μ=100 GeV) in the LAr layers. The total energy is obtained as the sum of all the cells with $|E|>2\sigma^{cell}_{noise}$ in a $\Delta\eta\times\Delta\phi$=0.4×0.4 cone around the Monte Carlo truth muon.

5.5.3 Pion Calorimeter Energy Deposition

Figure 5.44 shows the energy deposited by pions at the energies considered in each of the LAr layers, with a clear contrast with respect to the muon case (Figure 5.43), where only $\sim$1 GeV was released in each layer. Up to 40 GeV can be deposited in the thickest layer of LAr at E_π=50 GeV, and at E_π=200 GeV long tails up to 180 GeV in can be found for this layer.

Note than in the thinnest LAr layers (Presampler and Layer 1) even at high pion energies a substantial amount of events are distributed close to the origin, so that a non-negligible fraction of the particles go through these parts of the detector behaving like a MIP.

Regarding TileCal, Figure 5.45 shows the energy deposition in each of the 3 calorimeter layers, with increasing depositions as the pion energy increases. Note that in the outermost layer (Layer D), few energy is deposited in comparison to the 2 innermost layers, a clear sign that most of the shower is already contained in the first 2 layers, at least at the energies considered.

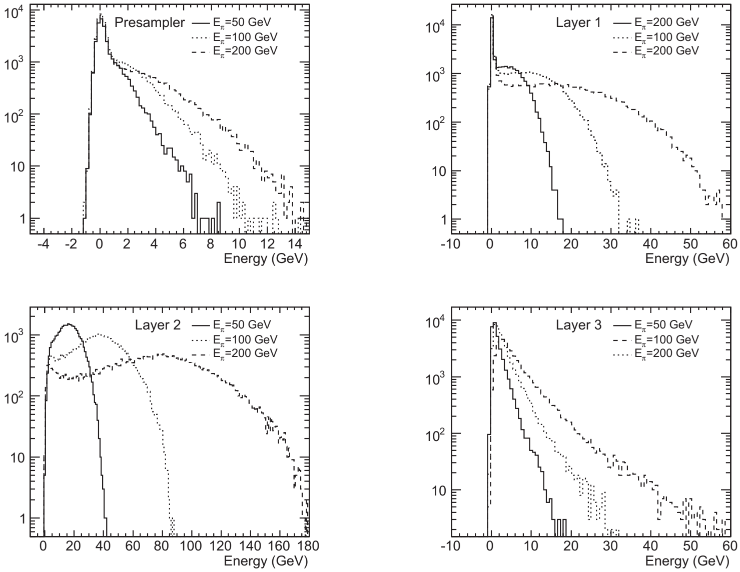

Figure 5.44: Energy deposition in the LAr calorimeter layers for simulated single pions at different energies. The total energy is obtained as the sum of all the cells with $|E|>2\sigma_{noise}^{cell}$ in a $\Delta\eta\times\Delta\phi$=0.4×0.4 cone around the Monte Carlo truth pion.

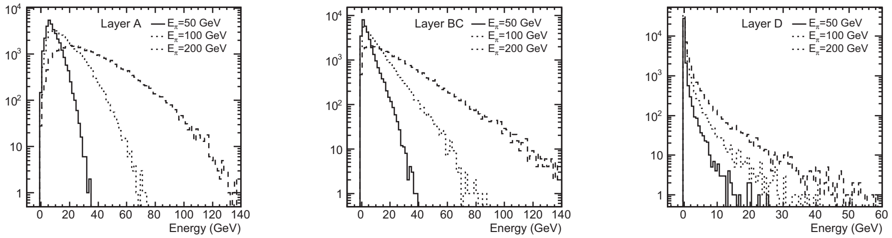

Figure 5.45: Energy deposition in the TileCal layers for simulated single pions at different energies. The total energy is obtained as the sum of all the cells with $|E|>\sigma_{noise}^{cell}$ in a $\Delta\eta\times\Delta\phi$=0.4×0.4 cone around the Monte Carlo truth pion.

5.5.4 Total Energy

Figure 5.46 shows the TileCal pion energy distributions, obtained following the procedure explained above for all the events and for the ones selected as MIP pions in LAr. In the raw distributions, a peak at $E\sim$35 GeV is found, although much more events are spread at lower energies. However, after the MIP selection in LAr is applied, a very clear peak is obtained, which follows a Gaussian distribution. Gaussian fits are performed iteratively in the $\langle E\rangle \pm 2\sigma$ range until convergence is reached in the sense that the fit parameters do not change in a 1‰.

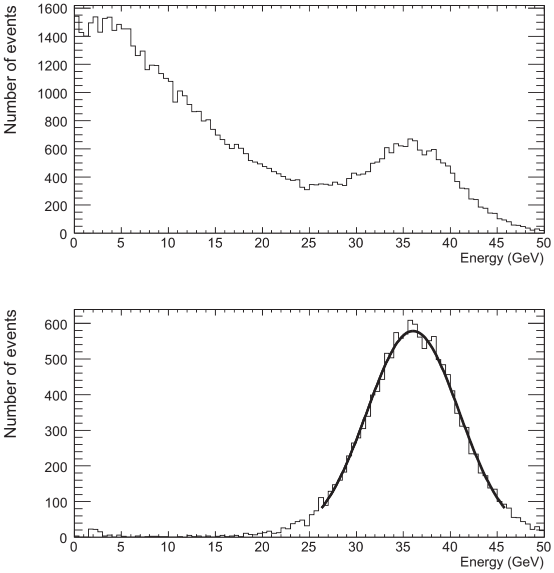

Figure 5.46: On the top, energy distribution in TileCal for all the simulated pions (with E_π=50 GeV). On the bottom, only the events where the LAr MIP selection cuts are fulfilled. Energy in TileCal is obtained in both cases as the sum of all the calorimeter cells with $|E|>\sigma^{cell}_{noise}$ in a $\Delta\eta\times\Delta\phi$=0.4×0.4 cone around the Monte Carlo truth pion.

Those distributions were obtained for all the $|\eta|<0.65$ range, but the resolution is known to depend on η [35], since at $\eta\sim0$ the particles go almost parallel to the scintillating tiles and the ratio between the active and passive materials is not the same as in the rest of the calorimeter. Figure 5.47 shows the same distribution but at different η intervals, with a significant width increase for the $|\eta|<0.15$ case.

5.5.5 Resolution and Response

Once the event selection in the Monte Carlo sample has been performed the resolution and response is computed using the mean ($\langle E\rangle$) and sigma (σ) from the distribution fits:

$$\text{Resolution} = \frac{\sigma}{\langle E\rangle}, \tag{5.5}$$

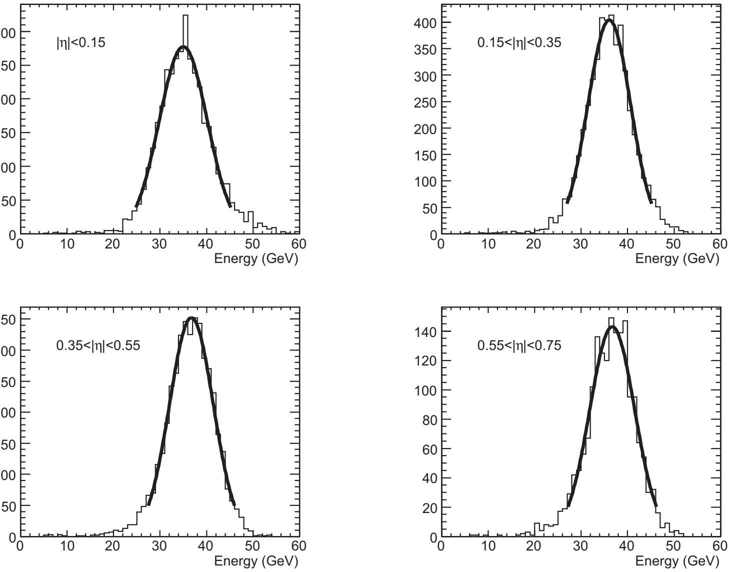

Figure 5.47: Distribution of the total energy in TileCal for MIP-like pions in LAr with E_π=50 GeV at different η intervals. The total energy is obtained in both cases as the sum of all the cells with $|E|>\sigma^{cell}_{noise}$ in a $\Delta\eta\times\Delta\phi$=0.4×0.4 cone around the Monte Carlo truth pion.

$$\text{Response} = \frac{\langle E \rangle}{E_\pi}, \tag{5.6}$$

where E_π is the nominal energy of the particle as generated in the simulation.

Table 5.8 shows the fit parameters for the energies and luminosities considered together with the resulting resolution and responses inclusively for the events where $|\eta|<0.65$, which are also shown in Figures 5.48 and 5.49. The values obtained for the resolution are larger for smaller pion energies, as expected from the general resolution expression in Eq. (3.8). The fact that the response increases with the particle energy was also observed in test beam [35].

Regarding the results from different methods which are obtained when pileup is not activated in the simulation, they are very similar, as expected from the comparisons at the channel level done in the section above. In all cases, the differences are small (~0.01%) and fully compatible with errors.

Small variations appear when low luminosity minimum bias pileup is added. The values found are very similar to the ones obtained when zero luminosity is used during digitization,

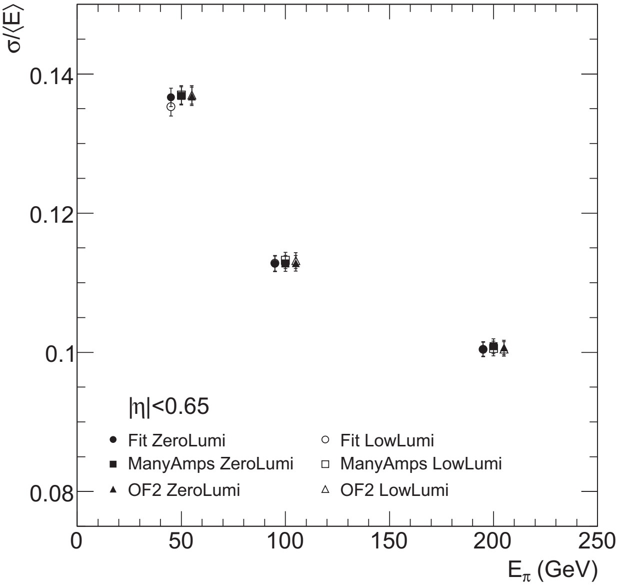

Figure 5.48: Resolution in TileCal as a function of the pion energy (E_π=50, 100, 200 GeV) for all the methods available and $\mathcal{L}$ = 0 (ZeroLumi), 2×10^{33} cm^{-2}s^{-1} (LowLumi). Only particles generated with $|\eta|$ <0.65 are considered.

almost compatible with errors in all cases. However, the biggest effect observed is the fact that larger responses are found for the Fit method when pileup is present, which is specially evident for the E_π=50 GeV, but it is also true for the other energies considered. The apparent improvement in resolution for those particular points is also a consequence of the increase of the $\langle E\rangle$ term. Hence, although the effects of pileup in TileCal are relatively small in the current simulation framework (see Figure 5.38), they become evident for the Fit method, the reconstruction algorithm which showed worst performance under minimum bias pileup noise (see Section 5.4.1).

The same procedure has been repeated at different intervals in η: $|\eta|$<0.15, 0.15<$|\eta|$<0.35, 0.35<$|\eta|$<0.55 and 0.55<$|\eta|$<0.75. Figures 5.50 and 5.51 show the values for the resolution and response obtained for each case (which are summarized in Tables 5.9 and 5.10). As expected form the Tile geometry, the resolution is worse at $\eta\sim0$, in about 1% in the current analysis, but the differences decrease at larger values of $|\eta|$, where larger response and smaller resolution are obtained.

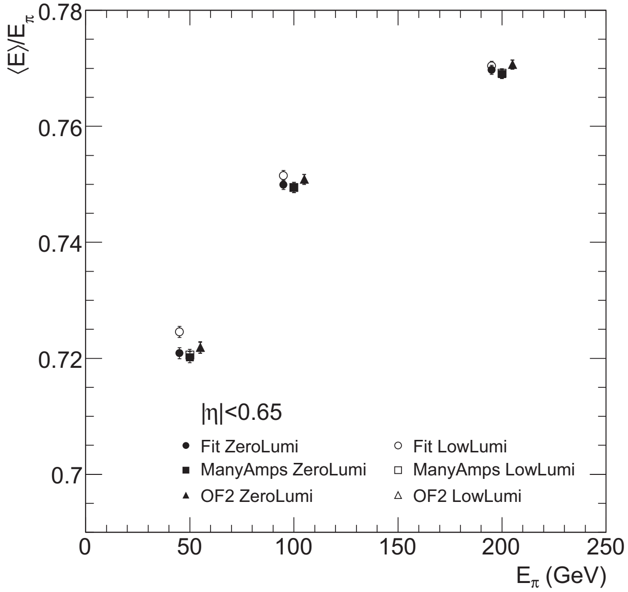

Figure 5.49: TileCal response as a function of the pion energy (E_π=50, 100, 200 GeV) for all the methods available and $\mathcal{L}$ = 0 (ZeroLumi), 2×10^{33} cm^{-2}s^{-1} (LowLumi). Only particles generated with $|\eta|$ <0.65 are considered.

However, even at intermediate η values, there is a clear disagreement between the results obtained here and the ones from test beam data [29, 35]. For instance for pions with E_π=100 GeV at η=0.35, in standalone test beam the resolution was found to be ∼6% and in combined test beam ∼8%, far from the ∼10% obtained here. This issue is treated extensively in Appendix B.

This disagreement can be qualitatively explained by the fact that some of the cuts employed for test beam analysis cannot actually be applied in this simulation. For instance, in the CTB additional information about the energy released in the cryostat between TileCal and LAr were obtained by the use of scintillators, allowing the removal of events where the shower started in the dead material instead than in TileCal. Furthermore, the topology of the simulated events doesn't correspond to a beam pointing the detector at fixed η but to single pions generated in different directions and, even worse, in the presence of the ATLAS magnetic field. Also one has to keep in mind that the procedure employed here, although being essentially the same as in past test beam periods, it is not based in clusters or jets, where more sophisticated algorithms are used.

Table 5.8: Reconstructed mean energy and sigma for all the data and methods used. Calorimeter resolution and responses are also shown. All particles generated with $|\eta|<0.65$ are considered.

E_π	Method	$\langle E\rangle$ (GeV)	σ (GeV)	$\sigma/\langle E\rangle$ (%)	$\langle E\rangle/E$ (%)
$|\eta|<0.65$, $\mathcal{L}=0$					
50	Fit	36.04 ± 0.05	4.92 ± 0.05	13.66 ± 0.13	72.09 ± 0.10
	ManyAmps	36.01 ± 0.05	4.93 ± 0.05	13.68 ± 0.13	72.02 ± 0.10
	OF2	36.09 ± 0.05	4.94 ± 0.05	13.68 ± 0.13	72.18 ± 0.10
100	Fit	74.99 ± 0.09	8.45 ± 0.08	11.27 ± 0.11	74.99 ± 0.09
	ManyAmps	74.95 ± 0.09	8.45 ± 0.08	11.28 ± 0.11	74.95 ± 0.09
	OF2	75.08 ± 0.09	8.47 ± 0.08	11.28 ± 0.11	75.08 ± 0.09
200	Fit	153.95 ± 0.16	15.47 ± 0.16	10.05 ± 0.10	76.97 ± 0.08
	ManyAmps	153.80 ± 0.16	15.52 ± 0.16	10.09 ± 0.11	76.90 ± 0.08
	OF2	154.12 ± 0.16	15.52 ± 0.16	10.07 ± 0.11	77.06 ± 0.08
$|\eta|<0.65$, $\mathcal{L}=2\times10^{33}$ cm^{-2}s^{-1}					
50	Fit	36.23 ± 0.05	4.90 ± 0.05	13.53 ± 0.13	72.45 ± 0.10
	ManyAmps	36.03 ± 0.05	4.94 ± 0.05	13.70 ± 0.13	72.06 ± 0.10
	OF2	36.09 ± 0.05	4.94 ± 0.05	13.70 ± 0.13	72.19 ± 0.10
100	Fit	75.15 ± 0.09	8.48 ± 0.08	11.28 ± 0.11	75.15 ± 0.09
	ManyAmps	74.95 ± 0.09	8.48 ± 0.09	11.32 ± 0.12	74.95 ± 0.09
	OF2	75.09 ± 0.09	8.50 ± 0.09	11.32 ± 0.11	75.09 ± 0.09
200	Fit	154.09 ± 0.16	15.47 ± 0.16	10.04 ± 0.10	77.04 ± 0.08
	ManyAmps	153.83 ± 0.16	15.47 ± 0.16	10.06 ± 0.11	76.91 ± 0.08
	OF2	154.13 ± 0.16	15.49 ± 0.16	10.05 ± 0.11	77.07 ± 0.08

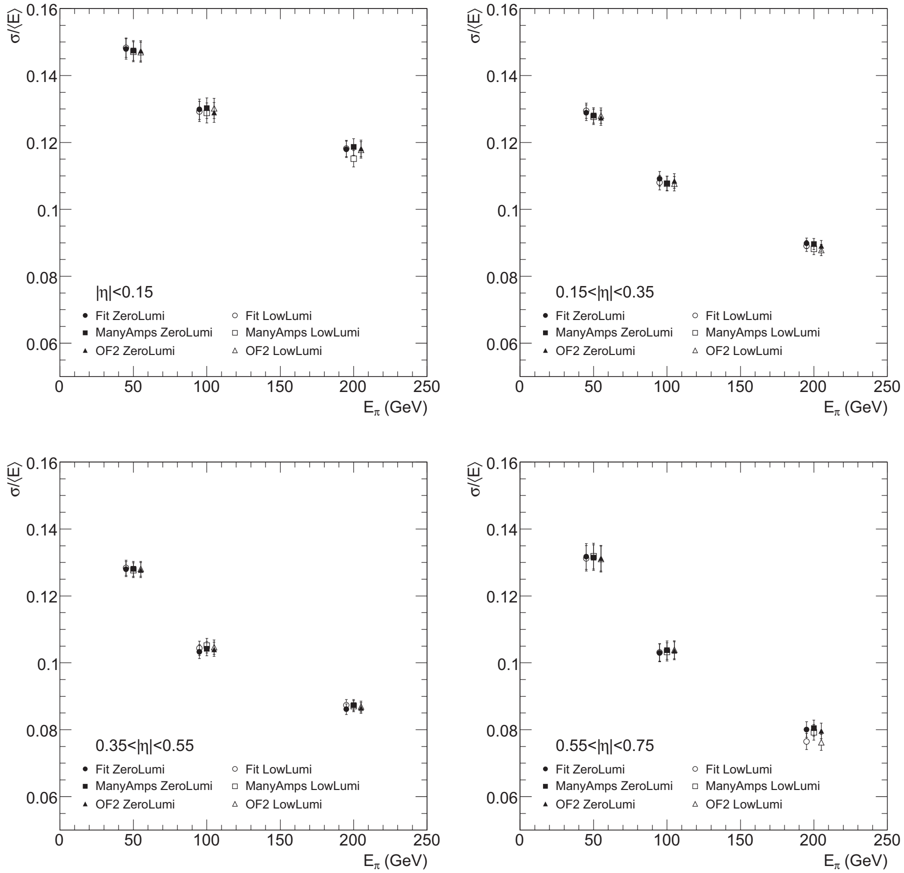

Figure 5.50: Resolution in TileCal as a function of the pion energy (E_π=50, 100, 200 GeV) for all the methods available and $\mathcal{L} = 0$ (ZeroLumi), 2×10^{33} cm^{-2}s^{-1} (LowLumi) at different intervals in η.

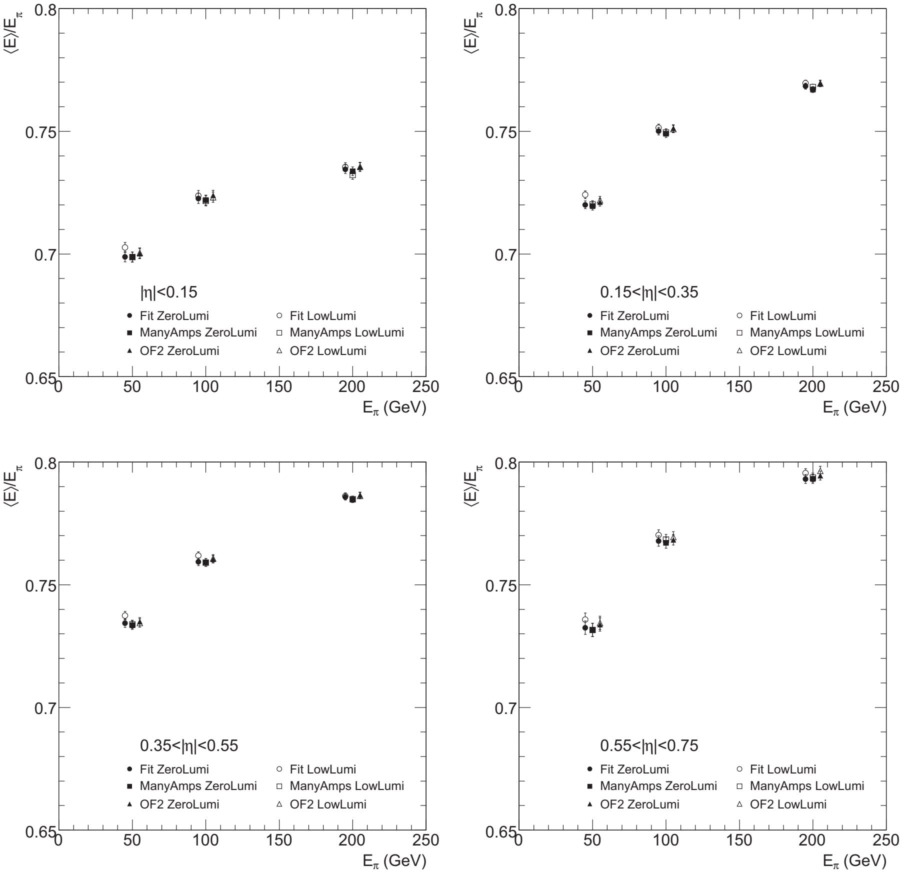

Figure 5.51: Response in TileCal as a function of the pion energy (E_{π}=50, 100, 200 GeV) for all the methods available and $\mathcal{L} = 0$ (ZeroLumi), $2{\times}10^{33}$ cm^{-2}s^{-1} (LowLumi) at different intervals in η.

Table 5.9: Reconstructed mean energy and sigma for all the data and methods used, considering only particles in the intervals $|\eta|<0.15$ and $0.15<|\eta|<0.35$. Calorimeter resolution and responses are also shown.

E_π	Method	$\langle E\rangle$ (GeV)	σ (GeV)	$\sigma/\langle E\rangle$ (%)	$\langle E\rangle/E$ (%)
$|\eta|<0.15$, $\mathcal{L}=0$					
50	Fit	34.94 ± 0.10	5.17 ± 0.10	14.79 ± 0.30	69.89 ± 0.21
	ManyAmps	34.94 ± 0.10	5.15 ± 0.10	14.74 ± 0.30	69.87 ± 0.20
	OF2	35.01 ± 0.10	5.16 ± 0.10	14.74 ± 0.30	70.01 ± 0.21
100	Fit	72.26 ± 0.21	9.39 ± 0.22	12.99 ± 0.30	72.26 ± 0.21
	ManyAmps	72.19 ± 0.21	9.40 ± 0.22	13.02 ± 0.31	72.19 ± 0.21
	OF2	72.39 ± 0.20	9.34 ± 0.21	12.90 ± 0.30	72.39 ± 0.20
200	Fit	146.91 ± 0.35	17.33 ± 0.36	11.79 ± 0.24	73.45 ± 0.18
	ManyAmps	146.75 ± 0.36	17.41 ± 0.36	11.86 ± 0.25	73.37 ± 0.18
	OF2	147.08 ± 0.35	17.39 ± 0.36	11.82 ± 0.25	73.54 ± 0.18
$|\eta|<0.15$, $\mathcal{L}=2\times10^{33}$ cm^{-2}s^{-1}					
50	Fit	35.13 ± 0.10	5.21 ± 0.10	14.83 ± 0.29	70.27 ± 0.20
	ManyAmps	34.94 ± 0.10	5.14 ± 0.10	14.71 ± 0.30	69.87 ± 0.20
	OF2	35.02 ± 0.10	5.15 ± 0.10	14.70 ± 0.30	70.04 ± 0.21
100	Fit	72.38 ± 0.21	9.36 ± 0.22	12.93 ± 0.30	72.38 ± 0.21
	ManyAmps	72.17 ± 0.21	9.30 ± 0.21	12.88 ± 0.30	72.17 ± 0.21
	OF2	72.31 ± 0.21	9.41 ± 0.22	13.02 ± 0.30	72.31 ± 0.21
200	Fit	147.09 ± 0.36	17.38 ± 0.36	11.82 ± 0.25	73.55 ± 0.18
	ManyAmps	146.45 ± 0.35	16.86 ± 0.35	11.51 ± 0.24	73.22 ± 0.18
	OF2	147.12 ± 0.35	17.32 ± 0.36	11.77 ± 0.25	73.56 ± 0.18
$0.15<|\eta|<0.35$, $\mathcal{L}=0$					
50	Fit	36.00 ± 0.08	4.64 ± 0.08	12.89 ± 0.23	72.00 ± 0.16
	ManyAmps	35.98 ± 0.08	4.61 ± 0.08	12.81 ± 0.23	71.95 ± 0.16
	OF2	36.06 ± 0.08	4.59 ± 0.08	12.74 ± 0.23	72.11 ± 0.16
100	Fit	75.01 ± 0.15	8.19 ± 0.16	10.91 ± 0.22	75.01 ± 0.15
	ManyAmps	74.90 ± 0.15	8.07 ± 0.16	10.78 ± 0.22	74.90 ± 0.15
	OF2	75.12 ± 0.15	8.15 ± 0.16	10.85 ± 0.22	75.12 ± 0.15
200	Fit	153.68 ± 0.24	13.81 ± 0.24	8.99 ± 0.16	76.84 ± 0.12
	ManyAmps	153.40 ± 0.25	13.75 ± 0.25	8.96 ± 0.17	76.70 ± 0.12
	OF2	153.93 ± 0.25	13.71 ± 0.25	8.91 ± 0.16	76.96 ± 0.12
$0.15<|\eta|<0.35$, $\mathcal{L}=2\times10^{33}$ cm^{-2}s^{-1}					
50	Fit	36.21 ± 0.08	4.69 ± 0.08	12.95 ± 0.22	72.42 ± 0.16
	ManyAmps	36.01 ± 0.08	4.60 ± 0.08	12.77 ± 0.23	72.01 ± 0.16
	OF2	36.09 ± 0.08	4.62 ± 0.08	12.80 ± 0.23	72.19 ± 0.16
100	Fit	75.14 ± 0.15	8.12 ± 0.16	10.80 ± 0.22	75.14 ± 0.15
	ManyAmps	74.95 ± 0.15	8.07 ± 0.16	10.77 ± 0.22	74.95 ± 0.15
	OF2	75.09 ± 0.15	8.08 ± 0.16	10.77 ± 0.21	75.09 ± 0.15
200	Fit	153.92 ± 0.25	13.71 ± 0.25	8.91 ± 0.17	76.96 ± 0.12
	ManyAmps	153.60 ± 0.25	13.54 ± 0.26	8.82 ± 0.17	76.80 ± 0.13
	OF2	153.89 ± 0.25	13.52 ± 0.26	8.79 ± 0.17	76.94 ± 0.12

Table 5.10: Reconstructed mean energy and sigma for all the data and methods used, considering only particles in the intervals $0.35<\lvert\eta\rvert<0.55$ and $0.55<\lvert\eta\rvert<0.75$. Calorimeter resolution and responses are also shown.

E_π	Method	$\langle E\rangle$ (GeV)	σ (GeV)	$\sigma/\langle E\rangle$ (%)	$\langle E\rangle/E$ (%)
$0.35<\lvert\eta\rvert<0.55$, $\mathcal{L}=0$					
50	Fit	36.72 ± 0.08	4.70 ± 0.08	12.80 ± 0.22	73.44 ± 0.17
	ManyAmps	36.68 ± 0.08	4.70 ± 0.08	12.81 ± 0.22	73.35 ± 0.17
	OF2	36.75 ± 0.08	4.69 ± 0.08	12.77 ± 0.22	73.50 ± 0.17
100	Fit	75.94 ± 0.15	7.85 ± 0.16	10.33 ± 0.21	75.94 ± 0.15
	ManyAmps	75.91 ± 0.16	7.91 ± 0.16	10.42 ± 0.21	75.91 ± 0.16
	OF2	76.04 ± 0.15	7.91 ± 0.16	10.40 ± 0.21	76.04 ± 0.15
200	Fit	157.15 ± 0.25	13.54 ± 0.25	8.61 ± 0.16	78.58 ± 0.12
	ManyAmps	156.96 ± 0.26	13.71 ± 0.26	8.74 ± 0.16	78.48 ± 0.13
	OF2	157.31 ± 0.25	13.61 ± 0.25	8.65 ± 0.16	78.65 ± 0.13
$0.35<\lvert\eta\rvert<0.55$, $\mathcal{L}=2\times10^{33}$ cm^{-2}s^{-1}					
50	Fit	36.87 ± 0.09	4.73 ± 0.08	12.84 ± 0.23	73.74 ± 0.17
	ManyAmps	36.69 ± 0.08	4.69 ± 0.08	12.77 ± 0.22	73.39 ± 0.17
	OF2	36.72 ± 0.08	4.70 ± 0.08	12.81 ± 0.22	73.44 ± 0.17
100	Fit	76.19 ± 0.16	7.95 ± 0.16	10.44 ± 0.21	76.19 ± 0.16
	ManyAmps	75.91 ± 0.16	7.98 ± 0.16	10.51 ± 0.22	75.91 ± 0.16
	OF2	76.07 ± 0.16	7.96 ± 0.16	10.47 ± 0.22	76.07 ± 0.16
200	Fit	157.23 ± 0.26	13.74 ± 0.26	8.74 ± 0.16	78.62 ± 0.13
	ManyAmps	156.97 ± 0.26	13.66 ± 0.26	8.70 ± 0.16	78.48 ± 0.13
	OF2	157.25 ± 0.25	13.67 ± 0.25	8.69 ± 0.16	78.63 ± 0.13
$0.55<\lvert\eta\rvert<0.75$, $\mathcal{L}=0$					
50	Fit	36.62 ± 0.14	4.83 ± 0.14	13.18 ± 0.39	73.25 ± 0.27
	ManyAmps	36.58 ± 0.14	4.81 ± 0.14	13.15 ± 0.38	73.16 ± 0.27
	OF2	36.69 ± 0.14	4.82 ± 0.14	13.13 ± 0.38	73.38 ± 0.27
100	Fit	76.78 ± 0.21	7.91 ± 0.20	10.30 ± 0.27	76.78 ± 0.21
	ManyAmps	76.71 ± 0.22	7.96 ± 0.21	10.38 ± 0.28	76.71 ± 0.22
	OF2	76.83 ± 0.21	7.96 ± 0.21	10.36 ± 0.27	76.83 ± 0.21
200	Fit	158.62 ± 0.37	12.70 ± 0.36	8.01 ± 0.23	79.31 ± 0.18
	ManyAmps	158.63 ± 0.37	12.77 ± 0.37	8.05 ± 0.24	79.32 ± 0.19
	OF2	158.90 ± 0.36	12.66 ± 0.36	7.96 ± 0.23	79.45 ± 0.18
$0.55<\lvert\eta\rvert<0.75$, $\mathcal{L}=2\times10^{33}$ cm^{-2}s^{-1}					
50	Fit	36.79 ± 0.14	4.83 ± 0.14	13.12 ± 0.38	73.58 ± 0.27
	ManyAmps	36.58 ± 0.14	4.82 ± 0.14	13.19 ± 0.39	73.16 ± 0.27
	OF2	36.72 ± 0.14	4.81 ± 0.14	13.10 ± 0.39	73.45 ± 0.27
100	Fit	77.03 ± 0.21	7.94 ± 0.20	10.31 ± 0.26	77.03 ± 0.21
	ManyAmps	76.84 ± 0.22	7.94 ± 0.21	10.33 ± 0.27	76.84 ± 0.22
	OF2	76.95 ± 0.22	7.99 ± 0.21	10.39 ± 0.27	76.95 ± 0.22
200	Fit	159.10 ± 0.37	12.17 ± 0.38	7.65 ± 0.24	79.55 ± 0.19
	ManyAmps	158.73 ± 0.37	12.57 ± 0.37	7.92 ± 0.23	79.37 ± 0.18
	OF2	159.28 ± 0.37	12.14 ± 0.38	7.62 ± 0.24	79.64 ± 0.18

5.5.6 Conclusions

Despite the fact that the resolution values found are not consistent with real test beam data, conclusions can be drawn about the different performance of the reconstruction methods in TileCal in a minimum bias noise environment as currently simulated in ATLAS in terms of the calorimeter resolution and response. About the comparison of the different methods, they all lead to the same results in the absence of minimum bias pileup, but with low luminosity minimum bias pileup the Fit method shows an increase in the detector response at the level of 0.5% for pions with 50 GeV, which decreases for larger energies. Similar results are found for OF and ManyAmps in all cases.

Of course, one has to bear in mind that Monte Carlo data has been used all over this Chapter, and the simulation model has to be cross-checked with real data and, for instance, the effects of QCD minimum bias pileup can scale significantly in real data as compared with the current simulation code. Furthermore, there is still room for improvements in the OF reconstruction for environments with heavier minimum bias pileup, such as the cut on reconstruction quality proposed in Section 5.4.1.

Chapter 6

Supersymmetry in ATLAS

“Enlairar-se és opcional, però és perentori aterrar.”
— Q. Portet, *Hostessa*, 2007

6.1 Introduction

As mentioned in Section 2.2.7, Supersymmetry at the TeV scale is an attractive extension of the Standard Model which gives a natural explanation for Higgs masses at the 100-MeV scale, consistency with the electroweak precision data from LEP, SLC and TeVatron with coupling unification at the GUT scale and a natural candidate for cold dark matter.

Minimal supergravity (mSUGRA) is one of the better studied SUSY breaking scenarios [36]. In this kind of models, supersymmetry is broken spontaneously in a hidden sector that connects only through gravitational strength interactions with the MSSM or visible sector. In the visible sector these interactions induce the appearance of the soft SUSY breaking terms. These are determined by only five parameters, which together with the 18 Standard Model parameters (excluding the Higgs mass) determine the model:

- m_0: the common scalar mass at the GUT scale.
- $m_{1/2}$: the common gaugino mass at the GUT scale.
- A_0: common soft trilinear SUSY breaking parameter at the GUT scale.
- $\tan\beta$: the ratio of the Higgs expectation values at the electroweak scale.
- $\mathrm{sgn}(\mu_0)$: sign of the Higgsino mass term.

This drastic reduction from MSSM-124 parameters to only 5 facilitates the scanning of interesting regions of the parameter space. This is usually done by fixing two parameters, although it is also possible to vary the four continuous parameters freely using Monte Carlo techniques. In mSUGRA models, the LSP is typically the lightest neutralino ($\widetilde{\chi}_1^0$) which is dominated by its bino component.

In order to perform studies of supersymmetric phenomenology at colliders, it has been a valuable exercise to compile a set of benchmark supersymmetric parameters, from which supersymmetric spectra and couplings can be derived (see below).

The masses of SUSY particles other than the gluino and the LSP have been constrained at LEP to be larger than $\sim$100 GeV, essentially independent of any specific model. Within the MSSM with unification of gaugino and sfermion masses, an indirect lower limit of 47 GeV has been set by the LEP experiments for the mass of a neutralino LSP. The mass reach at the TeVatron is much larger than at LEP, but the results need to be interpreted in the context of specific models. Based on an integrated luminosity of 1 fb^{-1}, the current squark and gluino mass lower limits are 375 and 289 GeV, respectively, within the mSUGRA framework at low $\tan\beta$. It is expected that 6-7 fb^{-1} will be accumulated at the TeVatron by 2009, and together with the LHC physics collisions starting in 2009 a whole new window for SUSY searches has been opened.

6.2 Gluino and Squark Searches at ATLAS in Multijets and Missing Transverse Energy Final States

Chapter 7 shows cleaning methods for the reduction of the fake $\not\!\!E_{\mathrm{T}}$ coming from QCD background, which have been developed within the contex of the SUSY inclusive analysis with at least four jets and $\not\!\!E_{\mathrm{T}}$ in the final state and a lepton veto (described in Chapter 8). All these studies have been carried on with simulated data and this section details SUSY production and signatures, the data simulation at selected points in the parameter space and the objects used during the analysis in the following Chapters.

6.2.1 Production and Decay Signatures

Supersymmetric particles can be produced at proton-(anti)proton colliders according to the following partonic reactions, where they are created in pairs due to the R-parity conservation:

- $\widetilde{q}\overline{\widetilde{q}}$ production: $q_i + \overline{q}_j \to \widetilde{q}_k + \overline{\widetilde{q}}_l$ and $g + g \to \widetilde{q}_i + \overline{\widetilde{q}}_j$.
- $\widetilde{q}\widetilde{q}$ production: $q_i + q_j \to \widetilde{q}_i + \widetilde{q}_j$.
- $\widetilde{g}\widetilde{g}$ production: $q_i + \overline{q}_j \to \widetilde{g}\widetilde{g}$ and $g + g \to \widetilde{g}\widetilde{g}$.
- $\widetilde{q}\widetilde{g}$ production: $q_i + g \to \widetilde{q}_i\widetilde{g}$.

Figure 6.1 [37] shows the fraction of final states produced by each mechanism at the TeVatron and LHC energies, respectively, for two cases of $m_{\widetilde{q}}/m_{\widetilde{g}}$. For a light squark, the dominant mechanism at the TeVatron is $\widetilde{q}\overline{\widetilde{q}}$ while this represents only a small contribution at the LHC, with $\widetilde{q}\widetilde{q}$ as $\widetilde{q}\widetilde{g}$ as dominant sources. For a heavy squark, $\widetilde{g}\widetilde{g}$ is the most relevant for both TeVatron and LHC, with also a relevant fraction of $\widetilde{q}\widetilde{g}$ in this latter case.

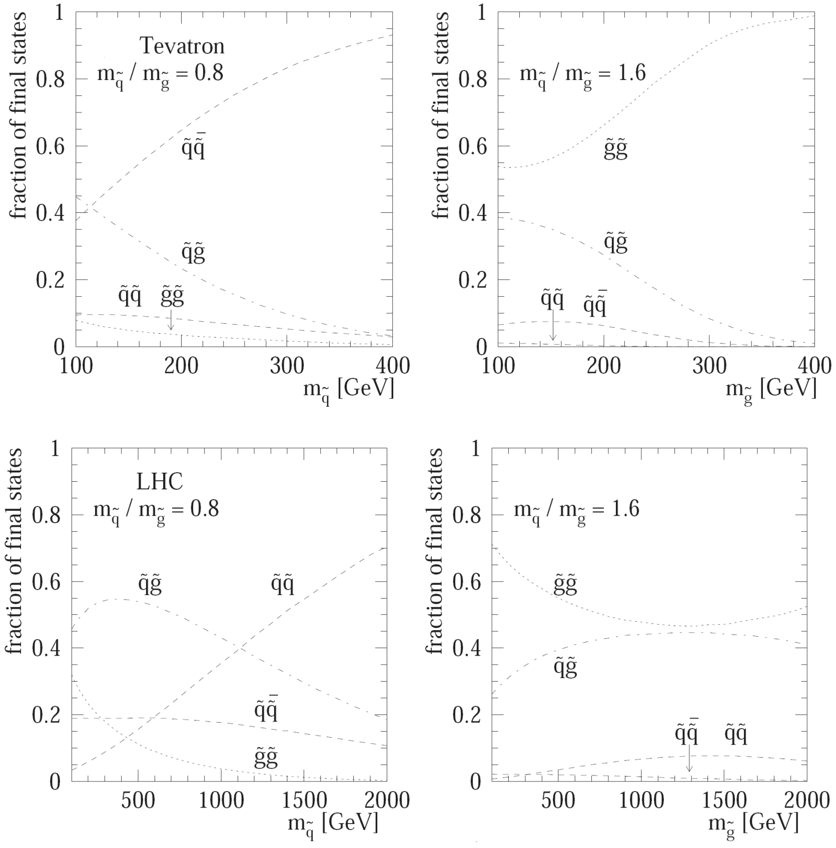

Figure 6.1: Fraction of final states coming from each $\widetilde{q}$-$\widetilde{g}$ production mechanism at the TeVatron (top) and LHC energies (bottom) for the case when $m_{\widetilde{q}}$=0.8 $m_{\widetilde{g}}$ (left) and $m_{\widetilde{q}}$=1.6 $m_{\widetilde{g}}$ (right) [37].

Since all the supersymmetric particles are unstable except the LSP, they will decay into SM particles right after being produced. This cascade will result in a final state with consisting of several jets (coming from the squark and/or gluinos) plus $\not{E}_{\mathrm{T}}$ coming from the LSPs which scape undetected. Two cases can be distinguished: if squarks are significantly ligther than gluinos ($m_{\widetilde{q}} < m_{\widetilde{g}}$), they will tend to decay as $\widetilde{q} \to q\widetilde{\chi}_1^0$ and $\widetilde{g} \to q\overline{q}\widetilde{\chi}_1^0$. On the contrary, for a heavier squark ($m_{\widetilde{q}} > m_{\widetilde{g}}$) it will decay as $\widetilde{q} \to q\widetilde{g} \to qq\overline{q}\widetilde{\chi}_1^0$.

Table 6.1 shows a summary on the different decay modes which can be present as function of the production mode, with the common features of a high jet multiplicity and the presence of $\not{E}_{\mathrm{T}}$.

Table 6.1: Posible SUSY signatures according to the values of $m_{\widetilde{q}}$ and $m_{\widetilde{g}}$.

$m_{\widetilde{q}} < m_{\widetilde{g}}$	$m_{\widetilde{q}} < m_{\widetilde{g}}$
• $\widetilde{q}\overline{\widetilde{q}}$ or $\widetilde{q}\widetilde{q}$: 2 acoplanar jets and $\not{E}_{\mathrm{T}}$ • $\widetilde{q}\widetilde{g}$: 3 jets and $\not{E}_{\mathrm{T}}$ • $\widetilde{g}\widetilde{g}$: 4 jets and $\not{E}_{\mathrm{T}}$	• $\widetilde{q}\widetilde{g}$: 5 jets and $\not{E}_{\mathrm{T}}$ • $\widetilde{g}\widetilde{g}$: 4 jets and $\not{E}_{\mathrm{T}}$

6.2.2 Monte Carlo Benchmark Points at ATLAS

Although TeV-scale SUSY gives qualitatively the right amount of cold dark matter in the Universe, detailed calculation shows that enhanced $\widetilde{\chi}_1^0$ annihilation is required to obtain a relic density compatible with the cosmological results provided by experiments like WMAP [38]. Several regions are found in the mSUGRA parameter space which meet this requirements, as shown qualitatively in Figure 6.2. Dedicated Monte Carlo data production has been carried out in ATLAS for selected benchmark points inside the allowed regions in the parameter space, which are the following:

- Coannhilation: in this region a light $\widetilde{\tau}_1$ is in equilibrium with $\widetilde{\chi}_1^0$ so that it annihilates via $\widetilde{\tau}_1\widetilde{\chi}_1^0 \to \gamma\tau$ reducing the relic density. A couple of ATLAS SUSY benchmark points are sitting in this region with the following parameters:
  - SU1: m_0=70 GeV, $m_{1/2}$=350 GeV, A_0=0, $\tan\beta$=10, $\mathrm{sgn}(\mu_0)=+$.
  - SU8.1: m_0=210 GeV, $m_{1/2}$=360 GeV, A_0=0, $\tan\beta$=40, $\mathrm{sgn}(\mu_0)=+$.
- Focus Point: it is characterized by small μ_0^2, leading to an efficient $\widetilde{\chi}_1^0$ annihilation into gauge bosons. ATLAS Monte Carlo data have been produced for the following point:
  - SU2: m_0=3550 GeV, $m_{1/2}$=300 GeV, A_0=0, $\tan\beta$=10, $\mathrm{sgn}(\mu_0)=+$.

- Bulk: in this case the $\widetilde{\chi}_1^0$ is the $\widetilde{b}$ and a light $\widetilde{l}_R$ enhances its annihilation. The ATLAS SU3 benchmark point is placed in this region of the parameter space:
    - SU3: m_0=100 GeV, $m_{1/2}$=300 GeV, A_0=-300, $\tan\beta$=6, $\text{sgn}(\mu_0)=+$.
- Funnel: here the H/A poles enhance the $\widetilde{\chi}_1^0$ annihilation for large values of $\tan\beta$. Another ATLAS SUSY benchmark point is placed in this region with the following parameters:
    - SU6: m_0=320 GeV, $m_{1/2}$=375 GeV, A_0=0, $\tan\beta$=50, $\text{sgn}(\mu_0)=+$.

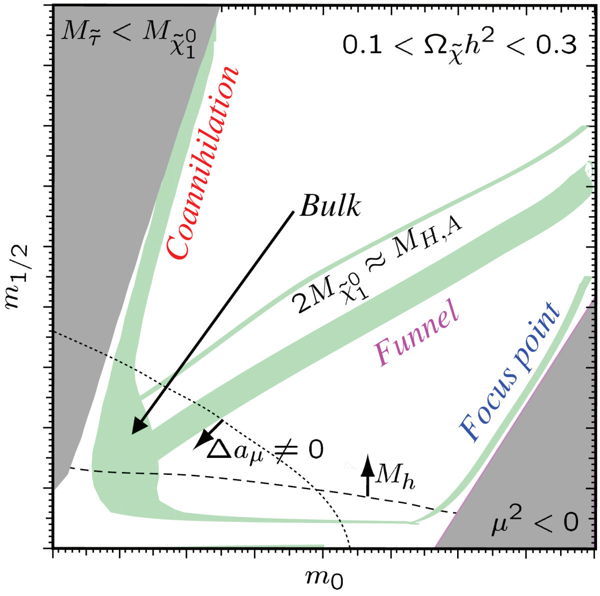

Figure 6.2: Qualitative picture of the different SUSY regions in the m_0-$m_{1/2}$ plane.

One additional benchmark point was used in ATLAS (SU4), with parameters near to the expected TeVatron Run-II sensitivity limit with the following parameters:

$$m_0\text{=200 GeV}, m_{1/2}\text{=160 GeV}, A_0\text{=-400}, \tan\beta\text{=10}, \text{sgn}(\mu_0)=+.$$

Table 6.2 shows the mass values for all the particles in the model for the 6 benchmark points discussed.

Table 6.2: Masses (in GeV) for the particles in the ATLAS mSUGRA benchmark points.

Particle	SU1	SU2	SU3	SU4	SU6	SU8.1
$\tilde{d}_L$	764.90	3564.13	636.27	419.84	870.79	801.16
$\tilde{u}_L$	760.42	3563.24	631.51	412.25	866.84	797.09
$\tilde{b}_1$	697.90	2924.80	575.23	358.49	716.83	690.31
$\tilde{t}_1$	572.96	2131.11	424.12	206.04	641.61	603.65
$\tilde{d}_R$	733.53	3576.13	610.69	406.22	840.21	771.91
$\tilde{u}_R$	735.41	3574.18	611.81	404.92	842.16	773.69
$\tilde{b}_2$	722.87	3500.55	610.73	399.18	779.42	743.09
$\tilde{t}_2$	749.46	2935.36	650.50	445.00	797.99	766.21
$\tilde{\mathrm{e}}_L$	255.13	3547.50	230.45	231.94	411.89	325.44
$\tilde{\nu}_e$	238.31	3546.32	216.96	217.92	401.89	315.29
$\tilde{\tau}_1$	146.50	3519.62	149.99	200.50	181.31	151.90
$\tilde{\nu}_\tau$	237.56	3532.27	216.29	215.53	358.26	296.98
$\tilde{\mathrm{e}}_R$	154.06	3547.46	155.45	212.88	351.10	253.35
$\tilde{\tau}_2$	256.98	3533.69	232.17	236.04	392.58	331.34
$\tilde{\mathrm{g}}$	832.33	856.59	717.46	413.37	894.70	856.45
$\tilde{\chi}_1^0$	136.98	103.35	117.91	59.84	149.57	142.45
$\tilde{\chi}_2^0$	263.64	160.37	218.60	113.48	287.97	273.95
$\tilde{\chi}_3^0$	466.44	179.76	463.99	308.94	477.23	463.55
$\tilde{\chi}_4^0$	483.30	294.90	480.59	327.76	492.23	479.01
$\tilde{\chi}_1^+$	262.06	149.42	218.33	113.22	288.29	274.30
$\tilde{\chi}_2^+$	483.62	286.81	480.16	326.59	492.42	479.22
h^0	115.81	119.01	114.83	113.98	116.85	116.69
H^0	515.99	3529.74	512.86	370.47	388.92	430.49
A^0	512.39	3506.62	511.53	368.18	386.47	427.74
H^+	521.90	3530.61	518.15	378.90	401.15	440.23
t	175.00	175.00	175.00	175.00	175.00	175.00

6.3 Data Samples

Tables 6.3, 6.4 and 6.5 show the Monte Carlo data samples used for mSUGRA signals, non-QCD and QCD background, respectively (including the software used for the DPD[1] creation). All of them are produced using the ATLAS full simulation inside Athena release 12. The Pythia [21] event generator was used for the QCD multijet samples. HERWIG [39] was used for the diboson samples as well as for the signal samples, which also make use of the JIMMY generator for multiparton interactions inside HERWIG [40]. The $\mathrm{t\bar{t}}$ samples were generated using Mc@NLO [41], also inside HERWIG and finally the samples for W and Z boson were obtained with the Alpgen generator [42].

---

[1] The Derived Physics Data (DPD) is the entity in the ATLAS computing data model representing the light data suitable for final analysis in root format, such as the SusyView or combined ntuples.

Table 6.3: Monte Carlo samples used to describe the SUSY signal at selected mSUGRA benchmark points. The effective cross section and available number of events are shown.

Process	Sample ID	Generator	Filter	DPD maker	σ_{eff} (pb)	N$_{events}$
SU1	005401	HERWIG/Jimmy	-	SusyView	10.86	198350
SU2	005402	HERWIG/Jimmy	-	SusyView	7.18	49700
SU3	005403	HERWIG/Jimmy	-	SusyView	27.68	492150
SU4	005400	HERWIG/Jimmy	-	SusyView	402.19	188350
SU6	005404	HERWIG/Jimmy	-	SusyView	6.07	29950
SU8.1	005406	HERWIG/Jimmy	-	SusyView	8.70	39900

Several filters were applied in these samples in order to optimize the computing resources for SUSY analysis. Filters on the number of jets in the Monte Carlo truth ($N_{\mathrm{jet}}^{\mathrm{truth}}$) are applied for Z, W and QCD samples, requiring at least p_{T}>80 GeV for the leading jet and p_{T}>40 GeV in the second (QCD) or fourth jet (Z and W). The samples on Z and W are also filtered on the $\not{E}_{\mathrm{T}}$ at the Monte Carlo truth level ($\not{E}_{\mathrm{T}}^{\mathrm{truth}}$), with $\not{E}_{\mathrm{T}}^{\mathrm{truth}}$ >80 GeV, and official SUSY QCD samples have a filter of the estimated $\not{E}_{\mathrm{T}}$ in the event, $\not{E}_{\mathrm{T}}^{\mathrm{est}}$ >100 GeV. The $\not{E}_{\mathrm{T}}$ estimation is done by this filter using the jet truth η and p_{T} [43]. These QCD samples will be referred to as JX_FMET from now on.

To provide larger statistics and avoid biases introduced by the $\not{E}_{\mathrm{T}}^{\mathrm{est}}$ filter, additional QCD multijet samples have been used in this note: CBNT files obtained from unfiltered official production ESD[2] files and private productions with a filter applied at the generator level requiring at least 4 jets with p_{T}(jet$_1$)>80GeV and p_{T}(jet$_4$)>40 GeV without any further requirement on the event $\not{E}_{\mathrm{T}}$. These samples will be referred to as JX_CBNT and JX_4J, respectively.

6.3.1 Object Definition

The analysis documented in the following Chapters use several high level reconstruction objects following the common conventions agreed in ATLAS for particle identification. This Section review these objects (jets, electrons, muons, etc.) together with the selection criteria and algorithms used to identify them.

---

[2] The ESD (Event Summary Data) files contain the detailed output of the detector reconstruction and are produced from the raw data. They contain sufficient information to allow particle identification, track re-fitting, jet calibration etc. thus allowing for the rapid tuning of reconstruction algorithms and calibrations.

Table 6.4: Monte Carlo samples used to describe the non-QCD background. The filters applied in the generation as well as the effective cross section and available number of events are shown.

Process	Sample ID	Generator	Filter	DPD maker	σ_{eff} (pb)	N$_{events}$
TOP						
t$\bar{\text{t}}$	005200	MC@NLO	-	SusyView	450	570600
	005204	MC@NLO	-	SusyView	383	94600
DIBOSON						
WW	005985	HERWIG	-	SusyView	39.05	50000
ZZ	005986	HERWIG	-	SusyView	2.83	49800
WZ	005987	HERWIG	-	SusyView	14.06	49900
W BOSON						
W$e\nu$	005223	Alpgen	$N_{\text{jet}}^{\text{truth}} \geq 4$ + $\not\!\!E_{\text{T}}^{\text{truth}}$	SusyView	0.77	1000
	005224	Alpgen	$N_{\text{jet}}^{\text{truth}} \geq 4$ + $\not\!\!E_{\text{T}}^{\text{truth}}$	SusyView	3.90	15750
	005225	Alpgen	$N_{\text{jet}}^{\text{truth}} \geq 4$ + $\not\!\!E_{\text{T}}^{\text{truth}}$	SusyView	2.32	9900
	005226	Alpgen	$N_{\text{jet}}^{\text{truth}} \geq 4$ + $\not\!\!E_{\text{T}}^{\text{truth}}$	SusyView	0.69	2950
W$\mu\nu$	008203	Alpgen	$N_{\text{jet}}^{\text{truth}} \geq 4$ + $\not\!\!E_{\text{T}}^{\text{truth}}$	SusyView	0.79	750
	008204	Alpgen	$N_{\text{jet}}^{\text{truth}} \geq 4$ + $\not\!\!E_{\text{T}}^{\text{truth}}$	SusyView	2.13	5250
	008205	Alpgen	$N_{\text{jet}}^{\text{truth}} \geq 4$ + $\not\!\!E_{\text{T}}^{\text{truth}}$	SusyView	0.70	4000
W$\tau\nu$	008208	Alpgen	$N_{\text{jet}}^{\text{truth}} \geq 4$ + $\not\!\!E_{\text{T}}^{\text{truth}}$	SusyView	0.61	3000
	008209	Alpgen	$N_{\text{jet}}^{\text{truth}} \geq 4$ + $\not\!\!E_{\text{T}}^{\text{truth}}$	SusyView	3.27	2000
	008210	Alpgen	$N_{\text{jet}}^{\text{truth}} \geq 4$ + $\not\!\!E_{\text{T}}^{\text{truth}}$	SusyView	3.08	14000
	008211	Alpgen	$N_{\text{jet}}^{\text{truth}} \geq 4$ + $\not\!\!E_{\text{T}}^{\text{truth}}$	SusyView	0.94	4700
Z BOSON						
Z$\nu\nu$	005124	Alpgen	$N_{\text{jet}}^{\text{truth}} \geq 4$ + $\not\!\!E_{\text{T}}^{\text{truth}}$	SusyView	1.07	13000
	005125	Alpgen	$N_{\text{jet}}^{\text{truth}} \geq 4$ + $\not\!\!E_{\text{T}}^{\text{truth}}$	SusyView	3.06	44000
	005126	Alpgen	$N_{\text{jet}}^{\text{truth}} \geq 4$ + $\not\!\!E_{\text{T}}^{\text{truth}}$	SusyView	0.95	11500
Zee	005161	Alpgen	$N_{\text{jet}}^{\text{truth}} \geq 4$	SusyView	0.41	1500
	005162	Alpgen	$N_{\text{jet}}^{\text{truth}} \geq 4$	SusyView	4.15	4643
	005163	Alpgen	$N_{\text{jet}}^{\text{truth}} \geq 4$	SusyView	2.76	20600
	005164	Alpgen	$N_{\text{jet}}^{\text{truth}} \geq 4$	SusyView	0.70	6000
	005165	Alpgen	$N_{\text{jet}}^{\text{truth}} \geq 4$	SusyView	0.18	2000
Z$\mu\mu$	008109	Alpgen	$N_{\text{jet}}^{\text{truth}} \geq 4$	SusyView	0.24	2000
	008110	Alpgen	$N_{\text{jet}}^{\text{truth}} \geq 4$	SusyView	0.53	3450
	008111	Alpgen	$N_{\text{jet}}^{\text{truth}} \geq 4$	SusyView	0.17	1750
Z$\tau\tau$	008114	Alpgen	$N_{\text{jet}}^{\text{truth}} \geq 4$ + $\not\!\!E_{\text{T}}^{\text{truth}}$	SusyView	0.24	3750
	008115	Alpgen	$N_{\text{jet}}^{\text{truth}} \geq 4$ + $\not\!\!E_{\text{T}}^{\text{truth}}$	SusyView	0.53	7000
	008116	Alpgen	$N_{\text{jet}}^{\text{truth}} \geq 4$ + $\not\!\!E_{\text{T}}^{\text{truth}}$	SusyView	0.17	4000
	008117	Alpgen	$N_{\text{jet}}^{\text{truth}} \geq 4$ + $\not\!\!E_{\text{T}}^{\text{truth}}$	SusyView	0.17	1000

Table 6.5: Monte Carlo samples used to describe the QCD background. The filters applied in the generations as well as the effective cross section and available number of events are shown.

Process	Sample ID	Generator	Filter	DPD maker	$\sigma_{\rm eff}$ (pb)	N$_{events}$
J4_FMET	008090	Pythia	$N_{\rm jet}^{\rm truth}>2 + \not\!\!E_{\rm T}^{\rm est}$	SusyView	916.14	24500
J5_FMET	008091	Pythia	$N_{\rm jet}^{\rm truth}>2 + \not\!\!E_{\rm T}^{\rm est}$	SusyView	655	51650
J6_FMET	008092	Pythia	$N_{\rm jet}^{\rm truth}>2 + \not\!\!E_{\rm T}^{\rm est}$	SusyView	67.42	12750
J7_FMET	008093	Pythia	$N_{\rm jet}^{\rm truth}>2 + \not\!\!E_{\rm T}^{\rm est}$	SusyView	5.3	3500
J8_FMET	008094	Pythia	$N_{\rm jet}^{\rm truth}>2 + \not\!\!E_{\rm T}^{\rm est}$	SusyView	2.21×10^{-2}	4250
J4_CBNT	Private	Pythia	-	CBNT	3.16×10^{5}	16000
J5_CBNT	Private	Pythia	-	CBNT	1.25×10^{4}	120900
J6_CBNT	Private	Pythia	-	CBNT	344	97750
J7_CBNT	Private	Pythia	-	CBNT	5.3	213200
J4_4J	Private	Pythia	$N_{\rm jet}^{\rm truth}\geq4$	CBNT	28028	973275
J5_4J	Private	Pythia	$N_{\rm jet}^{\rm truth}\geq4$	CBNT	3500	197360
J6_4J	Private	Pythia	$N_{\rm jet}^{\rm truth}\geq4$	CBNT	126	176019

Jets

Because of the relatively large multiplicity of jets in SUSY events, a narrow cone is preferable in the reconstruction of jets. The algorithm used to reconstruct jets here is called Cone4Tower [44] with a cone size of 0.4. Jets matching within a cone of $\Delta R<0.2$ an isolated electron passing the reconstruction cuts described below are discarded. This procedure (*overlap removal*) prevents the same object to be reconstructed both as an electron and as a jet.

Electrons

The eGamma algorithm [45] was used for the electron identification and reconstruction, with the “medium” identification cuts recommended by the electron combined performance studies [45] for the Athena release 12.

The transverse isolation energy in a cone of $\Delta R<0.2$ around the electron, computed using the calorimetric information, is used to select isolated electrons. This variable is required to be smaller than 10 GeV. In the available Monte Carlo data sets for Athena release 12 this variable is incorrectly calculated, but only a small bias is introduced by this problem, except for the crack region $1.37<|\eta|<1.52$.

An electron is rejected if it is found within a distance $0.2 < \Delta R < 0.4$ of a jet, as in this case it is most likely associated to the decay of a particle within the jet. As mentioned above, in case $\Delta R(\mathrm{jet}, \mathrm{e}) < 0.2$ the jet is discarded instead.

In the region $1.37 < |\eta| < 1.52$, besides the problem with the isolation variable described above, the electron identification and measurement are degraded because of the large amount of material in front of the calorimeter and the crack between the barrel and extended barrel of the calorimeters.

Since both high quality for the electrons used in the analyses and an efficient electron veto are required, events with an electron candidate with $p_{\mathrm{T}} > 10$ GeV, passing the medium eGamma cuts and with a pseudorapidity in the crack region are rejected.

Muons

The muons were reconstructed using the Staco algorithm [46], based on the statistical combination of a standlone Muon Spectrometer track with an Inner Detector track, as recommended by the muon performance group.

A loose selection is applied on the track segment match χ^2, which is required to be smaller than 100. If more than one Inner Detector track matched one track from the Muon Spectrometer, only the one with smallest ΔR is kept. Calorimeter isolation is obtained by requiring the energy in $\Delta R < 0.2$ cone to be less than 10 GeV and muons found within a distance $\Delta R <$ 0.4 of a jet are discarded since they are likely associated to a decay of a jet particle.

Missing Transverse Energy

The measurement of transverse energy imbalance in the detector plays a crucial role in the searches for Supersymmetry with R-parity conservation, and the requirement of a large value of $\not{E}_{\mathrm{T}}$ is a common feature of all the analysis presented in this note.

For the studies presented here, the output of the most refined algorithm for the reconstruction of the transverse missing energy, known as MET_RefFinal, was used [47]. More details on $\not{E}_{\mathrm{T}}$ computation can be found in Section 7.2.

Other interesting variables

Effective Mass The effective mass is a measure of the total activity in the event, a variable which has been proved to discriminate between Standard Model background and SUSY signals in a wide parameter range. Furthermore, it is strongly correlated with the mass of the two s-particles produced in a SUSY event. The SUSY mass scale at the LHC ($M_{\rm susy}$) can be defined as the cross-section weighted mean of the masses of the two (in R-parity conserving models) SUSY particles initially produced in 14 TeV p-p collisions.

When attempting to measure $M_{\rm susy}$, the presence of a high mass Lightest Supersymmetric Particle can bias the results by reducing the number and $p_{\rm T}$ of observed jets. In practice it is therefore preferable to consider measurements of an appropriately defined effective mass scale $M_{\rm eff}$ which takes the LSP mass into account and that can be related to the predictions of a given SUSY model [48]. An accurate definition for $M_{\rm eff}$ is provided by the scalar sum of the $p_{\rm T}$ of the four leading jets, the leptons and the event $\not{E}_{\rm T}$:

$$M_{\rm eff} = \sum_{i=1}^{4} p_{\rm T}({\rm jet_i}) + \sum_{\rm j=1}^{\rm N_{leptons}} {\rm p_T}({\rm lepton_j}) + \not{E}_{\rm T}. \tag{6.1}$$

Transverse Sphericity Transverse sphericity is the measure of the isotropy of the event in the two-dimensional transverse plane [49]. It can vary from $0 \leq S_{\rm T} \leq 1$, so that events which are completely back-to-back have $S_{\rm T}=0$ and a fully isotropic event has $S_{\rm T}=1$. It is defined as:

$$S_{\rm T} = \frac{2\lambda_2}{\lambda_1 + \lambda_2} \tag{6.2}$$

where λ_1 and λ_2 are the eigenvalues of the sphericity tensor $S_{ij} = \sum_k p_{ki} p_{kj}$. Cuts on transverse sphericity are meant to remove the QCD background since are qualitatively less “spherical” than the typical SUSY event, with a large jet multiplicity coming from the SUSY decay chain, not just from the fragmentation of 2 jets. Here it will be computed using all jets with $|\eta|<2.5$ and $p_{\rm T}>20$ GeV.

Chapter 7

QCD Fake Missing Tranverse Energy Reduction

“Il semble que la perfection soit atteinte non quand il n’y a plus rien à ajouter, mais quand il n’y a plus rien à retrancher.”
— A. de Saint-Exupéry, *Terre des hommes*, 1939

7.1 Introduction

As mentioned above, $\not{E}_{\mathrm{T}}$ measurement is the most important observable for SUSY searches with R-parity conservation, as well as for many other scenarios beyond the Standard Model. Backgrounds from QCD jets are particularly relevant at high $\not{E}_{\mathrm{T}}$ due to several reasons: non-Gaussian tails in the ATLAS jet response due to inactive material, escaping muons and jet punch-through contribute in decreasing the $\not{E}_{\mathrm{T}}$ resolution, producing so-called fake $\not{E}_{\mathrm{T}}$ ($\not{E}_{\mathrm{T}}^{\mathrm{Fake}}$) in opposition to the true $\not{E}_{\mathrm{T}}$ ($\not{E}_{\mathrm{T}}^{\mathrm{True}}$), which is due to non-interacting particles like neutrinos or the Lightest Supersymmetric Particle in SUSY models.

The $\not{E}_{\mathrm{T}}^{\mathrm{Fake}}$ estimation from mismeasured events in ATLAS will be accurate enough only when the simulation is validated with real data. Furthermore, $\not{E}_{\mathrm{T}}^{\mathrm{Fake}}$ is expected to be larger with respect to the current Monte Carlo due to the non-ideal simulation of the detector effects which are sources of $\not{E}_{\mathrm{T}}^{\mathrm{Fake}}$ and need to be studied in data using QCD jets. On the other hand, theoretical uncertainties in QCD event generation, including uncertainties in matrix elements, renormalisation, factorization and matching scales, cross sections and PDFs, will all contribute in decreasing further the precision of Monte Carlo estimates.

Finally, large Monte Carlo data productions for studies about high $\not{E}_{\mathrm{T}}$ in QCD are unfeasible due to the large cross-section of the multijet processes together with their low probability of high $\not{E}_{\mathrm{T}}$. In consequence, usually Monte Carlo filtered samples are used for this kind of studies (see Section 6.3).

This Chapter studies methods to reduce the QCD jet background using the calorimeter and the tracking systems for identifying events showing problems in jet reconstruction and potentially leading to large $\not{E}_{\mathrm{T}}^{\mathrm{Fake}}$.

7.2 Measurement of the Missing Transverse Energy in ATLAS

The reconstruction of the $\not{E}_{\mathrm{T}}$ in ATLAS is described in [47]. In order to get a good $\not{E}_{\mathrm{T}}$ measurement the following points should be considered:

- Suppression of electronic noise and pileup must be done accurately, in particular, at high-luminosity.
- After the noise suppression, all calorimeters cells should be used, even low energy cells.
- The calibration of all calorimeters is very important for a good $\not{E}_{\mathrm{T}}$ resolution.
- The full detector coverage up to $|\eta|<5$ must be used.

Missing E_{T} is primarily reconstructed from the energy deposits in the calorimeter and the reconstructed muon tracks. Apart from the hard scattering process of interest, many other sources, such as the underlying event, multiple interactions, cosmics, beam halo, beam gas, pileup and electronic noise lead to energy deposits and/or fake muon tracks. Classifying these energy deposits into various types (e.g. electrons, taus or jets) and calibrating them accordingly is the essential key for optimal $\not{E}_{\mathrm{T}}$ measurement. In addition, the loss of energy in regions with inactive material and channels make the $\not{E}_{\mathrm{T}}$ measurement a real challenge.

The $\not{E}_{\mathrm{T}}$ reconstruction algorithm starts from the energy deposits in calorimeter cells or clusters of cells ("raw $\not{E}_{\mathrm{T}}$"). The raw $\not{E}_{\mathrm{T}}$ is then cleaned up from a number of sources of fake $\not{E}_{\mathrm{T}}$: hot cells, overlay of beam halo, cosmics, detector malfunctions, etc. Overall, the reconstruction of $\not{E}_{\mathrm{T}}$ is a challenging task and it requires a good understanding of the calorimeter response and the topology of different signatures. The $\not{E}_{\mathrm{T}}$ resolution roughly scales with $\sqrt{\sum E_{\mathrm{T}}}$ for $\sum E_{\mathrm{T}} \lesssim 1.5$ TeV, where $\sum E_{\mathrm{T}}$ is the scalar sum of the energies of the particles in the final state.

The energy losses in dead material in front of calorimeters (e.g. cryostats) as well as the transition between their different parts (cracks) contribute significantly to the deterioration of the $\not{E}_{\mathrm{T}}$ resolution. Moreover, the region around η=0 can also affect the resolution giving that the particles of a jet are almost parallel to the scintillator plates in TileCal producing larger sampling iron/scintillator ratio variation. Another important contribution comes from cosmic muons which may affect the $\not{E}_{\mathrm{T}}$ resolution and even worse create large $\not{E}_{\mathrm{T}}^{\mathrm{Fake}}$ [50, 51]. Finally, a bad muon reconstruction can generate a fake muon also leading to $\not{E}_{\mathrm{T}}^{\mathrm{Fake}}$. The total $\not{E}_{\mathrm{T}}^{\mathrm{Fake}}$ in MC samples can be defined as the vectorial difference of reconstructed and true $\not{E}_{\mathrm{T}}$:

$$\not{E}_{\mathrm{T}}^{\mathrm{Fake}} = \sqrt{(\not{E}_{\mathrm{x}}^{\mathrm{Fake}})^2 + (\not{E}_{\mathrm{y}}^{\mathrm{Fake}})^2} \tag{7.1}$$

with

$$\not{E}_{\mathrm{x,y}}^{\mathrm{Fake}} = \not{E}_{\mathrm{x,y}}^{\mathrm{Final}} - \not{E}_{\mathrm{x,y}}^{\mathrm{True}} \tag{7.2}$$

where $\not{E}_{\mathrm{x,y}}^{\mathrm{Final}}$ is the x-, y-component of the final reconstructed missing transverse energy (taking into account calorimeter and muon information), and $\not{E}_{\mathrm{x,y}}^{\mathrm{True}}$ is the x-, y-component of the missing transverse energy from non-interacting particles such as neutrinos and LSP in case of SUSY.

7.2.1 Fake Missing Transverse Energy from Muons

Fake $\not{E}_{\mathrm{T}}$ can be generated by either a bad muon reconstruction or random hits from high-p_{T} jet punch-through from calorimeter to the muon chambers leading to fake high p_{T} muon.

The total $\not{E}_{\mathrm{T}}^{\mathrm{Fake}}$ in MC samples can be defined as in Eq. (7.2) by the vectorial difference of reconstructed and true $\not{E}_{\mathrm{T}}$:

$$\not{E}_{\mathrm{x,y}}^{\mathrm{FakeMuon}} = \not{E}_{\mathrm{x,y}}^{\mathrm{FinalMuon}} - \not{E}_{\mathrm{x,y}}^{\mathrm{TrueMuon}} \tag{7.3}$$

where, $\not{E}_{\mathrm{x,y}}^{\mathrm{FinalMuon}}$ and $\not{E}_{\mathrm{x,y}}^{\mathrm{TrueMuon}}$ are calculated by summing the reconstructed and true $\not{E}_{\mathrm{T}}$ x-, y-components for muons only.

In order to separate the $\not{E}_{\mathrm{T}}^{\mathrm{Fake}}$ coming from muons from the one coming from calorimeter response the following cut is commonly used [47]:

$$\not{E}_{\mathrm{T}}^{\mathrm{FakeMuon}} > \not{E}_{\mathrm{T}}^{\mathrm{Fake}}/2 \tag{7.4}$$

This cut selects events with $\not{E}_{\mathrm{T}}^{\mathrm{Fake}}$ predominantly from muon misreconstruction. The opposite cut ($\not{E}_{\mathrm{T}}^{\mathrm{FakeMuon}} < \not{E}_{\mathrm{T}}^{\mathrm{Fake}}/2$) can be used to select events with $\not{E}_{\mathrm{T}}^{\mathrm{Fake}}$ from other sources like jet mismeasurement in the calorimeters.

Figure 7.1 displays the distributions of $\not\!\!E_{\mathrm{T}}^{\mathrm{True}}$ and $\not\!\!E_{\mathrm{T}}^{\mathrm{Fake}}$ for J6 events in three different cases: (a) with no cut applied, (b) after the separation cut $\not\!\!E_{\mathrm{T}}^{\mathrm{FakeMuon}} < \not\!\!E_{\mathrm{T}}^{\mathrm{Fake}}/2$ which selects events with $\not\!\!E_{\mathrm{T}}^{\mathrm{Fake}}$ coming mainly from jet mismeasurement and (c) after the separation cut $\not\!\!E_{\mathrm{T}}^{\mathrm{FakeMuon}} > \not\!\!E_{\mathrm{T}}^{\mathrm{Fake}}/2$ selecting events with $\not\!\!E_{\mathrm{T}}^{\mathrm{Fake}}$ dominated by muon misreconstruction.

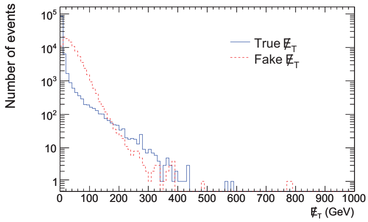

(a) All events

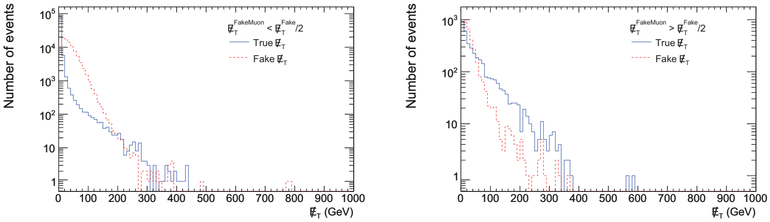

(b) Calorimeter as main source of $\not\!\!E_{\mathrm{T}}^{\mathrm{Fake}}$. (c) Muons as main source of $\not\!\!E_{\mathrm{T}}^{\mathrm{Fake}}$.

Figure 7.1: Distributions of the true and fake $\not\!\!E_{\mathrm{T}}$ for J6 QCD sample. The cases where the dominant source of $\not\!\!E_{\mathrm{T}}^{\mathrm{Fake}}$ is jet mismeasurement in the calorimeter or muons are shown separately.

The first conclusion which can be driven from those plots is that the $\not\!\!E_{\mathrm{T}}^{\mathrm{Fake}}$ in QCD background is dominated by jet misreconstruction in the calorimeter as the contribution from muons is two orders of magnitude smaller. Events dominated by the $\not\!\!E_{\mathrm{T}}^{\mathrm{Fake}}$ from muons (plot (c)) have a relatively large $\not\!\!E_{\mathrm{T}}^{\mathrm{True}}$ compared to the events dominated by $\not\!\!E_{\mathrm{T}}^{\mathrm{Fake}}$ from jet misreconstruction (plot (b)).

Apart from the muons in multijet events, cosmic ray muons can also introduce $\not\!\!E_{\mathrm{T}}^{\mathrm{Fake}}$. The effects of cosmics on $\not\!\!E_{\mathrm{T}}$ performance, which cannot be estimated from QCD MC data, are evaluated with real data taken on ATLAS commissioning in [50, 51].

7.2.2 Fake Missing Transverse Energy from Calorimeter

The response of the calorimeters to hadronic jets has large fluctuations due to the fragmentation process and the non-linear response to particles. This is expected to be the dominant source of $\not{E}_{\mathrm{T}}^{\mathrm{Fake}}$ from calorimeter. The finite thickness of the calorimeter system may not fully contain high-p_{T} jets or hadronic showers with late longitudinal development. Those jets will be leaking to the Muon Spectrometer and will not be properly measured. The cracks and gaps at the transition between the different calorimeter regions have poorer coverage and contribute to $\not{E}_{\mathrm{T}}^{\mathrm{Fake}}$ more than the rest of the regions. The gap and crack regions in ATLAS are in the following $|\eta|$ intervals:

- $1.3 < |\eta| < 1.6$: transition between Tile Calorimeter and Hadronic LAr End Cup.
- $3.1 < |\eta| < 3.3$: transition between Hadronic LAr End Cup and Forward Calorimeter.

7.3 Cleaning Methods

7.3.1 Study of Calorimeter Leakage

Jet leakage from the calorimeters or fluctuations of large jet energy depositions in innactive regions such as the cryostat between the Liquid Argon and Tile calorimeters can also be sources of $\not{E}_{\mathrm{T}}^{\mathrm{Fake}}$. The method used to detect cases with potential jet leakage proposed here is based on large energy depositions in the following regions: the outermost layers of TileCal and HEC, the outermost LAr layer and innermost TileCal layer and in the TileCal gap and crack scintillators. The study of the calorimeter variables which can be used to identify jets that have not been properly reconstructed has been performed by comparing the reconstructed jet energy with the truth jet energy in the Monte Carlo in different η intervals. These intervals have been selected according to the transition regions between the different calorimeter components. Only reconstructed jets with a good matching[1] with MC truth jets were used in the study and selection definition.

The variables chosen for the cleanup selection are described below:

- $E_{\mathrm{Tile2}}/E_{\mathrm{Total}}$: fraction of the total jet energy deposited in the outermost layer of the Tile Calorimeter for both long and extended barrel. Jets with a high fraction of energy deposition in the last layer of the Tile Calorimeter may not be fully contained.
- $E_{\mathrm{Tile10}}/E_{\mathrm{Total}}$: fraction of the total jet energy deposited in the two innermost layers of the Tile Calorimeter for both long and extended barrel. This variable has the same meaning as $E_{\mathrm{Tile2}}/E_{\mathrm{Total}}$ in the 1.4<$|\eta|$<1.7 region as the Tile Calorimeter outermost layer ends at $|\eta|$=1.4. In this region jets with high fraction of energy deposition in

---

[1] We assume that the reconstructed jet which matches one and only one MC jet within a cone of $\Delta R = 1$ is valid for the comparison study. The relatively large $\Delta R = 1$ cone gives a good separation and better matching results than a smaller one.

these two layers will most probably leak to the muon chambers of ATLAS, leading not only to fake $\not{E}_{\mathrm{T}}^{\mathrm{Fake}}$ from jets mismeasurement but also to fake muons.

- $E_{\mathrm{Cryo}}/E_{\mathrm{Total}}$: where E_{Cryo} is computed with the energy in the LAr outermost and TileCal innermost layers as $E^2_{\mathrm{Cryo}} = E_{\mathrm{LAr3}}E_{\mathrm{Tile0}}$. This variable gives an estimation of the energy deposition in the cryostat between both calorimeters.
- $E_{\mathrm{Gap}}/E_{\mathrm{Total}}$: fraction of the total jet energy deposited in the Tile Calorimeter gap and crack scintillators.
- $E_{\mathrm{HEC3}}/E_{\mathrm{Total}}$: fraction of the total jet energy deposited in the outermost layer of the LAr Hadronic EndCap calorimeter. As in the case of E_{Tile2}, large depositions in this layer are correlated with potential jet leakage.

Table 7.3.1 shows the selection cuts applied to the three leading jets with p_{T}>100 GeV. This requirement avoids cutting events with misreconstructed low-p_{T} jets which would not contribute significantly to $\not{E}_{\mathrm{T}}^{\mathrm{Fake}}$. Events are rejected if the relative energy deposition defined in the variables selected exceeds the values in Table 7.3.1.

The specific values of the cuts as well as the jet selection criteria could be changed according to the signal efficiency and topology. However, selecting at least the first two leading jets is necessary to perform a good and efficient $\not{E}_{\mathrm{T}}^{\mathrm{Fake}}$ cleaning for the QCD background.

Table 7.1: Cuts for QCD cleaning to be applied on the jets reconstructed at several regions in η.

	$\lvert\eta\rvert$<0.3	0.3<$\lvert\eta\rvert$<0.6	0.6<$\lvert\eta\rvert$<1.3	1.3<$\lvert\eta\rvert$<2.0	2.0<$\lvert\eta\rvert$<3.0
$E_{\mathrm{Tile2}}/E_{\mathrm{Tot}}$	0.05	0.05	0.1	0.02	-
$E_{\mathrm{Tile10}}/E_{\mathrm{Tot}}$	0.8	0.8	0.7	0.2	-
$E_{\mathrm{Cryo}}/E_{\mathrm{Tot}}$	0.2	0.2	0.2	-	-
$E_{\mathrm{Gap}}/E_{\mathrm{Tot}}$	-	-	0.2	0.3	-
$E_{\mathrm{HEC3}}/E_{\mathrm{Tot}}$	-	-	-	0.05	0.05

Moreover, Table 7.3.1 shows different cut values with respect to η. The η regions used in the present analysis are defined according to the detector design as follows:

- $|\eta|$<0.3 : In this region jets are parallel to the scintillating tiles which constitute the active material of the Tile Calorimeter. The particles in the jet which are very close to $|\eta| = 0$ may not cross the active material at all, generating an undermeasurement of the jet energy. Moreover, this is the region of the detector with the smallest thickness, so that very energetic jets may not be fully absorbed.

- $0.3<|\eta|<0.6$: The absorption length of this region is bigger than the region above and it covers the rest of the TileCal barrel, before the gap between the barrel and extended barrel.
- $0.6<|\eta|<1.3$: This region corresponds to the transition between the barrel and extended barrel in the Tile Calorimeter.
- $1.3<|\eta|<2.0$: This is a critical region since it includes the end of the Liquid-Argon Electromagnetic Calorimeter barrel and the Tile Calorimeter extended barrel and the beginning of the LAr Hadronic and Electromagnetic End-Cap.
- $2.0<|\eta|<3.0$ This is the last region considered in this study, it covers the Electromagnetic and Hadronic LAr End-Cap without any transition, but very energetic jets with such a high η may show leakage.

Regions with $|\eta|>3.0$ will not be considered in our study, as the probability of having jets with enough p_{T} in this area is much smaller than the rest of the detector.

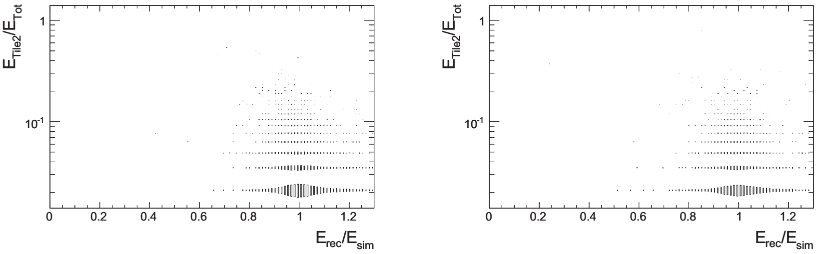

(a) $|\eta|<0.3$.

(b) $0.3<|\eta|<0.6$.

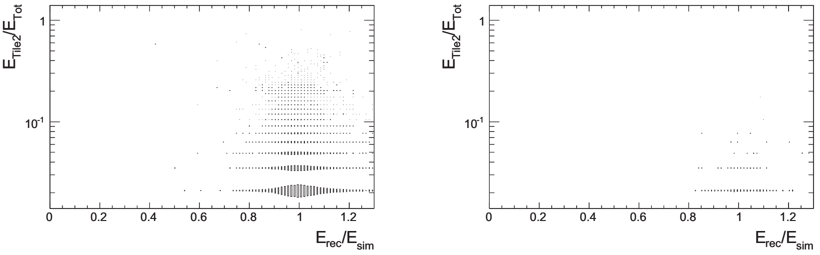

(c) $0.6<|\eta|<1.3$.

(d) $1.3<|\eta|<2$.

Figure 7.2: Fraction of the total jet energy deposited in the outermost TileCal layer as a function of the ratio between the reconstructed jet energy over the jet energy in the simulation for sample J6 at different η intervals. Only the first three leading jets are shown.

Figures 7.2-7.6 present the plots which were used to evaluate the cuts for the different η regions. They show the variables defined for the cut as a function of the ratio of the jet

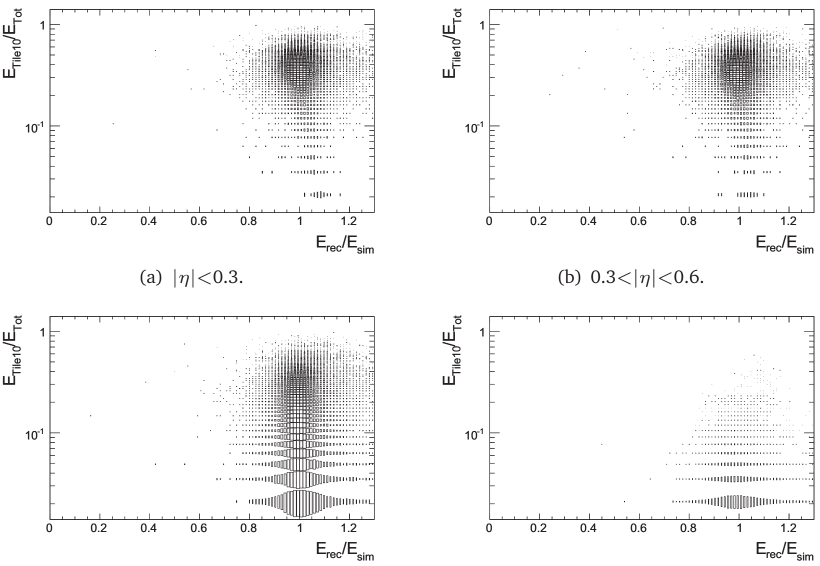

(a) $|\eta|<0.3$.

(b) $0.3<|\eta|<0.6$.

(c) $0.6<|\eta|<1.3$.

(d) $1.3<|\eta|<2$.

Figure 7.3: Fraction of the total jet energy deposited in the two innermost TileCal layers as a function of the ratio between the reconstructed jet energy over the jet energy in the simulation for sample J6 at different η intervals. Only the first three leading jets are shown.

total energy over the MC truth energy from the matched jet. The variables $E_{\rm X}$ (where X is Tile2, Tile10, Cryo, Gap or HEC3) are computed with the energies deposited on those calorimeter subsystems by the topo clusters which are within a ΔR cone of 0.4 around the reconstructed jet. For example, $E_{\rm Tile2}$ is the sum over the topo clusters of the energy released in the TileCal outermost layer within $\Delta R = 0.4$. The $E_{\rm Tot}$ variable is obtained summing the energy released by all the topo clusters in the calorimeters within ΔR=0.4.

As shown in Figures 7.2 and 7.6, at relatively high energy deposited in TileCal and HEC outermost layers (let's say 10%) a spread of events deviating about 25% or more from the corresponding MC jet energy is found. These events with such a bad energy reconstruction are clearly contributing to $\not\!\!E_{\rm T}^{\rm Fake}$ from calorimeter. In the region of $|\eta|$>1.3, $E_{\rm Tile10}$ (Figure 7.3) behaves the same way as $E_{\rm Tile2}$ and $E_{\rm HEC3}$ and other η regions: most of the events show a good jet energy reconstruction (around ± 10% of the MC) but at very large $E_{\rm Tile10}/E_{\rm Tot}$ values, events are scattered over a large jet reconstruction deviation with respect to the MC (up to 40%). A cut at around 70-80% of this quantity would remove those events.

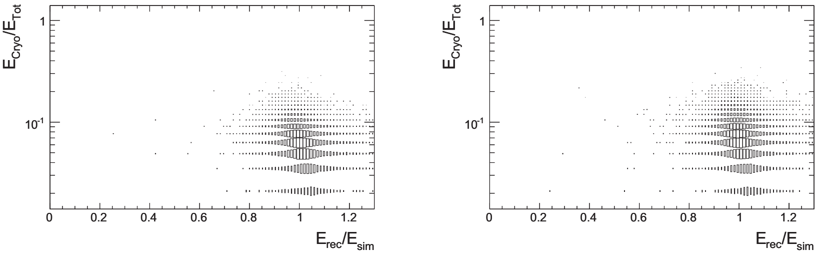

(a) $|\eta|<0.3$.

(b) $0.3<|\eta|<0.6$.

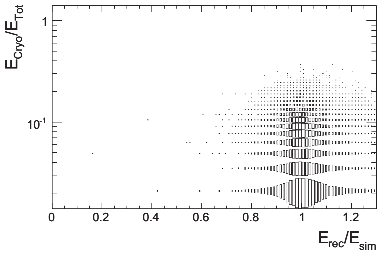

(c) $0.6<|\eta|<1.3$.

Figure 7.4: Ratio of the estimated energy deposited in the cryostat over of the total jet energy as a function of the ratio between the reconstructed jet energy over the jet energy in the simulation for sample J6 at different η intervals. Only the first three leading jets are shown.

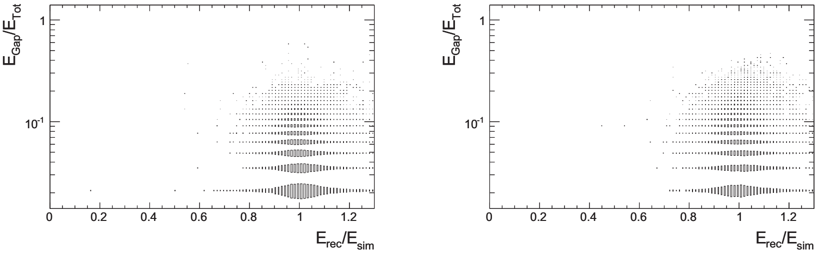

(a) $0.6<|\eta|<1.3$.

(b) $1.3<|\eta|<2$.

Figure 7.5: Fraction of the total jet energy deposited in the gap and crack scintillators as a function of the ratio between the reconstructed jet energy over the jet energy in the simulation for sample J6 at different η intervals. Only the first three leading jets are shown.

Regarding the variables used to estimate the energy released in dead materials in the calorimeter, $E_{\text{Cryo}}/E_{\text{Tot}}$ and $E_{\text{Gap}}/E_{\text{Tot}}$ (Figures 7.4 and 7.5), they have similar shapes and also display a large spread of events at relatively high fraction of energy deposition (20-30%) in the corresponding subsystems.

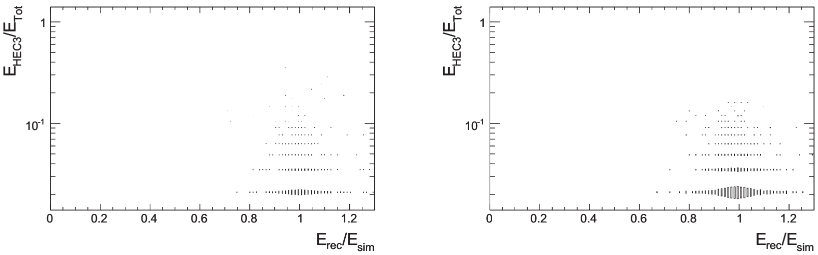

(a) $1.3<|\eta|<2.0$. (b) $2.0<|\eta|<3.0$.

Figure 7.6: Fraction of the total jet energy deposited in the outermost layer of the Hadronic EndCap as a function of the ratio between the reconstructed jet energy over the jet energy in the simulation for sample J6 at different η intervals. Only the first three leading jets are shown.

Figure 7.7 shows the fraction of remaining events after applying the method described above on J5, J6 and J7 QCD samples. The plots demonstrate that the cleanup process is more likely to eliminate events that have high $\not{E}_{\mathrm{T}}^{\mathrm{Fake}}$ contamination since the fraction of the remaining events decrease as a function of $\not{E}_{\mathrm{T}}^{\mathrm{Fake}}$. It can also be noticed from the left plot that these cuts, although capable of removing an important fraction of the events dominated by $\not{E}_{\mathrm{T}}^{\mathrm{Fake}}$, are not sensitive to the overall $\not{E}_{\mathrm{T}}$ in the event, and the fraction of remaining events constitute a plateau over the whole $\not{E}_{\mathrm{T}}$ range with deviations of less than ~5%. The large error bars in some points are a consequence of the very limited statistics available at high $\not{E}_{\mathrm{T}}$ or $\not{E}_{\mathrm{T}}^{\mathrm{Fake}}$.

7.3.2 Cleaning Cuts Based on Missing Transverse Energy from Tracks

In this section we propose an additional method for $\not{E}_{\mathrm{T}}^{\mathrm{Fake}}$ reduction which also reduces $\not{E}_{\mathrm{T}}$ from QCD jets. Due to the fact that the tracks found in the Inner Detector are not affected by the reconstruction issues stated for the calorimeters above, additional information on the QCD $\not{E}_{\mathrm{T}}^{\mathrm{Fake}}$ cleaning can be obtained using the $\not{E}_{\mathrm{T}}$ obtained only from tracks ($\not{E}_{\mathrm{T}}^{\mathrm{Trk}}$). This variable is defined as:

$$\not{E}_{\mathrm{T}}^{\mathrm{Trk}} = \sqrt{(\sum_{Tracks} p_{\mathrm{x}})^2 + (\sum_{Tracks} p_{\mathrm{y}})^2} \tag{7.5}$$

where $p_{\mathrm{x,y}}$ are is the x-, y-component of the track transverse momentum.

Figure 7.8 shows the difference between the reconstructed $\not{E}_{\mathrm{T}}$ and $\not{E}_{\mathrm{T}}^{\mathrm{Trk}}$ as a function of the reconstructed $\not{E}_{\mathrm{T}}$ for the J6 QCD background and a SU3 signal. Clearly, different trends are found between the signal and QCD background. QCD background events are

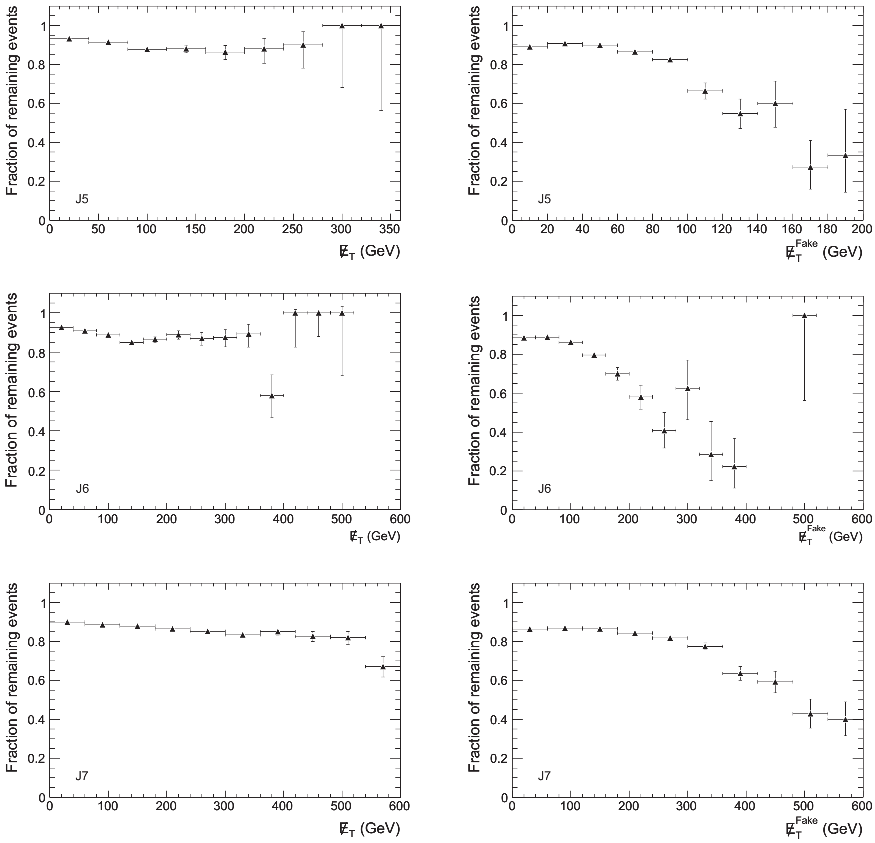

Figure 7.7: Fraction of remaining events after the selection cuts discussed in the text for $\not\!\!E_{\mathrm{T}}$ (left) and $\not\!\!E_{\mathrm{T}}^{\mathrm{Fake}}$ (right) in J5, J6 and J7 QCD sample.

concentrated in the high $\not\!\!E_{\mathrm{T}}^{\mathrm{Trk}}$ region with $\not\!\!E_{\mathrm{T}}^{\mathrm{Trk}} \gg \not\!\!E_{\mathrm{T}}$. Even at $\not\!\!E_{\mathrm{T}} \gtrsim 100$ GeV, the difference between $\not\!\!E_{\mathrm{T}}^{\mathrm{Trk}}$ and $\not\!\!E_{\mathrm{T}}$ can be as high as 500 GeV. On the contrary, for SU3 signal most of the events show $\not\!\!E_{\mathrm{T}}^{\mathrm{Trk}} < \not\!\!E_{\mathrm{T}}$. Therefore, a cut for rejecting QCD background in SUSY analysis can be set in $\not\!\!E_{\mathrm{T}} - \not\!\!E_{\mathrm{T}}^{\mathrm{Trk}} < -50$ GeV.

Figure 7.9 shows the difference between $\not\!\!E_{\mathrm{T}}$ and $\not\!\!E_{\mathrm{T}}^{\mathrm{Trk}}$ as a function of $\not\!\!E_{\mathrm{T}}^{\mathrm{Fake}}$ for the J6 QCD background and a SU3 signal. Note that the J6 events which show the highest $\not\!\!E_{\mathrm{T}}$ values in Figure 7.8 correspond to very low $\not\!\!E_{\mathrm{T}}^{\mathrm{Fake}}$ due to the fact that true $\not\!\!E_{\mathrm{T}}$ is need to achieved high $\not\!\!E_{\mathrm{T}}$ in QCD background. Nevertheless, an important amount of events with $\not\!\!E_{\mathrm{T}}^{\mathrm{Fake}} > 100$ GeV are indeed removed by the cut proposed above. Regarding the SU3 signal,

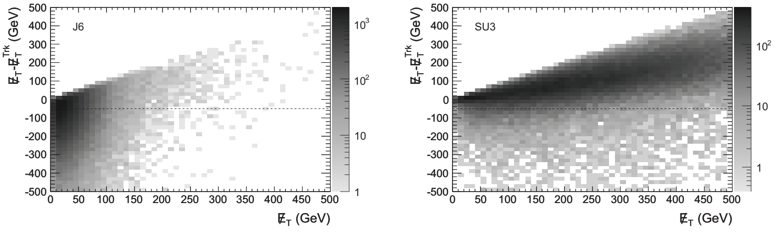

Figure 7.8: Difference between $\not{E}_T$ and $\not{E}_T^{\rm Trk}$ as a function of $\not{E}_T$ for J6 QCD sample (left) and for SU3 sample (right). The cut proposed in the text is shown with a dashed line.

almost all the events are concentrated at low $\not{E}_T^{\rm Fake}$ because true $\not{E}_T$ from the LSP is the dominant source of $\not{E}_T$ in this sample.

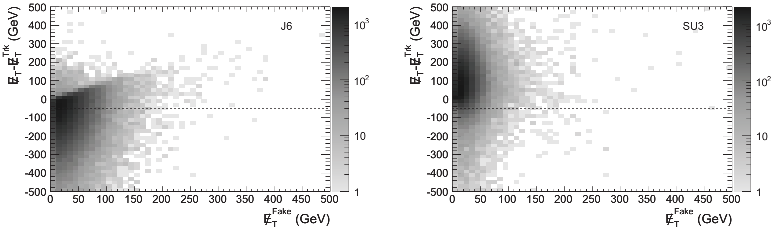

Figure 7.9: Difference between $\not{E}_T$ and $\not{E}_T^{\rm Trk}$ as a function of $\not{E}_T^{\rm Fake}$ for J6 QCD sample (left) and for SU3 sample (right). The cut proposed in the text is shown with a dashed line.

In particular, Figure 7.10 shows the true and fake component of the $\not{E}_T$ separately for the events accepted and rejected by this cut. Practically the same distribution is obtained for the $\not{E}_T^{\rm Fake}$ in both cases, although the accepted events show largest tails which are also correlated with largest tails for the $\not{E}_T^{\rm True}$.

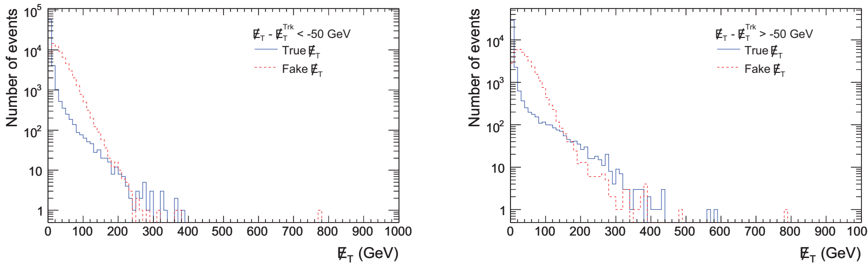

Figure 7.10: Distributions of true and fake $\not{E}_T$ for rejected (left) and selected (right) events by the $\not{E}_T - \not{E}_T^{\rm Trk} < -50$ GeV cut.

Figure 7.11 shows the correlation between $\not\!\!E_{\mathrm{T}}$ and $\not\!\!E_{\mathrm{T}}^{\mathrm{True}}$ for signal and J6 samples separately for the events selected and rejected by the cut on $\not\!\!E_{\mathrm{T}}^{\mathrm{Trk}}$. A strong correlation is found for the signal in both selected and rejected events. For the QCD sample, this correlation is also found for high $\not\!\!E_{\mathrm{T}}^{\mathrm{True}}$ but lots of events with $\not\!\!E_{\mathrm{T}}^{\mathrm{True}}\approx 0$ show high $\not\!\!E_{\mathrm{T}}$ due to detector effects inducing $\not\!\!E_{\mathrm{T}}^{\mathrm{Fake}}$.

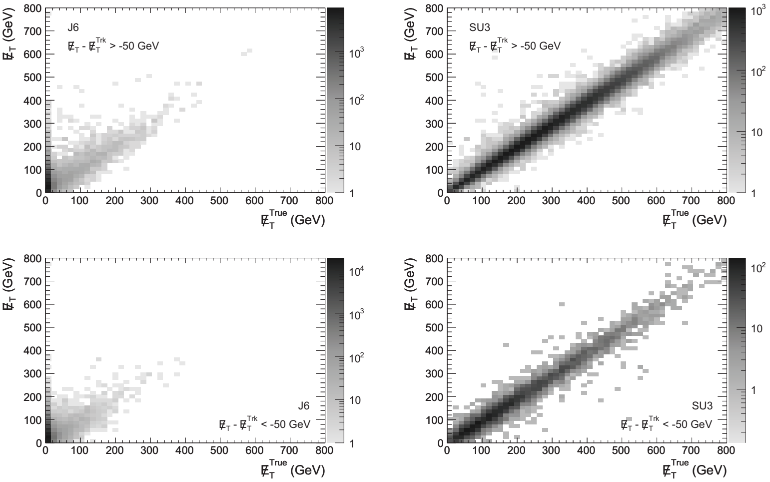

Figure 7.11: Distributions of $\not\!\!E_{\mathrm{T}}$ as a function of $\not\!\!E_{\mathrm{T}}^{\mathrm{truth}}$ for J6 QCD sample (left) and for SU3 sample (right) for the selected (top) and rejected (bottom) events by the $\not\!\!E_{\mathrm{T}} - \not\!\!E_{\mathrm{T}}^{\mathrm{Trk}} < -50$ GeV cut.

Figure 7.12 shows the same distribution but for $\not\!\!E_{\mathrm{T}}^{\mathrm{Trk}}$. In the background case, for both selected and rejected events the events with $\not\!\!E_{\mathrm{T}}^{\mathrm{True}}\approx 0$ show high $\not\!\!E_{\mathrm{T}}^{\mathrm{Trk}}$. On the contrary, at higher $\not\!\!E_{\mathrm{T}}^{\mathrm{True}}$ different trends are found for accepted and rejected events: $\not\!\!E_{\mathrm{T}}^{\mathrm{Trk}} \gg \not\!\!E_{\mathrm{T}}^{\mathrm{True}}$ for rejected events while $\not\!\!E_{\mathrm{T}}^{\mathrm{Trk}} \lesssim \not\!\!E_{\mathrm{T}}^{\mathrm{True}}$ for accepted events. This can be explained with the fact that $\not\!\!E_{\mathrm{T}}^{\mathrm{Trk}}$ is not sensible to the neutral particles within the jets in the event. When $\not\!\!E_{\mathrm{T}}\approx 0$ all the reconstructed jets in the event are balanced but the tracking system only considers the charged particles and the p_{T} of all jets is underestimated. Hence from the fluctuations in the fraction of neutral particles, the jet p_{T} imbalance can appear and therefore large $\not\!\!E_{\mathrm{T}}^{\mathrm{Trk}}$.

For events with high real $\not\!\!E_{\mathrm{T}}$ from neutrinos or the LSP, the additional jet imbalance when not considering the neutrals for the $\not\!\!E_{\mathrm{T}}$ computation produces a reduction on the $\not\!\!E_{\mathrm{T}}^{\mathrm{Trk}}$ with respect to $\not\!\!E_{\mathrm{T}}^{\mathrm{True}}$ as indeed happens for the SU3 sample as shown in Figure 7.12.

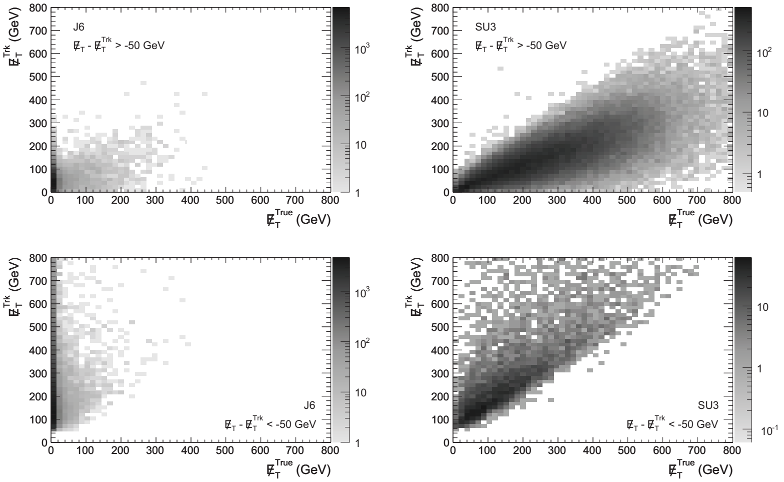

Figure 7.12: Distributions of the reconstructed $\not{E}_{\rm T}$ obtained from tracks as a function of the true $\not{E}_{\rm T}$ for J6 QCD sample (left) and for SU3 sample (right) for the selected (top) and rejected (bottom) events by the $\not{E}_{\rm T} - \not{E}_{\rm T}^{\rm Trk} < -50$ GeV cut.

7.4 Conclusions

In summary, this Chapter presents several variables which are correlated with fake $\not{E}_{\rm T}$ in QCD events. Events with high energy deposition in either the outermost calorimeter layers or in non-instrumented regions are shown to be associated with jet misreconstruction. Cuts on selected calorimeter variables render effective in rejecting QCD background events with high $\not{E}_{\rm T}^{\rm Fake}$.

In addition, the comparison of the $\not{E}_{\rm T}$ computed only with information from the tracking system and the overall reconstructed $\not{E}_{\rm T}$ can also be used to reject QCD background due to the different behaviour of these variables for multijet events and SUSY signals.

These cuts can be adapted to other applications and, since they have been obtained with Monte Carlo, they should be validated with real data after ATLAS operation startup. Due to the fact that the current simulation is probably idealizing the detector response, detector effects leading to $\not{E}_{\rm T}^{\rm Fake}$ are likely poorly modeled, and the effect of the cuts proposed will be more important in real data.

Chapter 8

Search for SUSY Particles in the Fully Hadronic Channel

“To be intelligent is to be open-minded, active, memoried, and persistently experimental.”
— L. Stein, 1810-1882

8.1 Introduction

This Chapter is devoted to the SUSY inclusive discovery analysis and, since the topology of this signal is multiple high-$p_\mathrm{T}$jets and large $\not\!\!E_\mathrm{T}$, a fully hadronic signature with at least 4-jets and 0-leptons in the final state has been chosen. The main backgrounds which affect this channel are $\mathrm{t\bar{t}}$, gauge bosons (produced individually or in diboson states) and QCD. Although similar analysis has been performed in the past [52], the main innovation presented here is the application of the $\not\!\!E_\mathrm{T}^\mathrm{Fake}$ from QCD background cleaning cuts proposed in the previous Chapter.

Multi-jet events represent the biggest challenge for attempts to understand the Standard Model backgrounds in any New Physics search with early data due to their large cross section at LHC. In the case of SUSY, the multiple high-p_T jets and $\not\!\!E_\mathrm{T}$ signature could be met by QCD events with large $\not\!\!E_\mathrm{T}^\mathrm{Fake}$ caused by instrumental effects. Although real $\not\!\!E_\mathrm{T}$ can be present in QCD due to the neutrinos produced in the fragmentation processes or jets at high η (close to the beam pipe), their importance is extremely small in comparison to the detector effects causing $\not\!\!E_\mathrm{T}^\mathrm{Fake}$.

8.2 No Lepton Analysis

This Section is devoted to the SUSY analysis in the inclusive 0-lepton mode with 4 or more jets in the final state. In consequence, the cuts used are the standard ones in this analysis [52, 53] with the addition of the QCD cleaning cuts. The specific values for the selection cuts are the following:

- **Cut 1**: Since the electron identification and measurement are degraded in the crack region due to the large amount of inactive material, events with reconstructed electrons in the region comprised by 1.37< $|\eta|$ <1.52 are discarded [53].
- **Cut 2**: This selection is based in the jet multiplicity requiring at least four jets with p_{T}(jet$_1$)$\geq$100 GeV and p_{T}(jet$_4$)$\geq$50 GeV.
- **Cut 3**: Cut on the missing transverse energy, requiring $\not\!\!E_{\mathrm{T}}$ $\geq$100 GeV.
- **Cut 4**: Cut on the ratio between the $\not\!\!E_{\mathrm{T}}$ and the event effective mass: $\not\!\!E_{\mathrm{T}} \geq 0.2 M_{\mathrm{eff}}$, where $M_{\mathrm{eff}} = \sum_{i=1}^{4} p_{\mathrm{T}}(\mathrm{jet_i}) + \not\!\!E_{\mathrm{T}}$.
- **Cut 5**: Cut on transverse sphericity: S_{T}>0.2, where S_{T} is computed from all the jets with p_{T}>20 GeV in $|\eta|$ <2.5.
- **Cut 6**: Requirement in the angular separation between the three leading jets and the $\not\!\!E_{\mathrm{T}}$ in the transverse plane: $\Delta\phi$(jet$_{1,2,3}$-$\not\!\!E_{\mathrm{T}}$)$\geq$0.2.
- **Cut 7**: The absence of isolated electrons or muons with E_{T} >20 GeV in $|\eta|$ <2.5 is required.
- **Cut 8**: The QCD cleaning cuts as defined in Section 7.3 are applied.

Section 8.2.2 shows the cut flow for signal and background samples, but in Section 8.2.1 the variables used to define the cuts above are presented in detail and their impact in this analysis is described.

Cuts 2-5 and 7 were already used in Ref. [52] and Cuts 1 and 6 are used in Ref. [53]. Cut 5 is used to reduce the dijet QCD background. The main purpose of Cut 6 is to discard QCD background events with real $\not\!\!E_{\mathrm{T}}$ from the neutrinos in heavy flavour jet semileptonic decays. Apart from those events which present real $\not\!\!E_{\mathrm{T}}$, events with problems in the jet reconstruction due to the losses in inactive materials or shower leakage caused by the finite containment of the calorimeters or with jets in the crack regions of the detector will have fake $\not\!\!E_{\mathrm{T}}$, meeting selection Cuts 3 and 4.

8.2.1 Control Plots

Jet Multiplicity and Momentum

Once the events with electrons in the crack regions are removed, the first requirement in this analysis is on the number of jets in the events and their momentum, since the signature for SUSY events are large multiplicity of high p_{T} jets together with large $\not{E}_{\mathrm{T}}$.

Figure 8.1 shows the number of jets per event with p_{T}>50 GeV for all backgrounds and SU3 SUSY signal after Cut 1 and the events selected by the jet multiplicity requirement specified in Cut 2. Note that filters on the number of jets were applied at the generation level for most of the samples as stated in Section 6.3, so the behaviour in the low jet multiplicity region is biased.

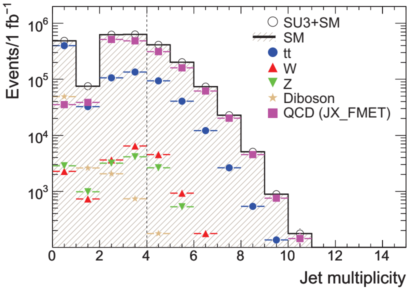

Figure 8.1: Distributions of the jet multiplicity (for jets with p_{T}>50 GeV and $|\eta|$<2.5) after Cut 1 for background and SU3 SUSY signal on top of the background with the QCD described by the JX_FMET samples. The value used to define Cut 2 (more than 4 jets with this momentum and η requirement) is shown with the vertical line.

The largest backgrounds found at this early stage in the analysis are QCD and $\mathrm{t\bar{t}}$ (more than one order of magnitude larger than the rest), which are also the ones that present the largest jet multiplicities. Diboson samples, together with its low cross section, have also the smallest multiplicity values with very few events above four jets although a significant amount of events from other samples have seven or more jets in the final state.

Figure 8.2 shows the p_{T} distributions for the four leading jets for all samples also after Cut 1 is applied. In this case jets with lower momentum (p_{T}>20 GeV and $|\eta|$ <2.5) are also considered. The most energetic jets are present in the QCD samples for the 4 cases, with big differences in p_{T} between the two leading jets and the third and fourth jets due to the dijet topology of QCD events.

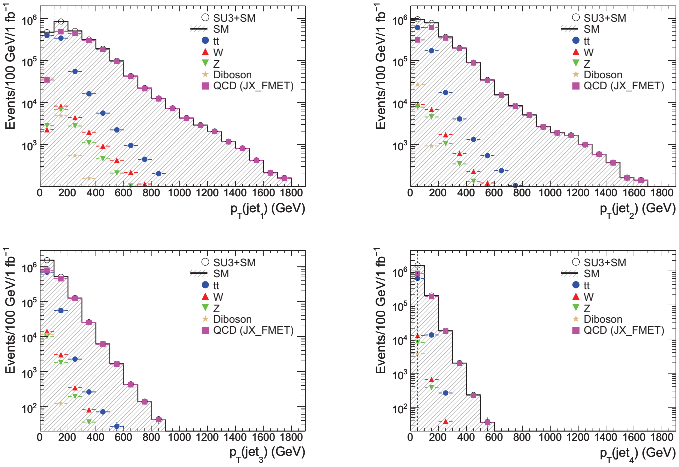

Figure 8.2: Distributions of the jet p_{T} for the four leading jets (considering jets with $p_{\mathrm{T}}>20$ GeV and $|\eta|<2.5$) after Cut 1 for background and SU3 SUSY signal on top of the background with the QCD described by the JX_FMET samples. The values used to define Cut 2 are shown with vertical lines.

This behaviour can be better understood when looking at the correlation between the jet p_{T} in the events. Figures 8.3 shows the scattering plots comparing the jet p_{T} values separately for SU3 signal, non-QCD (W, Z and $\mathrm{t\bar{t}}$) and QCD background after Cuts 1-2.

In the case of the QCD background, a strong correlation is found between the p_{T} of the two leading jets with a clear trend on $p_{\mathrm{T}}(\mathrm{jet}_1)\sim p_{\mathrm{T}}(\mathrm{jet}_2)$. Indeed, no cases are found with more than 500 GeV difference between the two leading jets momenta. This is due to the fact that those QCD events come mostly from two parton interactions which can be fragmented afterwards providing additional lower p_{T} jets. Less dependence is found for the case of $p_{\mathrm{T}}(\mathrm{jet}_{3,4})$ as a function of $p_{\mathrm{T}}(\mathrm{jet}_1)$.

On the other hand, non-QCD background and signal present very similar trends, with less correlation between the two leading jets momentum and much softer second to fourth jets.

Finally, Figure 8.4 shows the ratio of the jet p_{T} after Cuts 1-2. All the p_{T} ratios involving jet$_3$ and jet$_4$ in the numerator ($p_{\mathrm{T}}(\mathrm{jet}_{3,4})/p_{\mathrm{T}}(\mathrm{jet}_i)$) are dominated by the QCD background in the region of low values, clear sing of the presence of two very energetic jets in the final state with any additional jet with much less momentum in this kind of events. However, the $\mathrm{t\bar{t}}$ and diboson samples are the most important at high values of $p_{\mathrm{T}}(\mathrm{jet}_{3,4})/p_{\mathrm{T}}(\mathrm{jet}_i)$, showing that the 4 jets produced in those samples are much closer in

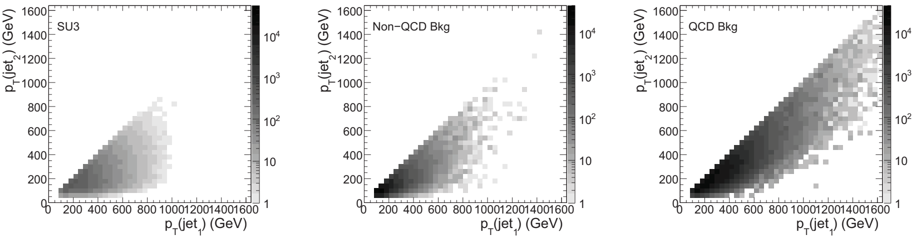

(a) $p_{\mathrm{T}}(\mathrm{jet}_2)$ and $p_{\mathrm{T}}(\mathrm{jet}_1)$ scatter plot

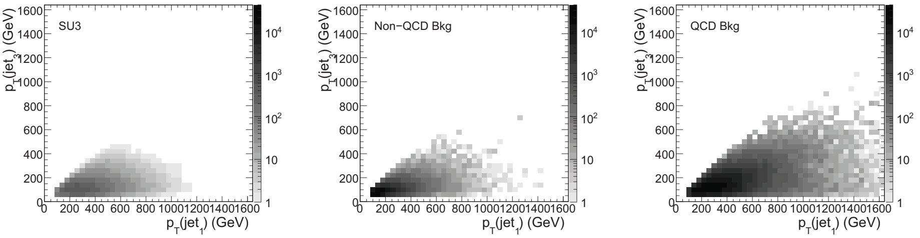

(b) $p_{\mathrm{T}}(\mathrm{jet}_3)$ and $p_{\mathrm{T}}(\mathrm{jet}_1)$ scatter plot

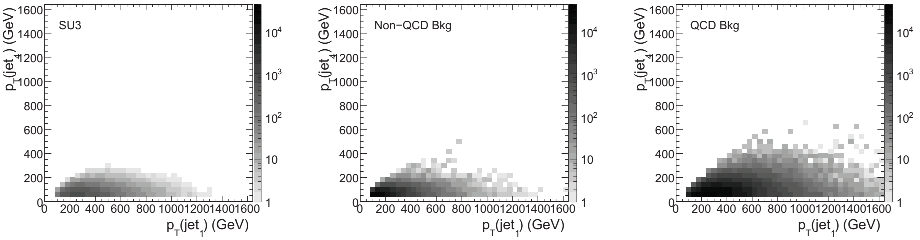

(c) $p_{\mathrm{T}}(\mathrm{jet}_4)$ and $p_{\mathrm{T}}(\mathrm{jet}_1)$ scatter plot

Figure 8.3: Transverse momentum of the second to fourth leading jets as a function of the p_{T} of the leading jet for SU3 SUSY signal (left), non-QCD background (center) and QCD background (right) for events passing Cuts 1-2. All the plots show number of events with an integrated luminosity of 1 fb^{-1}.

p_{T} than for QCD or single gauge boson events. Therefore, this set of variables can provide additional discrimination between the different backgrounds involved in the analysis.

Effective Mass as a Function of the Jet $\mathbf{p_T}$

Figures 8.5 and 8.6 show the distribution of the M_{eff} variable as a function of the ratios of the p_{T} of the four leading jets for Signal, QCD and non-QCD background separately after

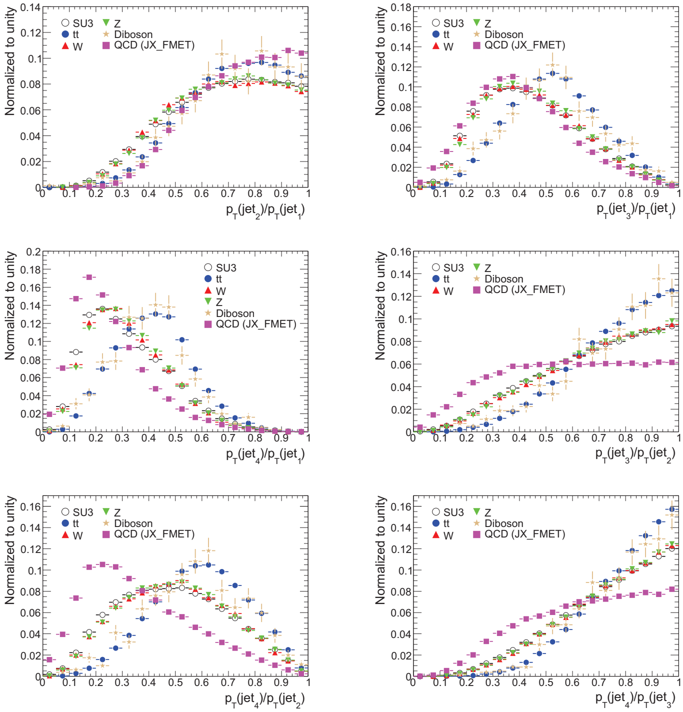

Figure 8.4: Distributions for the jet p_{T} ratios for the four leading jets after Cuts 1-2 for background and SU3 SUSY signal on top of the background with the QCD described by the JX_FMET samples.

Cuts 1-2 (4-jet events are already selected). For the QCD background, the highest M_{eff} values are strongly correlated with either a high $p_{\mathrm{T}}(\mathrm{jet}_2)/p_{\mathrm{T}}(\mathrm{jet}_1)$ (that is, with two leading jets with very similar energy) and/or with very small values of the $p_{\mathrm{T}}(\mathrm{jet}_{3,4})/p_{\mathrm{T}}(\mathrm{jet}_{1,2})$ ratio (that is, with very energetic leading jets). Neither in the signal nor in the non-QCD background there is a strong correlation between M_{eff} and the $p_{\mathrm{T}}(\mathrm{jet}_2)/p_{\mathrm{T}}(\mathrm{jet}_1)$ ratio.

Note also that for QCD the cases with $p_{\mathrm{T}}(\mathrm{jet}_2)/p_{\mathrm{T}}(\mathrm{jet}_1) < 0.5$ always have $M_{\mathrm{eff}} < 2000$ GeV because if the second jet is significantly less energetic that the leading jet, the total effective mass cannot be very large unless high energetic neutrinos are present since jet_3 and jet_4 are even less energetic. This is not the case for signal or non-QCD background.

However, in all the samples considered the lowest $p_{\mathrm{T}}(\mathrm{jet}_{3,4})/p_{\mathrm{T}}(\mathrm{jet}_1)$ values imply a high M_{eff}, either because of very low $p_{\mathrm{T}}(\mathrm{jet}_{3,4})$ (but at least with 50 GeV due to Cut 2) or, most likely, very large $p_{\mathrm{T}}(\mathrm{jet}_1)$, pulling M_{eff} up. In QCD this effect is quantitatively more important due to the fact that, as shown above, more events with low $p_{\mathrm{T}}(\mathrm{jet}_3)/p_{\mathrm{T}}(\mathrm{jet}_1)$

are present. Also note that the behaviour obtained for $p_{\rm T}$(jet$_{3,4}$)/$p_{\rm T}$(jet$_2$) is qualitatively the same as $p_{\rm T}$(jet$_{3,4}$)/$p_{\rm T}$(jet$_1$) but slightly displaced towards higher ratio values since $p_{\rm T}$(jet$_2$)<$p_{\rm T}$(jet$_1$).

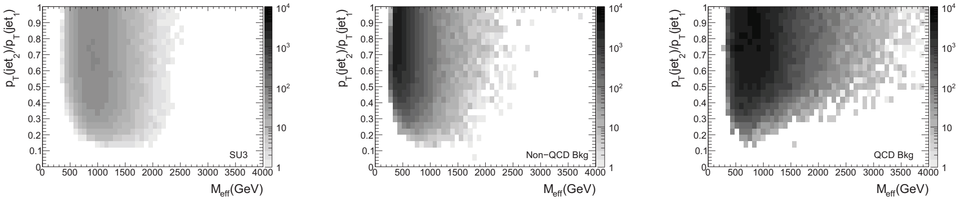

(a) $p_{\rm T}$(jet$_2$)/$p_{\rm T}$(jet$_1$) and $M_{\rm eff}$ scatter plot

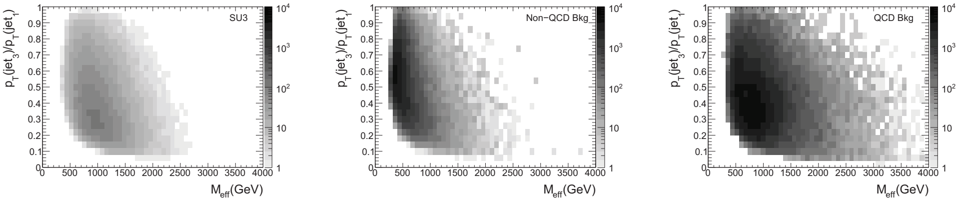

(b) $p_{\rm T}$(jet$_4$)/$p_{\rm T}$(jet$_1$) and $M_{\rm eff}$ scatter plot

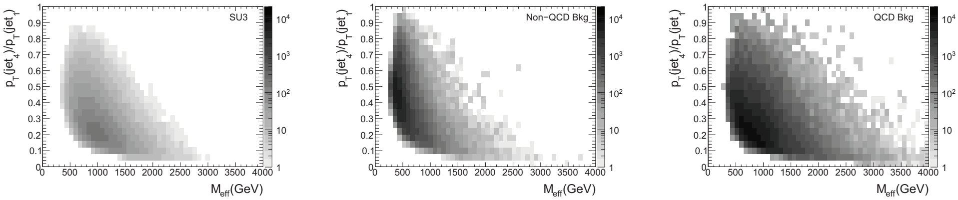

(c) $p_{\rm T}$(jet$_4$)/$p_{\rm T}$(jet$_1$) and $M_{\rm eff}$ scatter plot

Figure 8.5: Distributions for the jet $p_{\rm T}$ ratios over the leading jet $p_{\rm T}$as a function of $M_{\rm eff}$ for SU3 SUSY signal (left), non-QCD background (center) and QCD background (right) for events passing Cuts 1-2. All the plots show number of events with an integrated luminosity of 1 fb^{-1}.

Missing Transverse Energy

Large Missing transverse energy is a key part of the SUSY signature due to the escaping LSP, although real $\not\!\!E_{\rm T}$ from neutrinos or fake $\not\!\!E_{\rm T}$ from detector effects can contribute to Standard Model events to pass the SUSY selection cuts.

Figure 8.7 shows the distributions for the $\not\!\!E_{\rm T}$ after Cuts 1-2 are applied, showing also the values used to define Cuts 3 ($\not\!\!E_{\rm T}$>100 GeV). Note how this cut removes most of the $t\bar{t}$

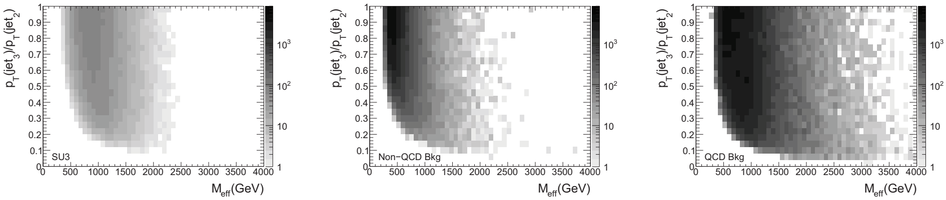

(a) $p_{\mathrm{T}}(\mathrm{jet}_2)/p_{\mathrm{T}}(\mathrm{jet}_2)$ and M_{eff} scatter plot

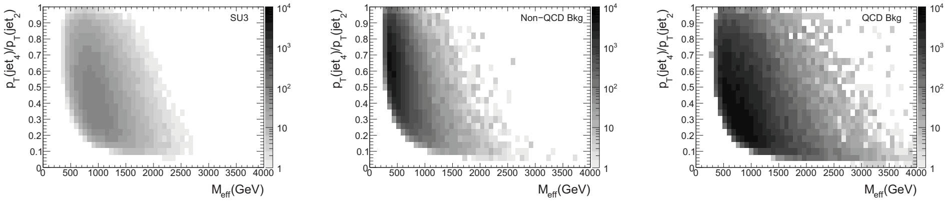

(b) $p_{\mathrm{T}}(\mathrm{jet}_4)/p_{\mathrm{T}}(\mathrm{jet}_2)$ and M_{eff} scatter plot

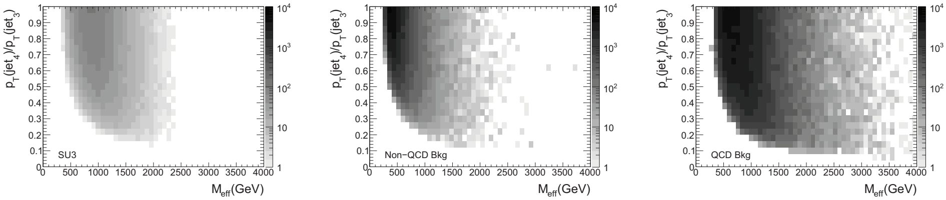

(c) $p_{\mathrm{T}}(\mathrm{jet}_4)/p_{\mathrm{T}}(\mathrm{jet}_3)$ and M_{eff} scatter plot

Figure 8.6: Distributions for the jet p_{T} ratios as a function of M_{eff} for SU3 SUSY signal (left), non-QCD background (center) and QCD background (right) for events passing Cuts 1-2. All the plots show number of events with an integrated luminosity of 1 fb^{-1}.

and, especially, the QCD background which are located in the very low $\not\!\!E_{\mathrm{T}}$ region. Note also how $\mathrm{t\bar{t}}$ becomes the most dominant background in the $\not\!\!E_{\mathrm{T}}>200$ GeV region, due to the presence of neutrinos coming from the W bosons in $\mathrm{t\bar{t}}$ decays.

Figure 8.7 also shows the $\not\!\!E_{\mathrm{T}}/M_{\mathrm{eff}}$ distributions precisely after Cuts 1-3 have been applied. This is the first time in the analysis cutflow where a clear signal excess can be seen, showing that the signal topology implies a much larger amount of $\not\!\!E_{\mathrm{T}}$ respect to the overall mass scale in the event than for Standard Model processes, which is a clear sing of a heavy non-interacting particle.

Note that the cut applied in this variable ($\not\!\!E_{\mathrm{T}}/M_{\mathrm{eff}}<0.2$) also reduces substantially the QCD background together with the $\mathrm{t\bar{t}}$. At $\not\!\!E_{\mathrm{T}}/M_{\mathrm{eff}}<0.05$, QCD is 2 orders of magnitude higher than the next background, even after the $\not\!\!E_{\mathrm{T}}>100$ GeV cut is applied. This implies that a non-negligible fraction of events has $\not\!\!E_{\mathrm{T}}$ >100 GeV in which it only represents a 5% of the event M_{eff}, that is, events with very energetic jets in which just jet reconstruction fluctuations of few percent lead a relevant amount of $\not\!\!E_{\mathrm{T}}$.

In the $0.15<\not\!\!E_{\mathrm{T}}/M_{\mathrm{eff}}<0.20$ region, QCD is still a factor of 3 higher than the next background and it also presents the quickest drop, with no events above $\not\!\!E_{\mathrm{T}}/M_{\mathrm{eff}}>0.4$, as expected for events where the $\not\!\!E_{\mathrm{T}}$ is coming form neutrinos within high energy jets and taking only a small fraction of the original parton momentum in the collision.

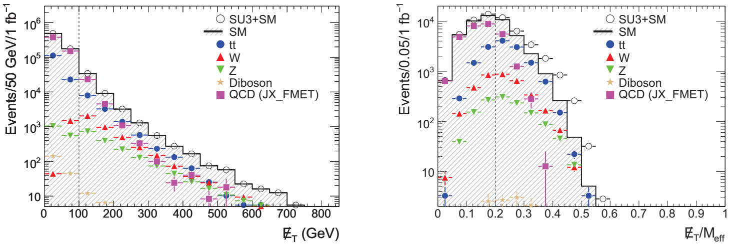

Figure 8.7: On the left, distributions of $\not\!\!E_{\mathrm{T}}$ after Cuts 1-2 for background and SU3 SUSY signal on top of the background with the QCD described by the JX_FMET samples. On the right the $\not\!\!E_{\mathrm{T}}/M_{\mathrm{eff}}$ distribution for events passing Cuts 1-3. Values used to define Cut 3 and 4 are shown with vertical lines.

Summing up, Cut 4 is very efficient in the rejection of QCD background, as well as other SM backgrounds with low energy neutrinos.

The power of these cuts in background rejection can also be seen when looking at the $\not\!\!E_{\mathrm{T}}$ as a function of M_{eff} after Cuts 1-2 (Figure 8.8). As shown, most of the QCD background is concentrated in the low-$\not\!\!E_{\mathrm{T}}$ region and most of the events with enough $\not\!\!E_{\mathrm{T}}$ to survive Cut 3 are at relatively high M_{eff}. In this case, clearly different topologies are found between signal and non-QCD background, although as mentioned before, an important fraction of the $\mathrm{t\bar{t}}$ is also removed with Cut 3.

Transverse Sphericity

Figure 8.9 show the transverse sphericity distributions after Cut 1 and after Cuts 1-4, with the values used to define Cut 5 shown. At the beginning of the analysis, the QCD background is enormous, and in the S_{T} distribution it is clearly peaked at S_{T}=0, with a quick drop as the sphericity increases. On the contrary, $\mathrm{t\bar{t}}$ background also decreases with S_{T} but in a much less abrupt way, with less than a factor 2 reduction for S_{T}=0.5, while QCD has been reduced by a factor of 20.

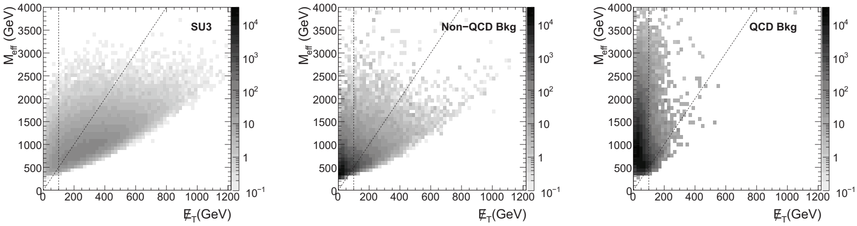

Figure 8.8: Distributions for the effective mass as a function of $\not{E}_\mathrm{T}$ for SU3 SUSY signal (left), non-QCD background (center) and QCD background (right) for events passing Cuts 1-2. All the plots show number of events with an integrated luminosity of 1 fb^{-1}

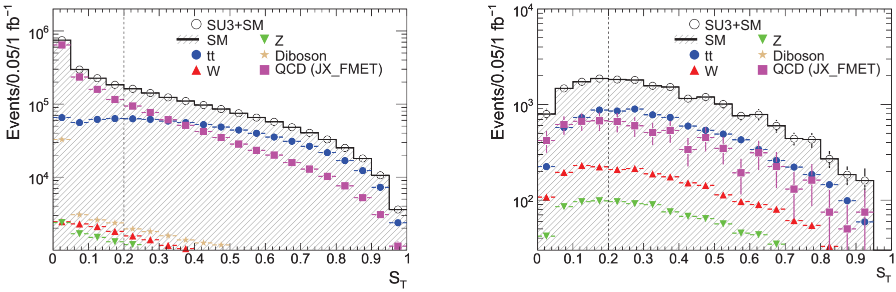

Figure 8.9: Distributions of S_T after Cut 1 (left) and after Cuts 1-4 (right) for background and SU3 SUSY signal on top of the background with the QCD described by the JX_FMET samples. The value used to define Cut 5 is shown with vertical lines in both cases.

Nevertheless, after all cuts described before, the QCD background has been strongly reduced, and it is even less important than the $\mathrm{t\bar{t}}$ background but in both cases the remaining events are concentrated at low S_T values. Although the S_T<0.2 cut would have been able to reduce the QCD in one order of magnitude at the beginning of the analysis, used here its effects is much smaller.

Figure 8.10 shows the normalized transverse sphericity distributions after Cut 1 and after Cuts 1-4 for the samples considered. Note that after Cut 1 the signal is also peaked at low-S_T values although not as strongly as the QCD background. After Cuts 1-4, signal and background distributions are almost identical and in consequence Cut 5 on S_T>0.2 turns out to be not efficient in discriminating signal from the background at this moment.

Figures 8.11 and 8.12 show the S_T as a function of $\not{E}_\mathrm{T}$ after Cuts 1-2 and Cuts 1-4 respectively for SUSY signal, QCD and non-QCD background. Regarding signal and non-QCD background, after Cuts 1-2 the tails towards highest $\not{E}_\mathrm{T}$ values are correlated to small

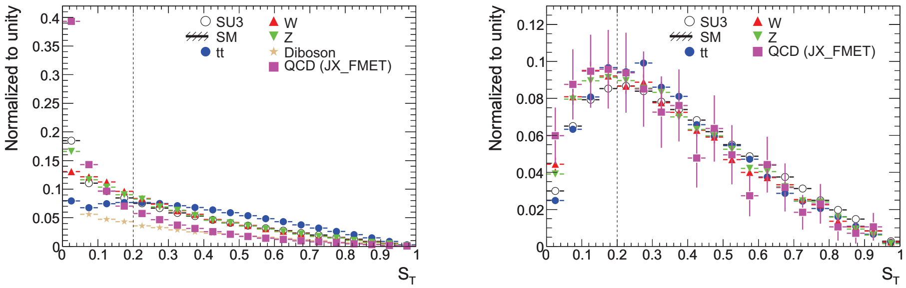

Figure 8.10: Normalized distributions of S_{T} after Cut 1 (left) and after Cuts 1-4 (right) for background and SU3 SUSY signal with the QCD described by the JX_FMET samples. The value used to define Cut 5 is shown with vertical lines in both cases.

S_{T} values, so the more energetic the escaping neutrino or LSP is, the less spherical the event is, as expected. Hence, this cut on S_{T} is selecting especially the events with real $\not{E}_{\mathrm{T}}$ where the amount of escaping energy is moderate.

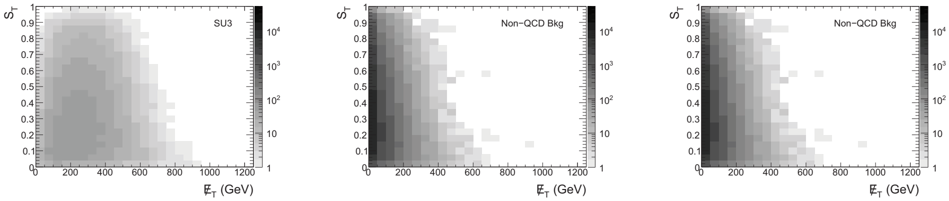

Figure 8.11: Distributions for the transverse sphericity as a function of $\not{E}_{\mathrm{T}}$ for SU3 SUSY signal (left), non-QCD background (center) and QCD background (right) for events passing Cuts 1-2. All the plots show number of events with an integrated luminosity of 1 fb^{-1}

Regarding QCD background, it is concentrated in the low-$\not{E}_{\mathrm{T}}$ region, as shown in Figure 8.9, with less evident correlation between S_{T} and $\not{E}_{\mathrm{T}}$. Later in the cut flow, once the cuts on $\not{E}_{\mathrm{T}}$ (Cut 3-4) have rejected most of the QCD background, still few high-$\not{E}_{\mathrm{T}}$ QCD events are also removed with the S_{T}>0.2 cut.

Angular Separation in the Transverse Plane ($\Delta\phi$)

Cuts on the separation in ϕ between the jets in the event and the $\not{E}_{\mathrm{T}}$ is used to reject QCD and other backgrounds characterized by fully hadronic decays. If all the sources of $\not{E}_{\mathrm{T}}$ are associated with jets, real $\not{E}_{\mathrm{T}}$ coming from neutrinos in the semileptonic decays inside the jet or simply jet misreconstruction, $\not{E}_{\mathrm{T}}$ can point in the same direction as the

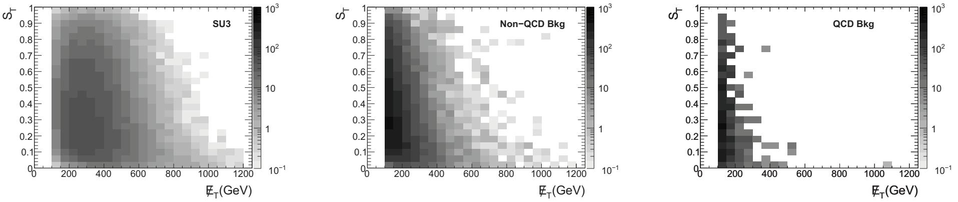

Figure 8.12: Distributions for the transverse sphericity as a function of $\not{E}_{\mathrm{T}}$ for SU3 SUSY signal (left), non-QCD background (center) and QCD background (right) for events passing Cuts 1-4. All the plots show number of events with an integrated luminosity of 1 fb^{-1}

jet (when neutrinos are produced or the jet energy is underestimated) or in the exactly opposite (when the jet energy is overestimated).

Figure 8.13 shows the $\Delta\phi$ distributions for the three leading jets after Cut 1 and after Cuts 1-5, with the values used to define Cut 6 shown. At the beginning of the analysis, for the three leading jets the QCD background is accumulated at $\Delta\phi(\mathrm{jet}_1)\approx0,\pi$ and $\Delta\phi(\mathrm{jet}_2, 3)\approx0$. The misreconstruction of the second and third jet is less important since they are less energetic their influence on the overall $\not{E}_{\mathrm{T}}$ is smaller and only the increase at $\Delta\phi(\mathrm{jet}_2, 3)\approx0$ is observed due to the neutrinos produced within jets. Note that since these distributions are obtained at the very beginning of the analysis, events with very small $\not{E}_{\mathrm{T}}$ are also included. Due to the dijet topology, the $\Delta\phi(\mathrm{jet}_1)$ and $\Delta\phi(\mathrm{jet}_2)$ are not independent (see below).

Regarding the other backgrounds, a flat distribution is seen for the second and third jets, but for the leading jet, they are accumulated at $\Delta\phi(\mathrm{jet}_1)\approx\pi$, but not at $\Delta\phi(\mathrm{jet}_1)\approx0$.

Once all the cuts already described are applied, the cut on $\Delta\phi$ is still able to remove a certain amount of the events at $\Delta\phi<0.2$, about 500 QCD background events for the leading jet and 100-200 for the next 2 jets for an integrated luminosity of 1 fb^{-1}. Furthermore, the effect in the other backgrounds is very small because they are either peaked at $\Delta\phi \approx \pi$ or with a flat distribution.

Figure 8.14 shows the $\Delta\phi(jet_i)$ as a function of $\Delta\phi(jet_j)$ for i, j=1,2,3 after Cuts 1-2, separately for signal, non-QCD and QCD background. At this moment in the analysis for signal samples most of the events have high values for $\Delta\phi(jet_1)$ or $\Delta\phi(jet_2)$ and that no event is seen in the region $\Delta\phi(jet_1)^2 + \Delta\phi(jet_2)^2<\pi/2$. Almost all the events are concentrated at $\Delta\phi(jet_1)>2$, specially at $\Delta\phi(jet_2)\approx0$ (with the $\not{E}_{\mathrm{T}}$ close to jet$_2$) or $\Delta\phi(jet_2)\approx\pi$ (with the two leading jets close in ϕ and opposite to the $\not{E}_{\mathrm{T}}$ direction). Note that the LSP produced in the SUSY decay is not aligned with the leading jet, and in an important fraction of cases is not aligned with the second jet either.

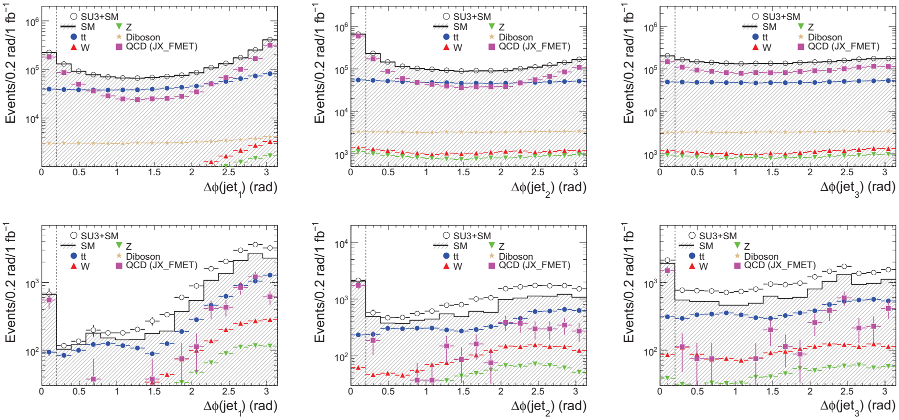

Figure 8.13: Distributions of $\Delta\phi$ between the $\not{E}_{\mathrm{T}}$ and the three leading jets after Cut 1 (top) and after Cuts 1-5 (bottom) for background and SU3 SUSY signal on top of the background with the QCD described by the JX_FMET samples. The value used to define Cut 6 is shown with vertical lines.

For the QCD background, a clear correlation is found and if $\Delta\phi(jet_1){\approx}0(\pi)$, then $\Delta\phi(jet_2){\approx}\pi(0)$, as a consequence of the dijet topology and the fact that the $\not{E}_{\mathrm{T}}$ in the event is introduced by the own jets. Note that the same structure is found for the correlation between jet$_1$ and jet$_3$, although less clear, which can be explained if this jet is close to jet$_2$.

For non-QCD background, the maximum in the distributions are found for the cases when $\not{E}_{\mathrm{T}}$ is also aligned with one of the leading jets, specially favoring the case of with $\Delta\phi(jet_1){\approx}0$, but the whole spectrum is populated.

Both for signal and background, much smaller correlations are found for $\Delta\phi(jet_2)$ and $\Delta\phi(jet_3)$, although for QCD the most populated regions correspond precisely to the cases when both jets are very close in ϕ: $\Delta\phi(jet_1){\approx}\Delta\phi(jet_2){\approx}0,\pi$.

Similarly, Figure 8.15 shows the $\Delta\phi(jet_i)$ as a function of $\Delta\phi(jet_j)$ for $i, j = 1, 2, 3$ after Cuts 1-5, separately for signal, non-QCD and QCD background.

In this case, most of the QCD background is already removed by the previous cuts but the remaining events correspond either to the region with $\Delta\phi(\mathrm{jet}_1(2)){\approx}\Delta\phi(\mathrm{jet}_2(3)){\approx}\pi$ or with $\Delta\phi(jet_i){\approx}0$ and $\Delta\phi(jet_j){\approx}\pi$. This latter kind of events are the ones rejected by Cut 6. Hence this cut provides an important reduction of the remaining QCD background.

The non-QCD background as well as the signal is concentrated at high values of $\Delta\phi(\mathrm{jet}_{1,2})$, with the small values completely unpopulated.

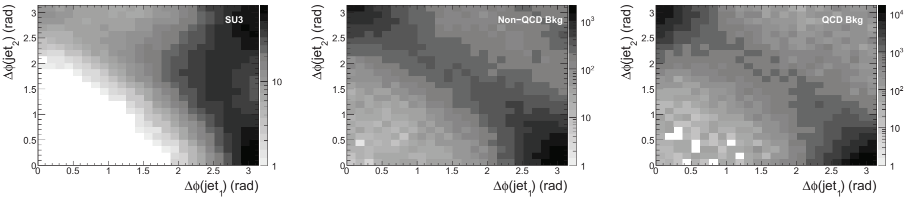

(a) $\Delta\phi(jet_2)$ and $\Delta\phi(jet_1)$ scatter plot

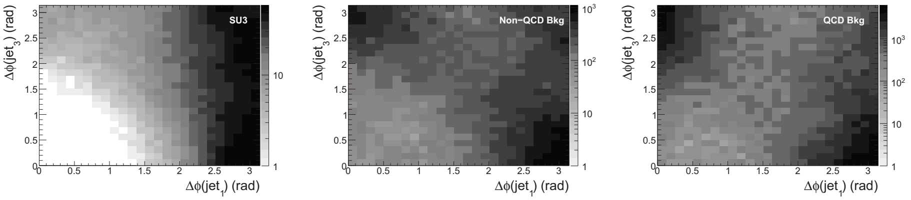

(b) $\Delta\phi(jet_3)$ and $\Delta\phi(jet_1)$ scatter plot

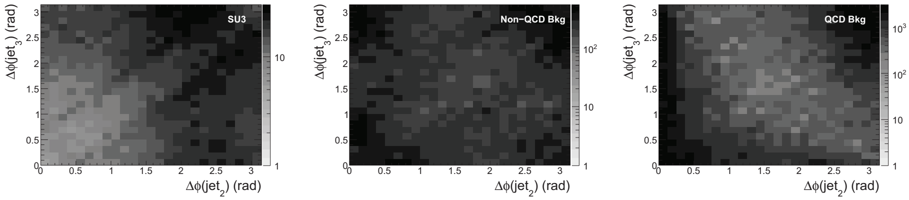

(c) $\Delta\phi(jet_3)$ and $\Delta\phi(jet_2)$ scatter plot

Figure 8.14: Correlation between the angular separation in ϕ between the $\not{E}_{\mathrm{T}}$ and the tree leading jets for SU3 SUSY signal (left), non-QCD background (center) and QCD background (right) for events passing Cuts 1-2. All the plots show number of events with an integrated luminosity of 1 fb^{-1}.

QCD Fake Missing Transverse Energy Cuts

As shown in the previous Chapters, some variables related with energy reconstruction based on large depositions in some parts of the calorimeter system are strongly correlated with jet leakage to the Muon Spectrometer or bad jet reconstruction, which can lead to large $\not{E}_{\mathrm{T}}^{\mathrm{Fake}}$. Cuts are applied in the selected calorimeter variables as described in Table 7.3.1 as well as a cut on $\not{E}_{\mathrm{T}} - \not{E}_{\mathrm{T}}^{\mathrm{Trk}} < -50$ GeV.

In order to evaluate the impact of these cuts, they have been applied at two different stages of the analysis: after Cuts1-3 (requiring only four jets and large $\not{E}_{\mathrm{T}}$) and after Cuts 1-7 (all the cuts already explained). Table 8.1 shows the cut flow table for SU3 signal and multi-jet background samples. As shown in the table, after Cuts 1-3 up to 60-80% of the

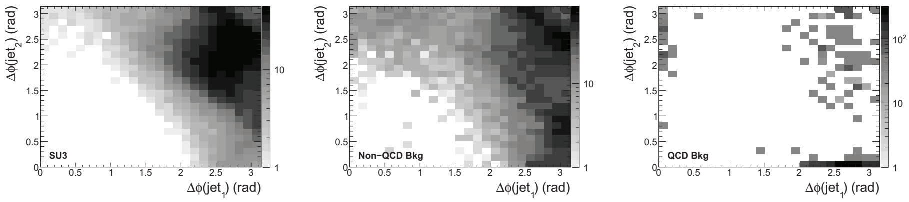

(a) $\Delta\phi(jet_2)$ and $\Delta\phi(jet_1)$ scatter plot

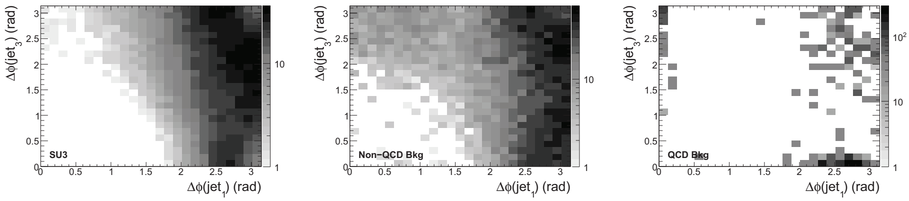

(b) $\Delta\phi(jet_2)$ and $\Delta\phi(jet_1)$ scatter plot

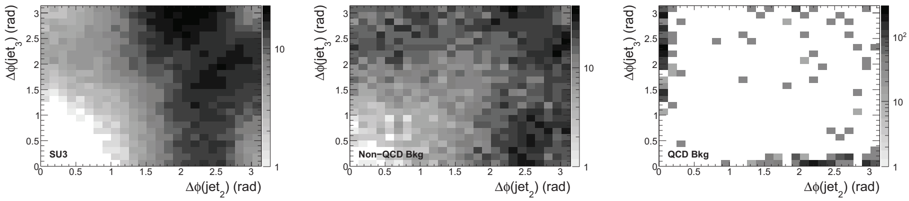

(c) $\Delta\phi(jet_2)$ and $\Delta\phi(jet_1)$ scatter plot

Figure 8.15: Correlation between the angular separation in ϕ between the $\not\!\!E_{\mathrm{T}}$ and the tree leading jets for SU3 SUSY signal (left), non-QCD background (center) and QCD background (right) for events passing Cuts 1-5. All the plots show number of events with an integrated luminosity of 1 fb^{-1}.

contribution from the QCD background can be removed by Cut 8, rejecting as well only $\sim$20% of the remaining signal events after the selection cuts.

After Cuts 1-7, the QCD cleaning cuts proposed are still able to remove a considerable part of this background. For instance in the JX_4J case, only one event in the Monte Carlo sample is removed due to jet misreconstruction but it has M_{eff} $\sim$3.5 TeV. Indeed, looking in detail at the event discarded in the J4_4J sample, it has $\not\!\!E_{\mathrm{T}}^{\mathrm{Fake}}$ = 980 GeV, while the other 3 events in that sample have large real $\not\!\!E_{\mathrm{T}}$ ($\not\!\!E_{\mathrm{T}}^{\mathrm{truth}}$> 300 GeV). For the J4_4J and J5_4J sample, no event is cut, but only 10 out of 20 have $\not\!\!E_{\mathrm{T}}^{\mathrm{Fake}} > 50$ GeV. In the case of the JX_CBNT samples, only the 2 events which are affected by large $\not\!\!E_{\mathrm{T}}^{\mathrm{Fake}}$ in the J6_CBNT and J7_CBNT are removed.

Hence, although the effect introduced by the QCD cleaning cut is not so important after the rest of the analysis selection is already applied, it is a good method to reject QCD background as most of the remaining QCD events dominated by $\not\!\!E_{\mathrm{T}}^{\mathrm{Fake}}$ are removed. Furthermore, the detector effect leading to $\not\!\!E_{\mathrm{T}}^{\mathrm{Fake}}$ in the Monte Carlo are probably underestimated and these effect can be much larger in real data.

Table 8.1: Cut flow table for selection and cleaning cuts proposed in the text expressed in number of events in the Monte Carlo samples and the corresponding cross section.

		Total	Cuts 1-3	Cuts 1-3 + Cut 8	Cuts 1-7	Cuts 1-8
SIGNAL SAMPLE						
SU3	N_{events}	492150	170784	132208	76687	63490
	σ (pb)	27.68	9.605	7.436	4.313	3.571
QCD OFFICIAL UNFILTERED SAMPLES						
J5_CBNT	N_{events}	120900	164	113	7	6
	σ (pb)	1.25×10^4	16.96	11.68	0.7237	0.6203
J6_CBNT	N_{events}	97750	1140	581	5	4
	σ (pb)	3.44	0.04012	0.02045	0.0176	0.01408
J7_CBNT	N_{events}	213200	16097	5083	1	0
	σ (pb)	5.71	0.4311	0.1361	2.5×10^{-5}	0
QCD PRIVATE FILTERED SAMPLES: 4 JETS						
J4_4J	N_{events}	973275	311	255	20	20
	σ (pb)	2.803×10^4	8.956	7.343	0.576	0.576
J5_4J	N_{events}	197360	733	539	5	5
	σ (pb)	3500	13	9.559	0.0887	0.0887
J6_4J	N_{events}	176019	5825	2908	4	3
	σ (pb)	126	4.17	2.082	0.00286	0.00215

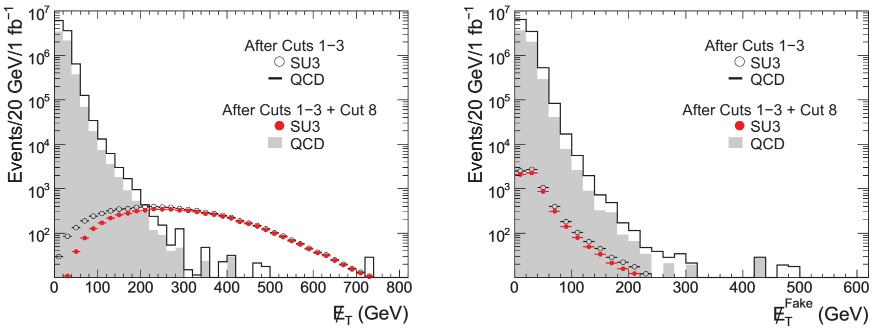

Figure 8.16: Comparison of $\not\!\!E_{\mathrm{T}}$ (left) and fake $\not\!\!E_{\mathrm{T}}$ (right) before and after QCD cleaning cuts for SU3 and QCD background from the JX_4J samples.

Figure 8.16 shows the $\not{E}_{\mathrm{T}}$ and $\not{E}_{\mathrm{T}}^{\mathrm{Fake}}$ distributions normalized to a luminosity of 1 fb^{-1}for signal and QCD background after Cuts 1-3 and also including the QCD cleaning cuts. The JX_4J samples were used in this case as they provide the largest statistics. The QCD cleaning cuts produce small effect on the signal and most of the rejected events have low $\not{E}_{\mathrm{T}}$, where the influence of detector effects is more important. Regarding QCD background, more events are removed as $\not{E}_{\mathrm{T}}^{\mathrm{Fake}}$ increases and most of the events with $\not{E}_{\mathrm{T}}^{\mathrm{Fake}} >$ 250 GeV are removed with the cuts proposed.

8.2.2 Analysis Cut Flow

Table 8.2 shows the cut flow for signal, non-QCD and QCD background. In the case of the QCD background, the 3 sets of samples with different MC filters (JX_FMET, JX_CBNT and JX_4J) are shown with the details on the individual jet p_{T} samples. Figure 8.17 shows the evolution of the M_{eff} distribution after each cut is applied for an integrated luminosity of 1 fb^{-1}. As shown, most of the background rejection is due to the first four cuts, although the rest of the cuts also contributes to improve the signal-to-background ratio.

Figure 8.18 shows the M_{eff} distributions after Cuts 1-7 and Cuts 1-8 using the 3 sets of the QCD background samples available. All the QCD points are affected by large errors bars as a combination of the large sample cross section and the reduced statistics available. No significant discrepancy is found between them, leading to the conclusion that the samples used are equally valid to represent the QCD background. The enhancement in the statistics provided by working with 3 sets of QCD samples and the possibility to combine MC data with different filters was very useful for QCD cleaning cut optimization.

Regarding the different SUSY signals used in this analysis, Figure 8.19 shows the M_{eff} distributions after Cuts 1-8 for an integrated luminosity of 1 fb^{-1} using the 6 SUSY signal points available and all SM backgrounds, using JX_4J samples for the QCD background. There are huge differences between the different signal points with a very small excess of signal events for the case of SU2 and much larger signal for SU4.

8.2.3 Significance Estimation

To properly compute the signal significance the background systematic uncertainty in the should be known first. With an integrated luminosity of 1 fb^{-1}, the approximate uncertainty for QCD background is estimated to be a 50%, while for the non-QCD SM background it is 20% [53].

Table 8.2: Cross section (in pb) cut flow table for selection and cleaning cuts proposed in the text.

Sample	All Events	Cuts 1-2	Cuts 1-4	Cuts 1-6	Cuts 1-7	Cuts 1-8
SU1	10.86	3.701	2.855	1.907	1.401	1.159
SU2	7.18	0.7467	0.3691	0.2787	0.1695	0.1423
SU3	27.68	10.56	7.568	5.28	4.313	3.571
SU4	402.2	121.2	57.8	42.41	34.97	29.84
SU6	6.07	2.696	2.063	1.383	1.08	0.8922
SU8_1	8.7	3.308	2.54	1.686	1.448	1.204
Non-QCD Bkg	923.2	158.6	12.46	8.078	5.87	4.96
Top	833	149.7	9.043	5.964	4.095	3.452
W	19.2	5.391	2.334	1.426	1.109	0.9305
Z	15.09	3.265	1.072	0.679	0.6632	0.5747
Diboson	55.95	0.21	0.016	0.0092	0.0035	0.0027
QCD_FMET	1644	560	7.049	0.8483	0.8483	0.6612
J4_FMET	917.4	202.7	5.99	0.824	0.824	0.637
J5_FMET	655	316	0.990	0.0254	0.0254	0.0254
J6_FMET	67.57	40.25	0.07419	0	0	0
J7_FMET	5.3	1.392	0.00151	0	0	0
J8_FMET	0.022	0.004845	1.55×10^{-5}	5.18×10^{-6}	5.18×10^{-6}	0
QCD_CBNT	3.29×10^{5}	2.36×10^{4}	1.712	0.741	0.741	0.634
J4_CBNT	3.16×10^{5}	2.11×10^{4}	0	0	0	0
J5_CBNT	1.25×10^{4}	2388	1.654	0.7237	0.7237	0.6203
J6_CBNT	344	101.4	0.05631	0.0176	0.0176	0.0141
J7_CBNT	5.3	1.66	0.0013	2.49×10^{-5}	2.49×10^{-5}	0
QCD_4J	3.17×10^{4}	1.05×10^{4}	4.018	0.714	0.668	0.667
J4_4J	2.80×10^{4}	8549	2.765	0.6047	0.576	0.576
J5_4J	3500	1837	1.206	0.106	0.089	0.089
J6_4J	126	81.52	0.048	0.0029	0.0029	0.0021

The discovery significance estimation has been evaluated using several approaches. The statistical discovery significance is simply computed as $S/\sqrt{B}$, but more appropriate definitions of the significance which include the systematic uncertainties in the background can also be used. The simplest is $S/\sqrt{B+\sigma_{syst}^2}$, but more sophisticated significance definitions are used in ATLAS SUSY searches with a Bayesian-frequentist mixed approach [54, 55].

In this approach, uncertainties on the background are incorporated in the significance by convoluting the Poisson probability that the background fluctuates to the observed signal with a Gaussian background probability density function with mean N_{b} and standard deviation δN_{b}.

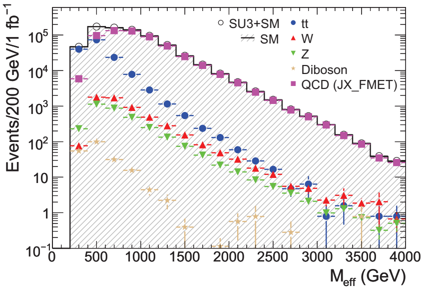

(a) After Cuts 1-2 ($N_{jet} \geq 4$)

(b) After Cuts 1-3 ($\not{E}_{\mathrm{T}} \geq$100 GeV)

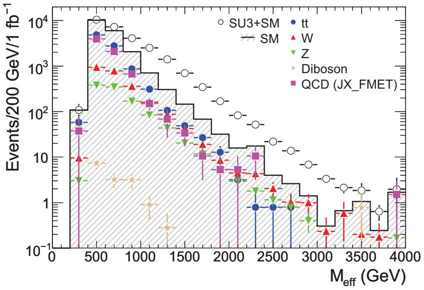

(c) After Cuts 1-4 ($\not{E}_{\mathrm{T}} \geq 0.2 M_{\mathrm{eff}}$)

(d) After Cuts 1-5 ($S_{\mathrm{T}} > 0.2$)

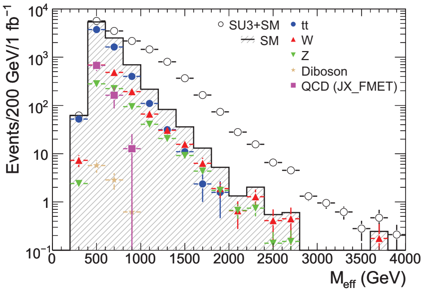

(e) After Cuts 1-6 ($\Delta\phi(jets - \not{E}_{\mathrm{T}}) \geq 0.2$)

(f) After Cuts 1-7 (No isolated lepton)

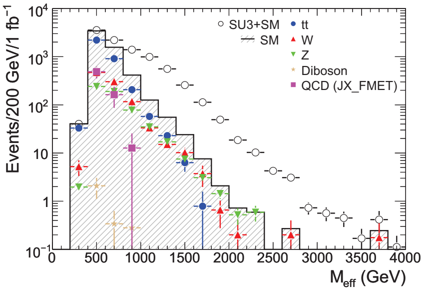

(g) After Cuts 1-8 (QCD cleaning)

(h) After $M_{\mathrm{eff}} \geq$800 GeV

Figure 8.17: Distribution of the M_{eff} after each of the selection cuts for background and SU3 SUSY signal on top of the background with the QCD described by the JX_FMET samples.

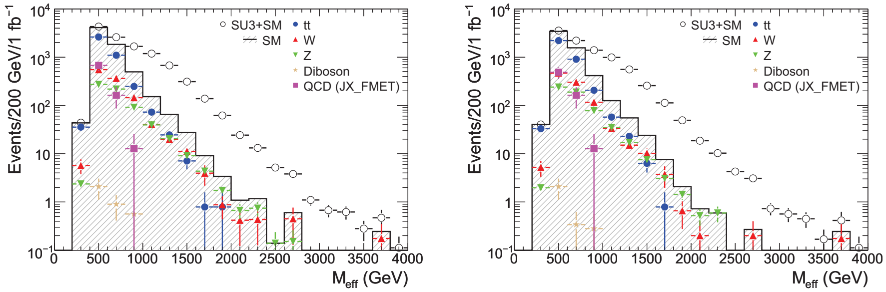

(a) After Cuts 1-7 (JX_FMET samples)

(b) After Cuts 1-8 (JX_FMET samples)

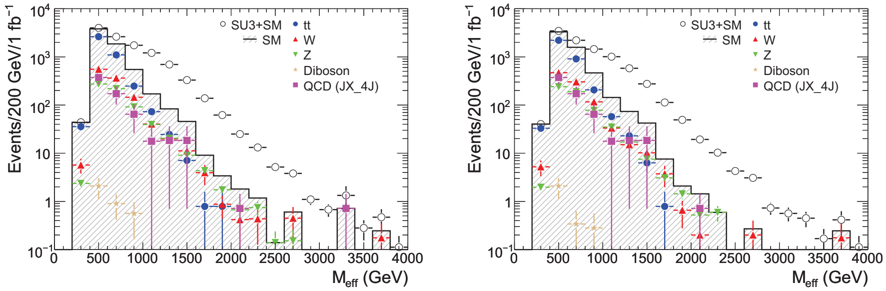

(c) After Cuts 1-7 (JX_CBNT samples)

(d) After Cuts 1-8 (JX_CBNT samples)

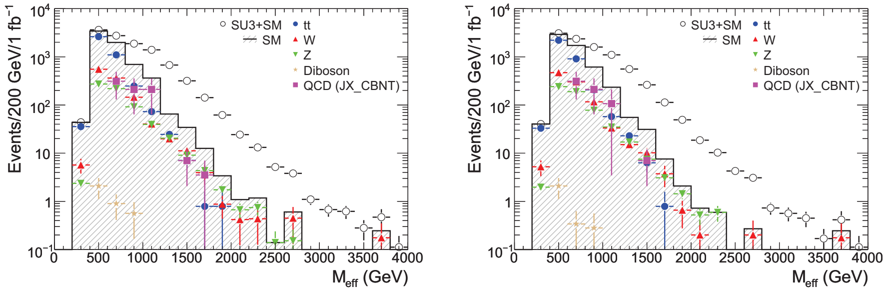

(e) After Cuts 1-7 (JX_4J samples)

(f) After Cuts 1-8 (JX_4J samples)

Figure 8.18: M_{eff} distributions for background and SUSY SU3 signal on top of the background with the QCD described by JX_FMET, JX_CBNT and JX_4J samples before and after Cut 8 is applied.

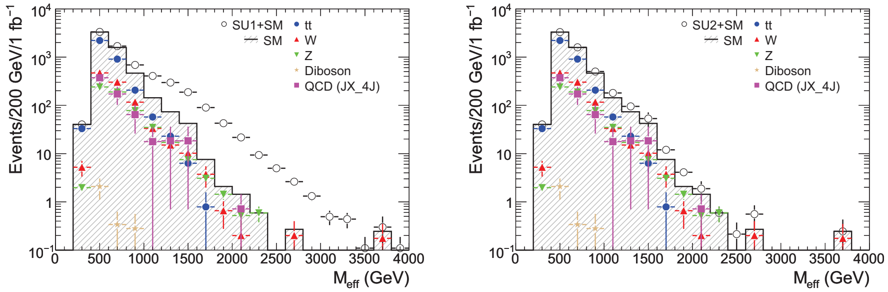

(a) SU1 (b) SU2

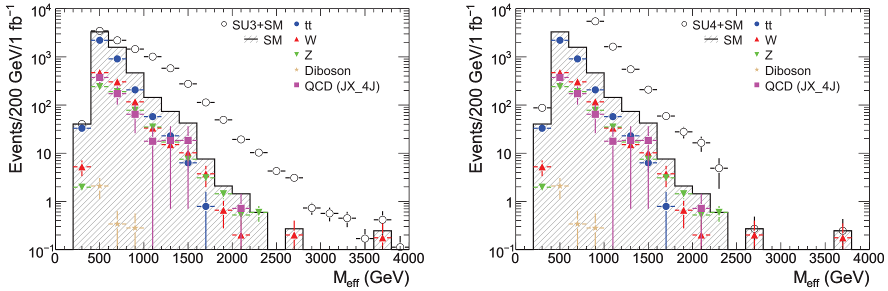

(c) SU3 (d) SU4

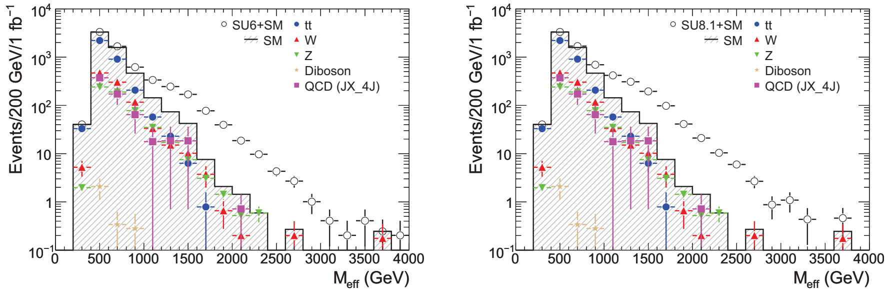

(e) SU6 (f) SU8.1

Figure 8.19: M_{eff} distributions for background and SUSY signal on top of the background for several SUSY points with the QCD described by the JX_4J samples after Cuts 1-8 are applied.

Given these assumptions, the probability p that the background fluctuates by chance to the measured value $N_{\rm data}$ or above is given by

$$p = A \int_0^\infty db\; G(b; N_{\rm b}, \delta N_{\rm b}) \sum_{i=N_{\rm data}}^{\infty} \frac{e^{-b} b^i}{i!}\,, \tag{8.1}$$

where $G(b; N_b, \delta N_{\rm b})$ is a Gaussian and the factor

$$A = \left[\int\limits_0^\infty db\; G(b; N_b, \delta N_b) \sum_{i=0}^{\infty} e^{-b} b^i / i! \right]^{-1} \tag{8.2}$$

ensures that the function is normalised to unity. If the Gaussian probability density function G is replaced by a Dirac delta function $\delta(b - N_b)$, the estimator p results in a usual Poisson probability.

The probability p is transformed into "standard-deviations", denoted in this note by the symbol Z_n, using the formula

$$Z_n = \sqrt{2}\,{\rm erf}^{-1}(1 - 2{\rm p}). \tag{8.3}$$

Table 8.3 shows the evolution of the significance during the event selection for SU3 signal sample and for the three sets of QCD background samples. Up to Cut 7 Z_n always increases as the cuts are being applied. Note that $S/\sqrt{B}$ decreases after Cut 5 is applied due to the fact that at that stage of the analysis this variable does not provide good signal discrimination from the background (see Section 8.2.1).

Table 8.3: Significance as a function of the cuts applied for SU3 sample for an integrated luminosity of 1 fb^{-1}. All 3 set of samples for the QCD background are shown.

		Cut 3	Cut 4	Cut 5	Cut 6	Cut 7	Cut 8	$M_{\rm eff}$>800 GeV
$S/\sqrt{B}$	FMET	43.41	54.06	47.82	55.68	52.49	47.51	110.3
	CBNT	39.01	63.37	56.27	56.01	52.91	47.62	111.4
	4J	44.96	58.79	51.64	56.1	53.21	47.49	111.4
$S/\sqrt{B+\sigma^2_{syst}}$	FMET	0.5157	1.254	1.351	2.569	2.684	2.684	20.91
	CBNT	0.3926	2.246	2.499	2.637	2.776	2.712	21.94
	4J	0.5661	1.674	1.768	2.655	2.844	2.679	21.94
Z_n	FMET	0.5119	1.253	1.35	2.567	2.682	2.681	12.59
	CBNT	0.3864	2.246	2.499	2.636	2.774	2.709	13.14
	4J	0.563	1.673	1.767	2.653	2.841	2.676	13.14

On the contrary, the significance does not increase for Cut 8, although the decrease is not significant either. Nevertheless, as mentioned above, the QCD cleaning cuts proposed should be considered as quality cuts which improves the purity of the final event sample ensuring a better rejection of events which meet the selection criteria due to QCD events with large $\not{E}_{\mathrm{T}}^{\mathrm{Fake}}$.

An additional cut on M_{eff} is applied on top of the selection to remove the small mass region, which has a big improvement in the significance. This way, very small significances (in the two versions which take into account the background uncertainty) can be improved and make a 2.6 significance increase to a value of 20.

Table 8.4: Significances for all the SUSY signals considered after two 2 final cuts. QCD background is represented by JX_FMET samples.

	Cuts 1-8			M_{eff}>800 GeV		
	$S/\sqrt{B}$	$S/\sqrt{B+\sigma_{syst}^2}$	Z_n	$S/\sqrt{B}$	$S/\sqrt{B+\sigma_{syst}^2}$	Z_n
SU1	15.42	0.8709	0.8707	40.44	7.668	7.701
SU2	1.893	0.107	0.1072	4.386	0.8318	0.8272
SU3	47.51	2.684	2.681	110.3	20.91	12.59
SU4	397	22.43	12.79	286.8	54.38	24.05
SU5	11.87	0.6707	0.6708	31.31	5.937	5.819
SU8.1	16.02	0.9051	0.9045	42.39	8.04	8.292

Finally, Table 8.4 shows the significances which can be obtained for all the signal samples available in the 3 definitions considered for an integrated luminosity of 1 fb^{-1}. It shows that a discovery could be achieved at that luminosity for all signal points except SU2.

8.3 Conclusions

This Chapter shows the inclusive SUSY analysis in ATLAS with a fully hadronic signature requiring no leptons and at least four jets in the event. The event selection includes cuts on the jet multiplicity and p_{T}, $\not{E}_{\mathrm{T}}$, transverse sphericity, angular separation between jets and $\not{E}_{\mathrm{T}}$, a lepton veto and QCD cleaning cuts for $\not{E}_{\mathrm{T}}^{\mathrm{Fake}}$. With an integrated luminosity of 1 fb^{-1}, more than 5σ discovery significances are obtained for all the SUSY points considered except SU2.

In particular, the QCD cleaning cuts based on the calorimeter energy are meant to detect events with problems in jet containment or reconstruction leading to high $\not{E}_{\mathrm{T}}^{\mathrm{Fake}}$. At early stages in the analysis these cuts can remove up to 60-80% of the QCD background while rejecting only 20% of the signal, with very good performance in the high-$\not{E}_{\mathrm{T}}^{\mathrm{Fake}}$ region. If they are used at the end of the event selection they provide slightly smaller discovery significances, but their effect in the QCD background rejection makes them worth being included in the analysis to increase the purity in the final signal obtained. Nevertheless high significances are obtained for all the signal points considered in the note.

Finally, note that the studies carried on here with Monte Carlo should be validated when ATLAS operation starts because large discrepancies would probably appear between real data and the current detector simulation. It is not unlikely that the QCD or other samples are underestimated by large factors. Therefore, quality cuts like the QCD cleaning used here which may not be significantly improving the results in the Monte Carlo available can play an important role in background rejection in the real ATLAS environment.

Chapter 9

Conclusions

"I have made this [letter] longer, because I have not had the time to make it shorter."
— Blaise Pascal, *Lettres provinciales*, letter 16, 1657

This thesis can be divided in two main parts, both focused on the calorimetry for the ATLAS experiment: the first one about the energy reconstruction in the Tile Calorimeter and the second about fake $\not{E}_{\mathrm{T}}$ cleaning methods for QCD rejection.

The Optimal Filtering (OF) algorithm is presented in the Chapters dedicated to the TileCal energy reconstruction (Chapters 4 and 5). Other algorithms are currently available for this task, like the Fit method (meant to handle data with unknown phase, e.g. cosmics) or ManyAmps (meant for data affected by minimum bias pileup). Nevertheless, OF by means of iterations can reconstruct non-synchronized data with a 1‰ agreement with the dedicated Fit method. And without iterations and under the only assumption of small time (but no necessarily fixed to zero), OF shows a reduced sensitivity to the presence of minimum bias pileup. In this environment, OF provides good reconstruction not only for amplitude, but also for timing, the main lack of the ManyAmps method.

The current results from simulated data at low luminosity show that minimum bias is actually having a small impact on TileCal data reconstruction and therefore calorimeter resolution and response are almost unaffected at this luminosity (except for Fit method). Nevertheless, the impact estimated with Monte Carlo can gauge with real data and energy reconstruction should be able to handle as good as possible this physics source of noise.

As shown all through this part, OF is a method which combines a good performance on unknown phase data with electronics noise and also on synchronized data even in the case of minimum bias pileup. Therefore, OF is currently the only method used by default to reconstruct TileCal simulated data on ATLAS Monte Carlo productions and it is used together with Fit for cosmics data reconstruction. Furthermore, due to its good offline performance shown here and its simplicity in the mathematical formulation, OF has also been implemented in the Read-Out Drivers for online purposes.

Chapters 7 and 8 are devoted to the study of the cleaning for fake $\not{E}_{\mathrm{T}}$ from QCD events and its application to SUSY searches present a method which is sensible to the main detector effects leading to fake $\not{E}_{\mathrm{T}}$ in events with multiple jets. Some variables which can be measured with real data have been considered because they are either related with jet leakage towards the muon spectrometer (such as large depositions in the outermost layers of the calorimeter system) or with huge part of the jet energy deposited in dead materials. In both cases, the jet misreconstruction by detector effects induces high $\not{E}_{\mathrm{T}}$ which can increase the background of New Physics searches with large $\not{E}_{\mathrm{T}}$, for instance Supersymmetry.

These cuts have been used in the inclusive SUSY discovery analysis with 4 jet and no lepton in the final state. Since this is a fully hadronic topology, the effects of fake $\not{E}_{\mathrm{T}}$ can be specially important in this case. The standard event selection is capable of removing most of the backgrounds in the analysis but the usage of the QCD cleaning method proposed here improves the situation due to its good removal capability for fake $\not{E}_{\mathrm{T}}$ events from QCD. A discovery is feasible in ATLAS for this signal in most of the parameter space points considered, although the impact of the QCD cleaning cuts on the overall significance is very small.

Nevertheless, as in the case of minimum bias, the results obtained with Monte Carlo should be validated with real data and the detector effects which induce fake $\not{E}_{\mathrm{T}}$ from QCD should are likely to be much more important in real ATLAS running. Therefore, this cleaning cuts can be a very useful tool to ensure a good purity of signal in the events accepted by this kind of discovery analysis.

Chapter 10

Resum

“Sóc optimista per temperament i per tàctica, puix que crec que el pessimisme només torna realitat quan hom no fa res.”
— M. Sanchis Guarner, *Lletres de resistència*, 1946

10.1 CERN, LHC i ATLAS

CERN és en l’actualitat el major centre d’investigació de Física de Partícules del món. Aquesta institució, fundada en 1954, està formada per 20 Estats Membres Europeus, però gran quantitat de països no europeus també participen de diverses maneres en les seves activitats. Dóna treball a 3000 persones i vora 6500 científics visitants (provinents de 500 universitats i centres d’investigació de més de 80 nacions) acudixen al CERN per a la seva tasca investigadora. A més de físics, la plantilla del CERN inclou enginyers altament especialitzats, tècnics, dissenyadors, etc.

El complexe d’acceleradors del CERN es culmina amb la construcció del Gran Col·lisonador d’Hadrons (*Large Hadron Collider*, LHC) [1]. LHC és un accelerador superconductor de 2 anells instal·lat en el túnel de LEP (de 27 km de longitud), dedicat al descobriment del bosó de Higgs i a l’estudi d’altres successos de Nova Física amb una energia de col·lisió en centre de masses de fins a 14 TeV.

LHC té 2 experiments de propòsit general: ATLAS [2] i CMS [3], dissenyats per a una lluminositat màxima de 10^{34} cm^{-2}s^{-1}. A més, LHC compta amb altres 3 experiments per a lluminositats més baixes : LHCb [4] per a l’estudi de la física del quark b a una lluminositat de 10^{32} cm^{-2}s^{-1}, TOTEM [5] per a la detecció de protons de dispersió elàstica a angles menuts dissenyat per a una lluminositat de 2×10^{29} cm^{-2}s^{-1} i LHCf [6] per a la mesura dels pions neutres produïts en direcció frontal a una lluminositat de 2×10^{28} $\text{cm}^{-2}\text{s}^{-1}$. A més de feixos de protons, LHC també s'operarà amb feixos de ions de plom i l'experiment ALICE [7] està dissenyat per a explorar la física de ions pesats a una lluminositat de 10^{27} $\text{cm}^{-2}\text{s}^{-1}$.

ATLAS (*A Toroidal LHC ApparatuS*) és un espectròmetre protó-protó de propòsit general dissenyat per a explorar tot el potencial de descobriment de l'LHC. Inclou una calorimetria electromagnètica que usa argó líquid (LAr) i de gran qualitat (per a la identificació i mesura d'electrons i fotons), una calorimetria hadrònica de cobertura total (per a mesurar amb precisió jets i la falta d'energia transversa), un sistema de mesura de muons d'altra precisió i un detector de traces de gran eficiència.

Dintre de la calorimetria hadrònica, el Calorímetre Hadrònic de Teules (*Tile Calorimeter*, TileCal) és un calorímetre de mostreig fet d'acer i teules de plàstic centelleador. La llum produïda per les partícules que creuen el medi actiu es convertix en llum i es dirigix a tubs fotomultiplicadors (PMTs), on es converteix en senyals elèctrics. L'estructura de lectura de TileCal es segmenta en cel·les, les quals s'agrupen en torres projectives en η o en 3 capes longitudinals (A, BC i D).

Una vegada es processen els senyals dels PMTs en l'electrònica frontal, l'amplitud dels polsos analògics és proporcional a l'energia dipositada per les partícules en el calorímetre. Aquestos polsos es digitalitzen en n intervals de 25 ns (amb n =7 per a presa de dades de Física) i s'envien a l'electrònica de *back-end* del detector. Per tant, l'única informació disponible de l'energia depositada per les partícules en el calorímetre són les mostres digitals S_i amb $i = 1, \ldots, n$, el valor de les quals es pot expressar com:

$$S_i = Ag(t_i - t) + ped, \tag{10.1}$$

on A és l'amplitud del pols, t_i és el temps en el qual es pren la mostra i, ped és el pedestal i el temps t és la diferència temporal entre la mostra major i el pic del pols.

10.2 Implementació, Validació de l'Algorisme de Filtrat Òptim

10.2.1 Mètodes de Reconstrucció d'Energia

Per a obtindre a partir de les mostres digitals arreplegades l'energia dipositada per les partícules junt amb el seu temps d'arribada, estimació de la qualitat de la reconstrucció, etc. s'han desenvolupat diversos mètodes de reconstrucció dins de la col·laboració TileCal:

Mètode d'Ajust del Pols (Fit)

Aquest mètode aprofita que es coneix la forma del pols per a mesurar el temps d'arribada i reduïr la contribució del soroll electrònic a la mesura de la energia. Està basat en un ajust a la funció de l'Eq. (10.1) amb 3 parametres lliures: amplitud, temps i pedestal. L'expressió a minimitzar és la següent:

$$\chi^2 = \sum_{i=1}^{n} \left(\frac{S_i - [Ag(t_i) - Atg'(t_i) + ped]}{\sigma_i} \right)^2 \tag{10.2}$$

on σ_i és l'error de la mostra i, amb valors típics d'1.5 comptes d'ADC per a alta ganància i 0.6 comptes d'ADC per a baixa ganància. L'Equació (10.2) usa una aproximació de primer ordre de l'Eq. (10.1):

$$S_i = Ag(t_i - t) + ped \approx Ag(t_i) - Atg'(t_i) + ped. \tag{10.3}$$

Per a successos compatibles amb pedestal (senyals menuts) i per a no introduir cap biaix cap a energies positives, també es realitza un ajust a 2 paràmetres (amplitud i pedestal) fixant el temps en 0 ns. La decisió sobre quin ajust és més apropiat, el de 2 o 3 paràmetres, es pren tenint en compte quin cas dona un valor menor del χ^2.

Aquest mètode s'ha empleat per defecte en dades de feix de proba i posta a punt del detector amb còsmics, tant per a dades reals com simulades.

Mètode de Múltiples Amplituds (ManyAmps)

Aquest mètode està basat en un ajust a múltiples amplituds per a processar els casos afectats per l'apilament de successos de *minimum bias* (MB). Comença per ajustar un amplitud en la mostra central (la que correspon a la interacció que ha donat el trigger) i a diverses amplituds auxiliars a t=$\pm$25, $\pm$50, $\pm$75,... ns (representant les amplituds d'interaccions de *minimum bias* en els encreuaments de feixos adjacents). Es realitzen ajustos a aquestes múltiples amplituds i un pedestal comú amb tots els temps fixos. El resultat final de la reconstrucció només incou l'amplitud central i en conseqüència t=0 ns sempre, ignorant la resta d'amplituds usades durant el procés d'ajust.

Aquest mètode s'ha usat per defecte per a dades simulades en ATLAS amb o sense apilament per *minimum bias* però la seva major limitació és la falta d'informació temporal.

Filtrat Òptim (OF)

El mètode de Filtrat Òptim fa ús de combinacions lineals de les mostres digitals per a obtindre l'amplitud del pols. Els coeficients d'aquestes combinacions, coneguts com a pesos d'OF, es trien de manera que la contribució del soroll a la resolució del calorímetre siga mínima. S'ha empleat OF per a la reconstrucció de dades durant els passats períodes de feix de proba [29] i degut a la seva simplicitat en la formulació matemàtica s'ha implementat OF dins dels Procesadors Digitals de Senyal (DSPs) dels *Read-Out Drivers* (RODs) [15] per a la reconstrucció de l'energia online [30].

La versió de l'algorisme que s'usa per defecte es diu OF2 i dona com a eixida A, t i ped amb les següents expressions:

$$A = \sum_{i=1}^{n} a_i S_i \tag{10.4a}$$

$$At = \sum_{i=1}^{n} b_i S_i \tag{10.4b}$$

$$ped = \sum_{i=1}^{n} c_i S_i. \tag{10.4c}$$

La bondat de la reconstrucció s'estima com en el següent factor de qualitat:

$$Q_F = 50 \sum_{i=1}^{n} \left| \frac{S_i - (Ag_i + ped)}{S_i} \right| \tag{10.5}$$

El desenvolupament d'aquest mètode està basat en l'aproximació que $t \approx 0$ i al créixer t la qualitat de la reconstrucció empitjora. Per tant, per a poder reconstruir successos de temps desconegut (feix de proba o còsmics) s'ha preparat un procés iteratiu. D'aquesta manera, s'usa el valor de t obtingut amb l'Eq. (10.4) per a recalcular el pesos d'OF i poder aplicar-los a les mateixes mostres en un nova iteració. Aquest procés acaba quan s'obté convergència en termes de la diferència entre τ (temps usat per al càlcul del pesos) i t o s'han efectuat el màxim nombre d'iteracions previstes en l'algorisme.

Per a poder usar OF per la reconstrucció de dades en TileCal, aquest mètode ha sigut implementat en l'entorn Athena [31], basat en el llenguatge C++, empleat per totes les tasques offline d'ATLAS (generació de Monte Carlo, simulació del detector, digitalització, reconstrucció, anàlisi, etc.). Per una banda, la ferramenta TileOptFiltTool s'encarrega de calcular els pesos d'OF usant per açò la classe TileOFCorrelation i, per una altra banda, una altra ferramenta anomenada TileRawChannelBuilderOptFilter aplica l'algorisme de reconstrucció sobre les dades reals o simulades.

10.2.2 Validació d'OF amb Soroll Electrònic

Variància de l'Amplitud en Successos Buits

S'han d'avaluar les variacions de l'amplitud obtinguda a partir dels algorismes de reconstrucció quan no hi ha cap senyal en el pols electrònic, tant si s'usen o no iteracions en OF. La Taula 10.1 mostra la mitjana i l'RMS per a les distribucions de l'amplitud per als diferents mètodes amb dades reals i simulades. Queda clar que el procediment iteratiu d'OF introdueix una major variància en l'amplitud, però no provoca resultats pitjors que Fit i, a més, és necessari per poder reconstruir dades de temps desconegut.

Table 10.1: Mitjana i RMS de la variància de l'amplitud per a diferent mètodes i dades.

	Mitjana (comptes d'ADC)	RMS (comptes d'ADC)
Run 46968 (dades reals, Novembre 2006)		
Fit	0.013938	1.579458
OF2 amb iteracions	0.003843	1.443401
Run 46968 (dades reals, Març 2008)		
Fit	0.023293	1.733377
OF2 amb iteracions	0.009521	1.597536
OF2 sense iteracions	0.000034	1.446327
Pions individuals (dades simulades, E=50 GeV)		
Fit	0.153798	1.579458
ManyAmps	0.000877	1.757498
OF2 sense iteracions	0.000851	1.75845

Amplitud i Temps

OF amb Iteracions La Figura 10.1 mostra la diferència relativa en amplitud entre els diferents mètodes estudiats per als canals amb A>70 comptes d'ADC en funció del temps per a dades simulades de pions individuals amb E=50 GeV. Els valors es concentren en la regió de diferencies relatives de menys de $\sim$1‰. Es veu una clara estructura en intervals d'1 ns (des de -0.5 a 0.5 ns, des de 0.5 a 1.5 ns, etc.). Cada interval està dividit en dues parts amb diferències positives ($A_{\mathrm{OF2}}>A_{\mathrm{Fit}}$) en la part baixa i amb diferències negatives ($A_{\mathrm{OF2}}<A_{\mathrm{Fit}}$) en la part alta.

La raó d'aquest comportament és que els pesos d'OF es calculen en passos d'1 ns. Quan el temps correspon exactament a la fase en que s'han calculat els pesos (τ=0 ns, ±1 ns,

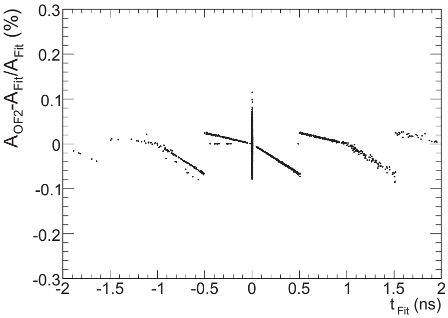

Figure 10.1: Diferència relativa de les amplituds obtingudes amb Fit i OF per a dades de Monte Carlo en funció del temps dels senyals.

± 2 ns, . . .), les amplituds que s'obtenen estan en complet acord. Quan el temps és diferent de la fase els pesos els resultats són pitjors, com està implícit en l'Eq. (10.3). Per la mateixa raó les diferències són positives o negatives a cada banda de l'interval i el diferent pendent és conseqüència de que la derivada de la forma del pols és diferent a cada costat del màxim.

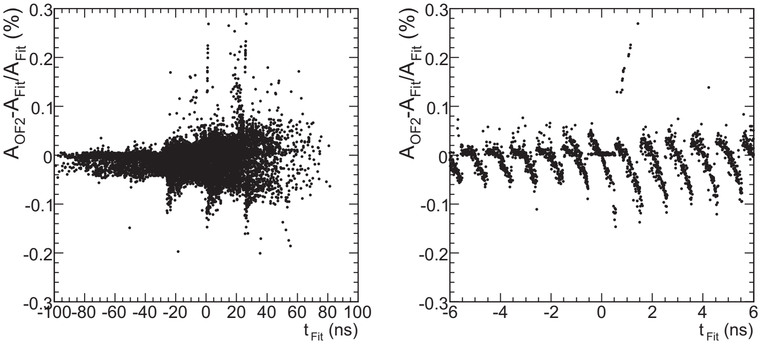

Figure 10.2: Diferència relativa de les amplituds obtingudes amb Fit i OF per a dades de còsmics en funció del temps dels senyals.

La Figura 10.2 mostra les mateixes distribucions obtingudes amb dades reals de còsmics. S'hi troba la mateixa estructura per la diferència de l'amplitud en funció del temps, encara que no tant ben definida com en Monte Carlo donat que no és un cas ideal i la forma del pols varia entre els diferents canals en dades reals. Encara que la major part del successos estan compresos en una banda de ±1‰, s'aprecia una clara estructura cada 25 ns, amb majors diferències al incrementar-se t. Açò és conseqüència del fet que cada 25 ns es perd una mostra del flanc de baixada del pols i les fluctuacions entre els resultats d'ambdós mètodes creix.

OF sense Iteracions La Figura 10.3 mostra les diferències relatives entre les amplituds proporcionades pels diferents mètodes en funció del temps per dades simulades (pions individuals amb E=50 GeV) quan no s'usen iteracions en OF.

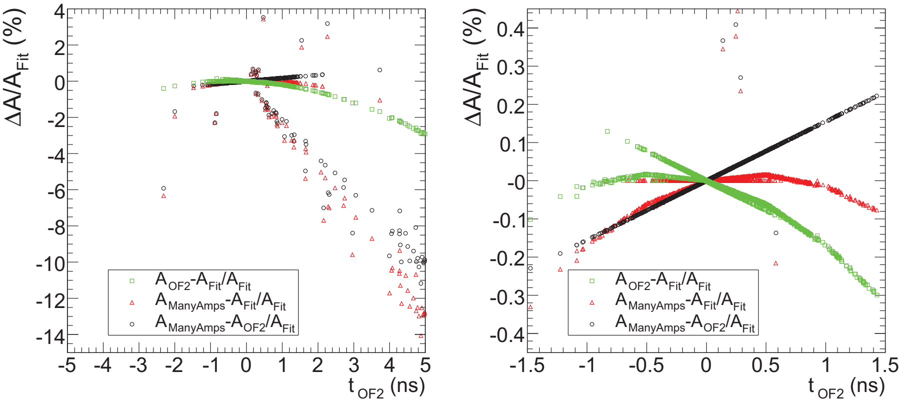

Figure 10.3: Diferència relativa de les amplituds obtingudes amb Fit, OF sense iteracions i ManyAmps per a dades de Monte Carlo en funció del temps. A l'esquerra, per a $|t|$<5 ns i a la dreta per a $|t|$<1.5 ns.

El més sorprenent d'aquesta comparació és que ManyAmps dona en alguns casos amplituds molt menors que en els altres mètodes, amb diferències de fins a $\sim$10-12% per a t=5 ns. Aquestos successos corresponen als casos que durant l'ajust s'obtenen valors menors de χ^2 a l'usar 2 o més amplituds en lloc de només 1. En altres paraules, el defecte en l'amplitud a t=0 ns es crea perquè s'usa una altra amplitud més menuda a t=±25 ns. A part d'açò, en la regió $|t| \lesssim$1.5 ns, hi ha una desviació lineal entre ManyAmps i Fit fins al 2‰ en t=1.5 ns. De totes maneres, per a temps majors aquesta tendència es trenca i tots els successos estan reconstruïts de manera incorrecta.

Respecte les diferències entre OF sense iteracions i Fit, s'observa el mateix comportament que amb iteracions per a $|t|$ <0.5 ns (diferències màximes de l'ordre de $\sim$1‰), però aquesta discrepància creix per a temps més altes fins al 3% en t=5 ns. La conclusió és que l'amplitud es veu molt afectada per l'ús de pesos no adequats. De totes maneres, aquestes diferències es poden el·liminar mitjançant una funció de correcció parabòlica en funció del valor de t obtingut en la reconstrucció. De fet, les desviacions en l'amplitud són molt més importants que per als temps en OF sense iteracions, ja que s'obtenen valors correctes per a t fins i tot a valors alts d'aquesta variable.

10.3 Comportament amb Apilament per Minimum Bias

La Figura 10.4 mostra la multiplicitat de canals afectats per l'apilament de MB per a les capes de TileCal, obtingudes amb una mostra de neutrinos digitalitzats només amb MB i sense soroll electrònic. S'han considerat en la Figura els tres escenaris normalment usats en la simulació de MB: lluminositat alta ($\langle n_{coll} \rangle$=23.0), lluminositat baixa ($\langle n_{coll} \rangle$=4.6) i lluminositat molt baixa ($\langle n_{coll} \rangle$=2.3). S'ha estimat l'amplitud sense cap algorisme de reconstrucció pròpiament dit, simplement com $\tilde{A}$=S_{max}-S_{min}. Encara que la quantitat de canals afectats d'alguna manera per la presència de l'apilament és elevada (1000 a lluminositat alta en la capa A), una vegada comparat amb l'amplitud resultant, molt pocs d'ells presenten amplituds considerables (menys de 20 amb $\tilde{A}$>50 comptes d'ADC i 4 amb $\tilde{A}$>150 comptes d'ADC per a lluminositat alta en la capa A).

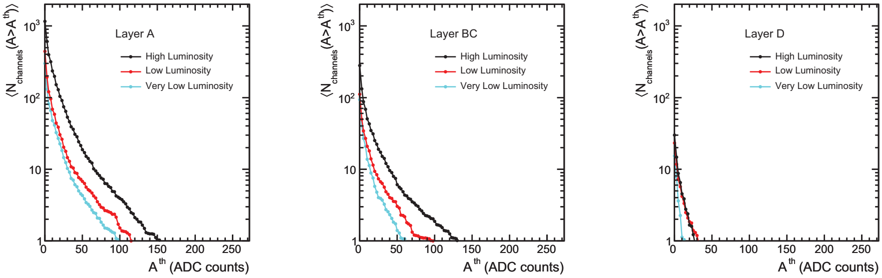

Figure 10.4: Multiplicitat de canals afectats per l'apilament de *minimum bias* per a cada capa de TileCal. Es mostra la mitjana de canals amb $\tilde{A}$> A^{th} (per a $\tilde{A}$=S_{max}-S_{min}) en funció de A^{th} per a tres escenaris de simulació de MB.

S'ha avaluat el comportament dels diferent algorismes de reconstrucció en un entorn amb apilament de successos de *minimum bias* a baixa lluminositat, és a dir, amb una mitjana de 4.6 col·lisions protó-protó per encreuament de feixos. En concret, si es consideren els successos que no presenten cap senyal quan es lleva l'apilament per MB, es veu que la amplitud resultant, a part de la gaussiana central conseqüència del soroll electrònic, presenta cues cap a amplituds positives i negatives. La part positiva es pot explicar intuïtivament com a creada pels successos de MB que cauen prop del temps de mostreig. La part negativa correspon als casos en els quals resulta millor termes de χ^2 fer un ajust a un pedestal major i una amplitud negativa en lloc de no variar el pedestal i usar una amplitud positiva.

La Figura 10.5 mostra aquestes distribucions per a ManyAmps i OF. Es veu que ManyAmps presenta un millor comportament amb cues molt menys pronunciades que OF. No obstant, si s'aplica un tall en la qualitat de la reconstrucció d'OF, la situació millora considerablement i les cues es retallen fins arribar a obtindre millors resultats que el mètode ManyAmps.

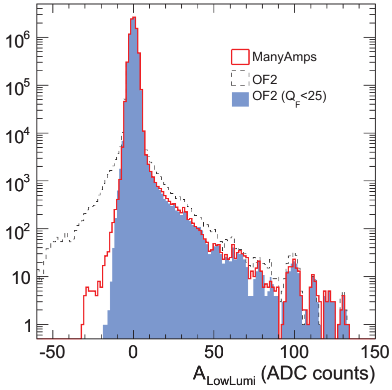

Figure 10.5: Distribució de les amplituds per a ManyAmps, OF i OF amb un tall en el factor de qualitat per a succesos buit amb apilament de MB.

10.4 Estudis de Resolució i Resposta del Calorímetre

Aquesta part està dedicada a l'avaluació de l'impacte dels mètodes de reconstrucció en la resolució i resposta de TileCal, no només amb soroll electrònic, sinó també amb apilament de MB a lluminositat baixa. S'ha triat mostres de pions individuals a diverses energies (E_π=50, 100, 200 GeV) simulats dintre la geometria completa d'ATLAS. Una vegada seleccionats els succesos on la major part de l'energia es diposita en TileCal i les partícules es comportanten com "Partícules al Mínim de Ionització" (MIPs) en LAr, la resolució i resposta es calcula amb la mitjana ($\langle E\rangle$) i sigma (σ) de la distribució d'energia:

$$\text{Resol.} = \frac{\sigma}{\langle E\rangle}, \tag{10.6}$$

$$\text{Resp.} = \frac{\langle E\rangle}{E_\pi}. \tag{10.7}$$

La resolució i resposta en funció de l'energia es mostra en la Figura 10.6. Les resultats de tots els mètodes quan no hi ha apilament de MB són molt similars, com era d'esperar a partir dels estudis a nivell de canal fets anteriorment. Per a tots els casos les diferències son menudes ($\sim$0.01%) i plenament compatible amb els errors.

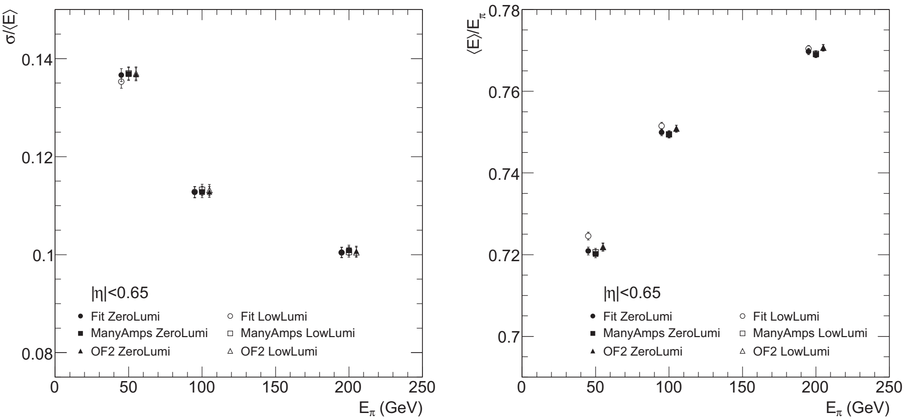

Figure 10.6: Resolució (esquerra) i resposta (dreta) de TileCal en funció de l'energia del pions (E_π=50, 100, 200 GeV) per a tots el mètodes i lluminositats $\mathcal{L}$ = 0 (ZeroLumi), 2$\times$10^{33} cm^{-2}s^{-1} (LowLumi). Només es consideren les partícules generades amb $|\eta|$ <0.65.

Quan s'inclou l'apilament de MB, els resultats són quasi compatibles amb els errors en tots els casos. El major efecte observat és l'increment de la resposta per al mètode Fit, el qual és més evident per a E_π=50 GeV, però també s'aprecia per a les altres energies considerades. L'aparent millora en la resolució per aquestos punts és un artefacte de l'increment en el terme $\langle E \rangle$. Per tant, encara que els efectes de l'apilament de MB son relativament menuts a la lluminositat considerada i dins de la simulació actual del detector (Figura 10.4), provoquen canvis en els resultats del mètode Fit mentres OF i ManyAmps no es veuen afectats per l'apilament de MB.

En resum, OF és un mètode que es mostra capaç de reconstruir l'energia en TileCal fiablement i robusta, fins i tot amb apilament de *minimum bias*. Cal recordar que, de totes maneres, a altres lluminositats els efectes poden resultar majors i que la simulació disponible en aquestos moments ha de ser validada amb dades reals i que els efectes de l'apilament de MB poden ser molt més grans durant l'operació d'ATLAS.

10.5 Supersimetria a ATLAS

Supersimetria (SUSY) és una generalització de les simetries espai-temporals de la Teoria Quàntica de Camps que transforma fermions en bosons i viceversa. SUSY també proporciona un entorn per a unificar la física de partícules i la gravetat a l'escala de Gran Unificació (GUT), $M_{\rm Pl} \sim 10^{19}$ GeV (on les interaccions gravitatòries són de magnitud comparable a les interaccions gauge). El sector de Higgs consisteix en dos doblets complexes que donen lloc a cinc estats físics: un pseudoescalar neutre (A), dos escalars neutres (h i H) i dos bosons carregats ($\mathrm{H}^{\pm}$). Els supercompanys dels fermions del SM es denoten amb el prefix s- (sleptó, squark, etc) i els supercompanys dels bosons del SM amb el sufix -ino (fotino, zino, wino, etc.).

SUSY a l'escala del TeV és una atractiva extensió del Model Estàndard (SM) la qual dóna una explicació natural a que el Higgs tinga una massa de vora els 100 MeV, consistència amb les dades electrodèbils de precisió de LEP, SLC i TeVatron amb acoblaments unificats a l'escala de GUT i un candidat natural per a la matèria fosca freda.

Si SUSY fora una simetria exacta de la naturalesa, les partícules i els seus âĂIJsupercompanysâĂİ (que diferixen en mitja unitat en espí) estarien degenerats en massa. Com que encara no s'han observat superpatícules, SUSY ha de ser una simetria trencada. Una de les possibilitats millor estudiades de trencament de SUSY són les teories de Supergravetat Mínima (mSUGRA) [36]. Dins d'aquestes teories, només es necessiten afegir 5 paràmetres, a més dels 18 del SM (excloent la massa del Higgs):

- m_0: valor comú per a la massa dels escalars a l'escala GUT.
- $m_{1/2}$: valor comú per a la massa dels gauginos a l'escala GUT.
- A_0: paràmetre de trencament trilineal de SUSY a l'escala GUT.
- $\tan\beta$: raó entre els valor esperats dels dos camps de Higgs a l'escala electrodèbil.
- $\mathrm{sgn}(\mu_0)$: signe del terme de massa del Higgsí.

Aquesta reducció tan dràstica des dels 124 paràmetres del MSSM a només 5 permet escanejar regions d'interès a l'espai de paràmetres. Habitualment es fixen dos paràmetres, encara que es possible variar lliurement els quatre paràmetres continus amb tècniques de Monte Carlo.

En gran quantitat de teories de SUSY s'inclou un simetria multiplicativa anomenada paritat R, amb $R = (-1)^{3(B-L)+2S}$ on B, L i S són el nombre bariònic, leptònic i l'espí. Les partícules ordinàries del SM tenen paritat R positiva i els seus supercompanys negativa. La conservació de la paritat R provoca que les partícules supersimètriques es produïxen en parells. D'aquesta manera, la partícula supersimètrica més lleugera (LSP) és estable sempre es produeix al final d'una cadena de desintegració de qualsevol partícula supersimètrica. Per tant, la signatura de successos de SUSY en colisionadors serà una gran multiplicitat de jets hadrònics i falta d'energia transversa ($\not{E}_{\mathrm{T}}$).

10.5.1 Reducció de la Fake Missing Transverse Energy per QCD

La mesura de la falta d'energia transversa es l'observable més important per a la recerca de SUSY amb conservació de la paritat R així com a en molts altres escenaris més enllà del SM. El fons de QCD és particularment rellevant a alta $\not{E}_{\mathrm{T}}$ per diverses raons. Gran quantitat d'efectes contribuïxen en empitjorar la resolució de $\not{E}_{\mathrm{T}}$, produint l'anomenada *fake* $\not{E}_{\mathrm{T}}$ ($\not{E}_{\mathrm{T}}^{\mathrm{Fake}}$): cues no gaussianes en la resposta d'ATLAS als jets degudes a material inactiu, muons que escapen del detector, la falta de contenció dels jets, múltiples interaccions, raig còsmics, halo i gas del feix, pileup i soroll electrònic, etc.

Esta Secció estudia mètodes de reducció del fons de jets de QCD jet usant els calorímetres i el detector intern d'ATLAS per a identificar successos amb problemes en la reconstrucció dels jets que potencialment donen lloc a gran $\not{E}_{\mathrm{T}}^{\mathrm{Fake}}$.

La resposta del calorímetres als jet hadrònics es veu afectada per grans fluctuacions degudes al procés de fragmentació i la resposta no lineal del detector. Segons les previsions, aquesta es la principal font de $\not{E}_{\mathrm{T}}^{\mathrm{Fake}}$ en el calorímetres. A més, l'espessor finit del calorímetres pot no ser suficient per contindre la totalitat de la cascada hadrònica. Aquestos jets escaparan cap a l'espectròmetre de muons i no es mesuraran correctament. Les regions que comprenen les transicions entre les diferents parts del sistema de calorímetres tenen una pitjor cobertura i contribuïxen a la $\not{E}_{\mathrm{T}}^{\mathrm{Fake}}$ més que la resta.

El mètode proposat ací per a detectar els casos en els que els jets potencialment escapen dels calorímetres està basat en deposicions d'energia relativament grans en les següents regions: capes més externes de TileCal i del Hadronic EndCap, entre la capa més externa de LAr i la més interna de TileCal i en els centelleadors del *gap* i del *crack* de TileCal. L'estudi d'aquestes variables s'ha efectuat mitjançant la comparació l'energia reconstruïda del jet amb l'energia de la simulació MC a diferents interval en η. S'han triat aquestos intervals segons les regions de transició entre els diferents components de la calorimetria de l'experiment.

Per tant, les variables triades per a la selecció són:

- $E_{\mathrm{Tile2}}/E_{\mathrm{Total}}$: fracció de l'energia total del jet dipositada en la capa més externa de TileCal, és més probable que els jets amb un valor molt alt d'aquesta variable escapen parcialment a l'espectrometre de muons.
- $E_{\mathrm{Tile10}}/E_{\mathrm{Total}}$: fracció de l'energia total del jet dipositada en les dues capes més internes de TileCal. Aquesta variable té el matex significat que $E_{\mathrm{Tile2}}/E_{\mathrm{Total}}$ en la regió $1.4 < |\eta| < 1.7$ donat que la capa més externa del calorímetre acaba en $|\eta| = 1.4$.
- $E_{\mathrm{Cryo}}/E_{\mathrm{Total}}$: on E_{Cryo} es calcula amb l'energia en la capa més externa de LAr i la més interna de TileCal com $E_{\mathrm{Cryo}}^2 = E_{\mathrm{LAr3}} E_{\mathrm{Tile0}}$. Aquesta variable representa una estimació de l'energia dipositada en el criostat entre els dos calorímetres.
- $E_{\mathrm{Gap}}/E_{\mathrm{Total}}$: fracció de l'energia total del jet dipositada en els centelleadors del *gap* i *crack* de TileCal.
- $E_{\mathrm{HEC3}}/E_{\mathrm{Total}}$: fracció de l'energia total del jet dipositada en en la capa més externa del LAr Hadronic EndCap, té el mateix significat que $E_{\mathrm{Tile2}}/E_{\mathrm{Total}}$.

La Taula 10.2 mostra els talls de selecció aplicats al tres jets més energètics sempre que tinguen $p_{\mathrm{T}} > 100$ GeV. Aquest requisit evita que es tallen els successos amb problemes en la reconstrucció de jets de baix p_{T}que no contribuiran de manera significativa a $\not\!\!E_{\mathrm{T}}^{\mathrm{Fake}}$. Es rebutja qualsevol succés en el qual la seva deposició d'energia excedisca els valors de la Taula 10.2. Els valor específics del talls així com el criteri de selecció dels jets es poden canviar depenent de la eficiència i topologia del senyal.

Table 10.2: Talls a aplicar en els jets reconstruïts per a la neteja de successos de QCD en diferents regions en η.

	$\lvert\eta\rvert < 0.3$	$0.3 < \lvert\eta\rvert < 0.6$	$0.6 < \lvert\eta\rvert < 1.3$	$1.3 < \lvert\eta\rvert < 2.0$	$2.0 < \lvert\eta\rvert < 3.0$
$E_{\mathrm{Tile2}}/E_{\mathrm{Tot}}$	0.05	0.05	0.1	0.02	-
$E_{\mathrm{Tile10}}/E_{\mathrm{Tot}}$	0.8	0.8	0.7	0.2	-
$E_{\mathrm{Cryo}}/E_{\mathrm{Tot}}$	0.2	0.2	0.2	-	-
$E_{\mathrm{Gap}}/E_{\mathrm{Tot}}$	-	-	0.2	0.3	-
$E_{\mathrm{HEC3}}/E_{\mathrm{Tot}}$	-	-	-	0.05	0.05

La Figura 10.7 mostra la fracció de successos que es conserven desprès de l'aplicació d'aquestos talls on mostres de simulació de QCD. Aquestes gràfiques demostren que el procés de neteja d'aquesta classe de successos elimina amb major probabilitat els successos amb gran $\not\!\!E_{\mathrm{T}}^{\mathrm{Fake}}$ donat que la fracció de successos decreix en funció de $\not\!\!E_{\mathrm{T}}^{\mathrm{Fake}}$. A més, aquestos talls no són sensibles a la $\not\!\!E_{\mathrm{T}}$ global del succés amb un *plateau* en tot el rang de $\not\!\!E_{\mathrm{T}}$ amb desviacions de menys de $\sim$5%. El fet que per a certs punts la incertesa és gran es deu a la limitada estadística disponible per a als valors de $\not\!\!E_{\mathrm{T}}$ o $\not\!\!E_{\mathrm{T}}^{\mathrm{Fake}}$.

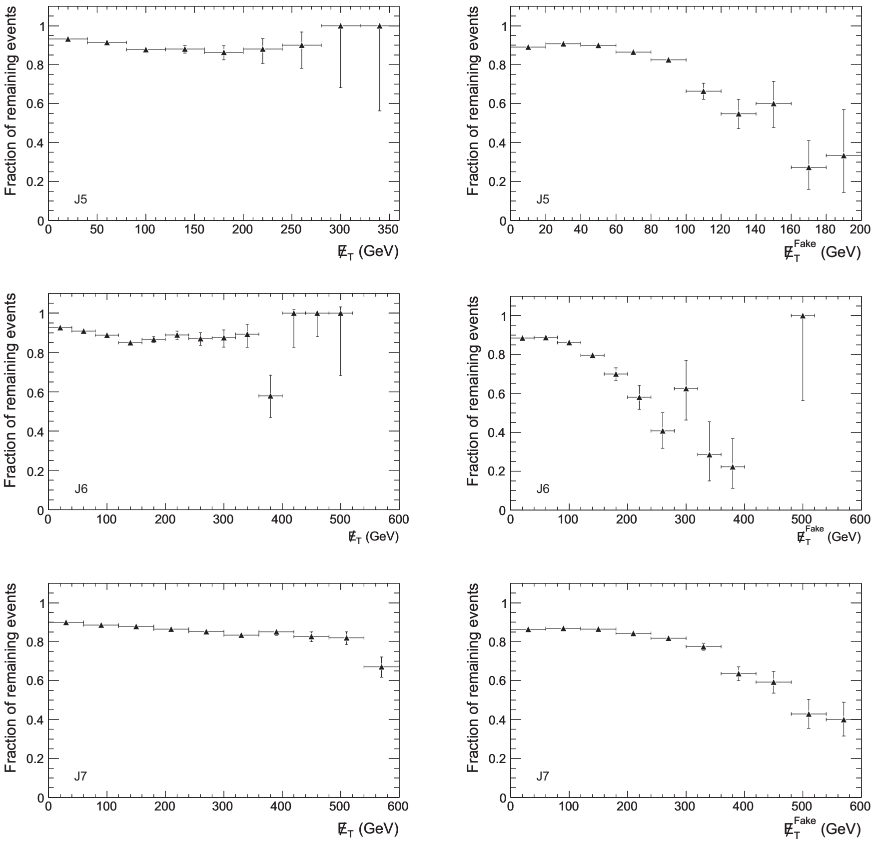

Figure 10.7: Fracció de successos després dels talls de selecció explicats al text en funció de $\not\!\!E_{\mathrm{T}}$ (esquerra) i $\not\!\!E_{\mathrm{T}}^{\mathrm{Fake}}$ (dreta) per a mostres de QCD.

Com a complement, també es proposa un altre mètode de reducció de $\not\!\!E_{\mathrm{T}}^{\mathrm{Fake}}$ basat en el detector de traces. Donat que les traces al detector intern no es veuen afectades pels possibles problemes dels calorímetres, es pot usar la $\not\!\!E_{\mathrm{T}}$ que s'obté només amb les traces ($\not\!\!E_{\mathrm{T}}^{\mathrm{Trk}}$) com informació addicional a l'hora d'eliminar la $\not\!\!E_{\mathrm{T}}^{\mathrm{Fake}}$ en QCD.

La Figura 10.8 mostra la diferència entre $\not\!\!E_{\mathrm{T}}$ i $\not\!\!E_{\mathrm{T}}^{\mathrm{Trk}}$ en funció de la $\not\!\!E_{\mathrm{T}}$ reconstruïda per a fons de QCD i el senyal de SUSY SU3[1]. S'observen tendències clarament diferenciades, amb els successos de QCD concentrat en la regió amb alts valors de $\not\!\!E_{\mathrm{T}}^{\mathrm{Trk}}$ amb $\not\!\!E_{\mathrm{T}}^{\mathrm{Trk}} \gg \not\!\!E_{\mathrm{T}}$. Fins i tot a $\not\!\!E_{\mathrm{T}} \gtrsim 100$ GeV, la diferència entre $\not\!\!E_{\mathrm{T}}^{\mathrm{Trk}}$ i $\not\!\!E_{\mathrm{T}}$ pot arribar a ser 500 GeV. Pel

---

[1] SU3 és un punt de l'espai de paràmetres de mSUGRA amb $m_0 = 100$; $m_{1/2} = 300$; $A_0 = -300$; $sign(\mu) = +$; $\tan\beta = 6$.

contrari, per a SU3 la major part dels successos tenen $\not{E}_{\mathrm{T}}^{\mathrm{Trk}} < \not{E}_{\mathrm{T}}$. Per tant, es pot fixar un tall en $\not{E}_{\mathrm{T}} - \not{E}_{\mathrm{T}}^{\mathrm{Trk}} < -50$ GeV per a rebutjar el fons de QCD en anàlisis de SUSY.

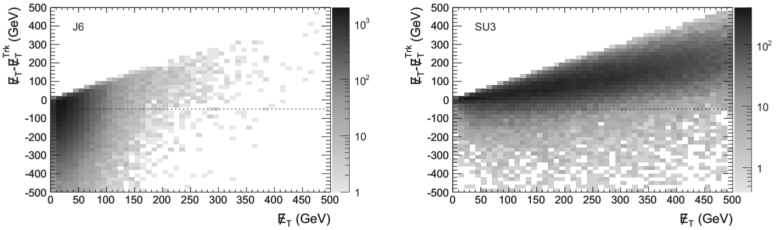

Figure 10.8: Diferència entre $\not{E}_{\mathrm{T}}$ i $\not{E}_{\mathrm{T}}^{\mathrm{Trk}}$ en funció de $\not{E}_{\mathrm{T}}$ per a QCD (esquerra) i senyal de SUSY (dreta). El tall proposat en el text es mostra amb una línia discontinua.

10.5.2 Anàlisi de Descobriment de SUSY en el Canal Hadrònic

En aquesta secció està dedicada a l'anàlisi inclusiu de descobriment de SUSY i, donat que la topologia d'aquest senyal es múltiples jets d'alt moment transvers (p_{T}) i $\not{E}_{\mathrm{T}}$, s'ha triat una signatura purament hadrònica amb 4 jets i 0 leptons en l'estat final. Els principals fons a considerar en aquest canal són $\mathrm{t\bar{t}}$, bosons de gauge (produïts individualment or en estats de dibosons) i QCD.

S'usaran una serie de talls estàndard en aquestos anàlisis [52] i els talls per a reduir la $\not{E}_{\mathrm{T}}^{\mathrm{Fake}}$ del fons de QCD proposats abans. Concretament els talls de l'anàlisi són els següents:

- **Tall 1**: La identificació i mesura d'electrons en la regió del crack es veu afectada per problemes en la simulació del detector, es rebutgen els successos amb electrons reconstruïts en 1.37< $|\eta|$ <1.52.
- **Tall 2**: Aquest tall es basa en la multiplicitat de jets demanant com a mínim 4 jets en l'estat final amb $p_{\mathrm{T}}(\mathrm{jet}_1) \geq 100$GeV i $p_{\mathrm{T}}(\mathrm{jet}_4) \geq 50$GeV.
- **Tall 3**: Tall en la falta d'energia transversa, requerint $\not{E}_{\mathrm{T}} \geq$100GeV.
- **Tall 4**: Tall en la falta d'energia transversa respecte a la massa efectiva: $\not{E}_{\mathrm{T}} \geq 0.2 M_{\mathrm{eff}}$, on $M_{\mathrm{eff}} = \sum_{i=1}^{4} p_{\mathrm{T}}(\mathrm{jet_i}) + \not{E}_{\mathrm{T}}$.
- **Tall 5**: Tall en la esfericitat transversa: S_{T} >0.2, on es calcula S_{T} amb tots els jets amb p_{T}>20 GeV en $|\eta|$ <2.5.
- **Tall 6**: Requisit en la separació angular entre els tres jets més energètics i la $\not{E}_{\mathrm{T}}$ en el pla transvers: $\Delta\phi$(jet$_{1,2,3}$-$\not{E}_{\mathrm{T}}$)$\geq$0.2.

- **Tall 7**: Es requereix l'absència de leptons (electrons o muons) aïllats amb E_{T} $>$20 GeV en $|\eta|$ $<$2.5.
- **Tall 8**: Els talls de neteja de QCD definits en la secció anterior.

Els Talls 1-5 i 7 ja van ser usats en la Ref. [52]. El Tall 5 s'usa per a reduir el fons de dijets de QCD. El principal objectiu del Tall 6 és descartar successos del fons de QCD amb $\not{E}_{\mathrm{T}}$ real pels neutrins produïts en el jets.

La Taula 10.3 mostra la secció eficaç en funció dels talls aplicats per a diversos punts de senyal de SUSY i fons del SM. La Figura 10.9 mostra l'evolució de la distribució de M_{eff} després de cada tall per a una lluminositat integrada de 1 fb^{-1}. La major part del fons s'elimina amb els primers quatre talls, encara que la resta també contribueix a millorar la raó senyal-soroll.

Table 10.3: Secció eficaç (en pb) en funció dels talls descrits al text.

Mostra	Total	Talls 1-2	Talls 1-4	Talls 1-6	Talls 1-7	Talls 1-8
SU1	10.86	3.701	2.855	1.907	1.401	1.159
SU2	7.18	0.7467	0.3691	0.2787	0.1695	0.1423
SU3	27.68	10.56	7.568	5.28	4.313	3.571
SU4	402.2	121.2	57.8	42.41	34.97	29.84
SU6	6.07	2.696	2.063	1.383	1.08	0.8922
SU8_1	8.7	3.308	2.54	1.686	1.448	1.204
Fons no de QCD	923.2	158.6	12.46	8.078	5.87	4.96
Top	833	149.7	9.043	5.964	4.095	3.452
W	19.2	5.391	2.334	1.426	1.109	0.9305
Z	15.09	3.265	1.072	0.679	0.6632	0.5747
Dibosó	55.95	0.21	0.016	0.0092	0.0035	0.0027
QCD	1644	560	7.049	0.8483	0.8483	0.6612

La definició més apropiada per a la significança és Z_n i inclou aquesta incertesa sistemàtica en els fons. Per a una lluminositat integrada de 1 fb^{-1}, s'estima que la incertesa en el fons de QCD és d'un 50%, mentre que per al fons no de QCD és d'un 20% [53].

La Taula 10.4 mostra quines siginificàncies es poden aconseguir per a totes les mostres de senyal considerades per a una lluminositat integrada de 1 fb^{-1}, de manera que es pot realitzar el descobriment per a tots els punts usats en l'espai de paràmetres excepte SU2.

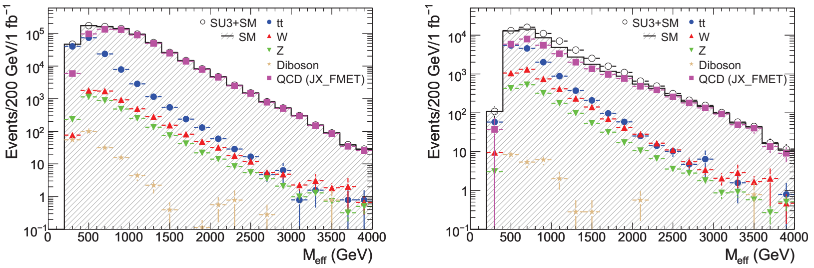

(a) Després dels Talls 1-2 (N$_{jet}$ $\geq$4)

(b) Després dels Talls 1-3 ($\not\!\!E_{\mathrm{T}}$ $\geq$100 GeV)

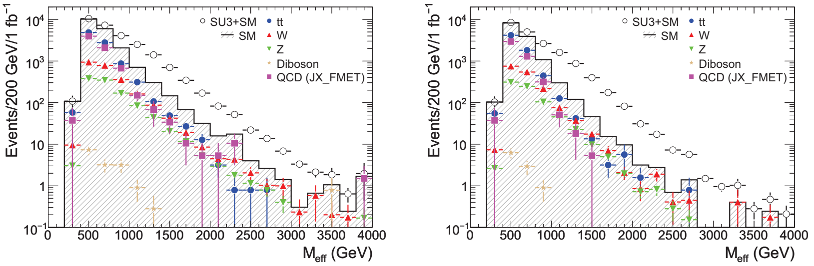

(c) Després dels Talls 1-4 ($\not\!\!E_{\mathrm{T}}$ $\geq 0.2 M_{\mathrm{eff}}$)

(d) Després dels Talls 1-5 (S_{T} $>$0.2)

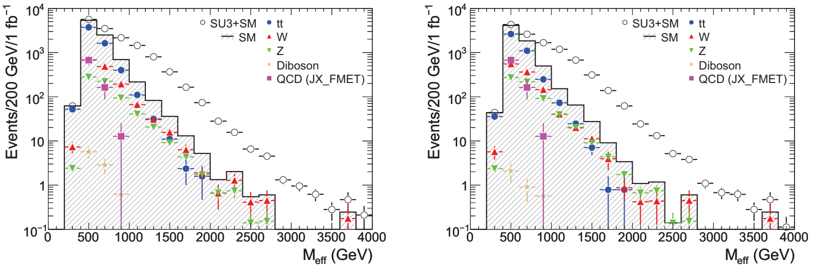

(e) Després dels Talls 1-6 ($\Delta\phi(jets - \not\!\!E_{\mathrm{T}})$ $\geq$0.2)

(f) Després dels Talls 1-7 (No isolated lepton)

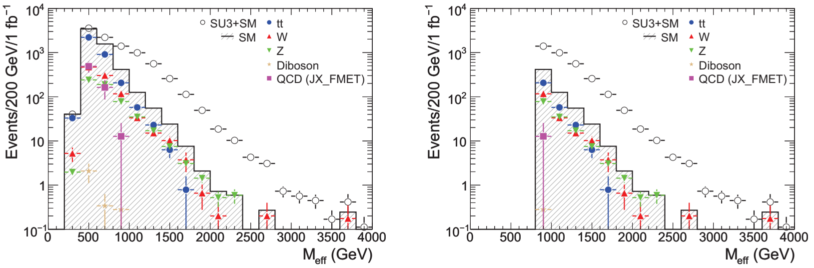

(g) Després dels Talls 1-8 (QCD cleaning)

(h) Després de M_{eff} $\geq$800 GeV

Figure 10.9: Distributcions de M_{eff} després de cadascun dels talls de selecció per a fons i senyal de SUSY (SU3).

Table 10.4: Significança per als senyals de SUSY considerades després dels 2 últims talls.

	Talls 1-8	M_{eff}>800 GeV
SU1	0.8707	7.701
SU2	0.1072	0.8272
SU3	2.681	12.59
SU4	12.79	24.05
SU5	0.6708	5.819
SU8.1	0.9045	8.292

Per tant, el descobriment de SUSY en ATLAS és viable per a la major part pels punts considerats en l'espai de paràmetres. De totes formes l'impacte dels talls per a la neteja de successos de QCD en la significança és relativament menut. De totes maneres, s'han de validar els resultats que s'obtenen amb Monte Carlo amb dades reals perquè els efectes del detector que provoquen *fake* $\not{E}_{\mathrm{T}}$ per QCD probablement seran molt més important en ATLAS. Per tant, aquestos talls són una ferramenta de gran utilitat per a assegurar la puresa de la mostra de successos seleccionats en aquesta classe de anàlisis de descobriment.

Appendix A

Details on Iterative Optimal Filtering Method

As mentioned in Chapters 4 and 5, iterations must be used in the OF algorithm to properly reconstruct unknown phase data. This Appendix illustrates the iteration procedure by means of some example events taken from cosmics commissioning data. This is implemented in athena by means of the *Iterator* method in the *TileRawChannelBuilderOptFilter* class (see Figure 4.6).

Table A.1 shows the raw samples, the final result of the reconstruction and the intermediate results provided by the iterative procedure on one of those events. Note that since in this case the maximum sample is the central one (S_4=234 ADC counts), the initial phase in the iterative reconstruction is set to τ_0=0 ns. As shown in the Table, three iterations are needed to achieve convergence in terms of the difference between τ_{i-1} and t_i, which should be less than half the time granularity used for OF weight storage in the ASCII files placed in the TileConditions package. The final time of the pulse after convergence is $t = t_3 - \tau_2$.

Table A.1: Example of event reconstructed with OF making use of iterations.

<table>
<tr><th colspan="4">Raw samples</th></tr>
<tr><td colspan="4">52 50 78 234 208 54 38</td></tr>
<tr><th colspan="4">Iterative Reconstruction</th></tr>
<tr><th>Iteration (i)</th><th>τ_{i-1} (ns)</th><th>A_i (ADC counts)</th><th>t_i (ns)</th></tr>
<tr><td>1</td><td>0</td><td>199.75</td><td>8.92</td></tr>
<tr><td>2</td><td>-9</td><td>215.10</td><td>-0.93</td></tr>
<tr><td>3</td><td>-8</td><td>215.26</td><td>0.18</td></tr>
<tr><th colspan="4">Final Result</th></tr>
<tr><td colspan="2">Amplitude: 215.26 ADC counts</td><td colspan="2">Time: 8.18 ns</td></tr>
</table>

Figure A.1 shows graphically the evolution of the reconstruction procedure in each of the iterations. Note the sign convention used for τ_i and t_i.

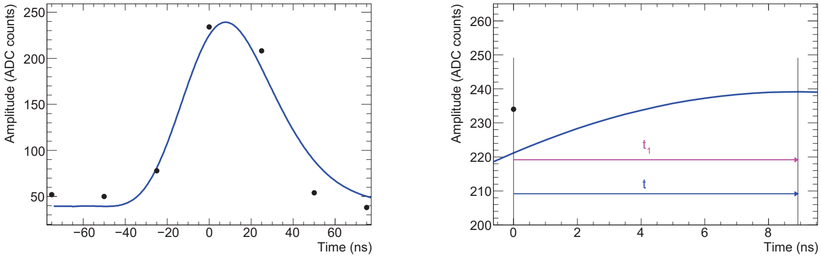

(a) After iteration 1

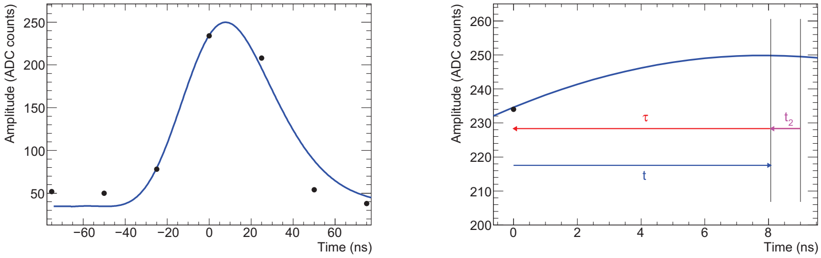

(b) After iteration 2

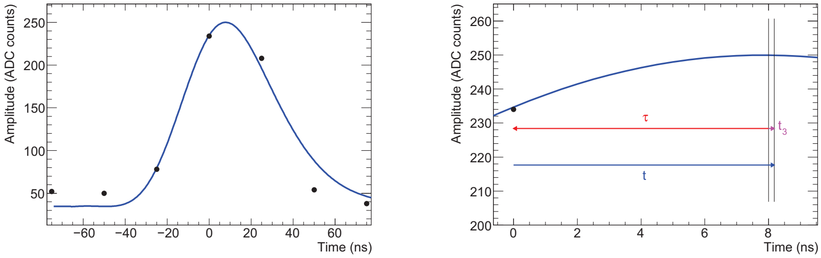

(c) After iteration 3

Figure A.1: Exmaple of iterations performed for the reconstruction of a cosmic event. On the left, the raw samples and the reconstructed pulse are shown in the full time range. On the right, detail on the central region showing τ_i, t_i and t.

Another example can be found in Table A.2. In this case, since the maximum sample is the S_6, the initial phase is set to τ_0=-50, but the iterative procedure is able to achieve convergence in three iterations setting the pulse timing in t=37.04 ns.

Table A.2: Example of event reconstructed with OF making use of iterations.

Raw samples						
47	47	46	63	195	219	56

Iterative Reconstruction			
Iteration (i)	τ_{i-1} (ns)	A_i (ADC counts)	t_i (ns)
1	-50	164.09	-16.39
2	-34	191.44	3.44
3	-37	193.33	0.04

Final Result	
Amplitude: 193.33 ADC counts	Time: 37.04 ns

Appendix B

Details on the TileCal Resolution and Response from Monte Carlo Data

As mentioned in Section 5.5.5, the resolution and response obtained for the calorimeter as elaborated there with Monte Carlo data from athena release 12.0.6 differs considerably from the results obtained with real data during test beam periods. This appendix is devoted to the detailed study of the resolution at different stages of the full ATLAS simulation procedure for a selected energy (E_π=50 GeV), always without minimum bias pileup. Only OF is considered when energy reconstruction is used since the same performance were found for all the reconstruction methods without minimum bias pileup.

Additional dedicated Monte Carlo samples using non-standard geometry setups and a reduced number of generated events (typically a few thousands). Much reduced statistics accuracy is obtained from these samples, but enough to explore the simulation results step by step.

Possible sources of such discrepancies can be the event selection or the reconstruction procedure. In consequence the following variables will be used in these studies:

a) Total energy deposited in the calorimeter in the simulation obtained as the sum of all the TileHits present. This variable represents simply the energy released in the calorimeter by the particles according to the Geant4 simulation, without any noise or reconstruction algorithm applied on top of that.

b) Sum of all the TileCells once digitization and reconstruction have been performed without electronics noise. It includes all the effect induced by the pulse shape convolution and digitization procedure, together with the energy reconstruction algorithms but excluding the smearing effects produced by the electronics noise. This is a raw sum, considering all the cells no matter its position respect to the incoming particles and without any noise removal cut.

c) Sum of all the TileCells reconstructed with electronics noise activated. No noise removal cut or further cell selection is applied in this sum.

d) Sum of the TileCells in a $\Delta\eta\times\Delta\phi$=0.4×0.4 cone around the truth pion with $E>2\sigma_{noise}^{cell}$. This is the same variable used for the total energy computation in Section 5.5.

Furthermore, in order to discard that the deviations found in the resolution are due to particularities in the Monte Carlo geometry or setup, several simulations have been performed:

1. Single pions generated at the interaction with fixed energy (E_π=50 GeV), random direction in ϕ and with an isotropic scan on $|\eta|$<0.65. Both LAr and Inner Detector are disbaled from the simulation so that the particles can only interact in TileCal. Figure B.1 shows the energy distribution obtained for the 4 variables explained above on these simulated data, which are fitted to Gaussians in the $\langle E\rangle \pm 2\sigma$ range.

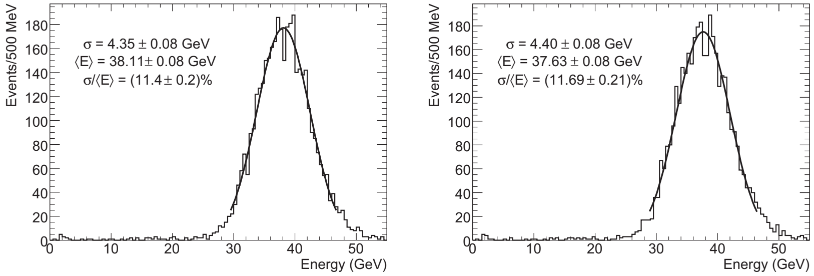

(a) Geant4 TileHits (b) Cells without electronics noise

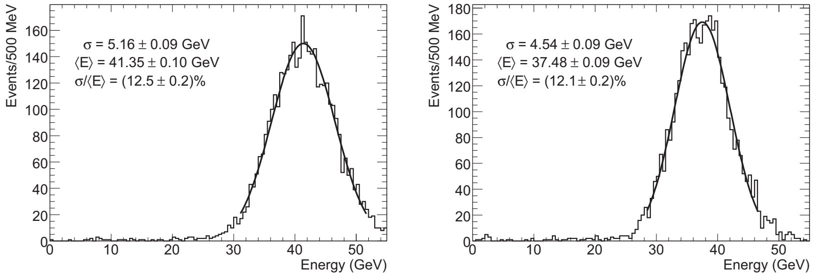

(c) Cells with electronics noise (d) Cells in cone with noise cut

Figure B.1: Energy distributions in TileCal obtained at different simulation levels for single pions generated at the interaction point with E=50 GeV and $|\eta|$<0.65. The LAr calorimeter and Inner Detector has been disabled in the Monte Carlo.

As shown, even at the TileHit level, with no issues related to the digitization or reconstruction, the resolutions obtained are already worse than the results from real data (11.4%). Small smearing appears when passing to the Cell level after reconstruction without noise (just 11.6%) and the sum of all the calorimeter cells obtained with electronics noise gives much worse results (12.5%). The energy summation used in Section 5.5 is capable of improving the resolution up to 12.1%.

2. Single pions generated at the interaction point with fixed energy (E_π=50 GeV), random direction in ϕ and fixed η=0.65. This simulation tries to reproduce the test beam setup where the beam hit the calorimeter in a fixed direction. Also in this case LAr and Inner Detector were deactivated in the simulation. Figure B.2 shows the energy distribution obtained for the 4 variables explained above in this simulation. The overall trends described in the first simulation are also found this time, but with smaller resolution values because the region with $\eta\sim0$ is excluded. However, the results obtained at the TileHit level are also worse than the values obtained at the test beam for this η value.

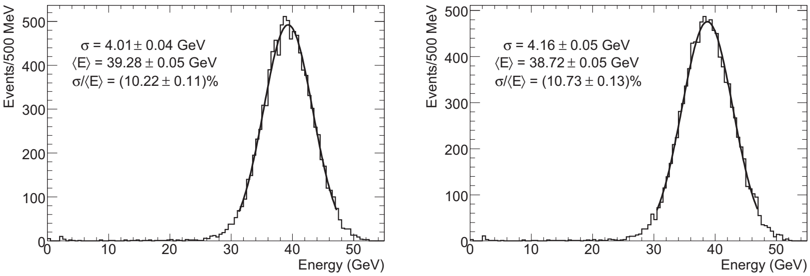

(a) Geant4 TileHits

(b) Cells without electronics noise

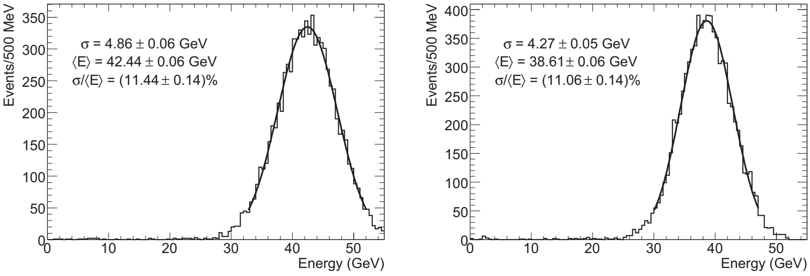

(c) Cells with electronics noise

(d) Cells in cone with noise cut

Figure B.2: Energy distributions in TileCal obtained at different simulation levels for single pions generated at the interaction point with E=50 GeV and fixed η=0.65. The LAr calorimeter and Inner Detector has been disabled in the Monte Carlo.

3. Single pions generated at a point in front of a calorimeter module (r=2.28 m, x=0.06 m, y=2.25 m, z=0.75 cm) pointing in the η=0.35 direction and with fixed energy (E_π=50 GeV). With this simulation, any possible effect from dead material which may remain in the ATLAS Geant4 simulation although LAr and Inner Detector are removed. Figure B.3 shows the energy distribution obtained for the 4 variables explained above in this simulation, with similar trends but slightly better results than in the previous case (with a resolution of 10% at the TileHit level).

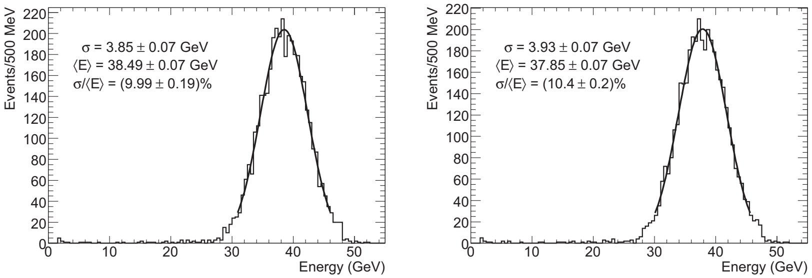

(a) Geant4 TileHits

(b) Cells without electronics noise

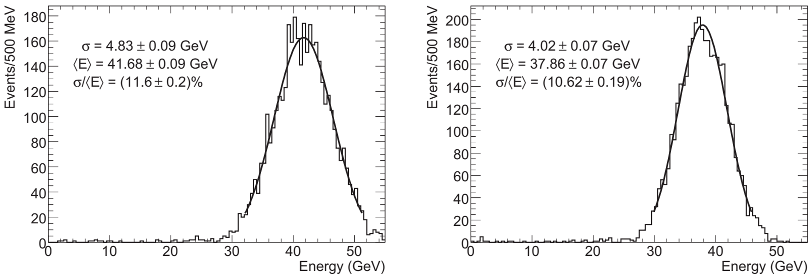

(c) Cells with electronics noise

(d) Cells in cone with noise cut

Figure B.3: Energy distributions in TileCal obtained at different simulation levels for single pions generated at the TileCal radius with E=50 GeV and following the η=0.35 direction. The LAr calorimeter and Inner Detector has been disabled in the Monte Carlo.

As a conclusion, the discrepancies between the resolution obtained with Monte Carlo data in the full ATLAS simulation and real combined test beam (as reported in [35]) are already present inside the Athena release 12 simulation environment at the TileHit level, as proved by all the simulations presented. Nevertheless, the event selection procedure used in Section 5.5 could be affected by some resolution smearing to the energy realeased in the upstream detectors and in dead materials, which can lead to a 12.1% resolution in TileCal standalone simulated data presented in this Appendix to the 13.68% obtained in Section 5.5.

All the data used have been simulated inside Athena release 12.0.6, which has been updated in more recent releases, including improvements in the Geant4 hadronic physics lists. Nevertheless, all the Monte Carlo data currently available will have to be extensively with real ATLAS data after LHC start-up.

Appendix C

List of Acronyms

ADC Analog to Digital Converter, a device for converting analogue signals into digital signals

ALICE A Large Ion Collider Experiment, one of the LHC experiments

ASCII American Standard Code for Information Interchange, a character encoding based on the English alphabet

ASIC Application-specific integrated circuit, an integrated circuit customized for a particular use

ATLAS A Toroidal LHC ApparatuS, one of the LHC experiments

CB Central Barrel, one of the TileCal barrels

CBNT ComBined NTuple, standard root file for ATLAS analysis

CDM Cold Dark Matter

CERN Conseil Européen pour la Recherche Nucléaire, the world's largest particle physics laboratory

CKM Cabibbo-Kobayashi-Maskawa, a unitary matrix which specifies the mixings between the quark mass eigenstates and the eigenstates for the weak force

CMS Compact Muon Solenoid, one of the LHC experiments

CMT Configuration Management Tool, a configuration management environment

CNGS CERN Neutrinos to Gran Sasso, project investigating the oscillation of neutrinos

CSC Cathode Strip Chambers, a chamber technology used in the ATLAS Muon system

CTB Combined Test Beam, period of data taking in ATLAS

CVS Concurrent Version System, a software version control system based on open-source codem

DMU Data Management Unit, ASIC chip in the TileCal digitizers

DONUT Direct Observation of NU Tau, an experiment at Fermilab dedicated to the search for tau neutrino interactions

DPD Derived Physics Data, a kind of ATLAS data file

DSP Digital Signal Processor, a specialized microprocessor designed specifically for digital signal processing

EB Extended Barrel, two of the TileCal barrels

EF Event Filter, one of the ATLAS trigger levels

EM Electromagnetic

EMEC Electromagnetic EndCap, one of the LAr calorimeters

ESD Event Summary Data, a kind of ATLAS data files

EWSB Electroweak Symmetry Breaking

FCal Forward Calorimeter, one of the LAr calorimeters

FCNC Flavor Changing Neutral Currents, expressions that change the flavor of a fermion current without altering its electric charge

FF Flat Filtering, a TileCal reconstruction method

FNAL Fermi National Accelerator Laboratory (Fermilab), is a U.S. Department of Energy national laboratory specializing in high-energy particle physics

GMSB Gauge Mediated Supersymmetry Breaking

GUT Grand Unification Theory, models that predicts that at extremely high energies all forces are unified.

HDM Hot Dark Matter

HEC Hadronic EndCap, one of the LAr calorimeters

HLT High Level Trigger, the ATLAS Level-2 Trigger and Event Filter

HV High Voltage

ID Inner Detector, one of the ATLAS subdetectors

IFIC Institut de Física Corpuscular, High Energy Physics research center at Valencia

ISOLDE Isotope Separator on Line DEvice, a facility at CERN dedicated to the production of radioactive ion beams

ISR Intersecting Storage Rings, a particle accelerator at CERN which was the world’s first hadron collider

KK Kaluza-Klein, an extra-dimensions theory

L1A Level-1 Accept, signal sent when an event passes Level-1 trigger

LAr Liquid Argon, one of the ATLAS calorimeters

LEP Large Electron Positron collider, an accelator at CERN

LHC Large Hadron Collider, an accelerator at CERN

LHCb Large Hadron Collider beauty, one of the LHC experiments

LHCf Large Hadron Collider forward, one of the LHC experiments

LQ LeptoQuarks, hypothetical particles with baryon and lepton number

LSP Lightest Supersymmetric Particle, the lightest of the additional hypothetical particles in supersymmetric models

LVL1 Level-1 trigger, one of the ATLAS trigger levels

LVL2 Level-2 trigger, one of the ATLAS trigger levels

MB Minimum Bias, events with low-p_{T} particles from elastic hadronic collisions

MC Monte Carlo data, data obtained with event generators and detector simulations

MDT Monitored Drift Tube, a chamber technology used in the ATLAS Muon system

MIP Minimum Ionizing Particle, a particle whose mean energy loss rate through matter is close to the minimum

MSSM Minimal Supersymmetric Standard Model, minimal extension to the Standard Model that realizes supersymmetry

mSUGRA minimal SUper GRAvity, a supersymmetric theory

OF Optimal Filtering, a TileCal reconstruction method

PDF Parton Distribution Function, the momentum distributions of a parton inside a proton

PDG Particle Data Group, an international collaboration that compiles and reanalyzes published results on the properties of particles and fundamental interactions

PMT PhotoMultiplier Tube, detector of light with high gain and sensitivity used in the TileCal front-end electronics

QCD Quantum Chromodynamics, a quantum field theory of the strong force

QED Quantum Electrodynamics, a quantum field theory of the electromagnetic force

RoI Region of Interest, in ATLAS a subset of the event data used for Level-2 trigger

ROD Read-Out Driver, TileCal back-end electronic board

RPC Resistive Plate Chambers, a chamber technology used in the ATLAS Muon system

SCT SemiConductor Tracker, one of the subdetector in the ATLAS Inner Detector

SLAC Stanford Linear Accelerator Center, a particel physics laboratory operated by Stanford University

SLC Stanford Linear Collider, an acceelerator at SLAC

SM Standard Model, a theory that describes three of the four known fundamental interactions between the elementary particles

SPS Super Proton Synchrotron, an accelerator at CERN

SUGRA SUperGRAvity, a field theory that combines the principles of supersymmetry and general relativity

SUSY Supersymmetry, a symmetry that relates elementary particles of one spin to another particle that differs by half a unit of spin

TDS Transient Data Store, a mechanism for shared memory used in athena to retrieve and store data

TGC Thin Gap Chamber, a chamber technology used in the ATLAS Muon system

TOTEM TOTal Elastic and diffractive cross section Measurement, a LHC experiment

TTC Trigger and Timing Control

TTCrx Trigger and Timing Control receiver ASIC chip

TRT ATLAS Transition Radiation Tracker, one of the subdetector in the ATLAS Inner Detector

VME Versa Module Eurocard bus, a computer bus standard

WLS WaveLength Shifter, a photofluorescent material that absorbs higher frequency photons and emits lower frequency photons

References

[1] O. Brüning *et al.* *LHC Design Report*. 2004. CERN-2004-003.

[2] ATLAS Collaboration. *ATLAS Technical Proposal for a General-Purpose pp Experiment at the Large Hadron Collider at CERN*. 1994. CERN-LHCC-94-43.

[3] CMS Collaboration. *The Compact Muon Solenoid, Technical Proposal*. 1994. CERN-LHCC-94-38.

[4] LHCb Collaboration. *LHCb: Technical Proposal*. 1998. CERN-LHCC-98-04.

[5] TOTEM Collaboration. *TOTEM, Total Cross Section, Elastic Scattering and Diffraction Dissociation at the LHC : Technical Proposal*. 1999. CERN-LHCC-99-07.

[6] LHCf Collaboration. *LHCf experiment : Technical Design Report*. 2006. CERN-LHCC-2006-004.

[7] Alice Collaboration. *Technical Proposal for A Large Ion Collider Experiment at the CERN LHC*. 1995. CERN-LHCC-95-71.

[8] ATLAS Collaboration. *ATLAS Inner Detector: Technical Design Report*, volume 1. 1997. CERN-LHCC-97-016.

[9] ATLAS Collaboration. *ATLAS Calorimeter Performance: Technical Design Report*. 1996. CERN-LHCC-96-040.

[10] ATLAS Collaboration. *ATLAS Liquid Argon Calorimeter: Technical Design Report*. 1996. CERN-LHCC-96-041.

[11] ATLAS Collaboration. *ATLAS Tile Calorimeter: Technical Design Report*. 1996. CERN-LHCC-96-042.

[12] ATLAS Collaboration. *ATLAS Muon Spectrometer: Technical Design Report*. 1997. CERN-LHCC-97-022.

[13] ATLAS Collaboration. *ATLAS Magnet System: Technical Design Report, 1*. 1997. CERN-LHCC-97-018.

[14] ATLAS Collaboration. *ATLAS Level-1 Trigger: Technical Design Report*. 1998. CERN-LHCC-98-014.

[15] J. Castelo *et al.* TileCal ROD Hardware and Software Requirements. 2005. ATLAS Note ATL-TILECAL-2005-003.

[16] A. Ruiz-Martínez *et al.* Monte Carlo Performance of the TileCal Low pT Muon Identification Algorithm. ATL-TILECAL-PUB-2008-008.

[17] Steven Weinberg. A Model of Leptons. *Phys. Rev. Lett.*, 19:1264–1266, 1967.

[18] S. L. Glashow, J. Iliopoulos, and L. Maiani. Weak Interactions with Lepton-Hadron Symmetry. *Phys. Rev.*, D2:1285–1292, 1970.

[19] Jogesh C. Pati and Abdus Salam. Unified Lepton-Hadron Symmetry and a Gauge Theory of the Basic Interactions. *Phys. Rev.*, D8:1240–1251, 1973.

[20] Peter W. Higgs. Broken symmetries, massless particles and gauge fields. *Phys. Lett.*, 12:132–133, 1964.

[21] S. Mrenna T. Sjostrand and P. Skands. A Brief Introduction to PYTHIA 8.1. Comput. Phys. Commun. **178** (2008) 852,[arXiv:0710.3820 [hep-ph]].

[22] CDF Collaboration. A Combination of CDF and D0 results on the mass of the top quark. arXiv:hep-ex/070303.

[23] L. Vacavant and I. Hinchliffe. Signals Of Models With Large Extra Dimensions in Atlas. J. Phys. G **27** (2001) 1839.

[24] R. Wigmans. *Calorimetry: Energy Measurement in Particle Physics*. 2000. Oxford: Clarendon Press.

[25] C. Amsler et al. Review of particle physics. *Phys. Lett.*, **B667**, 1, 2008.

[26] B. Rossi. *High energy particles*. 1952. New York, NY: Prentice-Hall.

[27] N. Gollub *et al.* Biases in the ATLAS Tile Calorimeter Signal Reconstruction due to Pulse Shape Variations. To be submitted as ATLAS Note.

[28] ATLAS TileCal Collaboration. Testbeam Studies of Production Modules of the ATLAS Tile Calorimeter. Preprint submitted to Elsevier Science. 2007.

[29] E. Fullana *et al.* Optimal Filtering in the ATLAS Hadronic Tile Calorimeter. 2005. ATLAS Note ATL-TILECAL-2005-001.

[30] B. Salvachúa *et al.* Online energy and phase reconstruction during commissioning phase of the ATLAS Tile Calorimeter. ATLAS Communication ATL-COM-TILECAL-2008-004, waiting for approval as ATLAS Note.

[31] *Athena. The ATLAS Common Framework. Developer Guide*, February 2004.

[32] LHCb software architecture group. *GAUDI-Architecture design document*. 1998. CERN-LHCb-98-064.

[33] Christian Arnault. CMT-Configuration Management Tool, 2006. `http://www.cmtsite.org/CMTDoc.html`.

[34] J. B. Birks. *The Theory and Practice of Scintillation Counting*. 1964. Pergamon Press, Oxford.

[35] V. Giangiobbe *et al.* Hadronic calorimeter performance in the ATLAS combined testbeam 2004. ATL-TILECAL-PUB-2005-008.

[36] H. P. Nilles. Supersymmetry, Supergravity And Particle Physics. Phys. Rept.**110** (1984) 1.

[37] M. Spira W. Beenakker, R. Hopker and P. M. Zerwas. Squark and gluino production at hadron colliders. Nucl. Phys. B **492** (1997) 51, [arXiv:hep-ph/9610490].

[38] D. N. Spergel *et al.* [WMAP Collaboration]. Wilkinson Microwave Anisotropy Probe (WMAP) three year results: Implications for cosmology. Astrophys. J. Suppl. **170** (2007) 377 [arXiv:astro-ph/0603449].

[39] G. Corcella *et al.* HERWIG 6.5: an event generator for Hadron Emission Reactions With Interfering Gluons (including supersymmetric processes). arXiv:hep-ph/0011363v3.

[40] J. R. Forshaw J. M. Butterworth and M. H. Seymour. Multiparton interactions in photoproduction at HERA. Z. Phys. C **72** (1996) 637 [arXiv:hep-ph/9601371].

[41] P. Nason S. Frixione and B. R. Webber. Matching NLO QCD and parton showers in heavy flavour production. JHEP **0308** (2003) 007 [arXiv:hep-ph/0305252].

[42] F. Piccinini R. Pittau M. L. Mangano, M. Moretti and A. D. Polosa. ALPGEN, a generator for hard multiparton processes in hadronic collisions. JHEP **0307** (2003) 001 [arXiv:hep-ph/0206293].

[43] R. Prabhu; K. Deschand P. Wienemann. Estimating Missing Transverse Energy at the Generator Level. ATL-COM-PHYS-2007-019.

[44] ATLAS Collaboration. Jet Reconstruction. Jet CSC Note 5/11.

[45] ATLAS Collaboration. Electron Identification. Egamma CSC Note 1.

[46] S. Hassani *et al.* A muon identification and combined reconstruction procedure for the ATLAS detector at the LHC using the (MUONBOY, STACO, MuTag) packages.

[47] ATLAS Collaboration. ATLAS MissingET Overall Performance. CSC $\not{E}_{\mathrm{T}}$ Note.

[48] M. D. Shapiro J. Soderqvist I. Hinchliffe, F. E. Paige and W. Yao. Precision SUSY measurements at LHC. Phys. Rev. D **55**, 5520 (1997) [arXiv:hep-ph/9610544].

[49] V. Barger, J. Ohnemus, and R. J. N. Phillips. Event shape criteria for single-lepton top signals. Physical Review D **48**, 3953 (1993).

[50] R. Teuscher *et al.* Fake Missing Transverse Energy from ATLAS Calorimeter Cosmic Ray Data. ATL-COM-CAL-2008-002.

[51] Y. Zhu *et al.* Study of Cosmic Ray Data with M5-M8. ATLAS note to be submitted.

[52] ATLAS Collaboration. ATLAS Performance and Physics Technical Design Report. ATLAS TDR 15, CERN/LHCC/99-15, 25 May 1999.

[53] ATLAS Collaboration. Prospects for SUSY discovery based on inclusive searches with the ATLAS detector at the LHC. ATLAS SUSY CSC5 Note.

[54] R. D. Cousins and V. L. Highland. Incorporating systematic uncertainties into an upper limit. Nucl. Instrum. Meth. A **320** (1992) 331.

[55] J. T. Linnemann. Measures of Significance in HEP and Astrophysics. [arXiv:physics/0312059], 2003.

Acknowledgements

“ These are the last words I have to say
Before another age goes by
But now it’s time to put this book away
Ain’t that the story of my life...”
— B. Joel, Famous Last Words, 1993

Ja fa 15 anys des de que vaig descobrir aquestes paraules però en aquest moment de la meva vida prenen significats nous i encara més intensos... i ara que escric estes linees és un bon moment per mirar enrere.

Vull agrair en primer lloc als que em van donar la confiança per a escomençar aquesta tasca i van fer possible que descobrira el que ara considere la meva professió: Toni Ferer i Juano Valls. I, com no, també vull agrair les coses que he aprés d’Emilio Higón i Victoria Castillo, per a mi tot un model de profesionalitat i dedicació.

I no puc oblidar a Bruce Mellado i Sau Lan Wu, per obrir-me les portes de l’anàlisi de dades en el moment que LHC està donant les seves primeres pases, moltísimes gràcies.

I també vull recordar amb gratitut a tots els meus companys de grup durant aquestos anys: Xosé, Diego, David, Esteban, Belén, Cristóbal, Aitor, Carmen, Arantxa, Carlos, Toni, Alberto, Jalal, Pablo, Ali, Eva, Yesenia, Javi i Núria. Cal escriure els vostres noms per adonar-me de que he compartit aquest temps amb moltes persones i de tots vosaltres n’he aprés coses, tant en l’aspecte profesional com en el personal.

La meva gratitut i admiració profunda cap a Sasha Solodkov, sempre amb la resposta adequada a qualsevol pregunta o problema de software, per complicat que puguera ser. I també he de donar les gràcies a Tomáš Davídek per totes les discussions que hem tingut sobre l’Optimal Filtering en les que sempre he eixit sabent molt més que abans. Vull dedicar unes paraules també a Nils Gollub, perquè admire la seva capacitat de mirar amb la ment

completament oberta el treball diari, sovint trobant els camins més senzills. I també a Vincent Giangiobbe i Claudio Santoni, sense la seva ajuda part d'aquesta tesi no existiria.

Mereixen que repetisca els seus noms Belén Salvachúa i Esteban Fullana per totes les lliçons que d'ells n'he aprés respecte a l'Optimal Filtering, l'heréncia del grup que ens hem anat canviant de mans.

En l'aspecte personal, vull tindre paraules plenes de gratitut cap a la meva família en general i especialment cap als meus pares, que no es poden imaginar quant m'assemble a ells, pràcticament en cada cosa que faig. I el meu major desig és que dintre d'uns anys els meus fills senten alguna cosa pareguda al gran orgull que són ells per a mi. I també a Asun, que és un gran suport per a mi encara que haja de ser en la distància i mai oblidaré que, encara que involutàriament, gràcies a ella vaig voler fer-me físic.

I, com no, als meus jaios Vicenta i Paco... y a mis abuelos Patrocinio y Pepe, perque eixes flors estranyes ara les veig créixer a les voreres gràcies a vosaltres. I als meus oncles i ties pel suport i l'estima que em tenen, que és mutua, i als meus cosins, que sou una alegria per a mi i una gran promesa del que haurà de vindre, del que haureu de portar. Fran sent un xiquet el veia tenint somnis que resulta que han acabat molt semblants als meus i que fins i tot ha complit part dels meus (el número de Vecina en la teva esquena... y un par de magdalenas, hágame usted el favor). I Paquito probablement no siga conscient de que unes de les seves primeres paraules em va donar l'espenta final per agafar el camí que ha desembocat en aquesta tesi.

També vull destacar ací els bons moments que he pasat amb els meus amics i molt especialment amb Paco, Carlos, Jose i Ivan, que encara que "les agendes són plenes, massa feina i problemes", sé que sempre puc contar amb la seva far-reaching friendship. No sabeu com m'ajudeu sense voler a mantindre els peus a terra, i "és perentori aterrar". I a Paco li he d'agrair a més totes les vegades que m'ha salvat la vida fent en València els tràmits d'aquesta tesi que jo no podia fer des del CERN, gràcies de tot cor.

I les últimes paraules d'aquesta tesi només poden ser per a Arantxa: la meva única fortuna és despertar-me amb ella cada dia i és el que em dona la llum no ja per brillar, sinó simplement per a poder plantar cara al matí. Ha arribat l'hora de començar un altre llibre una altra vegada, i no m'imagine com podria fer-ho sense ella al meu costat.